

Controlled *In Vivo* Mechanical Stimulation of Bone Repair Constructs

A Dissertation
Presented to
The Academic Faculty

by

Angel Osborne Duty

In Partial Fulfillment
of the Requirements for the Degree
Doctorate of Philosophy in Bioengineering

Georgia Institute of Technology

April 2004

Controlled *In Vivo* Mechanical Stimulation of Bone Repair Constructs

Approved by:

Dr. Scott Boden

Dr. Andrés García

Dr. Ray Vito

Dr. Randell Young

Dr. Robert Guldberg, Chair

April 12, 2004

DEDICATION

To my two favorite men.

Truly, my husband Chad is my hero. Without his encouragement, support, and patience this dissertation would never have been completed. He endlessly served as a sounding board for new ideas, provided technical advice on mechanical issues, and simply listened when things went wrong. He unselfishly put his career plans on hold so that I could complete my Ph.D. work. His words and actions daily make his love unquestionable. For all these things and so many others, he deserves this recognition and my sincere gratitude.

This dissertation is also dedicated to my infant son Brandon who has made me happier than I ever thought possible. Being his mother is a joy and a privilege. He kept me company during the final stages of research and writing, whether with a friendly kick during surgeries before he was born or banging on the keyboard as I type this manuscript. This work is dedicated to him because I hope it will be an example to him that he can do or become anything he wants and that those things are worthy of his dedication and hard work.

ACKNOWLEDGEMENTS

I have had the distinct privilege of receiving assistance and encouragement for my graduate research work from a huge community of personal and professional supporters. Each of the individuals mentioned here contributed in meaningful ways to this work and therefore has my sincere gratitude.

My advisor, Dr. Robert Guldberg, deserves special recognition since his guidance has had the most influence on the content of this work. Furthermore, all the surgical skills I acquired were directly from his instruction. I especially appreciate his availability, patience, and personable nature. Few advisors would be so accommodating as to allow their student's infant to intrude on research meetings, but Bob regularly welcomed my son Brandon to his office.

I feel fortunate to have a very balanced advising committee from different backgrounds whose wisdom and constructive criticisms have made this research have broader impact. I thank each of them for their eager involvement and honest reviews. Specifically, I must thank Dr. Andrés García for his genuine interest in the project, his insistence on high research standards, and for always seasoning his criticisms with praise and encouragement – qualities I admire and hope to emulate. Thanks to Dr. Ray Vito for accommodating my random “pop-in” visits and questions. His advisement helped me navigate equipment design issues for the mechanical loading system. When I first met Dr. Randell Young during an internship spent at Osiris Therapeutics, I was impressed by the range of research experiments he was involved in. This breadth of experience in both *in vitro* and *in vivo* systems, and his detailed knowledge of mesenchymal stem cells were

valuable assests to my work. Finally, I thank Dr. Scott Boden who reminded me that although academic research may be a generation or two away from clinical application, it should always keep improved patient care as an objective.

I am also greatly indebted to my fellow students within the Guldberg lab. You could not ask for a more helpful or more friendly group of people. Each of them have generously given of their time and skills to make this project a success, even when their own projects were more than enough to occupy their time. The easy-going spirit of the lab and lively conversation made coming to the lab everyday a pleasant experience and I will miss them terribly. As the “pioneers” of the lab, Natasha Case and I have shared our experiences throughout our graduate career. She has been a constant source of help, advice, and simply a shoulder to cry on for the last seven years. Without her significant contributions to the rabbit allograft study, the project would have been completely overwhelming. In much the same way, the hard work of Megan Oest allowed the timely completion of the rat subcutaneous study. But not just these two individuals alone, but every member of the laboratory including Blaise Porter, Rhima Coleman, Angela Lin, Srinidi Nagaraja, Galen Robertson, Gaylon Hollis, Craig Duvall, and Chris Gemmiti contributed to this work. In fact, each one of these individuals, in addition to Benjamin Byers and Jennifer Phillips, provided support services during the many long days performing surgeries.

Many others outside the laboratory also contributed their services, materials, and/or technical expertise to this project. Thanks to Dr. Laura O’Farrell, Cherry Corley, Lydia Weathers, Dr. Bent Swenson, Dr. Mike Fallon, Jim McNeil, and Sandy Yurevich for providing excellent animal care and husbandry at both the IBB Physiologic Research

Laboratory at Georgia Tech and the vivarium at the Emory Veteran's Administration Hospital. Most histologic processing was performed by Tracey Couse, one of IBB's best technical assets, but additional work was also provided by the Emory University Cardiology Histology staff, as well as the histology staff at the Emory Spine Center. All bone chambers were machined at the Georgia Tech School of Mechanical Engineering Machine shop by John Graham, Don Long, and cooperative education students in the shop. The electronics shop within the Mechanical Engineering department designed and built the external solenoid-driven hydraulic loading systems employed in this research. Special thanks to John Witzel, Vladimir Bortkevich, Jimmy Hill, Chaz Keller, and Kyle French for their work on the hydraulic system.

Dr. Louisa Titus and Dr. Scott Boden generously provided trabecular allograft tissue for this work and furthermore, my initial training in RNA extraction and RT-PCR techniques was acquired in their laboratories under the advisement of Dr. Greg Hair, Michelle Racine, and Dr. Modjala Viggewarapu. Osiris Therapeutics, Inc. of Baltimore, MD provided the mesenchymal stem cells and lot-tested serum for this work. Dr. Susan Peter offered technical assistance in the culturing of the MSCs. Dr. Andres Laib of Scanco, Inc. gave assistance with the microCT equipment and associated image processing language, while Dr. Bert van Rietbergen provided support for the Scanco Finite Element Modeling Software.

I gratefully acknowledge financial support for the rabbit allograft study from the Whitaker Foundation. Funding was provided for the subcutaneous tissue engineering study from the Georgia Tech/ Emory Center for Engineering of Living Tissues (NSF EEC-9731643) and the National Science Foundation (NSF BES-0101239). Additionally,

I thank the Whitaker Foundation and Medtronic Foundations for their provision of graduate student fellowships.

In addition to the overwhelming support of my husband, I have also received the generous support of many family members and friends. I have a great debt of gratitude to my parents Roger and Glenda Osborne who have *always* believed in my dreams and have done everything they could to make sure I had the tools to achieve them. This dream was certainly no exception. Not only did they verbally encourage me throughout the process, but also gave many weeks of their time to provide childcare so that I could continue my research even after the birth of my son. Likewise, my second family, my husband's parents Charles and Charlotte Duty also provided childcare to ensure my ability to complete my research. I have also had the support of my brother Brian Osborne and his wife Teresa. Furthermore, encouragement from my brother-in-law and sister-in-law Drs. Karl and Cheryl Martin has been especially meaningful to me since they both know from experience the challenges involved in graduate research. Finally, I thank the members of my Sunday School class at Eastside Baptist Church in Marietta, Georgia who have sheltered me in their prayers for many years, even specifically praying for my research – even though it was the first time many of them had ever prayed specifically for a rat!

Finally, I thank God the Creator since I am privileged to study His finest creation – the human body. Our vain attempts as tissue engineers produce but poor imitations of the complex, but perfectly orchestrated, symphony of cells, proteins, and regulatory molecules which He merely breathed into existence. But not only is His creation the source of inspiration for this work, but He has been my sustenance through this long experience.

Trust in the Lord with all your heart and lean not on your own understanding; in all your ways acknowledge Him, and He will make your paths straight.

Proverbs 3:5-6

TABLE OF CONTENTS

DEDICATION.....	iii
ACKNOWLEDGEMENTS	iv
TABLE OF CONTENTS	ix
LIST OF FIGURES	xii
LIST OF TABLES	xvii
LIST OF ABBREVIATIONS	xviii
SUMMARY.....	xix
CHAPTER 1: INTRODUCTION.....	1
1.1 MOTIVATION	1
1.2 GOAL & GLOBAL HYPOTHESIS.....	4
1.3 OBJECTIVES	4
1.4 SIGNIFICANCE.....	7
CHAPTER 2: LITERATURE REVIEW.....	9
2.1 BONE STRUCTURE.....	9
2.2 ROLE OF THE MECHANICAL ENVIRONMENT	10
2.3 BONE CHAMBER SYSTEMS.....	13
2.4 BONE DEFECT REPAIR.....	17
2.5 BONE TISSUE ENGINEERING.....	18
CHAPTER 3: EFFECTS OF CYCLIC MECHANICAL COMPRESSION ON THE REPAIR OF FROZEN ALLOGRAFTS IN A LAPINE BONE DEFECT MODEL.....	26
3.1 INTRODUCTION	26
3.2 METHODS AND MATERIALS	29
3.3 RESULTS.....	47
3.4 DISCUSSION	64
CHAPTER 4: DESIGN AND DEVELOPMENT OF A NOVEL MECHANICAL LOADING DEVICE FOR USE AS A SUBCUTANEOUS <i>IN VIVO</i> BIOREACTOR IN A RODENT MODEL.....	70
4.1 INTRODUCTION	70
4.2 SUBCUTANEOUS PILOT EXPERIMENTS.....	73
4.3 SYSTEM DESIGN.....	90
4.4 TUBING & LOADING PILOT EXPERIMENTS.....	99
4.5 DISCUSSION	102

CHAPTER 5: CYCLIC MECHANICAL COMPRESSION ENHANCES THE DEVELOPMENT OF ORTHOPAEDIC TISSUE CONSTRUCTS IN A SUBCUTANEOUS <i>IN VIVO</i> BIOREACTOR	104
5.1 INTRODUCTION.....	104
5.2 METHODS AND MATERIALS	107
5.3 RESULTS.....	130
5.4 DISCUSSION.....	158
CHAPTER 6: CONCLUSIONS AND RECOMMENDATIONS.....	164
6.1 CONCLUSIONS.....	164
6.2 RECOMMENDATIONS.....	168
APPENDIX A: MACHINE DRAWINGS	172
A.1 RABBIT ORTHOTOPIC BONE CHAMBERS.....	173
A.2 CLAMP FOR BISECTING RABBIT CHAMBER BIOPSIES.....	178
A.3 RAT SUBCUTANEOUS LOADING CHAMBER.....	179
A.4 PROTOTYPE MANIFOLD FOR RAT SUBCUTANEOUS LOADING CHAMBERS.....	183
A.5 PLATFORM HOUSING FOR LOAD CELL AND CALIBRATION RAT SUBCUTANEOUS CHAMBER	185
A.6 TABLETOP PLATFORM TO HOLD RAT SUBCUTANEOUS CHAMBER DURING COMPRESSION TESTING.....	188
APPENDIX B: SURGICAL PROCEDURES	189
B.1 PROCEDURE TO IMPLANT RABBIT HYDRAULIC BONE CHAMBER.....	190
B.2 PROCEDURE FOR A NON-TERMINAL BIOPSY OF THE RABBIT HYDRAULIC BONE CHAMBER.....	193
B.3 PROCEDURE TO IMPLANT SUBCUTANEOUS LOADING TUBING IN RABBITS.....	194
B.4 PROCEDURE FOR IMPLANTATION OF SUBCUTANEOUS RAT LOADING DEVICE ...	198
B.5 PROCEDURE FOR EXPOSING IMPLANTED TUBING FOR LOADING SESSIONS IN RATS.....	204
APPENDIX C: LOADING PROCEDURE FOR RABBIT HYDRAULIC BONE CHAMBER STUDIES.....	208
C.1 STANDARD LOADING PROCEDURE FOR RABBIT HBCS.....	209
C.2 DEALING WITH ANOMALIES EXPERIENCED DURING LOADING RABBIT HBCS...	211
APPENDIX D: RT-PCR PROTOCOLS	213
D.1 PROTOCOL WORKSHEET FOR REVERSE TRANSCRIPTASE REACTION TO CONVERT RNA INTO cDNA.....	214
D.2 PROTOCOL WORKSHEET FOR RADIOACTIVE PCR.....	216
APPENDIX E: PICO-GREEN ASSAY FOR DOUBLE-STRANDED DNA ON CELL-SEEDED HA/TCP OR PLDL.....	221
APPENDIX F: FINITE ELEMENT MODELING PROCEDURES FOR RABBIT TRABECULAR BONE.....	225
F.1 DETERMINATION OF THE TISSUE MODULUS OF RABBIT TRABECULAR BONE....	226
F.2 MODELING OF TWO REPRESENTATIVE RABBIT TRABECULAR BONE ALLOGRAFTS.....	229

F.3 POST-PROCESSING OF TWO REPRESENTATIVE RABBIT TRABECULAR BONE ALLOGRAFTS.....	232
APPENDIX G: FINITE ELEMENT MODELING PROCEDURES FOR PLDL .	235
G.1 DETERMINATION OF PLDL TISSUE MODULUS.....	236
G.2 MODELING OF THREE REPRESENTATIVE PLDL SAMPLES.....	239
G.3 POST-PROCESSING OF THREE REPRESENTATIVE PLDL SAMPLES.....	245
REFERENCES	283
VITA.....	300

LIST OF FIGURES

Figure 1. Hydraulic Bone Chambers for Rabbits.....	32
Figure 2. External Solenoid-Driven Loading System.....	32
Figure 3. Zones of Analysis for Fluorescent Microscopy.....	41
Figure 4. Mechanical Testing Setup: a) Sample in HBC, b) HBC in Platform Submerged in PBS bath, c) Loading Rod, d) MTS TestarIIm 858 Mini Bionix Load Frame	43
Figure 5. Coordinate System Used for Finite Element Models	45
Figure 6. Osteoblasts Line Trabecular Allograft Surface of a Loaded Allograft; H&E at 40x.....	48
Figure 7. Appositional Bone Formation on a Nonloaded Allograft; H&E at 20x.....	49
Figure 8. Intramembraneous New Bone Formation within a Loaded Sample; Goldner’s Trichrome at 20x.....	50
Figure 9. Endochondral Bone Formation in a Loaded Sample; H&E at 20x	50
Figure 10. Typical New Bone Formation on Allografts without Loading (Left) and with Four Weeks of Load (Right); A = Allograft, NB = New Bone; 20x	51
Figure 11. Photomicrographs of allografts: A,B) Goldner’s Trichrome; C,D) Tetracycline fluorochrome; E,F) Calcein fluorochrome. A, C, E are 4x. B, D, F are 20x.	52
Figure 12. New Bone Volume Normalized by the Available Graft Surface Area for Each Biopsy Pair from the Long-Term Loading Study of Rabbit Trabecular Allografts and the Overall Average for the Group (p=0.009).....	55
Figure 13. Representative sections of a loaded (left) and nonloaded (right) sample stained for α -SMA (bright pink) at 10X.	56
Figure 14. Number of vessels per section as identified by positive α -SMA staining for each loaded and nonloaded sample in the long-term study.....	57
Figure 15. Histogram of Normal Strain in the Z-direction.....	60
Figure 16. Histogram of Largest Principal Strain	60
Figure 17. Histogram for Von Mises Stress.....	61

Figure 18. Histogram for Strain Energy Density.....	61
Figure 19. Representative Cross-Sections (Central 340 microns) of Finite Element Model Coded for the Tissue Level Largest Principal Strain and Von Mises Stress....	63
Figure 20. Polycaprolactone Microarchitecture.....	74
Figure 21. Positions for Scaffold Implantation.....	77
Figure 22. Subcutaneous Implantation of a Tissue-Engineered Bone Scaffold within a Titanium Chamber.....	78
Figure 23. A Representative Cell-Seeded PLDL Scaffold Labeled for Live (Green) and Dead (Red) Cells; A) Single Slice, B) Normal Projection of All Confocal Slices, C) Side Projection of All Confocal Slices	81
Figure 24. Representatives of Each Scaffold Material at Time of Harvest; A) Ha/TCP, B) PLDL, C) PCL.....	82
Figure 25. MicroCT Images of Cell-Seeded Scaffolds Implanted Subcutaneously for Six Weeks. These Samples had No rhBMP-2 Treatment.....	83
Figure 26. Mean BVP Comparisons Based on Material Type, Enclosure in a Titanium Chamber, Treatment with rhBMP2, Cell Type and Passage Number	86
Figure 27. Mean BVP Comparison for PCL Samples Implanted Within a Titanium Chamber of Directly in the Subcutaneous Space	87
Figure 28. New Bone Formation on BMP2-Pretreated Ha/TCP Seeded with P4 rMSCs and Implanted Subcutaneously in a Titanium Chamber; Plastic Sections with Sanderson's Rapid Bone Stain viewed at 20x.....	88
Figure 29. Assembly of Initial Prototype for Manifold and Rat Subcutaneous Loading Chambers.....	94
Figure 30. Assembly of Prototype Manifold and Chambers with Necessary Hardware .	94
Figure 31. Assembly of Piston, Sample, and Base Platen (Left to Right) into the Rat Subcutaneous Chamber.....	95
Figure 32. Assembly of Standard Manifold with Subcutaneous Rat Chambers for Loading Experiments; Top (Loaded), Bottom (Nonloaded).....	98
Figure 33. Representative Stress-Strain Curves for Failure Tests of PLDL Made with 30% Porogen.....	111
Figure 34. Solenoid-driven Loading System used to Compressively Load Constructs in Rat Subcutaneous Chambers	120

Figure 35. Stainless Steel Manifold on External Loading System	121
Figure 36. Mock Chamber Setup for Calibration of the External Solenoid-Driven Loading System.....	122
Figure 37. Representative Cell-Seeded PLDL Scaffolds from Each of the Three Seeding Groups Labeled for Live (Green) and Dead (Red) Cells; View Shown is Along the Longitudinal Axis	132
Figure 38. Average Number of Cells Attached to Cell-Seeded Scaffold for Each Seeding Group, (Mean + Standard Error, n=3).....	133
Figure 39. Mineralization on PLDL Scaffolds Cultured <i>in vitro</i> for 1, 7, 8, or 14 weeks as a Function of the Seeding Group	134
Figure 40. Select MicroCT Images of Each of the In Scaffolds in Parallel Osteogenic <i>In vitro</i> Culture for 1, 7, 8, or 14 Weeks	135
Figure 41. Mineralization on PLDL Scaffolds Cultured <i>in vitro</i> for 1, 7, 8, or 14 weeks as a Function of Time in Culture (Mean + Standard Error, n=3).....	136
Figure 42. MSC-seeded PLDL cultured in osteogenic supplements for 8 weeks; A) interior surface, B) exterior surface; H&E stain at 20x.....	137
Figure 43. Von Kossa staining of PLDL cultured in osteogenic media for 8 weeks with cells (A & C) and without cells (B & D); 10x (A & B) and 40x (C & D).....	138
Figure 44. Loaded (left) and Nonloaded (right) Chambers <i>In Situ</i> at Time of Harvest.	139
Figure 45. Nonloaded 8-Week Preculture Sample With H&E Staining Showing Tissue Filling Pore Spaces; 4x.....	141
Figure 46. Cuboidal Shaped Cells Lining Polymer Pore In An 8-Week Preculture Nonloaded Sample; H&E 40x.....	141
Figure 47. Reddish-Orange Areas Indicating New Bone Formation In An 8-Week Loaded Specimen; mMAB 20x.....	143
Figure 48. Examples Of Positive Von Kossa Staining (Black) Both On A Polymer Surface And Within The Pore Space For An 8-Week Preculture Loaded Sample; 10X and 40X	143
Figure 49. Loaded 8-Week Preculture Sample With Positive Von Kossa Staining (Black) Concentrated More On One End Of Surface Than The Other; 4X...	144
Figure 50. Representative MicroCT Images of Mineral Formed on PLDL in the 8-Week Preculture Group Without <i>In vivo</i> Loading (Left) and With <i>In vivo</i> Loading (Right)	146

Figure 51. Mineralization after Six Weeks <i>In vivo</i> with or without Two Weeks Loading of PLDL with Different Scaffold Preparations (A: Cell-free, B: Cell-Seeded with No Preculture, C: Cell-Seeded with 1 Week Preculture, D: Cell-Seeded with 8 Weeks Preculture, E: All Preparation Groups); (Mean + Standard Error, 5 n 10).....	148
Figure 52. Longitudinal Differences in Bone Formation in 8-week Preculture Samples Loaded <i>in vivo</i>	149
Figure 53. Histogram of the Largest Principal Strain within the Polymer	151
Figure 54. Histograms of Largest Principal Strain within the Interstitial Tissue	151
Figure 55. Histogram of the Von Mises Stress within the Polymer	152
Figure 56. Histogram of the Von Mises Stress within the Interstitial Tissue	152
Figure 57. Histograms of the Strain Energy Density within the Polymer	153
Figure 58. Histograms of the Strain Energy Density within the Interstitial Tissue	153
Figure 59. Representative Cross-Sections (150 microns) of Finite Element Model Coded for the Tissue Level Largest Principal Strain and Von Mises Stress in Both the Polymer and the Interstitial Tissue.....	155
Figure 60. Longitudinal Variation in Stress/Strain Response in PLDL.....	157
Figure 61. Longitudinal Variation in Stress/Strain Response in Interstitial Tissue	157
Figure 62. Machine Drawing of Nonloaded Rabbit Orthotopic Bone Chamber	173
Figure 63. Machine Drawing of Cap for Nonloaded Rabbit Orthotopic Bone Chamber	174
Figure 64. Machine Drawing of Loaded Rabbit Orthotopic Bone Chamber.....	175
Figure 65. Machine Drawing of Cap for Loaded Rabbit Orthotopic Bone Chamber....	176
Figure 66. Machine Drawing of Piston for Loaded Rabbit Orthotopic Bone Chamber	177
Figure 67. Machine Drawing of Clamp to Hold Rabbit Chamber Biopsies During Bisection with Isomet Saw	178
Figure 68. Machine Drawing of Rat Subcutaneous Chamber	179
Figure 69. Machine Drawing of Base Platen for Rat Subcutaneous Chamber.....	180
Figure 70. Machine Drawing of Piston for Rat Subcutaneous Chamber.....	181

Figure 71. Compacted Assembly of Piston, Sample, and Base Platen in Rat Subcutaneous Chamber Illustrating How Sample Is Positioned Relative to Vascular Infiltration Ports	182
Figure 72. Machine Drawing of Prototype Manifold for Four Rat Subcutaneous Chambers; Top, Front, Side, and Isometric Views Shown	183
Figure 73. Machine Drawing of Prototype Manifold for Four Rat Subcutaneous Chambers; Bottom View Shown.....	184
Figure 74. Machine Drawing of Platform Base with Circular Hole Pattern to Match Omega’s Ten-Pound Button Load Cell	185
Figure 75. Machine Drawing of Platform Sides (Two Required)	186
Figure 76. Machine Drawing of Platform Top with Center Hole to Hold a Rat Subcutaneous Chamber with the Base Removed	187
Figure 77. Machine Drawing of Tabletop Platform for Mechanical Testing within Rat Subcutaneous Chamber	188
Figure 78. Incision Site for Rabbit Hydraulic Bone Chamber	190
Figure 79. A Pneumatic Drill with Trephine and Trephine Guide was Used to Score the Bone Surface to Remove the Cortex.....	191
Figure 80. Position of Implanted Hydraulic Bone Chamber in Rabbits	192
Figure 81. Thin-Walled Extraction Device.....	193
Figure 82. Bonded Felt Cuff on Polyurethane Tubing	194
Figure 83. Diagram of Tools Used to Route Tubing Subcutaneously in Rabbits.....	196
Figure 84. Placement of Silk Sutures to Anchor Rat Subcutaneous Loading Device ...	203
Figure 85. Steps to Expose Tubing for Rat Loading Procedure; A) Anesthesia Induction, B) Incision and Exposure of Tubing, C) Addition of Connector, and D) Re-implantation of Tubing and Wound Closure.....	205
Figure 86. Thin Plastic Cone Restrainers Used During Rat Loading Procedures	206

LIST OF TABLES

Table 1. Statistical Data for Graft and New Bone Measurements.	55
Table 2. Bone Volume Fraction of Biopsies from Long-Term Loading Group	58
Table 3. Average Predicted Tissue Level Response of Long-Term Loaded Samples.....	62
Table 4. Various Tissue-Engineered Scaffolds Tested in Feasibility Experiments	76
Table 5. Mean Bone Volume Parameter, Standard Error of the Mean, and Sample Size for Each Treatment Condition Tested	84
Table 6. Failure Test Results for PLDL with 30% Porogen.....	111
Table 7. Microarchitectural Parameters for PLDL Produced for <i>In vivo</i> Loading Experiment; Average \pm Standard Error.....	114
Table 8. Treatment Groups and Number of Each Implanted.....	119
Table 9. Number of Samples Harvested per <i>In vivo</i> Treatment Group	140
Table 10. Number of Samples Included in Statistical Analysis per <i>In vivo</i> Treatment Group.....	146
Table 11. Summary of the Mechanical Response Predicted by Finite Element Models for Both Polymer and Interstitial Tissue	154
Table 12. Working Plate Layout (12x8 Grid).....	217
Table 13. Worksheet for Adjusting Sample Volume for PCR Reaction	218
Table 14. Worksheet for Preparing PCR Master Mixes	219
Table 15. Relative Volumes (μ L) Of Cell Suspension, Media, And TTH Required For Each Solutioni In The Cell Ladder.....	224

LIST OF ABBREVIATIONS

MSC	Mesenchymal Stem Cell
HBC	Hydraulic Bone Chamber
SLC	Subcutaneous Loading Chamber
Micro-CT	Microcomputed Tomography
TRAP	Tartrate-Resistant Acid Phosphatase
PBS	Phosphate Buffered Saline
RT-PCR	Reverse-Transcriptase Polymeric Chain Reaction
mMAB	modified Mallory Aniline Blue
BVF	Bone Volume Fraction
PLDL	Poly(L-lactide-co-D,L-lactide 70:30)
PCL	Polycaprolactone
Ha/TCP	60-40 Hydroxyapatite/Tricalcium Phosphate
FBS	Fetal Bovine Serum
AsAp	Ascorbic Acid 2-Phosphate
Dex	Dexamethasone
H&E	Hematoxylin and Eosin
Ca	Calcium
Mg	Magnesium
Na	Sodium
α -SMA	α -Smooth Muscle Actin

SUMMARY

Bone grafts are used to treat more than 300,000 fracture patients yearly [1], as well as patients with congenital defects, bone tumors, and those undergoing spinal fusion. Given the established limitations of autograft and allograft bone, there is a substantial need for bone graft substitutes. Tissue engineering strategies employing the addition of osteogenic cells and/or osteoinductive factors to porous scaffolds represent a promising alternative to traditional bone grafts. While many bone defects are in load-bearing sites, very little is known about the response of bone grafts and their substitutes to mechanical loading, despite vast documentation on the ability of normal bone to adapt to its mechanical environment. The goal of this research was to quantify the effects of controlled *in vivo* mechanical stimulation on bone graft repair and bone graft substitutes and identify the local stress/strain environment associated with load-induced changes in bone formation.

The global hypothesis that cyclic *in vivo* mechanical loading improves mineralized matrix formation within bone grafts and bone graft substitutes was addressed in this work using orthotopic and ectopic models specifically designed to facilitate modeling of local stresses and strains. In the first study, a bone defect repair model utilizing an orthotopic implant capable of supplying a controlled mechanical stimulus to a trabecular allograft showed a significant reduction in new bone formation with controlled *in vivo* mechanical loading. Although the reason remains unclear, loading conditions may not have been ideal for increased bone formation or potential micromotion may have influenced the results. A second study demonstrated for the first time that controlled *in*

vivo mechanical stimulation enhances mineralized matrix production on a mesenchymal stem cell-seeded polymeric construct using a novel subcutaneous implant system. In addition, the local stresses and strains associated with this adaptive response were predicted. The novel subcutaneous implant represents technology which may be adapted for the preparation of tissue-engineered bone constructs, capitalizing on the benefits of mechanical loading and a vascularized *in vivo* environment. Such an approach may produce larger, stronger, and more homogeneous constructs than could be developed in a static culture system subject to diffusional limitations.

CHAPTER 1

INTRODUCTION

1.1 Motivation

Local bone loss from trauma or long-term degeneration is a major cause of patient disability. Given an adequate local supply of osteoprogenitors, osteoinductive proteins, and vascularity, bone displays a remarkable capacity for repair and regeneration. Unfortunately, 5-10% of the six million fractures occurring in the United States yearly require bone grafting procedures to augment the natural regeneration process [1]. Numerous other clinical applications, including spine fusion, bone tumors, metabolic bone disorders, and congenital defects, also commonly require some form of treatment. While commonly used clinically, autograft and allograft bone transplantation have well documented limitations that motivate the development of bone graft substitutes. Numerous strategies are being pursued to develop bone graft substitutes by combining osteoinductive factors or cells with porous scaffolds. The goal of such efforts is typically to provide an initial structural framework along with bioactive factors that will stimulate rapid formation of new bone and restoration of local function.

Two critical factors in bone repair and regeneration are vascularity and mechanical function. An adequate local vascular supply is required for bone formation to occur. Bone repair constructs developed *in vitro*, for example, are characterized by a non-physiologic distribution of mineralized matrix around the periphery of the construct.

An *in vivo* bone tissue engineering strategy that includes an integrated vascular supply may circumvent this limitation. The mechanical loading environment also plays a key role in bone function. Bone is an adaptive organ, capable of renewal, and responds to changes in its mechanical environment. Vast documentation exists on bone atrophy caused by disuse and conditions of microgravity, as well as on the ability of bone to remodel in response to exercise [2-9]. Controlled studies of *in vivo* loading of whole bones show an adaptive response to compensate for the applied stimulus [10, 11]. Under repair conditions, the local mechanical environment of a repairing fracture callus contributes to tissue differentiation [12-16]. Consistent with these observations, osteoprogenitors and osteoblasts in culture are highly responsive to mechanical stimuli [17-21]. Given the sensitivity of bone to mechanical cues, it is reasonable to consider the use of controlled mechanical stimuli as a means to enhance bone repair or the development of bone graft substitutes.

There are at least three possible settings in which mechanical loading may be employed to enhance the ability of a scaffold to repair a bone defect: 1) the *in situ* orthotopic environment, 2) the *in vitro* preparation of a bone replacement scaffold, and 3) finally, the *in vivo* ectopic preparation of a bone replacement construct. A few therapies have capitalized on *in vivo* mechanical loading. Distraction osteogenesis represents a successful application of *in situ* application of mechanical forces to enhance bone repair in the distraction gap [22]. However, the application of a controlled load to a scaffold filling a bone defect is a more challenging situation since the scaffold often has inadequate mechanical integrity and poor bone/implant stability initially. It has also been postulated that the application of a low magnitude, high frequency vibration could be

used to prevent or possibly treat osteoporosis [23, 24]. In addition, control of the local mechanical environment can be used *in vitro* on monolayer or three-dimensional cultures to direct the differentiation of cells toward an osteoblastic phenotype and enhance mineralization of the secreted matrix [25-27]. Diffusional limitations however hamper the use of *in vitro* technologies to adequately prepare three-dimensional constructs for bone defect repair. Finally, mechanical loading may potentially be employed ectopically in an *in vivo* “culture” environment to enhance the development of scaffolds intended for bone replacement. Such an approach could capitalize on the presence of an adequate vascular supply to promote bone formation. This third area represents an as yet unexplored avenue of research.

While mechanical loading of normal bone has been extensively studied, the effects of mechanical loading on three-dimensional architectural bone grafts and bone graft substitutes have not been characterized. Since the structure is distinctly different from normal bone in that cells simply line a three-dimensional structure without the benefit of an established canalicular network, the mechanism(s) by which the cells respond to mechanical signals may be altered or absent. To gain a better understanding of mechanically-induced changes in bone formation for any three-dimensional structure, whether normal bone or a tissue-engineered construct, knowledge of the local stresses and strains at the trabecular level provide useful indices of mechanical signals associated with adaptive responses. Unfortunately, this information has not been fully characterized for normal bone and no investigations have considered the local mechanical environment of a tissue-engineered bone substitute subject to a mechanical stimulus. Examination of the local mechanical environment can currently only be performed using theoretical

models using finite element analysis and therefore require the use of specially designed testbeds which provide stringent control of the specimen's boundary conditions. A well-defined knowledge of the local stresses and strains associated with adaptive changes in bone formation on a three-dimensional structure would provide useful design information for the production of future tissue-engineered bone substitutes.

1.2 Goal & Global Hypothesis

The goal of this dissertation work is to quantify the effects of controlled *in vivo* mechanical stimulation on bone graft repair and bone graft substitutes and identify the local stress/strain environment associated with load-induced changes in bone formation. The global hypothesis that cyclic *in vivo* mechanical loading enhances mineralized matrix formation within bone grafts and bone graft substitutes was tested using experimental devices implanted at orthotopic and ectopic sites.

1.3 Objectives

The following three objectives were outlined to test the global hypothesis.

*Objective #1: To correlate the local mechanical stress/strain environment with patterns of bone formation on trabecular bone allografts subject to cyclic *in vivo* mechanical stimulation in an orthotopic site.*

While others have investigated effects of mechanical compression on bone *in vivo*, the effect of *in vivo* mechanical compression on cell-populated matrix materials has not been determined. Furthermore, correlation of the local trabecular mechanical environment to local patterns of bone formation has not been accomplished. An

academic model of defect repair utilizing an orthotopic bone chamber capable of supplying a controlled mechanical stimulus to a repairing trabecular allograft within the implant was used to address this objective. Although not a clinical model of bone defect repair, this model, when used to study loading of a scaffold with a known architecture such as traditional allografts, provides the necessary controlled environment to determine the local tissue strains and stresses that result in adaptive bone formation. Knowledge of a specific adaptive mechanical environment will help define design criteria for more clinically relevant applications of mechanical loading for the development of tissue-engineered bone replacement constructs. It is hypothesized that cyclic *in vivo* mechanical loading will increase mineralization of the trabecular bone allografts in an orthotopic site and that areas of new bone formation will positively correlate with higher local trabecular strains.

Objective #2: To design and develop a novel implantable bioreactor system to apply controlled mechanical stimuli to tissue-engineered constructs in a subcutaneous in vivo environment.

An original implant system capable of applying a controlled mechanical stimulus to cylindrical scaffolds implanted subcutaneously in a rat was designed and created. Such a system may provide the ability to develop larger, stronger, and more homogeneous vascularized bone tissue replacements than could be developed in a diffusionally limited *in vitro* culture system. Such pre-conditioned constructs may be better able to meet the functional demands of the bony environment. Furthermore, if

constructs are developed in the final host, they may be populated with receptive host cells that will reduce the immunologic challenge presented to the patient when the bone defect is repaired. Furthermore, such an implant would provide a well-controlled environment suitable for modeling tissue-level stresses and strains, allowing for characterization of adaptive mechanical signals.

Objective #3: To quantify the effects of construct preculture time and controlled in vivo mechanical loading on mineralized matrix formation within cell-seeded scaffolds implanted into a subcutaneous bioreactor including characterization of the associated local mechanical stresses and strains.

Finally, work was undertaken to demonstrate the ability of *in vivo* cyclic mechanical compression to improve bone formation on a tissue-engineered construct. However, the development of an ideal bone replacement product may also involve some form of *in vitro* preculture as well, so the influence of various amounts of exposure to osteogenic supplements in *in vitro* culture prior to implantation and loading was examined. It is hypothesized that cyclic *in vivo* mechanical loading and longer times in *in vitro* preculture will increase mineralized matrix formed within tissue-engineered constructs implanted in a subcutaneous bioreactor. In order to establish the local mechanical signals associated with potential load-induced changes in mineralization on tissue-engineered constructs, the trabecular level stresses and strains were modeled.

1.4 Significance

While most fractures heal suitably, over 300,000 of these injuries experience complications that may be remedied by a tissue-engineered bone substitute [1]. Currently, the market for bone grafts and bone substitutes represents more than a \$270 million industry [28]. Significant donor site morbidity, compromised structural integrity, and limited quantities of available bone restrict the clinical value of autograft bone and recent incidents of disease transmission from banked tissues have created increased interest in alternatives. A tissue-engineered bone replacement product could find a substantial place in the bone graft and substitute market.

Tissue engineering however is a field still quite in its infancy. There are many challenges to be met in the design of tissue replacements. They must not only meet the biological requirements of the tissue, but also must consider the biomechanical requirements of the tissue, especially for tissues that are normally mechanically challenged such as musculoskeletal tissues. In September 2000, a group of engineers, biologists, and clinicians convened a Functional Tissue Engineering Workshop in which key target areas of future research for this emerging field were outlined. One of the stated critical areas was to “determine how mechanical stimulation of cell-matrix implants modulates engineered tissue structure and function.” Furthermore, a need was also expressed to “solve implant size issues by exceeding functional limitations of diffusion” [29]. The research presented in this body of work targets these two critical areas.

This research seeks to translate knowledge about the mechanoresponsiveness of bone into a mechanism to improve cell-seeded constructs for bone defect repair. While a

great deal is known about the adaptive properties of bone to mechanical loading, there has been little translation of this knowledge into therapeutic applications for bone defect repair. This work is the first research to demonstrate the ability of controlled *in vivo* mechanical stimulation to enhance mineralized matrix production on a polymeric scaffold seeded with osteogenic cells. The use of mechanical loading during construct development may improve mineralization of such constructs allowing them to better support the mechanical demands of the orthotopic environment. Combining mechanical preconditioning of cell-seeded constructs with the benefits of a vascular *in vivo* environment may be able to produce larger, more homogeneous, and potentially stronger constructs, circumventing the size and diffusional limitations of current tissue engineering approaches. Furthermore, a set of tissue level stresses and strains experienced by the loaded tissue-engineered constructs were predicted to facilitate the design of future tissue-engineered constructs which may be subject to mechanical forces either *in vivo* or during construct development.

CHAPTER 2

LITERATURE REVIEW

2.1 Bone Structure

Bone serves many important roles including hematopoiesis, mineral homeostasis, and several mechanical functions such as the protection of vital organs and provision of the necessary supportive framework for skeletal mobility. It is the dynamic nature of a person's mobility requirements that drives bone's organization, making the structure and function of bone intimately intertwined. A bone's organization is typically classified as either cortical or trabecular. The microstructural unit of cortical bone consists of many concentric layers of matrix that is penetrated by a single longitudinal canal and various transverse canals. Many of these units placed longitudinally side-by-side make up the overall structure. Cortical bone is therefore very dense and is found in areas requiring high strength and stiffness, typically the shafts of long bones. While trabecular bone is comprised of a layered microstructural unit, the layers are not concentric and the overall structure is a porous network that may resemble either plates or rods. The ratio of plates to rods is modulated by the mechanical demands placed on the tissue [30]. As a result of this porous network, trabecular bone is lightweight and effectively absorbs and distributes loads making it an ideal architecture for the epiphyseal region of long bones where load distribution across an articulating joint surface reduces the impact of loading on adjoining bone and cartilage.

2.2 Role of the Mechanical Environment

Bone is an adaptive organ, capable of renewal and responds to changes in its mechanical environment. While Wolff receives most credit for formally postulating in the late 19th century that bone's architecture and function are inextricably linked [31, 32], Galileo had observed that the shape of a bone corresponded to its mechanical integrity as early as 1638. After Lanyon first instrumented *in vivo* bone tissue with strain gages in 1973 providing the first quantification of the mechanical signals that regulate adaptation [33], Frost presented his Mechanostat theory in 1987 which proposed that strain magnitude thresholds could predict the adaptive response of bone [34-36]. Observations of deteriorating properties of bone in naturally occurring instances of disuse such as bedrest [2, 37, 38], microgravity [3-5, 39], paralysis [40], surgery recovery [41], and edentation [42, 43] are plentiful. Controlled research involving models of disuse such as tail-suspension of rats [44, 45] and limb immobilization [46-48] demonstrate both the changes in architecture and mechanical properties that result when mechanical loads on bone are reduced or removed. Conversely, research involving exercise has demonstrated that sedentary individuals have less bone mass than those who exercise [6] and that exercise programs can increase bone mass at least temporarily [7, 8]. Furthermore, exercise programs have been shown to reduce bone loss in post-menopausal women [9, 49].

While much research has focused on the role of mechanical factors in remodeling of normal bone, the mechanical environment of a fracture site also plays a direct role in repair of bone, directing tissue differentiation. Both transmitted loads and interfragmentary motion can be used to predict the clinical outcome of a fracture. The

removal of all transmitted loads such as occurs when a fracture is treated with rigid internal fixation will often result in intramembraneous ossification with delayed union accompanied by reduced final bone strength. Conversely, if there is too much interfragmentary motion, cartilage or fibrous tissue will form rather than bone. An intermediate level of mechanical stimulation where interfragmentary motion is restricted but not eliminated tends to enhance the inflammatory stage, encouraging greater vascularity, which promotes bone healing [12-16, 50].

Given the important role of mechanical loading on bone formation, the potential to develop therapies utilizing mechanical loading to enhance bone repair and regeneration has been noted. Much research has focused on determining the characteristics of an optimal loading regimen. Overall, studies consistently show that bone formation is influenced by strain rate, frequency, amplitude, and duration of loading [51-55]. Furthermore, cyclic loading is absolutely necessary to elicit an adaptive response. Static loads simply do not invoke a significant amount of bone formation [56-58]. Furthermore, it has been shown that more bone will form if there are periods of rest between loading sessions [59]. It has recently been reported that shorter, more frequent bouts of loading produce greater increases in bone formation [60, 61].

In recent years, the focus of much research has been elucidation of the mechanism wherein mechanical signals are sensed by cells and translated into a cellular response of matrix production and/or degradation. The mechanism of mechanotransduction continues to be disputed. While the apparent effect of mechanical strain overall is not in question, the strain the cell senses may or may not be the primary stimulator of

adaptation. Some researchers postulate that fluid shear caused by matrix deformation may be able to explain bone's adaptive properties [62-66], while others present evidence that electromagnetic fields may be the primary mechanism [67-69]. There has been other evidence to suggest that adaptation is triggered by accumulation of microdamage in the bone's matrix [70-73]. Whether or not the true answer is any one of these options or even a combination of them, it is apparent that mechanical signals play an important role in the natural adaptive responses of bone. Furthermore, the molecular signaling pathway mediating the response is also under investigation [74, 75].

There has also been a wide range of research performed in *in vitro* culture systems demonstrating the mechanosensitivity of bone cells. Several types of *in vitro* monolayer culture systems have been devised to provide mechanical stimulation to bone-like cells based on flexible substrate deformation [18, 20, 76], application of vacuum pressure [18, 20, 76], and oscillatory flow [17, 26, 77]. These studies have illustrated that mechanical stimulation results in cytoskeletal modulation, including upregulation of actin and vinculin and downregulation of tubulin [78]. Other work has demonstrated increased proliferation and changes in cellular alignment in response to deformation of the substrate supporting osteoblast-like cells [18]. Research has also shown a downregulation of osteocalcin [19, 79] and upregulation of prostaglandin E [65, 80], nitric oxide [66], and collagen type I [81]. Stretch on osteoblastic cells has been shown to increase the expression and DNA binding activity of the osteoblast-specific transcriptional factor *cbfa1* [21].

Evidence has been obtained from various cells sources containing osteoprogenitors that suggests mechanical stimulation may have an effect on bone lineage progression. Much work has been done to characterize the effects of intermittent hydrostatic compression (IHC) on rat calvarial cells subcultured into two subpopulations, one exhibiting an osteoblastic-like phenotype and one with a more osteoprogenitor-like phenotype. These studies show that mechanical stimulation may be necessary to maintain a differentiated phenotype in the osteoblast-like cells, but the osteoprogenitor cells act somewhat differently and were not as mechanosensitive as their differentiated counterparts for osteopontin upregulation [82] However, osteoprogenitor-like cells did upregulate alkaline phosphatase activity and TGF- β secretion [27, 62]. Other research shows that mechanical strain downregulates the number of osteoclasts formed in murine stromal cell populations [83, 84]. Recently, Weyts has shown that the response of osteoblastic cells to mechanical stretch depends on the length of time the cells were exposed to dexamethasone, possibly indicating that mechanosensitivity varies with differentiation of osteoblastic cells [85].

2.3 Bone Chamber Systems

To date, bone chamber technology has been utilized in the academic study of bone formation and chemical and physical regulators of that process. An early predecessor of modern bone chambers are simple diffusion chambers which house a selected population of cells within cellulose acetate membranes and are placed either intraperitoneally, intramuscularly, or in the subcutaneous space of an animal. The cells receive nutrition by diffusion from the surrounding host environment and are exposed to

endogenous bioactive factors, while isolating the cell population so that any measured response can be attributed to the implanted cell population. These systems have been used to investigate a variety of cells, primarily to investigate cell and tissue physiology as well as cell immunity and tumor growth. These chambers have also been used to demonstrate the osteogenic capacity of a population of cells within the periosteum and bone marrow. The scope of the investigations of bone formation that can be performed using diffusion chambers is limited however because nutrition is diffusionally mediated since a vascular network is absent from the chamber interior. Because of size and nutritional limitations, fully structured bone cannot develop within a diffusion chamber.

A wide range of chamber designs have been developed for studying orthotopic bone formation. These chambers may reside in the cortex only or may transverse both the cortex and trabecular regions of a bone. These chambers have been used to study both normal *de novo* bone ingrowth as well as the effect of many biological factors on bone growth [86-88]. The chambers have even been manufactured with different surface finishes to study bone/implant interactions [89, 90]. Some bone chamber systems have features to provide easy access to the chamber contents in a non-terminal procedure without disturbing the chamber itself [91, 92]. Bone chamber systems have been modified to supply an electrical stimulus to developing bone to study the induction effects of electrical current [93]. One transcutaneous bone chamber system even provides a translucent port to study developing bone in the chamber using an optical microscope in real-time [94].

Only a few chamber systems have been designed to impart a mechanical stimulus to developing bone. Aspenberg has developed a micromotion bone chamber system which applies a small micromotion to bone within the chamber via a rotating inner sleeve resulting in fibrous tissue formation and inhibition of bone [95, 96]. Tagil developed the rat bone conduction and load chamber which penetrates the bone cortex and allows bone growth into a chamber space sitting atop the cortex. A subcutaneous piston is used to apply a known force to the tissue via an extracutaneous dynamometer. Tagil found that when *de novo* bone formation was allowed in this chamber system for three weeks and then loaded for an additional seven weeks, a cartilage layer resulted next to the loading piston in four out of seven samples [97]. It should be noted however, that at the onset of loading the tissue within the chamber is mostly fibrous tissue next to the piston with a bony callus forming at the opposite end of the chamber. Thus it may be postulated that loading of fibrous tissue in a potentially less vascular setting produced a cartilage layer, rather than concluding that loading of *de novo* bone produced cartilage. Although not a true chamber system, Lamerigts developed the subcutaneous pressure implant to study how controlled loading would affect incorporation of morsellized bone graft into an orthotopic defect site in goats. The system consists of a titanium rod which passes through the cortex and into the epiphysis of a long bone to serve as an actuating piston to compress the graft chips placed in the epiphysis. A cap enclosing the exterior end of the rod and lying in the subcutaneous space over the cortex is connected to a subcutaneous air pressure cannula which conveys compressed air to actuate the piston. Lamerigts found that after 12 weeks of loading, loaded graft chips exhibited greater incorporation, remodeling, and higher overall bone density [98].

The hydraulic bone chamber system developed by Guldberg was the first chamber system to apply a controlled cyclic compressive stimulus to repairing bone within the chamber. The system resembles a hollow titanium screw with large tissue infiltration openings on the distal end which resides in the trabecular bone, while the opposite cap end remains in the subcutaneous space flush with the bone cortex. Subcutaneous hydraulic tubing is connected to the cap end to supply pressurized saline to actuate a piston within the chamber to compress tissue within the chamber. This system provides the ability to apply a controlled mechanical stimulus *in vivo* to a volume of tissue isolated from 98.6% of ambulatory loads [99]. The easily accessible subcutaneous cap allows for repeated non-terminal biopsy procedures. This system was first used to investigate the effects of cyclic compression on *de novo* bone growth in a canine model. Twelve weeks of loading resulted in bone samples with increased mineralization and decreased collagen fiber organization. Architectural changes with loading included increased connectivity and trabecular plate thickness resulting in a 6-fold increase in the apparent modulus of loaded bone cores [100]. Although this study demonstrated the adaptive nature of regenerating bone to intermittent mechanical compression, it failed to demonstrate an adaptive set of local tissue strains resulting in new bone formation since the architecture of the developing bone scaffold was unknown.

Moalli subsequently used the canine hydraulic bone chamber model to investigate early changes in cellular activity and gene expression resulting from short term mechanical loading of *de novo* bone growth. This work illustrated a biphasic upregulation of c-fos and zif-268 gene expression within the first 24 hours following a single loading episode and increases in the synthesis of type I procollagen and alkaline

phosphatase after six consecutive days of loading [101]. In a separate experiment, Moalli also demonstrated load-induced activation of focal adhesion kinase (FAK) and its association with Src using the canine hydraulic bone chamber model [75]. Recently, the hydraulic chamber system has been modified for use in a rabbit model and was used to investigate the ability of tissue-engineered cartilage constructs to support bone formation under controlled mechanical loading conditions. This work demonstrated a nine-fold increase in mineralized bone formation on cartilage constructs receiving a daily controlled intermittent mechanical stimulus [102].

2.4 Bone Defect Repair

Over six million fractures occur in the United States every year. While most fractures heal suitably, between 5-10% of these injuries experience complications that may be remedied by a tissue-engineered bone substitute. These situations may be subsequent to an osseous infection, improper alignment of bone fragments, excessive motion or periosteal stripping, as well as interfering soft tissue damage. Further clinical uses for tissue-engineered bone substitutes include bone regeneration following or complicated by osteomyelitis, osteonecrosis, or the removal of a malignant or benign osteosarcoma [1]. The market for bone grafts and bone substitutes is experiencing tremendous growth, demonstrated by gains of 40% from 1997 to 1999 when the market represented a 270 million dollar industry [28]. While autograft bone is considered the gold standard for bone replacement therapies, its use is not without complication [103]. Significant donor site morbidity, compromised structural integrity, and limited quantities of available bone restrict its clinical value. Allografts are an option, but limited supply

and recent incidents of disease transmission from banked tissues have created increased medical and financial interest in alternatives. Researchers are actively seeking bone replacement scaffolds and tissue-engineered bone substitutes.

2.5 Bone Tissue Engineering

2.5.1 Overview

Bone formation requires osteogenic cells with an extracellular matrix in an appropriate chemical and physical environment [104]. Each element represents one piece of the complex puzzle that is the *in vivo* bone environment. Exact recreation of the physiologic *in vivo* environment may or may not be necessary to develop an effective bone replacement. Tissue engineering strategies attempt to mimic the natural bone formation process by exogenously providing one or more of the following: an osteoconductive scaffold, osteogenic cells, and chemical and physical inductors of bone formation. The location, functional needs, and local cellular and vascular supplies of the defect site will determine how aggressive the tissue engineering approach must be and which of the aforementioned components must be incorporated in the replacement scaffold.

Typically, tissue engineering approaches employ a scaffold material to serve as the framework for bone formation as well as a structural and potentially load-bearing intermediary until complete remodeling occurs. These scaffolds may be augmented with osteogenic cells or resident host cells may be relied upon to mediate matrix secretion. The provision of additional osteogenic cells with a matrix is particularly important for patients with certain clinically challenging bone repair situations where the host wound

bed may have an impaired cellular supply such as older patients, smokers, patients receiving chemotherapy or radiation and patients with severely damaged wound beds [104]. Certain strategies employ the use of bioactive factors involved in induction or regulation of the bone formation process. In certain instances, additional osteogenic cells may not need to be provided if such osteoinductive factors are supplied to cause the resident population of cells to form new bone. Often the supplied cells are genetically engineered to overexpress such factors to overcome the challenges associated with delivering the actual soluble factor itself [105]. This approach has been used with some success to heal bone defects using cells expressing bone morphogenetic proteins [106] and the transcriptional factor Runx2 [107]. Although a less explored approach than chemical stimulation of bone formation, it may be possible to use mechanical loading as a stimulant of new bone formation on tissue-engineered constructs given bone's native capacity to respond to local mechanical signals.

2.5.2 Scaffold Selection

Scaffold selection is critically important in the development of a bone replacement construct. The scaffold must be biocompatible, osteoconductive, and be able to be sterilized. Porous osteoconductive matrices have been shown to provide an excellent framework for new bone formation. Ideally, the matrix would promote protein adsorption, cell adhesion, mitosis, and differentiation while providing initial mechanical stability, depending on the local loading requirements of the defect site. While natural materials like collagen and hyaluronan are an option [108, 109], their lack of mechanical integrity makes them suitable only for certain non-loadbearing environments. Calcium

phosphate ceramics such as hydroxyapatite [110-113], tricalcium phosphate [110, 114, 115], bioactive glass [116] and coralline materials [117] are a natural choice because of excellent osteoconduction on these surfaces. However, the brittle nature of these materials and the lack of a completely interconnected pore structure limit their usefulness. Polymers are gaining a great deal of attention as possible matrices for bone replacement constructs since their architecture and mechanical properties can often be tailored easily. Polymers that have been investigated for use in bone tissue engineering include polypropylene fumarate (PPF) [118], polyurethane (PUR) [119, 120], polycaprolactone (PCL) [121, 122], and other poly ether esters [123], but the most commonly used polymer options are polylactides and polyglycolides and their copolymers [113, 124-126] due to their ability to rapidly degrade in the *in vivo* environment.

2.5.3 Cell Sources

The choice of cells to incorporate in a tissue-engineered bone construct is also crucial. Options include terminally differentiated osteoblasts, osteoprogenitors, or cell populations containing stem cells capable of osteogenesis. Cells expressing the osteoblast phenotype however are typically harvested in small numbers, demonstrate limited expansion capacity and are prone to phenotypic dedifferentiation [127]. Bone marrow stroma has been used in many instances to augment bone repair with some success [128-131]. Unfortunately, it is estimated that humans have only one osteoprogenitor per every 100,000 nucleated bone marrow cells [132]. Purified *ex vivo* expanded mesenchymal stem cells derived from a variety of sources including marrow

[110, 127], muscle [133], and adipose tissue [134-136] represent a more concentrated source of osteogenic cells for bone replacement scaffolds. Osteoprogenitors from fetal calvaria [126] and periosteal cells [106] may also be used.

There are many advantages to using MSCs for tissue-engineered bone products including the ability for *ex vivo* expansion. Since human MSCs are capable of a billion-fold expansion over ten passages [132], this represents a commercially viable source for osteoprogenitor cells for tissue-engineered bone substitutes. Furthermore, since mesenchymal stem cells are easily obtained from adult bone marrow aspirates, MSCs are a readily available cell source. Preliminary work also shows that these cells may exhibit some immune tolerance, making an allogeneic off-the-shelf product more feasible. Research performed at Osiris Therapeutics has demonstrated that allogeneic canine stem cells implanted on a ceramic scaffold into a canine segmental gap defect model provide comparable healing of the defect when compared to an autologous product [137][138]. Host response to the donor cells was evaluated in a mixed lymphocyte reaction and no adverse reactions were detected [139]. Further studies showed that rat MSCs do not stimulate alloreactive T cell responses [140]. Mesenchymal stem cells have shown strong osteogenic capacity *in vitro* when cultured in the presence of a standard set of osteogenic supplements including Na- β -glycerophosphate, L-ascorbic acid-2-phosphate, and the synthetic glucocorticoid dexamethasone for 14 to 21 days. The osteoblastic phenotype is evidenced by a change from a fibroblastic to a cuboidal morphology, expression of alkaline phosphatase, reactivity with anti-osteogenic cell surface monoclonal antibodies, osteocalcin mRNA expression, and mineralized nodule formation [127, 141]. Excellent availability, ease of culturing, ability to use allogeneic cells, and

sensitivity to osteogenic stimuli make mesenchymal stem cells an excellent choice for clinical tissue-engineered bone products.

2.5.4 Construct Preparation

While most researchers recognize the critical nature of scaffold and cell selection for a bone replacement scaffold, the importance of construct preparation is somewhat less acknowledged. Typical bone tissue engineering approaches simply seed primary or *ex vivo* expanded cells on a three-dimensional matrix and immediately implant it in the defect site [106, 110, 114, 131]. This approach does not allow for extracellular matrix formation prior to implantation or predifferentiation of osteoprogenitor cells. While more common for cartilage [142], tendon [143], vascular tissue engineering [144], some researchers however have used three-dimensional *in vitro* culture to prepare constructs for bone replacement. Such an approach allows for cellular differentiation and matrix secretion prior to implantation, often utilizing a set of media supplements to induce osteogenesis or accelerate matrix secretion [115, 117, 145, 146]. Yoshikawa has demonstrated that a two-week subculture in dexamethasone-containing media caused hydroxyapatite scaffolds seeded with bone marrow-derived cells to have increased bone formation once implanted subcutaneously in rats [147, 148]. Constructs developed in this manner were shown to have higher osteoblastic activity than autogeneous trabecular allograft [149]. Providing a construct in which the cells already have an established extracellular matrix may enhance cell retention after implantation. Furthermore, a construct that already has a mineralized matrix may actually promote ensuing bone

formation as the resident mineral may provide nucleation sites for subsequent mineralization.

In vitro preculture of bone constructs is limited however by diffusional limitations. Scaffolds tend to have a necrotic core because of insufficient transport of nutrients into the scaffold and degradation products and metabolic waste out of the center of the scaffold. Ingrowth limitations on cell-seeded scaffolds for tissue engineering have been observed [126, 150-152]. Research involving rat marrow cells and rat calvarial cells on PLGA in static *in vitro* culture for up to 56 days only showed osseous tissue penetrating to a depth of 200-300 microns [126, 150]. Additional studies have shown that cell-seeded constructs developed in static culture show preferential cell growth on the scaffold exterior [151-154]. Recently, researchers have begun to develop *in vitro* perfusion systems to culture three-dimensional constructs [25, 155-157]. The flow of medium not only enhances transport but applies a shear stress to the cells within the construct which has been shown to improve matrix deposition within constructs. Wang has performed the only research in which cell-seeded scaffolds were prepared for *in vivo* implantation using a perfusion culture technique. Wang perfused β -tricalcium phosphate scaffolds seeded with bone marrow derived cells for two weeks before subcutaneous implantation and found increase alkaline phosphatase and osteocalcin synthesis accompanied by increased bone formation compared to static controls after four and eight weeks *in vivo* [155].

A few other researchers have also developed systems to capitalize on the stimulatory effect of mechanical loading on bone cells. Jones has developed a 3-D cell

culture system capable of applying either a known strain or a known force to developing bone constructs [158]. Porter has developed an *in vitro* bioreactor system for the development of three-dimensional bone constructs that is capable of applying both perfusion and axial mechanical compression [159]. As yet neither of these systems have been used to mechanically precondition bone tissue engineering scaffolds prior to *in vivo* implantation, but such systems will undoubtedly be employed for such purposes in the near future [160]. Researchers are already employing *in vitro* mechanical conditioning to the development of tenogenic constructs for *in vivo* use [161].

Another potential way to circumvent the complications arising from diffusional limitations associated with *in vitro* preculture is to utilize the *in vivo* environment as a bioreactor for the preparation of tissue-engineered bone replacements. Ingrowth of blood vessels into the scaffold may provide adequate nutrient and metabolite transport, potentially resulting in larger, more homogeneous, and mechanically stable mineralized constructs. While many cell-seeded constructs have been implanted into the subcutaneous space, the purpose of such experiments has primarily been evaluation of biocompatibility [162, 163], comparison of cell and scaffold technologies [114, 115, 148], or the efficacy of bioactive factors to induce bone formation [164-166]. To date, the effects of controlled *in vivo* mechanical loading on a cell-seeded construct have not been investigated.

The concept of using the *in vivo* environment to develop tissues is not altogether new, but to date use of the *in vivo* environment as a means of preparing bone replacement scaffolds has been explored only marginally. In 1998, Tsukagoshi published work

describing the revascularization of autograft bone by embedding it in muscle and implanting it subcutaneously for several weeks before transplanting it to a cranial defect site. Blood vessels from the muscle flap were anastomosed to temporal vessels to maintain a vascular supply to the graft [167]. Jingushi has proposed a similar approach using BMP2 to induce bone on β -tricalcium phosphate within muscle which could then be transplanted with the muscle pedicle to repair a bony defect [168]. Likewise, Pelissier has investigated the ectopic development of bone constructs using bone marrow-derived cells on a coralline scaffold with a vascular pedicle [169]. At this point however, the ability of constructs developed in this way to heal an actual bone defect has not yet been tested. Furthermore, researchers have been developing shaped tissue-engineered constructs for bone replacement resembling the mandibular condyle and phalanges [117, 170, 171]. Vacanti and Bonasser have proposed that such constructs developed *in vivo* could then be transplanted to repair large bone defects [172]. As yet, no one has employed mechanical stimulation *in vivo* to aid in the development of tissue-engineered constructs for bone replacement. Given the evidence suggesting better bone formation occurs on tissue-engineered bone constructs developed in *in vitro* bioreactors [155] and the proven responsiveness to osteoblasts *in vivo* and *in vitro*, it is likely that mechanical stimulation in an *in vivo* bioreactor will improve bone construct development. Combining mechanical preconditioning with the vascular benefits of an *in vivo* environment may represent a successful approach for developing tissue-engineered constructs for bone defect repair.

CHAPTER 3

EFFECTS OF CYCLIC MECHANICAL COMPRESSION ON THE REPAIR OF FROZEN ALLOGRAFTS IN A LAPINE BONE DEFECT MODEL

3.1 Introduction

3.1.1 Summary

The ability of bone to adapt to its mechanical environment is undisputed. However, the effects of controlled *in vivo* mechanical loading on a repairing bone graft or bone graft substitute have not been investigated. It is unknown whether new bone on a three-dimensional scaffold will show a positive adaptive response to an applied cyclic mechanical stimulus. Although the adaptive ability of mature bone is well documented, the absence of a fully connected canalicular network, relative tissue immaturity, and other factors may impact the ability of the cells to respond to *in vivo* mechanical signals. The effect of controlled *in vivo* mechanical loading on repairing trabecular allografts may also be indicative of the response of tissue-engineered bone replacement constructs since both systems are typically characterized by a three-dimensional scaffold populated by osteogenic cells and scant mineralized matrix.

Of a practical nature, controlled mechanical stimulation may represent an attractive method of preconditioning tissue-engineered scaffolds to improve cellular distribution and mechanical properties for bone defect repair. Whether systems for mechanical preconditioning are utilized in an *in vivo* or an *in vitro* environment, determination of a regime of tissue strains resulting in a positive adaptive outcome will

provide a target level of deformation for these systems to achieve [173]. Foreknowledge of a target adaptive strain regime will aid in the design of mechanical preconditioning systems. To date, the local mechanical stresses and strains resulting in bone adaptation have not been determined in either mature or regenerating bone.

A bone chamber system capable of applying a controlled intermittent mechanical stimulus was utilized to study *in vivo* bone formation on rabbit trabecular allografts. A similar system was used previously to investigate mechanical adaptation in canine *de novo* bone and found increased mineralization and adaptive architectural changes in loaded specimens [100]. However, this study was unable to predict an adaptive regime of tissue strains because the architecture of the *de novo* bone at the time of loading was unknown. The work presented here involves trabecular allografts of a known architecture in a controlled environment with known boundary conditions to facilitate finite element modeling of the applied loading conditions. Predictions of the tissue level stresses and strains can be compared to histological sections showing areas of new bone formation to estimate a set of adaptive tissue strains.

After four weeks of *de novo* bone growth and four additional weeks of daily controlled *in vivo* loading, a significant decrease in bone formation was observed. Since an increase in bone formation did not result from loading, an adaptive set of local tissue stresses and strains could not be determined. Finite element models show that the average normal strains at the tissue level fell in the range of $-1060 \mu\text{a}$ to $+140 \mu\text{a}$ while the overall apparent strain was $8740 \mu\text{a}$. The decrease in bone formation may be a result of impaired vascularity resulting from micromotion between the implant and the

anchoring bone or it may reflect a true vulnerability of immature bone on a scaffold to *in vivo* mechanical stimulation. This work demonstrated that cellular responsiveness to mechanical stimulation is complex and a positive adaptive response cannot be assumed. Furthermore, this research underscored the need for a stable vascular environment for bone repair.

3.1.2 Specific Aims and Hypotheses

Specific Aim #1: To quantify new bone formation on trabecular allografts in a rabbit bone chamber model applying cyclic mechanical compression.

Hydraulic bone chambers were implanted in the distal metaphysis of male New Zealand rabbits. After four weeks of bone formation on trabecular allografts implanted in the chambers, cyclic mechanical compression was applied for an additional four weeks. New bone formation was quantified using fluorochromes injected intravenously just prior to onset of loading and harvest. It is hypothesized that cyclic mechanical compression will increase new bone formation on trabecular allografts implanted at an orthotopic site.

Specific Aim #2: To predict trabecular strains employed by cyclic in vivo mechanical compression of trabecular allografts in a rabbit bone chamber system to identify an adaptive tissue strain regime.

Micro-computed tomography images of implanted trabecular allografts were used to create a digital image based finite element mesh for the basis of finite element models representing the applied *in vivo* loading conditions. Predicted tissue stresses and strains were generated. It was hypothesized that larger local tissue strains will correlate with

greater bone formation induced by cyclic mechanical compression of a trabecular allograft implanted at an orthotopic site.

Specific Aim #3: To compare early mRNA response for collagen type I and osteopontin from repairing trabecular allografts in a rabbit bone chamber model experiencing cyclic mechanical compression.

Hydraulic bone chambers were implanted in the distal metaphyses of male New Zealand rabbits. After four weeks of bone formation on trabecular allografts implanted in the chambers, cyclic mechanical compression was applied for an additional three days. The harvested tissue was used to examine early gene expression using reverse-transcriptase polymerase chain reaction methods. It was hypothesized that cyclic mechanical compression will increase early gene expression of bone-related proteins in trabecular allografts implanted at an orthotopic site.

3.2 Methods and Materials

3.2.1 Hydraulic Bone Chamber (HBC) System

A bone chamber model capable of supplying a controlled intermittent mechanical stimulus to regenerating bone or bone scaffolds *in vivo* was developed. The chamber can be biopsied repeatedly within a given animal without disturbing the implant to provide excellent within-animal controls and reduce the number of animals required in a given study. While not a traditional clinical model, this system represents a hybridization of classical *in vivo* and *in vitro* models. This three-dimensional system retains the relevant

in vivo environment, which provides appropriate growth factors, cytokines, hormones, and vascularity to the tissue. This system also creates an environment for the tissue that is completely mechanically isolated from the surrounding tissue such that the local mechanical environment is tightly controlled [99]; a feature that is typically only obtained with *in vitro* cell culture systems. Guldberg and colleagues at the University of Michigan originally developed the hydraulic bone chamber model for canine studies [100]. At Georgia Tech, several changes have been made to the hydraulic bone chamber system for use in rabbits. To ensure the best chance of demonstrating differences between treatment conditions, a more challenging bone repair model was created by restricting vascular access to the regenerating tissue in the chamber. In addition, the overall size was reduced and the cap design was significantly modified to lower the chamber's profile, keeping it close to the bone's surface.

The basic rabbit hydraulic bone chamber can be represented as a hollow threaded titanium bolt with a removable cap (Figure 1). The base of the bone chamber has an inner diameter of 0.25" and a depth of 0.25". Those chambers intended to supply a mechanical stimulus also have a flat piston inside separating a tissue space from a superior plenum. The tissue space contains twelve regularly spaced holes to allow cellular invasion and new vascularization. The superior plenum is filled with saline and has a barbed outlet to which polyurethane tubing is connected and routed subcutaneously to an exit site on the animal's back. The external end of this tubing can be connected to a solenoid-driven loading system (Figure 2). This actuating system is capable of applying an intermittent compressive stimulus controlled by active pressure transducer feedback. The saline in the tubing is pressurized which displaces the piston within the bone

chamber applying a deformation to the regenerating tissue in the chamber.



Figure 1. Hydraulic Bone Chambers for Rabbits

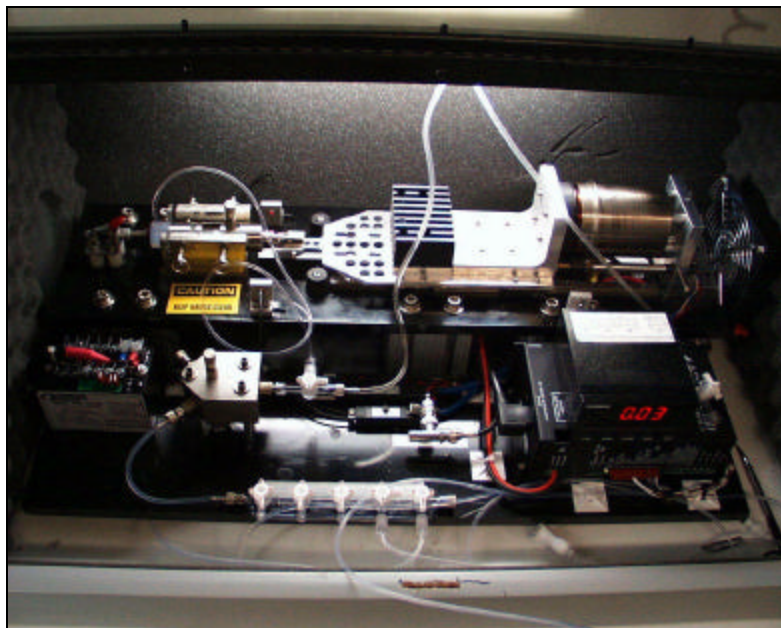


Figure 2. External Solenoid-Driven Loading System

3.2.2 Surgical Procedures

Hydraulic bone chambers were implanted bilaterally into the distal femoral metaphyses of 19 male New Zealand White rabbits using a sterile surgical technique. Each animal received one basic implant and one loaded implant with a piston and barb to allow for compression of the tissue inside the chamber. A detailed surgical procedure can be found in Appendix B.1 Procedure to Implant Rabbit Hydraulic Bone Chamber. The chambers were allowed to integrate into the bone for four or five weeks. In a second surgical procedure, the chambers were opened, cleared of *de novo* tissue ingrowth using a thin-walled extraction tool. This procedure is described in Appendix

B.2 Procedure for a Non-Terminal Biopsy of the Rabbit Hydraulic Bone Chamber. Trabecular bone allografts (0.25" diameter, 0.25" length) that had previously been sterilely harvested from the distal femoral metaphyses of other New Zealand White rabbits and then stored at -80C were thawed and placed inside the cleared bone chambers. During this surgical procedure, tubing was attached to the barb of the loaded chamber and routed subcutaneously to an exit site on the rabbit's back between the shoulder blades. Appendix B.3 Procedure to Implant Subcutaneous Loading Tubing in Rabbits contains a detailed description of the surgical procedure to implant this tubing.

All animal procedures were approved by the Georgia Tech and Emory University's Institutional Animal Care and Use Committees (Protocol # V043-98).

3.2.3 Loading Procedure and Harvest

New bone was allowed to form on the implanted trabecular allografts for four weeks before loading sessions began. Each animal's tubing was connected to the external solenoid-driven loading system so that the saline within the tubing and hydraulic bone chamber could be pressurized to apply a compressive load to the allograft within the loaded chamber. Each loading session applied a compressive stimulus in a sinusoidal wave pattern applying 2.22 N to 22.2 N compression (upper limit of loading system) to the allograft. The loading stimulus was applied at 1 Hz for 30 minutes similar to previous experimental work [100][81][79][75]. A detailed protocol for operating the hydraulic loading system can be found in Appendix C. Each animal was loaded for three consecutive days. The tissue was then extracted from the chamber in a sterile surgical procedure using a thin-walled biopsy extraction tool (Figure 81) for subsequent analysis

of gene expression. A second trabecular allograft was placed in the chamber and new bone formation allowed for an additional four weeks prior to initiation of a four week loading regimen identical to the one described for the short-term loaded group. This second allograft was then extracted from the chamber in a terminal surgical procedure. All biopsied tissue was fixed in 10% neutral buffered formalin for 48 hours then stored at 4C in 70% ethanol.

3.2.4 Fluorochrome Labeling

Fluorochrome labels were administered intravenously to mark newly deposited calcium within the allograft during the long-term loading sessions. Oxytetracycline was administered 1 day before the initial loading session at a dosage of 25 mg/kg, while calcein was given at a dosage of 10 mg/ml 1 day before the termination of the four week loading period. Each dose was administered intravenously in a volume of 80-100ml over a thirty minute period. Animals were given an injectible anesthetic of ketamine/xylazine/acepromazine (19/9/0.4 mg/kg) prior to the procedure.

3.2.5 Animal Grouping and Infection Problems

The study was conducted using three separate groups of animals since it would be prohibitive to perform the experiment with a large number of animals at one time. The first group of seven animals (GW1-7, Spring 1999) was plagued with infection along the indwelling tubing and no useable data was collected. The second group of six animals (GW8-13, Fall 1999) fared somewhat better, in part due to daily exit wound care and anchoring of the tubing with a felt cuff as described previously. Four samples from the short-term loading segment were obtained and three from the long-term loading segment.

The third group of six animals (GW14-19, Spring 2000) had the lowest incidence of infection, primarily because the animal's exposure to the tubing was minimized by implanting the tubing in a separate procedure just one week prior to the onset of loading. Additionally, the application of silver-impregnated glass powder to the exit wound improved the incidence of infection in the third group. Six samples from the long-term loading group and four from the short term loading groups were successfully obtained from Group #3, making the overall number of usable biopsies for analysis from the long-term loading group nine and eight for the short-term loading group. It should be noted that unlike animals in Group #2, animals in Group #3 received the long-term loading treatment first and then the short-term loading in an effort to balance for any biopsy sequence effects.

3.2.6 RNA Extraction

Samples harvested after a four-week tissue formation period and a 3-day loading regimen were handled with RNase-free tools and immediately flash frozen in liquid nitrogen. Samples were stored at -80C prior to RNA extraction. Naï ve rabbit trabecular bone and *de novo* clearout tissue from the HBC integration period were also examined as a control for the loaded and nonloaded allograft samples.

RNA was isolated from samples in Group #2 using Promega's RNeasy Total RNA Isolation System. Briefly, 3ml of denaturing solution was added to each sample and homogenized using a rotor-stator homogenizer, and then 300 µl of sodium acetate was added and inverted to mix. Next 3ml of Phenol:Chloroform:Isoamyl Alcohol was added and mixed then chilled. Samples were centrifuged 30 minutes at 10,000g and 4C.

About 2/3 of the aqueous phase was aspirated and transferred to a clean tube. Then a second volume of Phenol:Chloroform:Isoamyl Alcohol equal to the aspirated volume was mixed in and chilled. Samples were again centrifuged 20 minutes at 10,000g and 4C. Again, about 2/3 of the aqueous phase was aspirated and transferred to a clean tube. An equal volume of isopropanol was added and incubated 30 minutes at -20C then centrifuged at 10,000g and 4C. The pelleted RNA at the base of the tube was resuspended in 1ml of chilled 75% RNase-free ethanol and centrifuged 10 minutes at 10,000g and 4C. The supernatant was discarded and any residual volume was dried in a speed vac being careful not to completely dry the pellet. The RNA pellet was resuspended in 20ul RNase-free water and optical density measurements performed to determine the quantity and purity of RNA extracted.

RNA was isolated from samples in Group #3 using Qiagen's RNeasy Kit (#75163). Briefly, samples were snipped with bone cutters and then homogenized using a rotor-stator homogenizer in the presence of 7.5 ml of Buffer RLT with β -mercaptoethanol. The mixture was placed in the Qiagen spin column and spun at 3800g for 10 minutes. The supernatant was transferred to a clean spin column and 7.5 ml of 70% ethanol was added before another spin for 5 minutes. Then 7.5 ml of Buffer RW1 was added and spun for 5 minutes. A buffered DNase solution (Qiagen # 79254) was applied to the column for 30 minutes. Additional Buffer RW1 was added to the column and spun for 5 minutes. The membrane was washed twice with Buffer RPE and then spun until dry. The column was placed in a clean elution tube and 500ul RNase-free water was applied directly to the membrane of each column. The extracted RNA was

then collected in the elution tube in two consecutive spins. Optical density measurements were performed to determine the quantity of RNA extracted.

RNA samples from Group #2 were reverse-transcribed using a standard protocol involving Invitrogen's SuperScript II Rnase H- RT enzyme on a 4 μ g quantity of RNA primed with OligodT(12-18). Please see Appendix D.1 Protocol Worksheet for Reverse Transcriptase Reaction to Convert RNA into cDNA for the complete RT procedure. The resultant cDNA was amplified using PCR (see Appendix D.2) for a housekeeping gene hGAP.

3.2.7 Microcomputed Tomography Imaging & Analysis

Each chamber biopsy from the long-term loading group was subsequently scanned on a compact fan-beam-type tomograph (μ CT 20, Scanco Medical, Bassersdorf, Switzerland) also referred to as a desktop micro-CT [174]. The system uses a microfocus X-ray tube with a focal spot of 10 μ m as a source. To perform a measurement, the specimen was mounted on a turntable with axial automation. Six hundred projections were collected over 216° (180° plus half the fan angle on either side). CT images in 512 x 512 pixel matrices were reconstructed using a standard convolution-backprojection procedure with a Shepp and Logan filter. A complete set of micro-tomographic slices, with a slice increment of 34 μ m, was acquired per sample. Measurements were stored in three-dimensional (3-D) image arrays with an isotropic voxel size of 34 μ m. Noise in the volumetric image data was partially suppressed using a constrained 3-D Gaussian filter. Mineralized tissue was segmented from surrounding soft tissue using a global thresholding procedure [174]. These high resolution images of the chamber biopsies

were used as input in finite element models described later to estimate the tissue level strains experienced by the allograft during compression.

3.2.8 Histology

After long-term loading specimens were scanned using micro-CT, they were cut longitudinally using a custom designed cutting jig and razor saw blades. Half the sample was decalcified and embedded in paraffin and the other half was embedded in methyl-methacrylate. All biopsy samples were sectioned longitudinally for subsequent analysis. Paraffin biopsy sections were stained with H&E and a modified Mallory aniline blue stain (mMAB) [175], as well as a stain for tartrate-resistant acid phosphatase (TRAP). Immunohistochemistry was performed using a monoclonal antibody (Sigma A2547) for α -smooth muscle actin (α -SMA) on paraffin sections. This stain was used to quantify the vascularity present in the samples. Vascular structures were simply counted for the entire section at a magnification of 10X. Plastic biopsy sections were either left unstained for fluorochrome analysis or stained with Goldner's trichrome stain. Immunohistochemical assays were also performed on paraffin sections of the chamber biopsies. Assays utilized monoclonal antibodies for Type I procollagen (IgG M-38) and osteopontin (IgG1 MPIIB10₁) obtained from the Developmental Studies Hybridoma Bank (The University of Iowa, Iowa City, IA).

3.2.9 Fluorochrome Analysis

Unstained plastic sections were viewed using a Nikon Eclipse TE300 microscope with a motorized stage and a Toshiba 3 CCD camera run by ImagePro Plus software. New bone formation was quantified using fluorescent microscopy of the calcein green

label which encompassed the earlier tetracycline red label and co-localized to areas of new bone formation seen using Goldner's Trichrome staining. The implanted graft bone picked up the label to a lesser extent than the new mineralizing bone. Using a magnification of 4X, nine fields of view were analyzed for each specimen representing the regions diagrammed in Figure 3. The total bone volume was measured as an area expressing a green fluorolabel. Because this measurement included both the implanted graft bone and new bone, a higher threshold was also applied to eliminate the graft bone and provide a measure of the total new bone volume (NBV). The difference between the total bone volume and the new bone volume gave a measure of the implanted graft bone volume (GBV) as well. Furthermore, if the bone formed along the surface of the graft, it was designated as appositional bone formation, while bone forming within the pore spaces was designated as intramembraneous bone. Both appositional bone volume (ABV) and intramembraneous bone volume (IBV) were quantified individually. In addition, a linear measurement of all graft bone surfaces was made to approximate the graft surface area (GSA). Regional comparisons were made by averaging scores for all sections in a given zone. Two radial zones were defined such that the inner zone includes fields 2, 5, and 8 while the outer zone includes fields 1, 3, 4, 6, 7, and 9. Three longitudinal zones (top/middle/bottom) were defined as well (Figure 3). Variance was analyzed using a General Linear Model with two factors: Animal and Load, for the following parameters: graft bone volume (GBV), graft surface area (GSA), total new bone volume (NBV), new intramembraneous bone volume (IBV), new appositional bone volume (ABV), total new bone volume/ graft bone volume (NBV/GBV), new bone volume/ graft surface area (NBV/GSA), and new appositional bone volume/ graft bone

volume (ABV/GBV), new appositional bone volume/ graft surface area (ABV/GSA). All statistical analyses were performed for an alpha of 0.05.

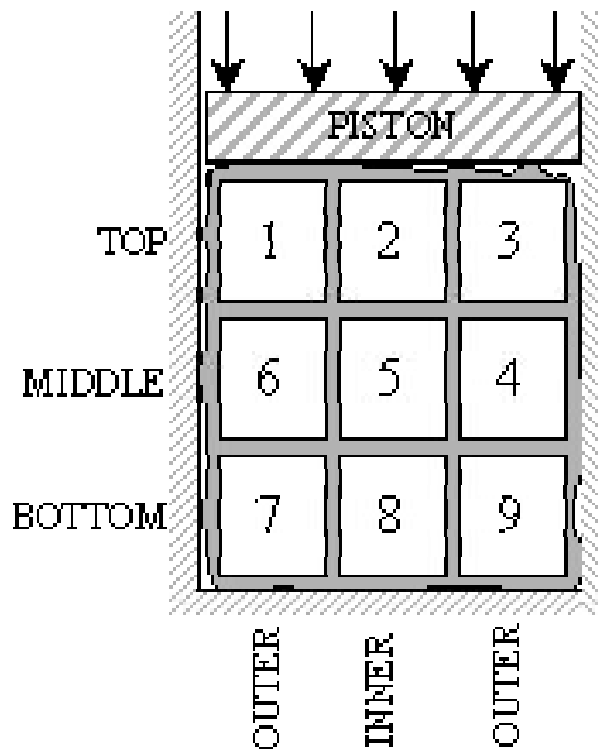


Figure 3. Zones of Analysis for Fluorescent Microscopy.

3.2.10 Finite Element Modeling & Analysis

The accuracy of any finite element model depends on the accuracy of the material properties supplied to the model. Therefore, a reasonable value for the tissue-level modulus of the rabbit trabecular bone exposed to one freeze/thaw cycle must first be determined. By matching known force/displacement data of a representative allograft to the output of a finite element model based on that sample's architecture, a reasonable estimate of the tissue-level modulus may be obtained.

Twelve bone cores were biopsied from the distal femoral metaphyses of New Zealand White rabbits and sized to fit the HBC (1/4" diameter x 1/4" length) in a procedure identical to that used to obtain trabecular allografts for the *in vivo* study. Like the long-term loaded chamber biopsies, these bone cores were also scanned using micro-CT. A newer desktop CT (μ CT 40, Scanco Medical, Bassersdorf, Switzerland) was available providing a resolution of 16 microns. The samples were then frozen at -80C, thawed and mechanically tested in a confined compression scenario to simulate the rabbit HBC environment. A rabbit HBC (Figure 4a) was threaded through a table-top platform which was immersed in room temperature PBS (Figure 4b). A MTS TestarIIIm 858 Mini Bionix II hydraulic test frame (Figure 4d) with a 100lb load cell and LVDT with a working range of 100mm was used to test these specimens in cyclic compression. A 0.5N preload was applied and then ramped linearly to -2.24 N in 1 second and then cycled sinusoidally between -2.22 N and -22.2 N in force control at 1 Hz for 30 minutes simulating the daily loading regimen experienced by the allografts tested in the *in vivo* experiment.

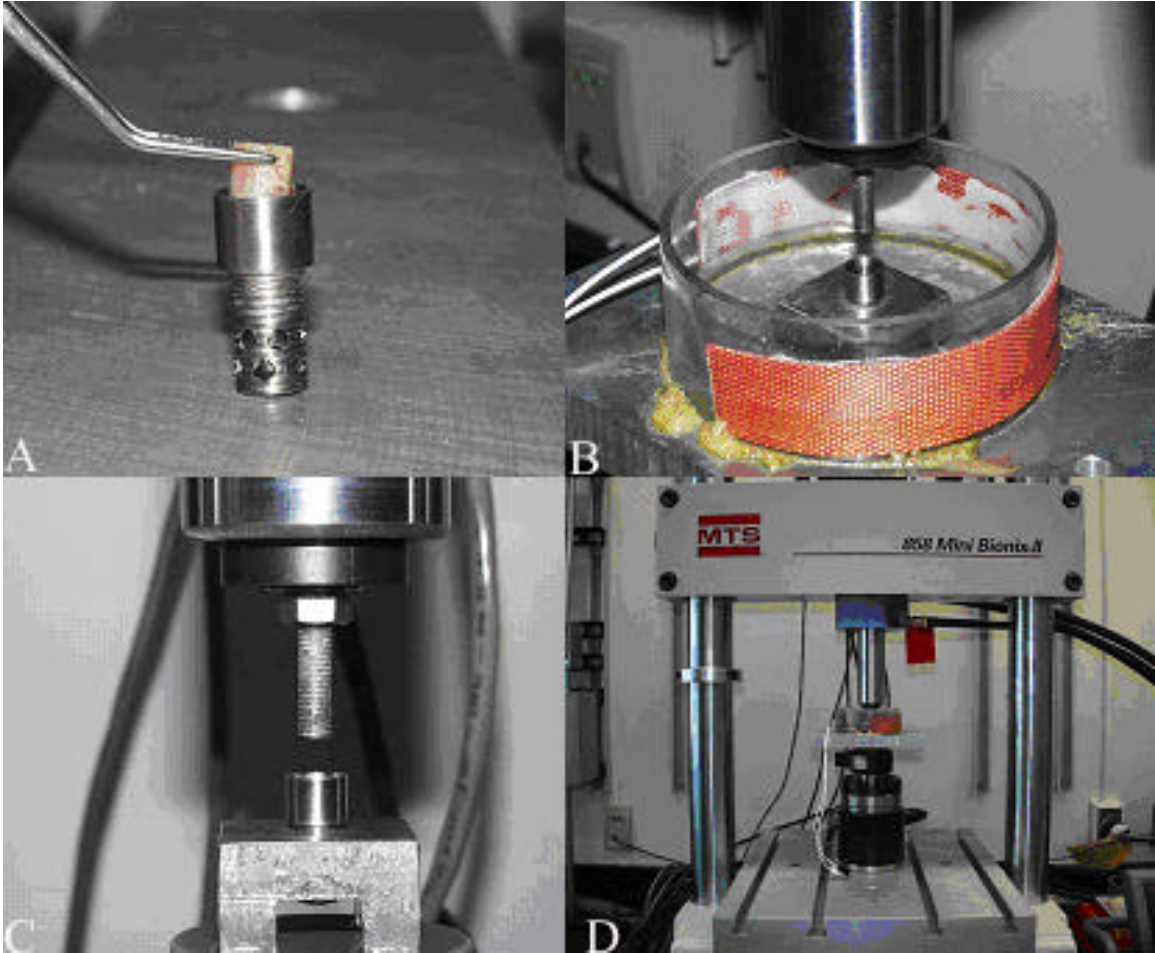


Figure 4. Mechanical Testing Setup: a) Sample in HBC, b) HBC in Platform Submerged in PBS bath, c) Loading Rod, d) MTS TestarIIm 858 Mini Bionix Load Frame

A representative bone core was chosen from among these samples to be modeled using finite element analysis to determine the tissue modulus of rabbit trabecular bone. Sample XII was chosen because its architecture most represented a right cylinder without holes and its bone volume fraction was close to the average of the actual *in vivo* samples. To create the input mesh, the microCT images were first filtered using a constrained 3-D Gaussian filter (sigma = 1.2, support = 2) to partially suppress noise in the volumetric image data, and then mineralized tissue was segmented from surrounding soft tissue by using a global thresholding procedure (threshold = 143). Scanco Medical's Finite Element-software v1.0 (Basserdorf, Switzerland) was employed to generate and solve a model based on the microCT image data. To limit the size of the model, the voxel data was first coarsened to a resolution of 32 microns. A volume of interest was selected that tightly encompassed the allograft. Next, a component labeling technique was employed and only the largest component kept, ridding the model of unconnected structures which carry no load in the scaffold, but will complicate the solution of the model. This single component represented over 99.5% of the voxels in the model. Using a voxel conversion technique known as digital image-based finite element meshing (DIBFEM), a 32 micron brick element was created to represent each voxel in the microCT image for a total of 1.84e6 elements. A distributed compressive load of 18.17N was applied to the top surface of the model ($z = 0$) to match the actual force amplitude applied during cyclic mechanical testing of Sample XII. In addition, the base ($z = z_{\max}$) was constrained to have no displacement in the z direction and the walls of the cylinder were constrained to have no displacement in the x or y directions. Figure 5 illustrates the coordinate system used and the distributed load across the top surface.

Like most finite element modeling software, this software package makes several a priori assumptions about the material being modeled. It is assumed that the model represents a continuum. Harrigan has shown that this assumption is valid for trabecular bone when the size of the model exceeds five intertrabecular lengths [176]. A set of 48 trabecular bone grafts harvested from the distal metaphyses of New Zealand White rabbits were scanned and the average trabecular spacing for this population of bone was determined to be 800 microns, suggesting that any sample size over 4 mm meets the continuum assumption. The samples modeled were 6 mm in both diameter and length. The software also assumes the material is elastic. Mechanical testing as described above confirms that the tissue responds in an elastic manner in the range of loads analyzed. Furthermore, the software assumes small deformations in the material. Since the applied apparent strain is less than 1%, this assumption is also appropriate. The software uses an iterative conjugate gradient solver in combination with an element-by-element matrix-vector multiplication scheme [177].

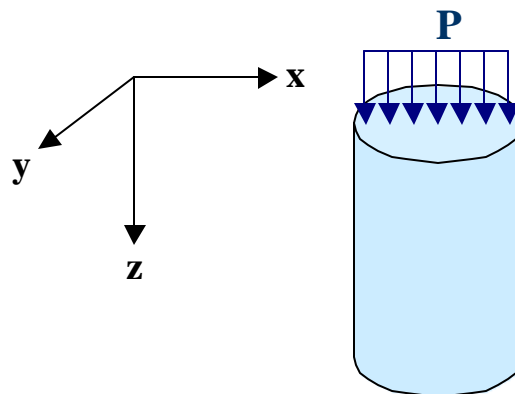


Figure 5. Coordinate System Used for Finite Element Models

The model was solved using an initial guess of 5000 MPa for the tissue modulus and 0.3 for Poisson's ratio. The actual tissue modulus was approximated by multiplying the initial guess by the ratio of the apparent strain in the z-direction from the model to the actual apparent strain measured in the mechanical test as shown in Equation 1. The tissue modulus of rabbit cancellous bone from the distal femoral metaphysis was approximated as 6.48 GPa. Although supporting data is not available for rabbit bone tissue, van Rietbergen has shown that the tissue modulus of human cancellous bone can range from 2.23 to 10.1 GPa, with an average of 5.91 GPa [178]. Given this range for human cancellous bone, a value of 6.48 GPa seems a reasonable value.

Equation 1

$$TMOD_{actual} = TMOD_{guess} \frac{\mathbf{e}_{zz}^{model}}{\mathbf{e}_{zz}^{test}} = 5 \text{ GPa} \left(\frac{0.00514}{0.00397} \right) \approx 6.480 \text{ GPa}$$

Two representative samples were chosen from the nine long-term loaded chamber biopsies obtained from the *in vivo* study. Specimens GW19L and GW14R were chosen for their architecture and were then modeled in a fashion similar to the naïve rabbit bone cores. Since the resolution of the original microCT images was 34 microns, no coarsening of the mesh was needed. Each voxel was modeled as a 34 micron brick element. Local errors associated with DIBFEM should be minimal at this resolution since the average trabecular thickness of allografts in the long-term loading study was 194 microns allowing 5-6 elements across each trabecular strut on average [179, 180]. The models were constrained as described earlier but the distributed load was increased to 22.24 N to represent the actual applied load in the *in vivo* loading procedure. Furthermore, the trabecular bone's tissue modulus was modeled as 6.48 GPa. The

interstitial marrow space was not represented in the model. Again, Scanco Medical's Finite Element-software v1.0 was used to determine the solution. The models were considered converged when the force and displacement residuals were less than $1e-4$. Four output parameters were examined including the normal compressive strain along the longitudinal axis of the sample, the largest principal strain, Von Mises Stress, and strain energy density. An interpolation algorithm was employed during post-processing to smooth any oscillating stress/strain response on the surface produced from "jagged" edges produced by the DIBFEM technique. In addition, histograms of each parameter were generated ignoring the top and bottom 5% of voxels since these voxels most likely represent artefactual surface responses. Appendix F includes a step-by-step guide to the necessary Image Processing Language (IPL, ©Andres Laib, Scanco Medical AG) commands required for pre-processing, solving, and post-processing these models.

3.3 Results

The overall number of usable biopsies obtained for analysis was eight pairs from the short-term loading group and nine pairs from the long-term loading group. Five rabbits were euthanized prematurely due to infections along the indwelling tubing or complications unrelated to surgery. One loaded sample was excluded from analysis due to implant instability that was discovered at the time of final harvest.

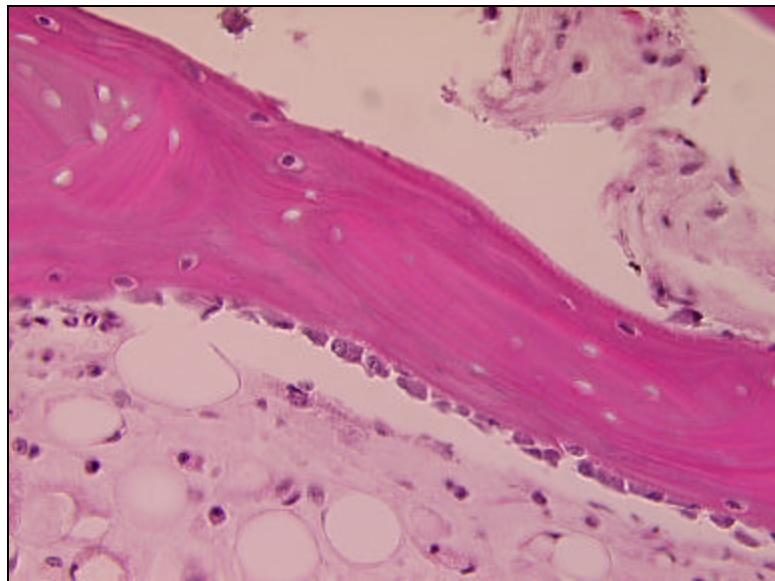
3.3.1 RNA Extraction & RT-PCR

While sufficient quantities of relatively pure RNA were extracted from the short-term loading samples in Group #2, the expression of the housekeeping gene hGAP as determined using RT-PCR techniques was undetectable, indicating that the RNA

obtained was significantly degraded. Therefore no gene expression data could be gathered from Group #2 specimens. In Group #3, the purity of RNA was excellent, but only one nonloaded sample and three loaded samples had sufficient RNA to perform an RT reaction. With such a low sample size, it was decided not to proceed with the subsequent investigation of early gene expression changes with a short-term loading.

3.3.2 Qualitative Histology Results

The analysis of the paraffin and plastic histological sections provided qualitative information about the tissue regeneration that occurred on the trabecular allografts in the hydraulic bone chamber model. Histology confirmed that osteoblasts repopulated the allograft and began lining the graft surfaces as clearly shown along the bottom surface of the trabecula in Figure 6.



**Figure 6. Osteoblasts Line Trabecular Allograft Surface of a Loaded Allograft;
H&E at 40x**

Three types of new bone formation were observed. The majority of new bone was appositional new bone formation along surfaces of the implanted allograft (Figure 7). There were also fewer areas of new *de novo* intramembraneous bone not associated with an allograft surface (Figure 8). Furthermore, one loaded sample showed large amounts of endochondral bone formation (Figure 9). A few instances of osteoclastic remodeling through new bone into the implanted allograft were also observed. H&E stained samples visually confirmed the existence of less new bone formation in the loaded experimental treatment group as seen in the panels below. Immunohistochemical staining confirmed that areas of new bone formation were expressing the bone-associated proteins pro-collagen type I and osteopontin. Gross observation of loaded versus nonloaded samples indicated a reduction in new bone formation in loaded samples as depicted in Figure 10.

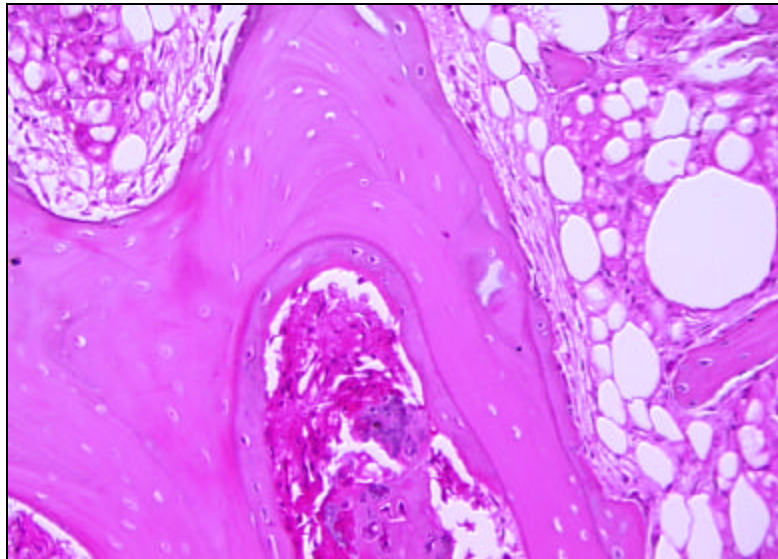


Figure 7. Appositional Bone Formation on a Nonloaded Allograft; H&E at 20x

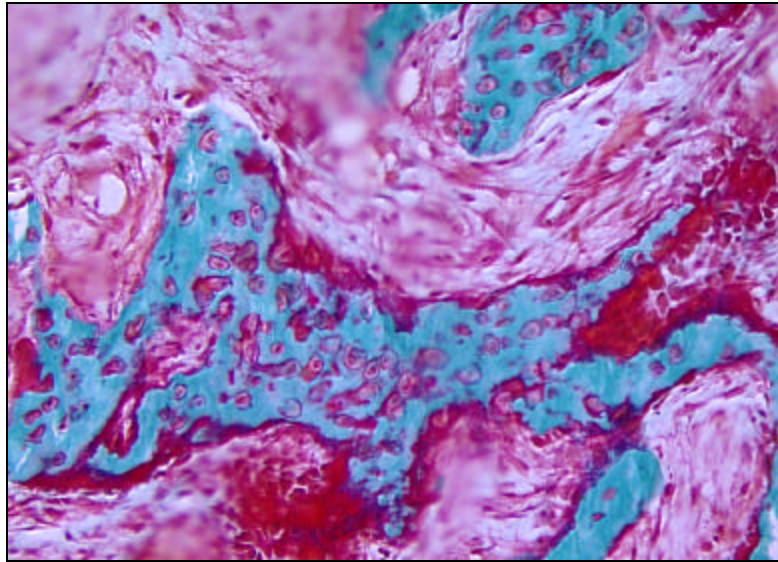


Figure 8. Intramembraneous New Bone Formation within a Loaded Sample; Goldner's Trichrome at 20x

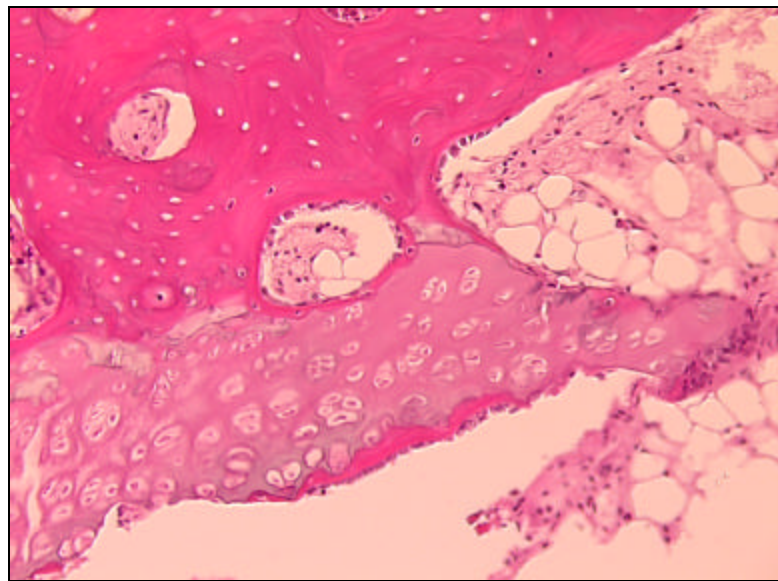


Figure 9. Endochondral Bone Formation in a Loaded Sample; H&E at 20x

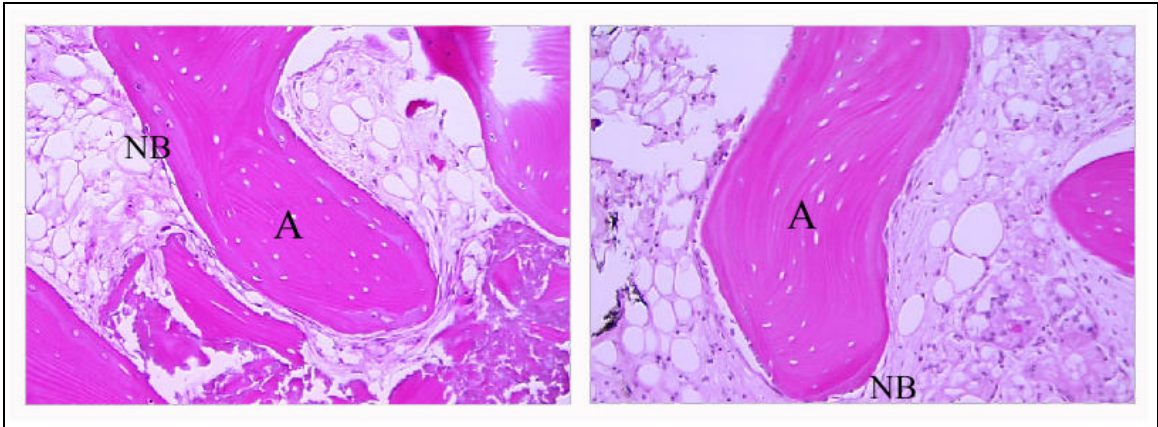


Figure 10. Typical New Bone Formation on Allografts without Loading (Left) and with Four Weeks of Load (Right); A = Allograft, NB = New Bone; 20x

Similar patterns of bone formation were seen in both the paraffin and plastic sections. Comparisons of serial plastic sections either unstained for fluorescence detection or stained with Goldner's Trichrome illustrated that the fluorescent labels were diffusely spread throughout areas of new woven bone with some background labeling of the implanted allograft, unlike typical sequential fluorescent labeling of cortical bone. Figure 11 illustrates this colocalization.

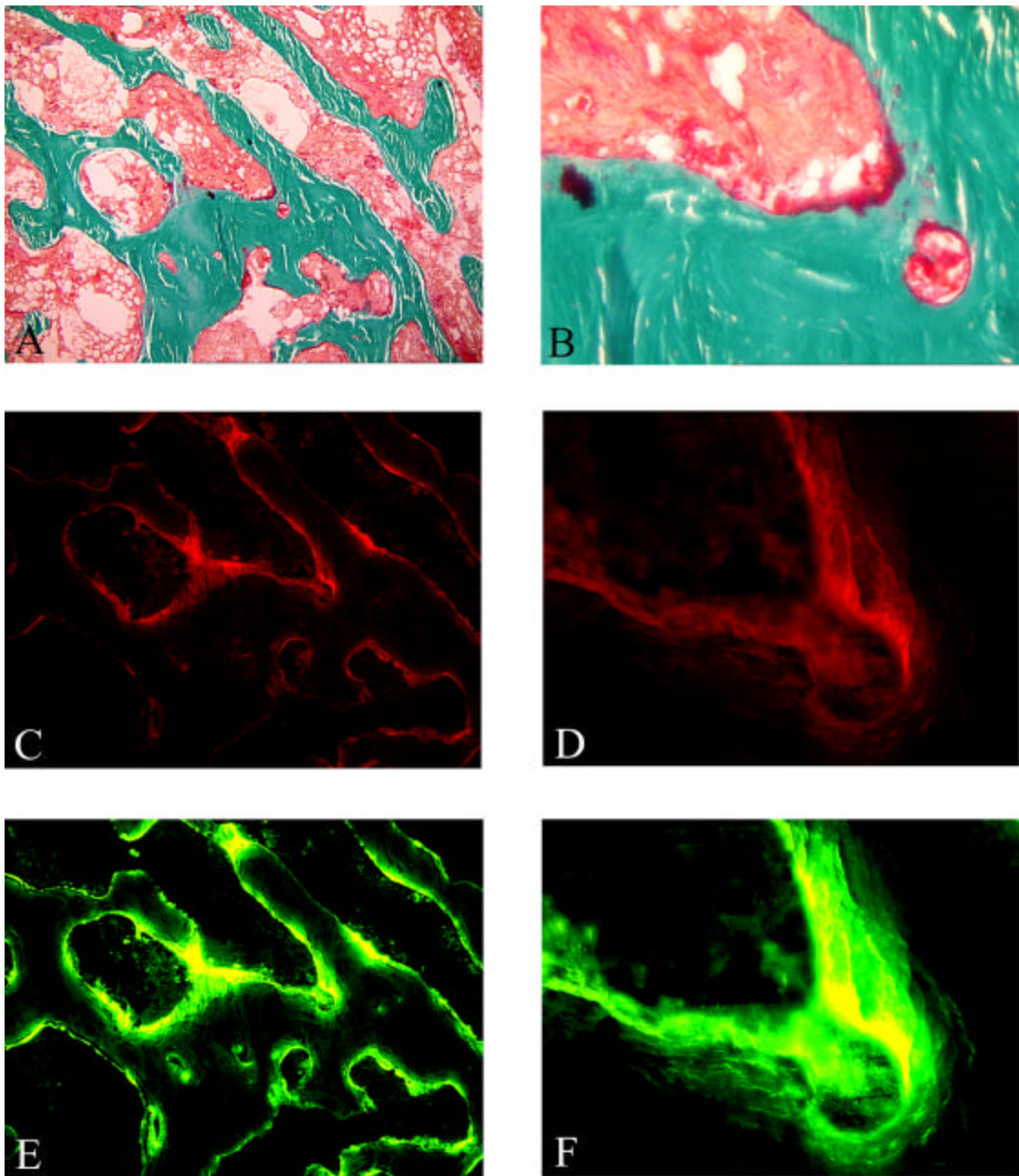


Figure 11. Photomicrographs of allografts: A,B) Goldner's Trichrome; C,D) Tetracycline fluorochrome; E,F) Calcein fluorochrome. A, C, E are 4x. B, D, F are 20x.

3.3.3 Quantitative Results of Fluorochrome Label

New bone formation was quantified using fluorescent microscopy of the calcein green label on unstained plastic sections which encompassed the earlier tetracycline red label and co-localized to areas of new bone formation seen using Goldner's Trichrome staining as seen in Figure 11. Of the nine pairs of samples obtained from the long-term loading study, seven pairs were considered for analysis. Samples from animal #16 were excluded due to a lack of fluorescent signal in the loaded biopsy. The loaded chamber never securely integrated into the surrounding bone in this animal. The subsequent motion probably prevented vascularization of the graft since no fluorescent signal (even background) was seen in the loaded specimen only. The nonloaded specimen showed typical results, but including it in the models would cause the sample to exert unusually high leverage since the sample is unpaired. After an initial analysis of the remaining eight pairs of data, the specimen pair from animal #17 was removed from the data set as an outlier. The DFITS values for these samples were ± 3.42 and ± 4.20 for new bone volume/graft surface area and new appositional bone/graft surface area respectively. Belsey [181] suggests considering any observation to be unusual with $\text{abs}(\text{DFITS}) > 2 \sqrt{p/n}$ or 1.41 for this model. Upon review of this animal's history, the loading piston was extremely difficult to position during surgery which may indicate that load transmission was compromised in this animal. New bone volume averaged 8.20 mm^2 in the nonloaded group and 5.88 mm^2 in the loaded group.

Models of the graft bone volume and surface area confirmed that the assignment of rabbit trabecular allografts was random between the nonloaded and loaded groups

since there were no significant differences in graft properties between the groups. An initial model of total new bone volume showed a trend toward a significant difference ($p=0.060$) between loading groups. Ignoring the intramembraneous bone formation and considering just new appositional bone formation, the effect becomes significant ($p=0.047$). Volumes of intramembraneous bone were small and exhibited no differences between loading groups.

In an effort to normalize the new bone formation to the graft properties, general linear models were also performed on total new bone volume (NBV) and new appositional bone volume (ABV) normalized by either the graft volume (GBV) or graft surface area (GSA). Normalization of NBV and ABV by the graft bone volume did not help explain the variability in the data but normalization by the graft surface area did improve the model. Loading resulted in a significant change in NBV/GSA ($p=0.017$) and ABV/GSA ($p=0.010$). Figure 12 shows new bone volume for each pair normalized by that graft's surface area illustrating a consistent decrease in bone formation with loading for each biopsy pair.

The mean and standard error for each of the statistical groups is listed in Table 1 along with the p -values for each output parameter for a General Linear Model with Load and Animal used as factors to explain the variance in the data. An analysis of regional zones showed no significant differences between radial or longitudinal zones as defined in Figure 3.

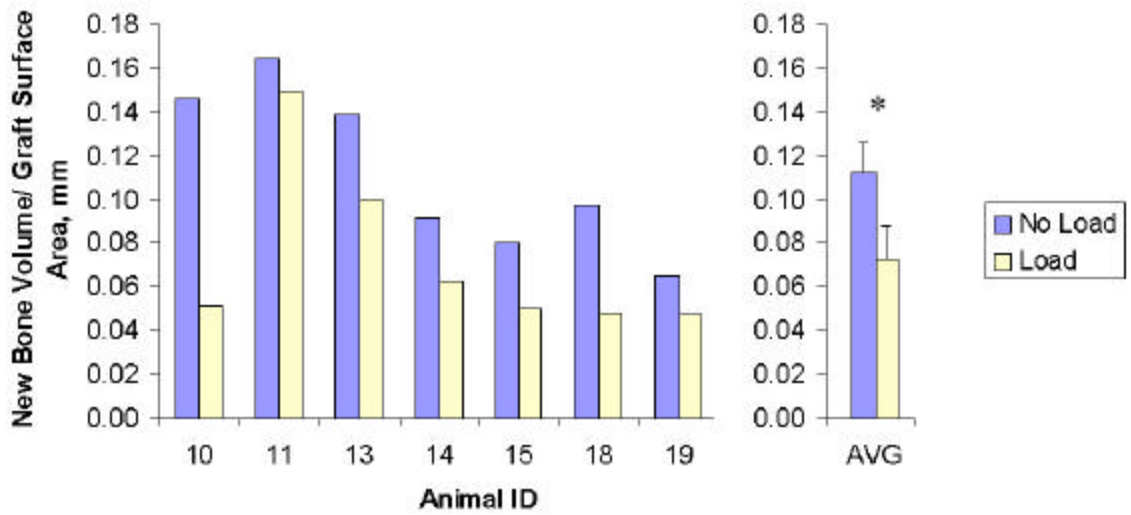


Figure 12. New Bone Volume Normalized by the Available Graft Surface Area for Each Biopsy Pair from the Long-Term Loading Study of Rabbit Trabecular Allografts and the Overall Average for the Group (p=0.009).

Table 1. Statistical Data for Graft and New Bone Measurements.

		GBV mm ²	GSA mm	NBV mm ²	IBV mm ²	ABV mm ²	NBV/ GBV	ABV/ GBV	NBV/ GSA mm	ABV/ GSA mm
Mean	No Load	11.68	74.55	8.20	0.88	7.31	0.73	0.64	0.112	0.099
	Load	10.12	81.98	5.88	0.86	5.02	0.58	0.50	0.072	0.062
SE	No Load	0.85	8.95	1.26	0.20	1.18	0.12	0.11	0.014	0.014
	Load	0.89	7.61	1.29	0.54	0.80	0.12	0.07	0.015	0.009
p-value	Animal	<i>0.077</i>	<i>0.413</i>	0.060	<i>0.555</i>	0.047	<i>0.126</i>	<i>0.103</i>	0.017	0.010
	Load	<i>0.107</i>	<i>0.532</i>	0.090	<i>0.969</i>	0.038	<i>0.294</i>	<i>0.168</i>	0.009	0.003

3.3.4 Vascularity

In an effort to explain the observed reduction in bone formation with loading, the vascularity within each construct was investigated. An initial qualitative assessment suggested there might be more new blood vessels in the nonloaded samples. Representative samples for both a loaded and nonloaded construct are shown in Figure 13.

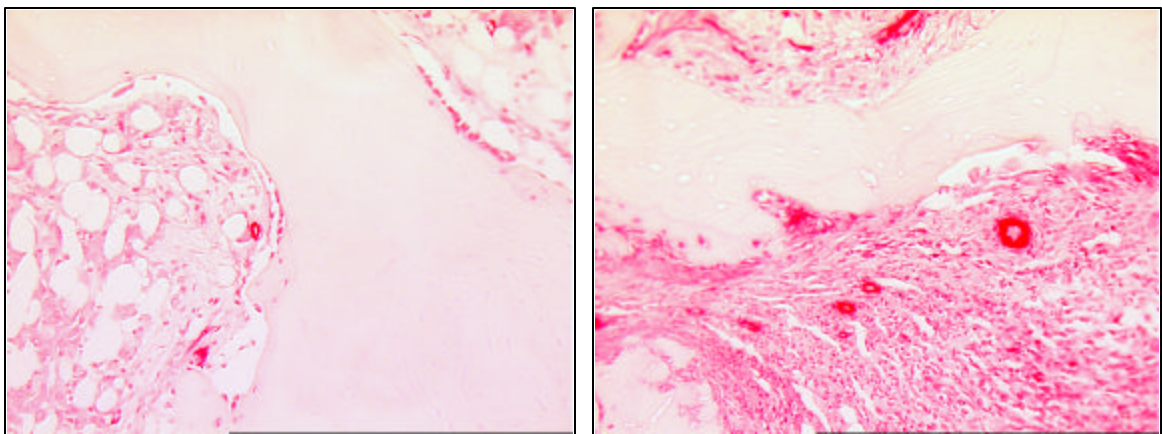


Figure 13. Representative sections of a loaded (left) and nonloaded (right) sample stained for α -SMA (bright pink) at 10X.

A subsequent quantitative analysis was performed by counting the number of vessels staining positive for α -SMA at 10X. illustrates the number of apparent vessels in a given section for each sample within the long-term study. Both a two-way General Linear Model using load and animal as factors and a paired t-test reported $p=.68$, indicating no significant differences exist between the loaded and nonloaded groups.

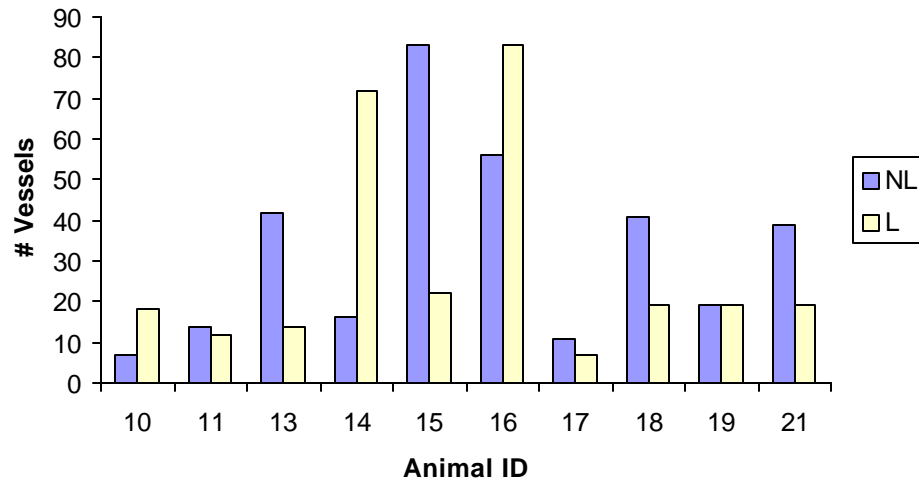


Figure 14. Number of vessels per section as identified by positive α -SMA staining for each loaded and nonloaded sample in the long-term study.

3.3.5 Micro-CT and Finite Element Model Output

A general analysis of the micro-CT images of samples from the long-term loading studies showed that the overall average bone volume fraction (BVF) was 37.5%. While comparisons of morphology parameters do not provide meaningful data on the effect of loading since new bone can not be thresholded from the implanted allograft bone, these images do provide a useful basis for finite element models of the loaded samples. Since relatively little new bone was formed overall, the endpoint image is a reasonable approximation of the geometry of the sample throughout the loading period. Table 2 lists the individual bone volume fractions of each of the samples in the long-term loading study.

Table 2. Bone Volume Fraction of Biopsies from Long-Term Loading Group

ANIMAL ID	LOADED BVF	NONLOADED BVF
10	20.70	41.11
11	35.58	34.99
13	43.97	43.84
14	43.92	43.92
15	42.43	48.98
16	32.66	52.40
17	44.48	26.07
18	23.36	25.46
19	39.73	31.79

Finite element analysis of two representative samples from the long-term loading group was performed with reasonable agreement in the predicted tissue response between both samples. At the apparent level, the average predicted normal strain in the z-direction was $8740 \mu\text{a}$ and the average predicted normal stress in the z-direction was 0.55 MPa. Normal tissue strains in the z-direction range from $-1060 \mu\text{a}$ to $+140 \mu\text{a}$ with the peak of the histogram near zero strain (Figure 15). The profile of the predicted largest principal strains was similar to the normal strain in the z-direction but covered a wider range from $-1420 \mu\text{a}$ to $+480 \mu\text{a}$ (Figure 16). Von Mises stress ranged from 0 to 11.9 MPa with the most common value being 1.2 MPa (Figure 17). The predicted strain energy density ranged from 0 to 0.0115 MPa (Figure 18). The average predicted value of each of the four tissue parameters is given in Table 3 for each representative sample along with the overall average. Figure 19 shows a representative cross-section from the

center of each of the models with its architecture color-coded for largest principal strain and Von Mises Stress. To better delineate patterns in the schematic, the only voxels represented are those ranging from the mean value minus one standard deviation to the mean value plus one standard deviation.

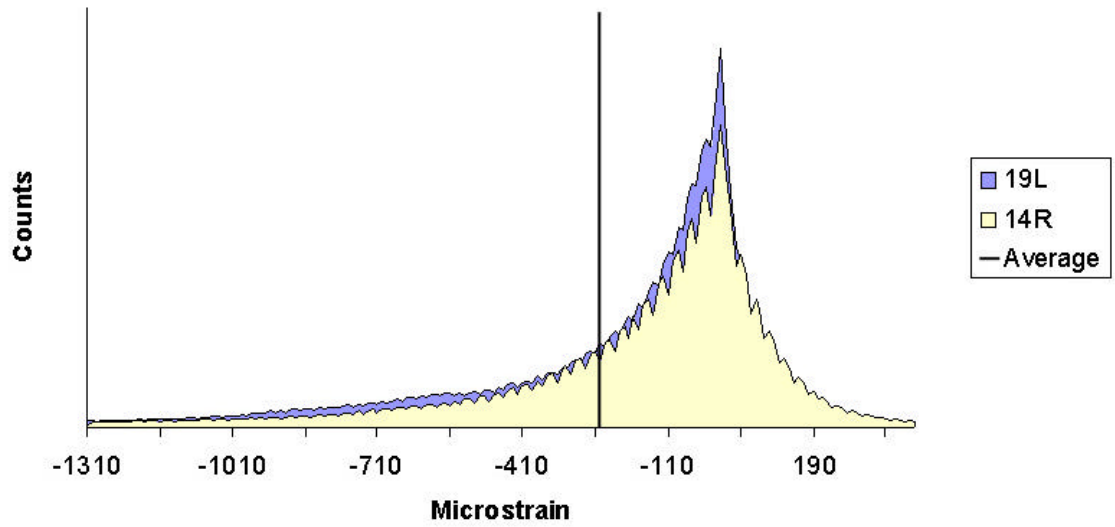


Figure 15. Histogram of Normal Strain in the Z-direction

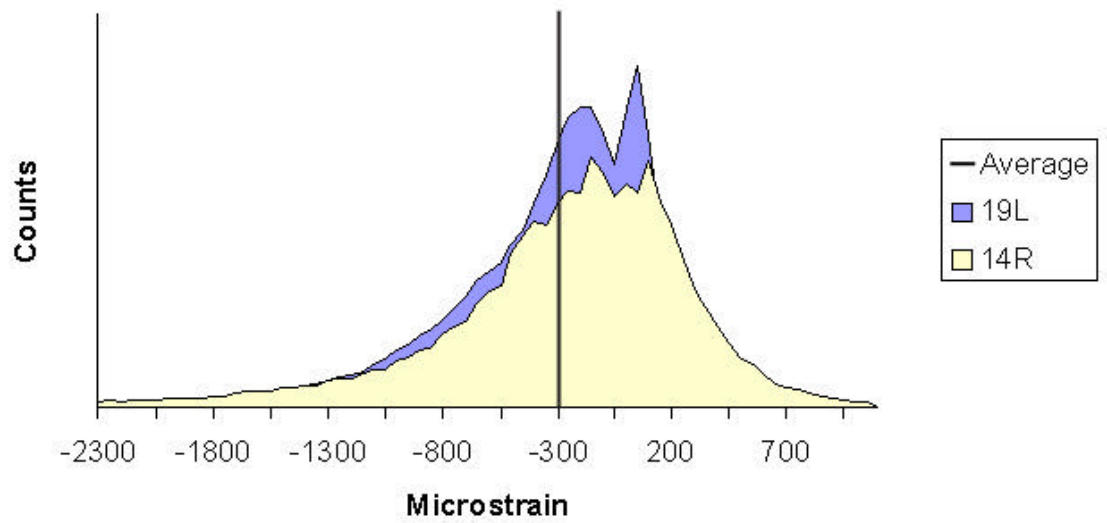


Figure 16. Histogram of Largest Principal Strain

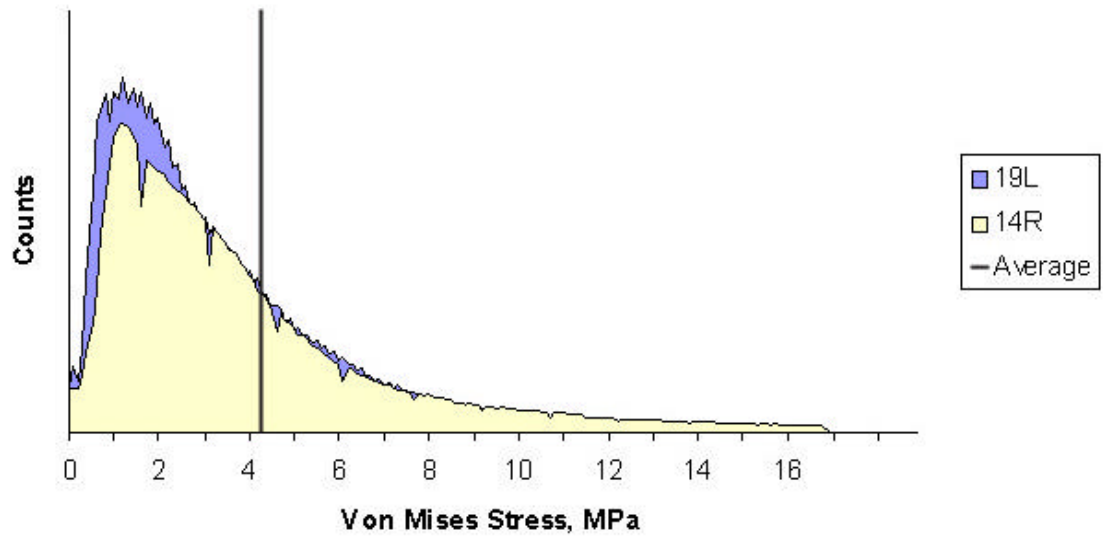


Figure 17. Histogram for Von Mises Stress

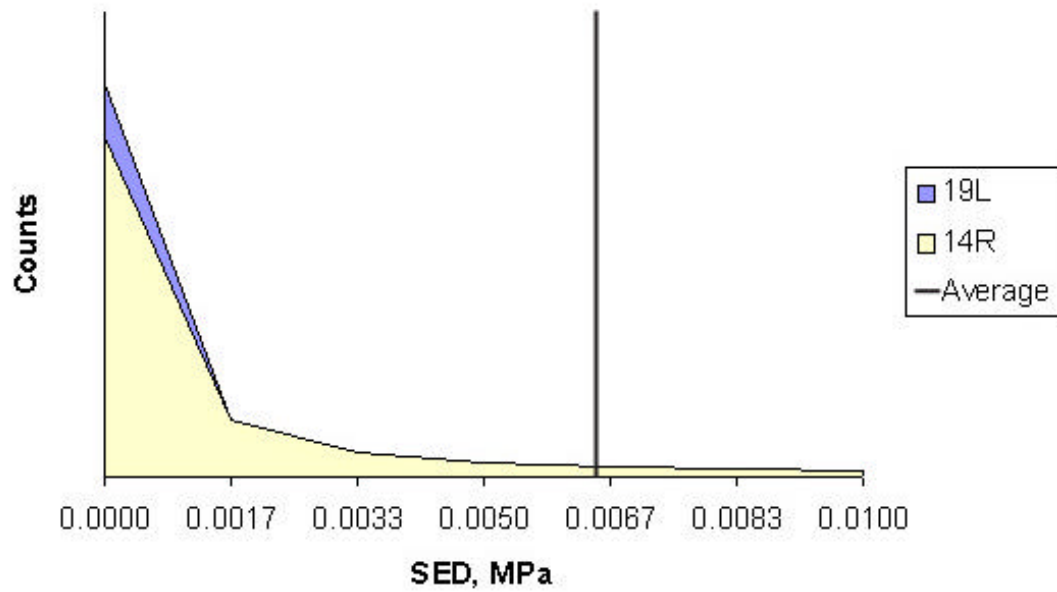


Figure 18. Histogram for Strain Energy Density

Table 3. Average Predicted Tissue Level Response of Long-Term Loaded Samples

	14R	19L	Average	Std. Dev.
$\dot{a}_z, \text{m}\dot{\text{a}}$	-246.1	-246.7	-246.4	0.42
$\dot{a}_l, \text{m}\dot{\text{a}}$	-306.4	-285.8	-296.1	14.57
VMS, MPa	4.98	3.45	4.21	1.08
SED, MPa	0.0109	0.0020	0.0064	0.0063

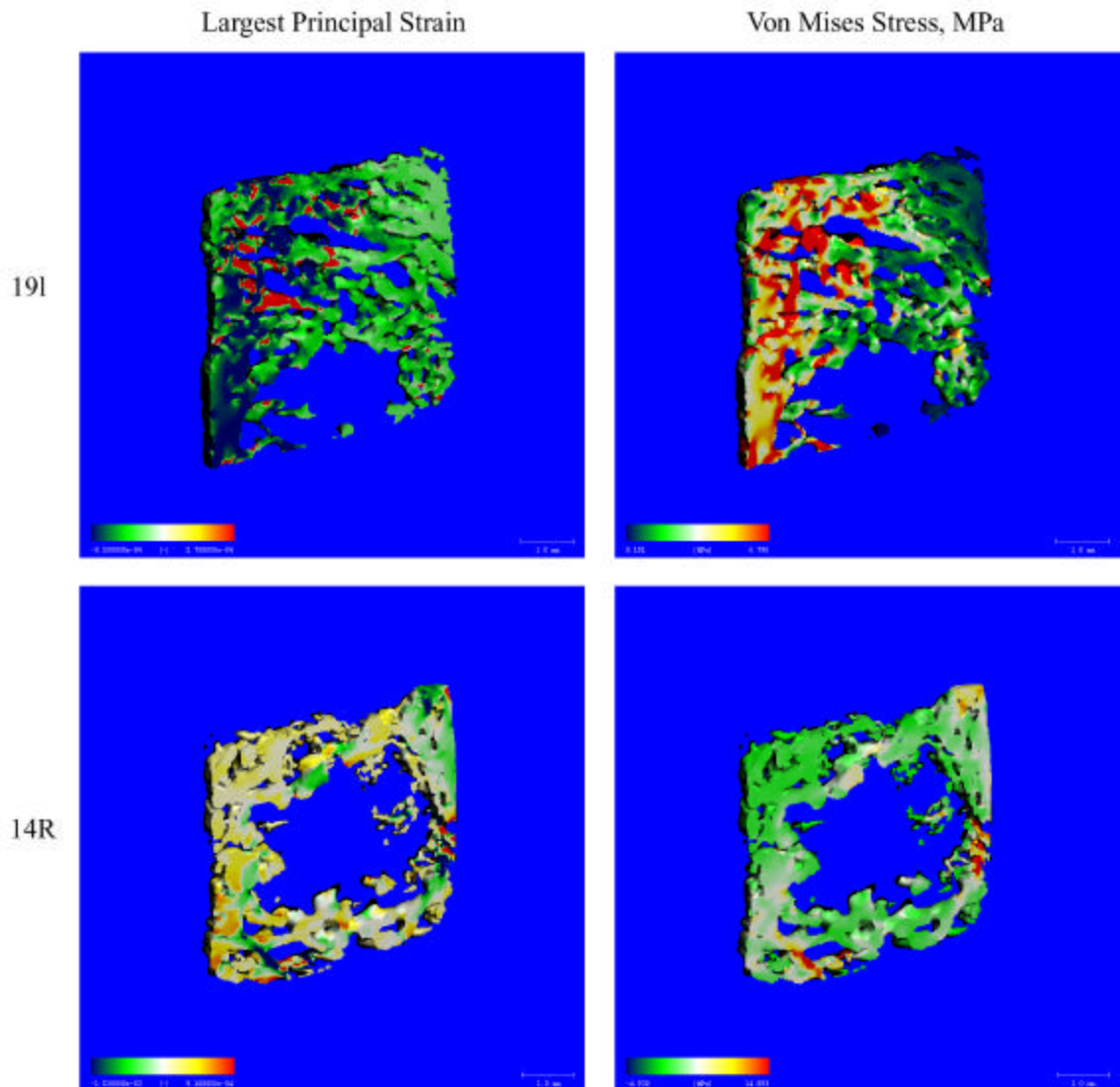


Figure 19. Representative Cross-Sections (Central 340 microns) of Finite Element Model Coded for the Tissue Level Largest Principal Strain and Von Mises Stress

3.4 Discussion

The first specific aim of this study was to characterize and quantify new bone formation in response to *in vivo* mechanical loading of trabecular bone allografts in an orthotopic site. This objective was successfully met. Several patterns of *de novo* bone formation were apparent in histological sections of the rabbit trabecular allografts in the long-term loading experiment. *De novo* bone formation in the canine hydraulic bone chamber study [100] followed an intramembraneous bone formation pathway, and while intramembraneous bone was observed in the rabbit trabecular allografts, the majority of new bone formation occurred by direct apposition to the allograft. The mineralized allograft provides an ideal surface for osteoconduction supporting such appositional bone formation.

Unlike studies performed in most bone chamber models including the canine hydraulic bone chamber, endochondral bone formation was also observed. Tagil however did report cartilage formation in a loaded bone chamber study of *de novo* tissue formed in a chamber resting atop the bone cortex. The tissue in this conduction chamber at the time of loading represented a layered arrangement of tissues that varied from bone and marrow components away from the loading platen to fibrous tissue in direct contact with the loading platen. Upon loading, a cartilage layer was observed only at the top of the biopsy near the platen [97]. For Tagil's study, it is reasonable to postulate that loading of fibrous tissue in a potentially restricted vascular setting produced a cartilage layer, rather than concluding that loading of *de novo* bone formation produced cartilage.

In healing fracture calluses, cartilage tissue differentiation is commonly noted in areas of poor vascularity and/or areas of unstable interfragmentary micromotion [13, 14, 16]. Probst describes how spreading capillaries are disrupted by shear forces in mechanical unstable fractures causing a hypoxic environment favoring chondrogenic differentiation [15]. Furthermore, it has been demonstrated that preosseous tissue will be diverted to a chondrogenic fate in regions of low oxygen tension [50]. One loaded hydraulic bone chamber in the long-term loading study never fully integrated into the femoral bone, allowing free rotation of the implant in the host bone. Micromotion on a much smaller scale may have occurred in other loaded implants as well explaining the observance of cartilage and endochondral bone formation. Either the motion itself and/or subsequent disruption in vascularity may have predisposed cartilage formation. However, a disruption in vascularity could not be confirmed from an analysis of histologic sections stained for α -SMA.

General histological observation of loaded and nonloaded samples indicated a reduction in new bone formation with loading. Quantification of the fluorescent signal from injected bone labels confirmed a significant reduction in new bone volume per graft surface area available for bone formation. Intuitively, this result seems unexpected given the positive results of similar experiments on *de novo* bone formation in canines [100] as well as the abundance of literature supporting enhanced bone formation with mechanical loading. There are a few possible explanations. First, *in vivo* compression of regenerating bone formation on a three-dimensional scaffold has never been investigated. While previous work in the rabbit hydraulic bone chamber confirmed the presence of osteoblasts lining trabecular surfaces and a thin layer of mineralized tissue on allografts

implanted in the chamber for four weeks, the number of responsive cells and the quality of matrix present at the time of load onset was probably inferior to that in the canine hydraulic bone study of *de novo* bone formation in which loading was delayed for eight weeks. No studies at present have been conducted to examine the impact of a connected matrix network on conduction of mechanically induced molecular signals, but results may have been different if loading had been delayed further allowing additional *de novo* bone formation prior to initiating mechanical loading. Furthermore, it is possible that the loading stimulus chosen was not significant enough to induce bone formation. The normal compressive strains predicted by finite element analysis in the trabecular tissue ranged from +140 $\mu\epsilon$ to -1060 $\mu\epsilon$. Frost's Mechanostat Theory predicts that strains in this range would fall in the physiological range of loading and are therefore suitable for the maintenance of bone mass [34]. However, Frost's strain guidelines are based roughly on apparent strains which might suggest that tissue level strains in this range may actually fall toward more of a disuse regime. Interestingly, Guo modeled compression of rat tail vertebra using a set of loading parameters known to induce bone formation and predicted normal compressive tissue strains ranging from +380 $\mu\epsilon$ to -1994 $\mu\epsilon$ for a 100 N load [182]. While this range is broader than the strain range predicted for this study, the difference does not seem large enough to separate resorptive from formative regimes.

However these theories more likely explain the absence of an effect of loading on new bone formation, when in fact a significant reduction in new bone was observed in loaded trabecular allografts. Given that one loaded chamber never stably integrated with the femoral bone and another loaded sample demonstrated signs of chondrogenesis suggests that unexpected micromotion between the bone and the implant may have

occurred in other samples as well. While cartilage was not observed in all loaded samples, micromotion may still have been significant enough to disturb the vascular supply such that bone formation was impeded in loaded specimens. Given the small apparent deformation of 8740 μm in the axial direction, it seems possible but unlikely that the motion of the loading piston resulted in disrupted vascularity since local displacements would be even smaller and apparent deformation of 2-5% in the canine hydraulic bone chamber did not seem to disturb the vascular supply. However, it is also possible that radial micromotion of the implant occurred due to the presence and pressurization of the attached indwelling tubing. Since the tubing is transcutaneous, the tubing was subject to disturbances caused by the animal's motion even though precautions were taken to minimize this eventuality. Furthermore, the required pressure in the tubing to adequately deform the trabecular allograft was 100 psi which is the recommended maximum working pressure for the polyurethane tubing used. This pressure was large enough to cause significant motions of the unrestricted connecting tubing external to the animal and palpable vibrations through the skin from the indwelling tubing. Given the perpendicular orientation of the tubing attachment to the chamber, such vibrations may have resulted in a net moment on the chamber causing radial micromotion. Such micromotion may have disturbed the vascular supply to the regenerating allograft through the radial infiltration ports, however a disruption in vascularity could not be confirmed from the histology. Currently, no single explanation given can provide an adequate explanation of the observed reduction in bone formation with loading.

The second specific aim of this study was to use finite element modeling to predict tissue strains in the loaded trabecular allografts for comparison with patterns of local bone formation in order to determine a regime of adaptive tissue strains. Predictions of tissue level strains ranged from $-1420 \mu\epsilon$ to $+480 \mu\epsilon$ for the largest principal strain with most of the bone experiencing strains near $-300 \mu\epsilon$. Because a positive adaptive response in bone formation on rabbit trabecular allografts was not achieved however, it was impossible to meet the primary objective of the study to determine a set of local tissue strains resulting in mechanical adaptation.

The third specific aim of the study was examination of early gene response to mechanical loading of trabecular allografts *in vivo*. Investigation of early gene expression using RT-PCR methods of trabecular allografts loaded for three days proved unsuccessful. While others have analyzed mRNA expression in *de novo* bone formation regenerating in an empty defect [101], RNA extraction from bone forming on a trabecular allograft proved difficult. Obstacles included a low ratio of metabolically active cells to the overall mineralized matrix present. The trabecular allograft represents a large volume of devitalized matrix with only a small number of active cells on its surface. The presence of an abundant mineralized matrix also interferes with and acts as a contaminant in the RNA extraction process.

The outcomes of this study, although unexpected, do not suggest that pursuit of an *in vivo* bioreactor employing mechanical preconditioning of cell-seeded polymeric constructs should be abandoned. The vast majority of literature supports the enhancement of mineralization through mechanical loading. However, a large number of

factors play a role in tissue differentiation and mineralization of mesenchymal tissue including cellularity, vascularity, and a host of mechanical loading parameters. Disrupted vascularity from micromotion, is less of a concern in a subcutaneous system because, unlike the rigid environment around an orthotopic chamber, the compliant nature of the subcutaneous environment is more likely to move with the chamber even if micromotion of the implant occurs. In fact, the protocol for using the *in vivo* bioreactor developed avoided the use of transcutaneous tubing, reducing the likelihood of animal disturbance to the tubing which might disrupt blood supply to the regenerating scaffolds enclosed in the *in vivo* bioreactor. In addition, the forces required to deform polymeric constructs are much lower due to their lower moduli, reducing the likelihood of micromotion associated with the actuation mechanism. Moreover, an *in vivo* bioreactor may be employed to accomplish the same task of identifying a regime of local tissue strains resulting in bone formation on a three-dimensional scaffold as intended by the present study. The results reported here even suggest that loading of a more cellular scaffold with a less variable architecture may prove a better scenario for identifying adaptive tissue strains.

CHAPTER 4

DESIGN AND DEVELOPMENT OF A NOVEL MECHANICAL LOADING DEVICE FOR USE AS A SUBCUTANEOUS *IN VIVO* BIOREACTOR IN A RODENT MODEL

4.1 Introduction

4.1.1 Summary

Technology for construct development is a crucial area for tissue engineering. Cell-seeded scaffolds may benefit from chemical or physical preconditioning before implantation. Such preconditioning may allow the construct to better meet the functional demands of its environment. Most current tissue-engineered bone replacements typically do not utilize such preconditioning strategies, but researchers are beginning to examine the benefits of *in vitro* preculture of three-dimensional scaffolds. This preculture period may promote cellular proliferation, differentiation, and/or matrix mineralization, usually from exposure to an array of tissue culture supplements including dexamethasone, bone morphogenetic proteins, and Na- β -glycerophosphate. Wang has demonstrated the additional benefit of *in vitro* preculture to final *in vivo* mineralization [155]. However, current *in vitro* development of three-dimensional cell-seeded scaffolds for bone defect repair is limited by poor transport in and out of the scaffold of nutrients, degradation products, and metabolic wastes. Construct development *in vivo* may be able to avoid such complications due to the presence of invading blood vessels into the construct. Others have used the *in vivo* environment to revascularize bone autografts and prepare other vascularized tissue engineering constructs [155, 167, 168].

The development of an *in vivo* bioreactor system capable of applying a controlled mechanical stimulus to developing bone tissue-engineered constructs may be able to capitalize on the mechanoresponsiveness of osteoprogenitors to produce constructs with greater mineralization. Such constructs may have greater amounts of more evenly distributed mineralization, possibly suited for loadbearing situations. Because of improved transport in an *in vivo* system, larger constructs may be produced with cells present throughout the scaffold. For certain constructs, it may be possible to maintain the developed vascular structure to the orthopedic defect site, anastomosing the construct's vasculature to the bone's blood supply. A tissue chamber system was designed and developed for use in the subcutaneous space of a rat. This system is capable of applying a controlled intermittent stimulus via a hydraulically actuated piston to the three-dimensional scaffold developing inside the chamber. This chapter describes not only the system design, but feasibility and pilot experiments associated with the system development.

4.1.2 Specific Aims

Specific Aim #1: To verify that enclosure of a cell-seeded scaffold in a titanium chamber does not impede subcutaneous bone formation.

An initial prerequisite for a subcutaneous *in vivo* mechanical loading system was assurance that bone formation could occur on cell-seeded scaffolds placed within titanium chambers in the subcutaneous space of rats. A variety of cell/polymer and cell/ceramic combinations were placed within titanium bone chambers and implanted in the subcutaneous space. Bone formation was quantified by micro-computed tomography

after six weeks. It was demonstrated that enclosing a construct within a titanium chamber did not reduce bone formation compared to control specimens implanted directly into the subcutaneous space.

Specific Aim #2: To design and develop a novel system to apply mechanical compression to tissue-engineered scaffolds prepared in a subcutaneous in vivo environment.

An original implant system capable of applying a controlled mechanical stimulus to cylindrical scaffolds implanted subcutaneously in a rat was designed and created. Such a system may provide the ability to develop larger, stronger, and more homogeneous bone tissue replacements than could be developed in a diffusionally limited *in vitro* culture system. Such pre-conditioned constructs may be better able to meet the functional demands of the bony environment. Furthermore, if constructs are developed in the final host, they may be populated with receptive host cells that will reduce the immunologic challenge presented to the patient when the bone defect is repaired.

Specific Aim #3: To verify the functionality of new subcutaneous loading system hardware in vivo.

Finally, an initial test of the performance of the newly designed subcutaneous tissue loading system was performed. These experiments gave key insight into appropriate surgical protocols and animal post-operative care for studies utilizing this novel system.

4.2 Subcutaneous Pilot Experiments

4.2.1 Introduction

Before proceeding with the idea of a subcutaneous *in vivo* bioreactor capable of applying a controlled compressive load *in vivo*, it was necessary to determine the feasibility of such an idea. The first goal of the feasibility experiments was to determine if enclosing a tissue-engineered bone construct within a titanium chamber would hinder bone formation on the construct when implanted subcutaneously on a rat's back. The second goal of the feasibility experiments was to determine the best possible choice of scaffold material, cells, and culture conditions for the implanted constructs. Therefore a variety of materials and cell preparation conditions were employed in these experiments.

4.2.2 Methods

Seventy-six scaffolds were prepared for the experiment. Each scaffold had a cylindrical shape 0.25" in diameter and 0.25" in length. Twenty-eight 60:40 hydroxyapatite/tricalcium phosphate (Ha/TCP) samples were purchased from Berkeley Advanced Biomaterials (San Leandro, CA) with an average pore size of 250 microns and then sterilized with a 2.5 Mrad dose of gamma irradiation. Eight polycaprolactone (PCL) were manufactured by a fused deposition modeling technique compliments of Dr. Dietmar Hutmacher at the National University of Singapore and were disinfected in ethanol. The scaffolds had a defined repeatable architecture similar to that shown in Figure 20.

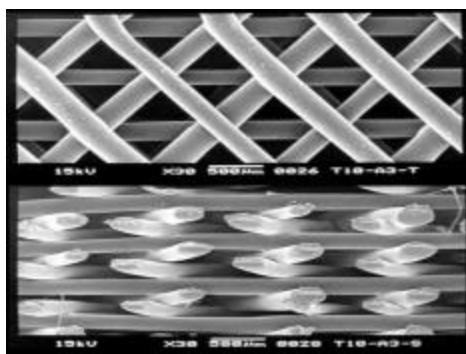


Figure 20. Polycaprolactone Microarchitecture

Forty poly(L-lactide-co-D,L-lactide 70:30) (PLDL) samples were manufactured as published previously [183]. Briefly, PLDL was combined with 30% azodicarbonamide solvated in acetone and then repeatedly coated on 316 stainless steel wires. Wires were bundled in heat shrink tubing and heated 20 minutes at 60C to fuse them together before the bundles were heated to 260C in peanut oil to decompose the porogen. The wires were then removed and the bundles rinsed in hexane. Bundles were cut to 0.25" lengths and rinsed in ethanol and allowed to dry. PLDL samples were also sterilized with a 2.5 Mrad dose of gamma irradiation. Scaffolds were incubated in a 20-25 $\mu\text{g/ml}$ suspension of rat plasma fibronectin (Sigma #F0635) for 16 hours at 4C, then rinsed three times with PBS and remained hydrated in PBS until seeded with cells. Some scaffolds received a coating of rhBMP2 prior to fibronectin coating. These samples were immersed in 100 μl of a 24 $\mu\text{g/ml}$ solution of rhBMP2 (Sigma) and allowed to dry at room temperature under a vacuum for 3 days similar to a method described previously [166].

Rat mesenchymal stem cells were obtained from Osiris Therapeutics and were isolated from the pooled marrow of seventeen Fisher rats and then frozen after the initial confluence. Cells were expanded in alpha-MEM (Invitrogen #32561-037) with 10% fetal bovine serum (FBS) (Valley Biomedical lot # L7938) and 1% antibiotic/antimycotic (Invitrogen #15240-062). Passaging was performed every fourth day with 0.05% trypsin, .53 mM EDTA-4Na (Invitrogen #15400-054) and replated at 10,000 cells/cm². Some cells were expanded in the standard media supplemented with 50 μM ascorbic acid 2-phosphate (AsAp) and 10 nM dexamethasone to predifferentiate the cells toward an osteoblastic phenotype. Since these cells were actively secreting extracellular matrix, treatment with a collagenase solution (150 U/ml collagenase type I and 50 U/ml collagenase type II (Worthington #LS004196) in serum-free alpha-MEM) was required prior to trypsinization to lift the cells to passage them.

Scaffolds were seeded with a 7.5e6/ml or 9e6/ml cell suspension using a vacuum syringe technique. Scaffolds were sterilely placed in the barrel of a 3ml syringe with a 3 way stopcock on the syringe luer. A 500 μl volume of the cell suspension was added to the syringe through the stopcock. The valve was closed and a vacuum was pulled and released at least five times to help pull the cell suspension within the scaffold pores. Scaffolds were incubated at 37C for two hours before 1.5 ml media was added to nourish the cells. Scaffolds were kept in a 37C incubator overnight until *in vivo* implantation. Table 4 lists the various scaffolds and cell treatments investigated in this pilot experiment and the number of samples used for each group. A few extra scaffolds were prepared for analysis of cell viability using a Live/Dead fluorescent staining kit (Molecular Probes L-3224) employing calcein and an ethidium homodimer. After overnight incubation,

samples were rinsed three times in PBS, stained with a solution containing 4 μ M concentrations of calcein and ethidium homodimer each, rinsed in PBS three more times and imaged using confocal microscopy. Confocal images were taken at multiple depths and stacked to create a three dimensional representation of the scaffold using a Zeiss LSM 510 Confocal Microscope (Carl Zeiss, Inc.). Additional samples were analyzed for double stranded DNA content using PicoGreen dsDNA Quantitation Kit (Molecular Probes P-11496). See Appendix E for a detailed protocol employed to analyze DNA content from cells seeded on a three-dimensional scaffold.

Table 4. Various Tissue-Engineered Scaffolds Tested in Feasibility Experiments

Material	Dex	Passage	BMP2	# Scaffolds
Ha/TCP	No	P2	No	16
Ha/TCP	No	P4	No	6
Ha/TCP	No	P4	Yes	6
PCL	No	P2	No	8
PLDL	No	P2	No	8
PLDL	No	P4	No	6
PLDL	No	P4	Yes	6
PLDL	Yes	P1	No	4
PLDL	Yes	P1	Yes	4
PLDL	Yes	P4	No	6
PLDL	Yes	P4	Yes	6

Scaffolds were implanted subcutaneously into the backs of 19 male Fisher rats, each weighing more than 175 g, using a blunt dissection technique. Four scaffolds were implanted in each animal at each of the four positions shown in Figure 21. Two of the scaffolds were implanted in titanium chambers identical to the nonloaded chambers used in the experiments described in Chapter 2 (Figure 1). Each scaffold/cell combination outlined in Table 4 had half the samples implanted within chambers and half were implanted directly into the subcutaneous space. Scaffolds implanted in chambers were always positioned diagonally at either positions A and D or B and C.

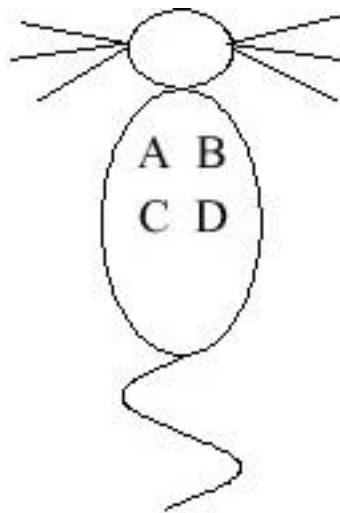


Figure 21. Positions for Scaffold Implantation

Anesthesia was induced using 4% isoflurane and maintained on 1-2% isoflurane by mask. The rat's back was shaved and scrubbed. The site was draped and covered in Ioban, a sterile antimicrobial film. A 1.5 cm incision was made through the skin between positions A and B on the dorsal side of the rat parallel and slightly offset from the spine. Blunt scissors were used to make small pouches in the subcutaneous space on either side

of the incision away from the midline as shown in Figure 22. A single scaffold or a scaffold enclosed in a titanium chamber was placed in each pouch. The incision was closed with wound clips. The process was repeated for scaffolds implanted at positions C and D.



Figure 22. Subcutaneous Implantation of a Tissue-Engineered Bone Scaffold within a Titanium Chamber

After six weeks, animals were euthanized via carbon dioxide overdose and scaffolds were harvested. Scaffolds enclosed in chambers were retrieved using a thin-walled kerchunker as shown in Figure 81. All samples were fixed in 10% neutral buffered formalin for 48 hours and then stored in 70% alcohol.

All animal procedures involving subcutaneous implants in rats without applied *in vivo* loading were approved by Georgia Tech's Institutional Animal Care and Use Committee in Protocol #A02003.

Scaffolds were imaged using a microCT 40 in a process similar to that described in Section 2.2.6. The microCT 40 differs from the microCT 20 in that serial tomograms are reconstructed from the raw data using a cone-beam filtered backprojection algorithm adapted from Feldkamp et al [184] rather than a fan-beam approach. These samples were scanned at a resolution of 16 microns with the scanner operating at a voltage of 50 kVp and a current of 160 μ A. MicroCT images were first filtered using a constrained 3-D Gaussian filter (sigma = 1.2, support = 2) to partially suppress noise in the volumetric image data prior to segmentation to reveal the mineralized tissue from the surrounding soft tissue using a global thresholding procedure. A threshold of 45 was selected for all PCL and PLDL samples in this experiment. For the Ha/TCP samples, a double thresholding technique was attempted to isolate new bone formation from the implanted ceramic phase but was unsuccessful.

For subsequent statistical analysis of PCL and PLDL bone formation, a normalized bone volume parameter (BVP) was examined. Since sample diameters were very consistent, BVP was defined to be the bone volume per unit length of the sample minus the background bone volume per unit length of the polymer. PCL had no background noise, but PLDL had a very small level of background noise that might appear as an additional 0.00228 mm² of bone volume per unit length. One observation out of 48 was removed from the data set as an outlier since its BVP was more than four times larger than any other sample and its corresponding DFITS value was almost eight times larger than the recommended maximum by Belesley [181]. General Linear Models were performed to search for patterns in the variance that may be attributable to the cell type or passage, scaffold material, BMP treatment, or enclosure in the titanium chamber.

Models also looked at animal, implantation position, and harvest date to further account for variability in the data. All analyses per performed with alpha of 0.05.

After scanning, samples were cut in half longitudinally using an Isomet 1000 Precision saw (Beuhler). If the scaffold material was PCL or PLDL, one half the sample was processed in paraffin and sectioned at 10 microns. Sections were stained with H&E, Safranin-O, mMAB, or Goldner's Trichrome. Ha/TCP samples were processed in plastic and stained with either Sanderson's Rapid Bone Stain [185] or Toluidine Blue.

4.2.3 Results

Confocal microscopy of representative PLDL samples stained with calcein and ethidium homodimer 24 hours after seeding revealed reasonable quantities of live cells. The longitudinal macroporosity allowed for deep penetration of the cells within the scaffold. Of the four PLDL samples examined, the depth of penetration recorded ranged from 1.0 mm to 1.7 mm. Figure 23 shows confocal images of a Live/Dead stained PLDL sample. These images were acquired from the top of the cylinder looking along the longitudinal axis. The side projection in Figure 23C illustrates that the cells were collecting in the longitudinal macroporosity of the scaffold.

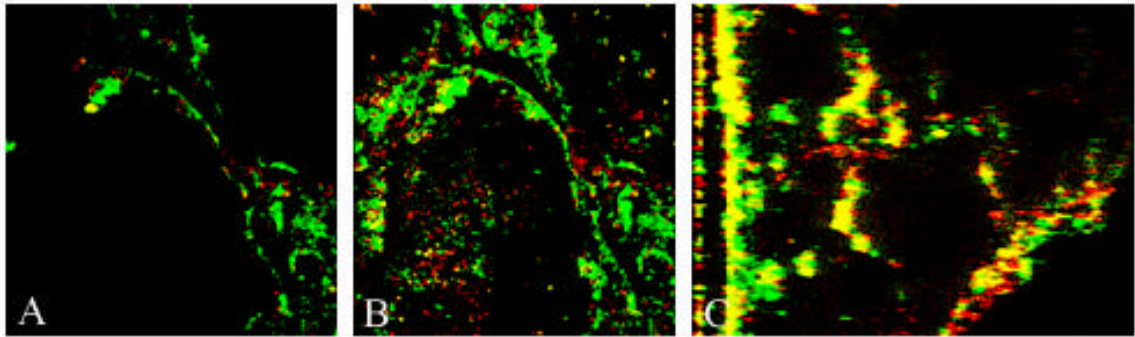


Figure 23. A Representative Cell-Seeded PLDL Scaffold Labeled for Live (Green) and Dead (Red) Cells; A) Single Slice, B) Normal Projection of All Confocal Slices, C) Side Projection of All Confocal Slices

Double-stranded DNA was quantified on four representative PLDL samples using a relatively untested protocol employing Pico-Green. These results indicate that only 0.7-1.2e6 cells attached to the scaffolds out of an original 4.5e6 cells in the cell-seeding suspension. This represents cell-seeding efficiencies between 16-28%.

All *in vivo* scaffolds appeared to be vascularized at time of harvest and did not appear to have initiated a significant foreign body reaction. Such vascularization is apparent in Figure 24. By visual observation, scaffolds implanted inside titanium chambers actually appear more vascular than those implanted directly into the subcutaneous space.

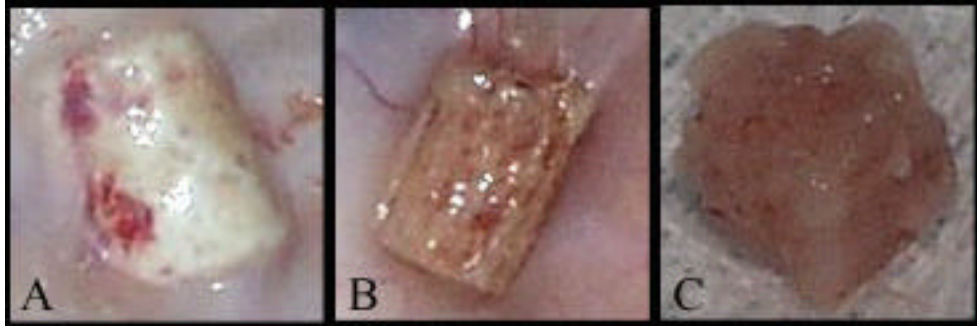


Figure 24. Representatives of Each Scaffold Material at Time of Harvest; A) Ha/TCP, B) PLDL, C) PCL

Analysis of new bone formation from microCT images revealed that small volumes of new bone formed on PCL and PLDL. New bone formation was evident throughout the construct, not just on the periphery (Figure 25).





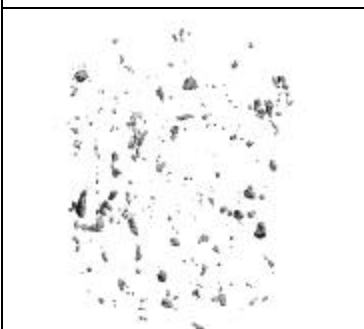

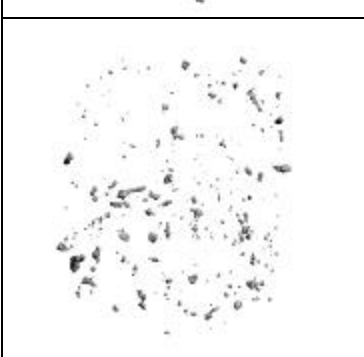
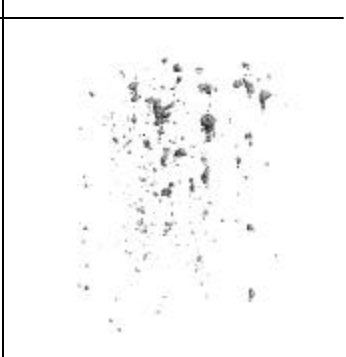
	Enclosed Implant	Open Implant
PCL, P2 rMSCs		
PLDL, P2 rMSCs		
PLDL, P4 rMSCs		
PLDL, P4 rMOPs		

Figure 25. MicroCT Images of Cell-Seeded Scaffolds Implanted Subcutaneously for Six Weeks. These Samples had No rhBMP-2 Treatment.

BVP values ranged from 0 to 0.08 mm³/mm. Although data was collected on 48 samples, sample sizes per ranged from 2 to 4 per treatment group due to a wide variety of treatments investigated. The mean, standard error, and sample size of each treatment group is reported in Table 5.

Table 5. Mean Bone Volume Parameter, Standard Error of the Mean, and Sample Size for Each Treatment Condition Tested

TRT #	Material	Cell Type	BMP2	Chamber	BVP mm ²	Standard Error	n
1	PLDL	P4 MSC	NO	NO	0.0453	0.0058	3
2	PLDL	P4 MSC	NO	YES	0.0232	0.0081	3
3	PLDL	P4 MSC	YES	NO	0.0088	0.0023	3
4	PLDL	P4 MSC	YES	YES	0.0343	0.0194	3
5	PLDL	P4 MOP	NO	NO	0.0180	0.0019	3
6	PLDL	P4 MOP	NO	YES	0.0222	0.0047	3
7	PLDL	P4 MOP	YES	NO	0.0346	0.0044	3
8	PLDL	P4 MOP	YES	YES	0.0108	0.0074	3
9	PLDL	P1 MOP	NO	NO	0.0079	0.0001	2
10	PLDL	P1 MOP	NO	YES	0.0032	0.0038	2
11	PLDL	P1 MOP	YES	NO	0.0182	0.0088	2
12	PLDL	P1 MOP	YES	YES	0.0314	0.0209	2
13	PLDL	P2 MSC	NO	NO	0.0269	0.0179	4
14	PLDL	P2 MSC	NO	YES	0.0186	0.0052	3
15	PCL	P2 MSC	NO	NO	0.0019	0.0010	4
16	PCL	P2 MSC	NO	YES	0.0134	0.0043	4

Figure 26 compares the mean bone volume parameter for the major factor groups. General Linear Models of the BVP did not show a significant difference between MSCs with or without predifferentiation to an osteoblastic phenotype. Furthermore, there was no significant difference in BVP due to passage number or pretreatment of the scaffold with rhBMP2. There was little variability from animal to animal or between implant position assignments. Overall, the models could not show a significant difference

between bone formation on a scaffold implanted inside a titanium chamber versus on a scaffold implanted directly into the subcutaneous space. However, in PCL, there was a significant ($p=0.040$) increase in BVP when the sample is enclosed in a titanium chamber (Figure 27). Despite the increase in BVP for PCL when enclosed in a chamber, PLDL formed significantly ($p=0.036$) more bone overall than PCL.

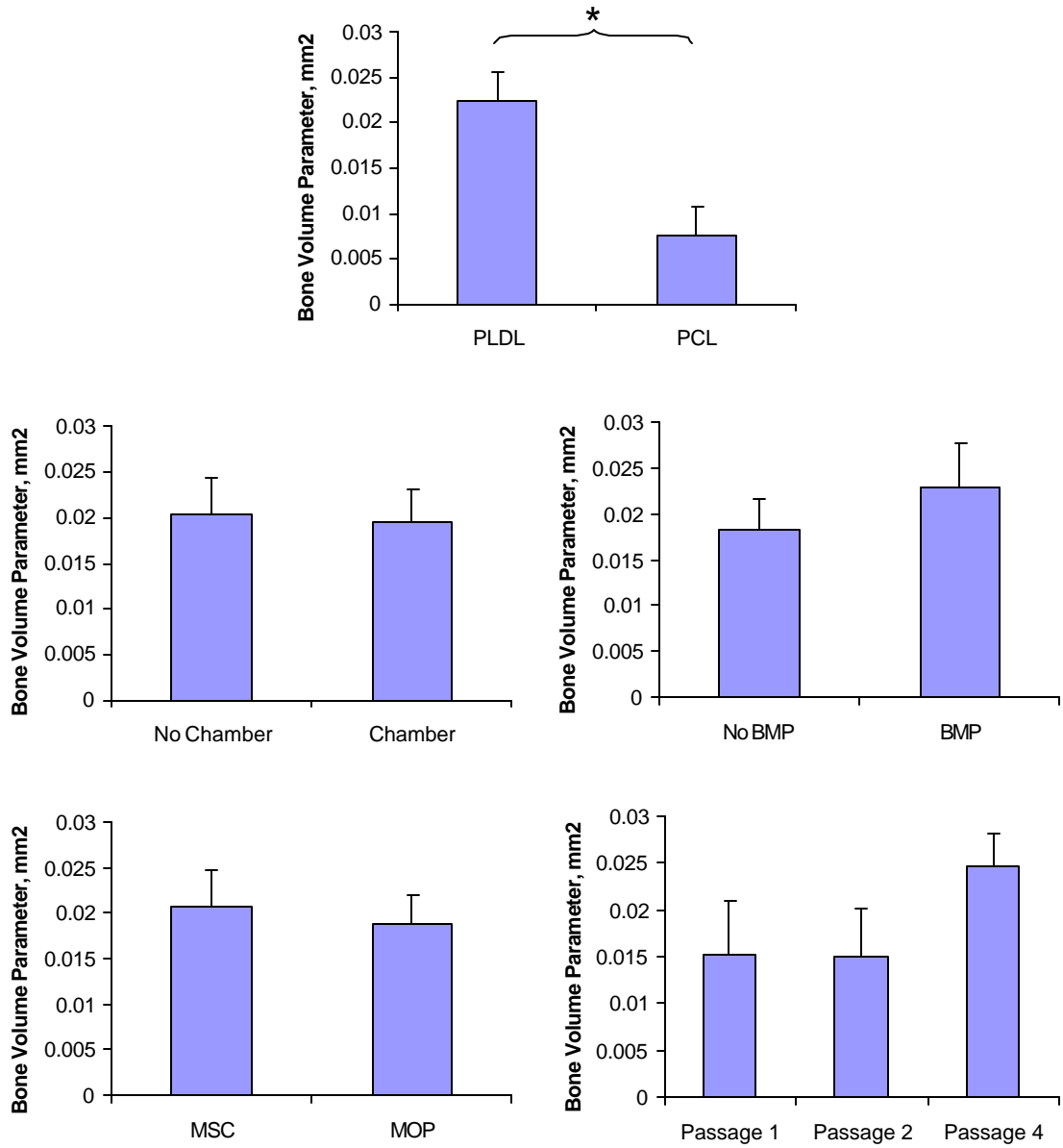


Figure 26. Mean BVP Comparisons Based on Material Type, Enclosure in a Titanium Chamber, Treatment with rhBMP2, Cell Type and Passage Number

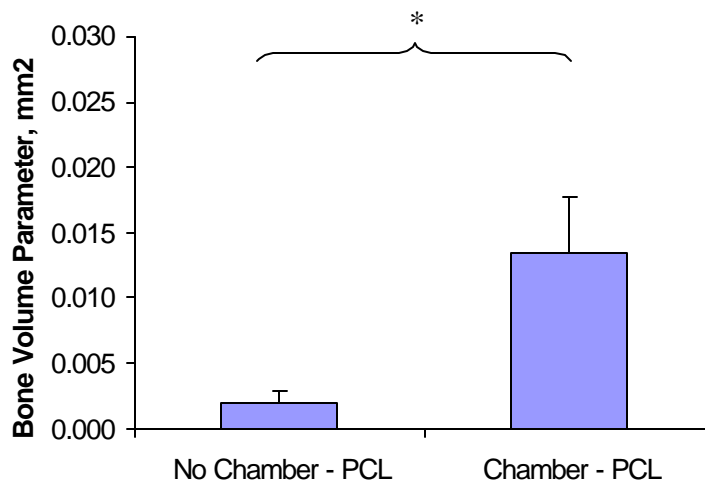


Figure 27. Mean BVP Comparison for PCL Samples Implanted Within a Titanium Chamber of Directly in the Subcutaneous Space

While histological processing was performed for many of these samples, techniques for processing tissue on polymeric scaffolds are highly experimental at this point, and consequently most of the results were unusable. However, the tissue was used to try many different processing, sectioning and staining techniques, providing crucial experience which added in the successful histologic processing of polymeric scaffolds in future experiments. A section of a Ha/TCP scaffold seeded with Passage 4 rat MSCs and implanted subcutaneously for six weeks is shown in Figure 28 to illustrate the osteogenic capacity of this cell source. While the section shown is a BMP-treated scaffold, similar results were seen in untreated controls.

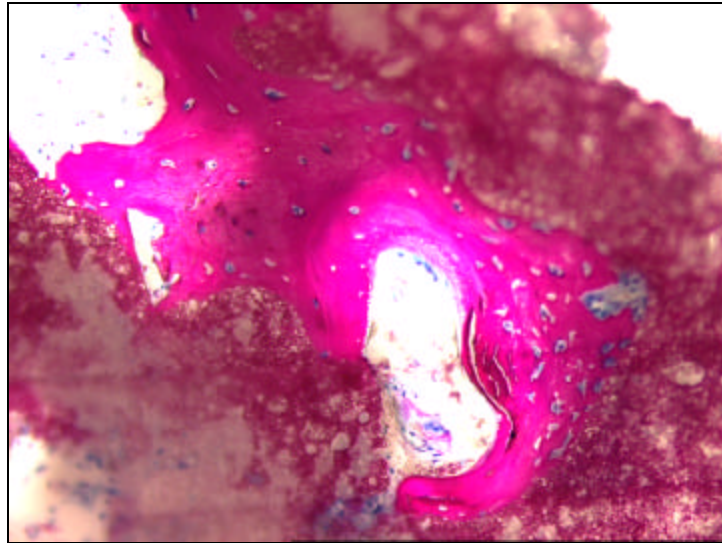


Figure 28. New Bone Formation on BMP2-Pretreated Ha/TCP Seeded with P4 rMSCs and Implanted Subcutaneously in a Titanium Chamber; Plastic Sections with Sanderson's Rapid Bone Stain viewed at 20x

4.2.4 Discussion

With a sample size of 24 pairs of scaffolds implanted subcutaneously in chambers or directly into the subcutaneous space, this work clearly demonstrates that enclosing PLDL seeded with MSCs in a titanium chamber does not impede subcutaneous bone formation in rats (statistical power = 0.95). Such results indicate that the development of a subcutaneous *in vivo* bioreactor applying controlled mechanical loads to tissues developing within a loading device *in vivo* is a feasible option. It also suggests that tissue-engineered constructs could be developed *in vivo* in shapes specified by titanium chambers. Implanted titanium systems may also be used to deliver bioactive factors to constructs developing subcutaneously as well. In light of visual observations of increased vascularity in enclosed chambers and the significant increase in bone formation

on PCL when enclosed in a chamber, a study quantifying the vascularization between enclosed and direct subcutaneous implantation may be worthwhile.

This work also provides direction toward a cell/scaffold combination which might respond favorably to loading in an *in vivo* bioreactor. While scaffolds with any of the experimental conditions tested may respond to mechanical compression, these data prescreened scaffold materials and several treatment options which may improve the ability of bone to form on the scaffold *in vivo*. Few significant differences between treatment conditions were demonstrated but this may simply be a result of a small sample size. Because many different treatments were considered, sample sizes ranged from only two to four samples per group. The absence of a difference in bone formation on scaffolds seeded with MSCs expanded in standard versus osteogenic media was somewhat unexpected since the polymeric scaffold materials themselves are not necessarily osteoinductive. However, since 20 scaffolds were tested using predifferentiated cells and 28 using undifferentiated MSCs, it may suggest that the cell population used was not completely undifferentiated but may have contained some committed osteoprogenitors. Treatment of the polymers with rhBMP2 was employed in the hopes of showing an upper limit of achievable bone formation in a titanium chamber implanted subcutaneously for six weeks. Unexpectedly, no benefit was gained from treating the scaffolds with rhBMP2. Although the BMP was applied to the scaffolds using a previously published technique [166], the subsequent application of rat plasma fibronectin may have competed with the BMP and obscured the ability of the BMP to induce bone formation in surrounding cells. Furthermore, the dosage (2.4 $\mu\text{g}/\text{implant}$ or 3.82 mg per cm^3 of scaffold material) may have been inadequate. While the dosage was

based on research involving a ceramic scaffold material, recent evidence suggests that proper dosing of BMP2 may vary with species and carrier material [186]. While scaffolds seeded with Passage 4 cells performed better than those seeded with Passage 1 or Passage 2 cells, the difference was not significant. However, these data do demonstrate that bone forms more readily on PLDL seeded with rMSCs than PCL.

4.3 System Design

4.3.1 Design Requirements

Several features were considered requirements for the system design. First, a rat model was chosen for the availability of cells, molecular markers, and ease of animal handling. Because of this choice, the system design must be small enough to be comfortably situated subcutaneously. The implant would be designed for subcutaneous implantation on the rat's back since this location would provide a large amount of workable space while minimizing the obstruction to the animal. Furthermore, any transcutaneous access needs to be on the back to minimize the animal's interference with the tubing or port. Furthermore, the design must allow for adequate vascular infiltration to the chamber sample. By definition, the design must incorporate a mechanism to deliver a controlled, compressive mechanical stimulus to the chamber sample, preferably in a manner compatible with our existing external solenoid-driven actuation system. Finally, the design must also provide for a convenient way to nondestructively remove the sample from the device at the time of harvest.

Several other features were considered advantageous but not critical to the design. The design should allow for multiple samples to be loaded simultaneously maximizing

the experimental conditions that can be examined in a given animal. As much as possible, the design should consider the animals comfort and minimize the implant profile. The design of the system should also consider maximizing the flexibility of the system to test a variety of tissue scaffolds and perhaps apply a variety of both mechanical and biologic stimulants of tissue differentiation. Furthermore, when possible, commercial components should be utilized for repeatability, supply, and reduced cost.

A few features of the rabbit HBC system were not considered necessary for the design of this new system, including the ability to repeatedly biopsy the scaffold contents in a non-terminal procedure. Since the design of the system may allow several samples per animal and is not necessarily constrained to two samples per animal, a variety of experimental conditions may be tested in a single animal simultaneously. Therefore, the need for repeated biopsy was not considered great.

4.3.2 Preliminary Ideas

Many options were considered ranging from the basic chamber with a single transcutaneous tubing line similar to the rabbit hydraulic bone chamber to more complex systems involving manifolds to load many chambers and potentially completely implantable loading systems. For the chamber itself, the main design challenges were vascularization, hydraulic access, the ability to easily biopsy the sample, and achieving watertight seals. In addition, the overall profile of the chamber should allow for close contact between the subcutaneous tissue and the vascular ports of the chamber. Several designs with suture holes were considered to pull the subcutaneous tissue close to the implant. For vascular access, several hole patterns in the chamber walls were considered.

Hydraulic access could be achieved either through barbs and tubing similar to the rabbit HBC system or fixed metal ports through the skin similar to those used for electrical lead access in neurological studies. Since the design requirements do not specify non-terminal repeated biopsies, easy sample retrieval can occur after the chamber is removed from the animal by either removable caps on both ends or plunger type designs.

While the decision about hydraulic access to the chamber involves barbs or other metal ports, the challenge of hydraulic access to the animal is a more complicated one. A fully implantable design would be optimal in which no external access is required and the actuating mechanism is implanted alongside the chamber. Such designs might include radio controlled motors or piezoelectric materials or even the use of shape memory alloys. However, the design of such a system would be complex, requiring electrical and controls background beyond the scope of this work. Furthermore, the design would require miniaturization to fit in a rat's back. The components to create this design at this scale are not readily available. One possible design might even include a fluid-filled diaphragm just under the skin that could be physically deformed through the skin, but obtaining feedback from the system to actively control the pressure applied would be problematic. An intermediate concept might include a vascular access port just under the skin that could be repeatedly pierced transcutaneously for hydraulic access. The problem with this design is obtaining a water-tight seal in this diaphragm under the required high pressures.

Due to the complications involved with creating a fully implantable system, it was chosen to create a design that could work easily with the existing external solenoid-

driven system with active pressure feedback control (Figure 34). Therefore during loading sessions, there must be some transcutaneous access to the implanted chamber. However, any transcutaneous access involves increased risk of infection. Since one of our design requirements is a system that allows for loading of several samples per animal, an implanted manifold to connect all chambers to a single transcutaneous port will reduce the risk of infection to the animal. Manifolds could be custom-designed to accommodate as many chambers as the animal can tolerate. A manifold design should also consider the animal's comfort and have a profile that keeps the chambers close to the underlying tissue. To facilitate the removal of air bubbles from the system, the manifold must also include a bleed port.

4.3.3 First Prototype Design

The first prototype design that was manufactured and tested includes a custom manufactured manifold capable of linking four rat subcutaneous loading chambers (SLC) that are connected via commercial connectors (Beswick, Inc.). A 3D rendered schematic of the custom pieces is shown in Figure 29 and the assembled manufactured prototype in Figure 30. Complete machine drawings can be found in Appendix A.3 Rat Subcutaneous Loading Chamber and in Appendix A.4 Prototype Manifold for Rat Subcutaneous Loading Chambers.

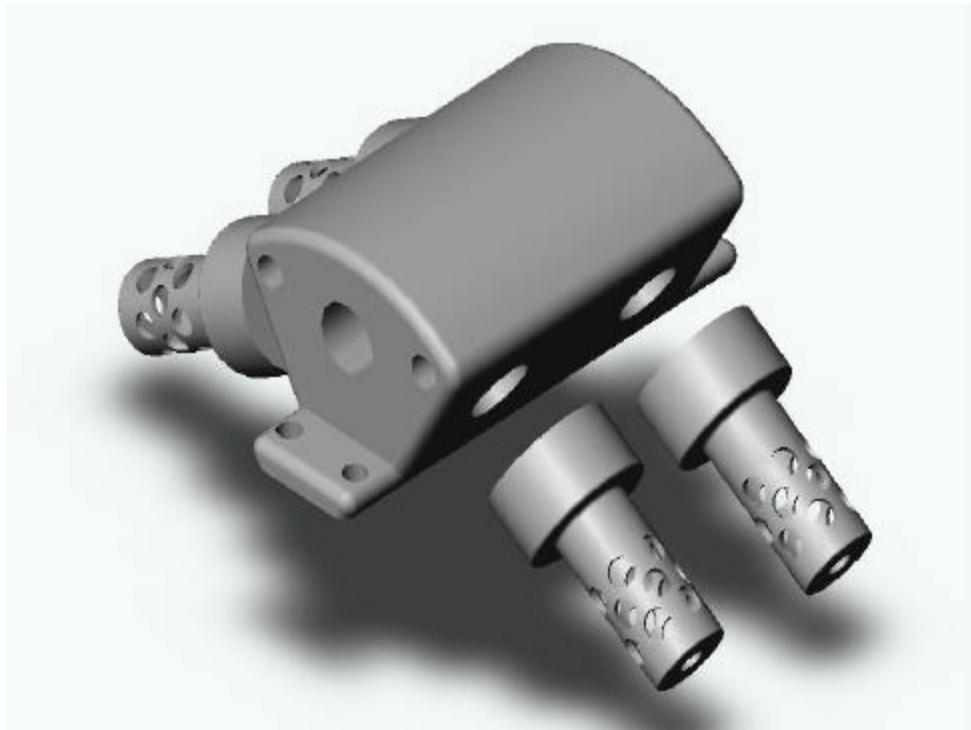


Figure 29. Assembly of Initial Prototype for Manifold and Rat Subcutaneous Loading Chambers

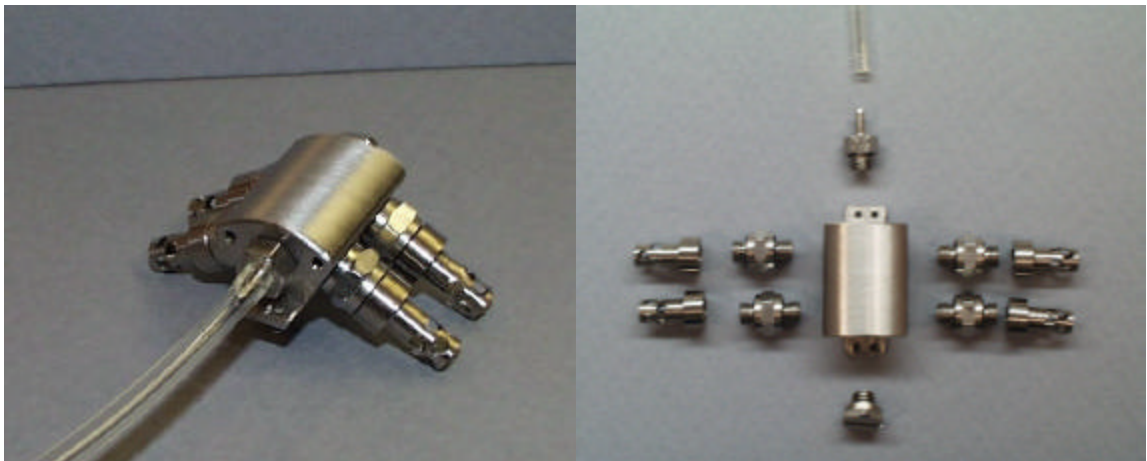


Figure 30. Assembly of Prototype Manifold and Chambers with Necessary Hardware

The rat subcutaneous loading chamber design resembles the nonloaded rabbit HBC with several substantial changes. Overall, the chamber is much smaller having an inner diameter of 4mm. No external threads on the chamber are needed since the chamber is not anchored in bone and instead of a cap the chamber has internal threads to mate with a standard 10-32 male connector. Hole pattern designs were created for vascular access involving 2 or 3 rows of portals. Machining complications ruled out the 3-row design as shown in Figure 29 in favor of a 2-row design with larger diameter holes (Figure 30). The design features a thin platen that sits in the bottom of the chamber. A small diameter hole in the base of the chamber allows for a rod passed through the hole to lift the base platen, acting as a plunger to conveniently lift the sample residing in the chamber out during harvest procedures. This feature was chosen over a removable end cap to minimize the chamber's profile keeping the underlying tissue in close apposition to the chamber's vascularization ports. The chambers are assembled by first inserting the base platen, then the experimental scaffold, and finally a small piston with a .085x.036" Buna-N o-rings (custom order from Apple Rubber, Inc.) as diagrammed in Figure 31.

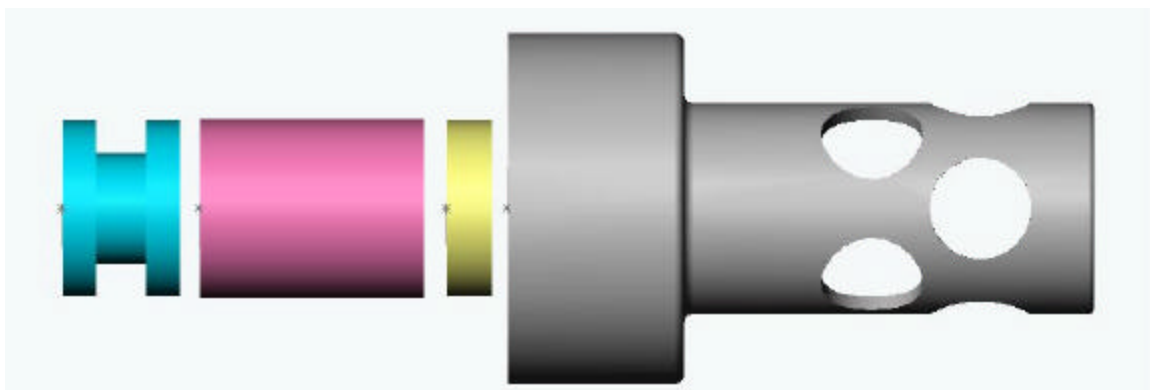


Figure 31. Assembly of Piston, Sample, and Base Platen (Left to Right) into the Rat Subcutaneous Chamber

The custom manifold allows for simultaneous loading of four SLCs. The contoured shape creates smooth edges that are unlikely to cause lesions on the animal's skin. The SLCs mate to the manifold on 60° angled faces on either side. When the manifold is aligned parallel to the vertebra, the chambers and manifold create an arcing shape that resembles the curvature of the rat's back. This allows the chambers to lie closer to the underlying tissue without creating as large empty tissue pockets as would be created if the chambers mated against an orthogonal manifold. The manifold features a small flange on the bottom at the front and back of the manifold with small holes intended to be used for suturing anchor points to attach the manifold to the underlying tissue. The manifold features a central longitudinal hole along the length with two angled holes intersecting from either side. All holes have 10-32 internal threads. Chambers can be mated using 10-32 male nipples and a 10-32 male connector with a hose barb is used on the front face to connect hydraulic loading tubing to the manifold. Finally a 10-32 male cap can be placed on the back face and used as a bleed valve.

The largest perceived disadvantage of the manifold design is its large size and weight. A long slot was added to the base and small through holes along the length of the manifold in the upper corners in an attempt to remove material and reduce the weight of the manifold. This primary disadvantage spurred a second smaller design that could be used in the event the large manifold is too heavy for a rat.

4.3.4 Second Design Prototype

To create a smaller overall implant, a second design was made incorporating a small commercially available manifold (Beswick #MX-1010-303). The manifold is

simply a small metal block with female 10-32 ports on all four sides. Two SLCs as described earlier can be attached on opposite sides of the manifold using 10-32 male threaded nipples. One of the remaining ports serves as a bleed valve and can be capped with a 10-32 plug, while the final remaining port receives an adjustable elbow barb with 10-32 threads to a 1/16" hose barb (Beswick # SMLS-1012-303) to connect the hydraulic loading tubing to the manifold (Figure 32). The miniature elbow barb keeps the overall size of the design small and allows the tubing to approach the chamber parallel to the implant. This feature is very important since the overall design is somewhat long and linear, requiring the implant to lie parallel but offset to the rat's vertebra. The tubing must exit between the rat's shoulder blades to minimize the chances of the animal interfering with the tubing. In nonloaded controls, the elbow barb may simply be replaced by another 10-32 plug as shown in Figure 32. Complete instructions for assembling this implant can be found in Appendix B.4.2 Assembly Instructions for Subcutaneous Rat Loading Device.

The advantages of this design include its small size and weight as well as the use of a commercially available manifold, avoiding the expense and delay associated with a custom-machined manifold. Unfortunately, this design is strictly limited to two chambers per manifold, restricting the number of experimental treatment conditions that can be investigated in a given animal. The length and linearity of the design may also affect the animal's comfort.

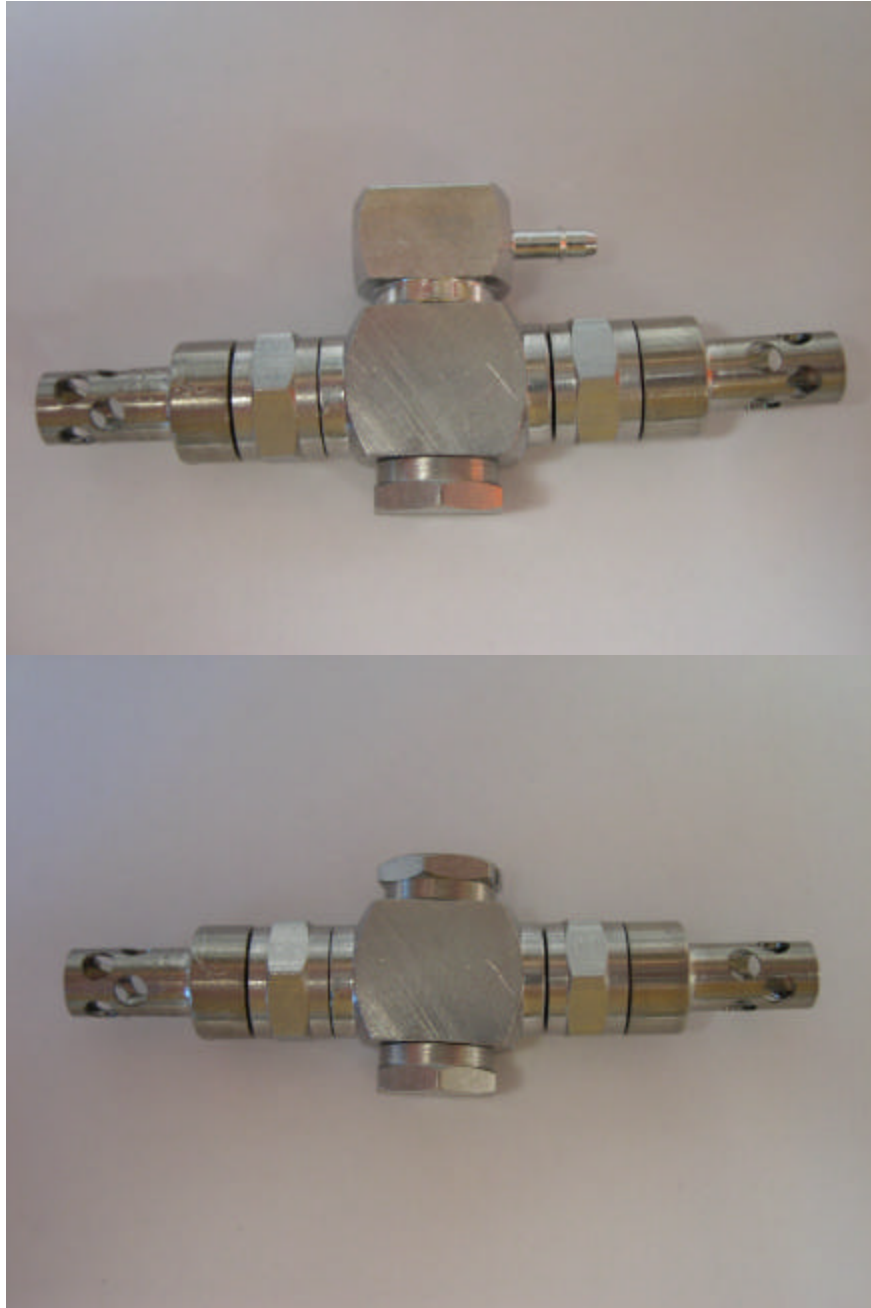


Figure 32. Assembly of Standard Manifold with Subcutaneous Rat Chambers for Loading Experiments; Top (Loaded), Bottom (Nonloaded)

4.4 Tubing & Loading Pilot Experiments

Several small pilot experiments were performed to decide procedural details about conducting loading experiments subcutaneously in rats. Although, rats are considered relatively infection resistant, given our previous experience with infection along indwelling transcutaneous tubing in rabbits, the risk of infection was ascertained in several small pilot experiments meant to find a suitable tubing diameter and the appropriate surgical techniques and post-operative care to minimize infection and animal discomfort. Since this work was performed in parallel with the design of the rat subcutaneous chamber and manifold system, the initial work was performed using the larger rabbit hydraulic bone chambers simply implanted subcutaneously with attached transcutaneous tubing for six weeks.

The work investigated both 1/16" and 1/32" ID tubing with the hopes that smaller tubing may reduce the incidence of infection; however, no difference was seen in the occurrence of infection. Although smaller tubing seemed more comfortable for the animal, hardware for 1/32" ID tubing is difficult to obtain and proved less effective at creating a watertight seal. Anchoring the tubing to the underlying tissue by suturing a polyester cuff attached to the tubing with medical grade silicone glue was also attempted similar to the procedure described in Appendix B.3 Procedure to Implant Subcutaneous Loading Tubing in Rabbits (see Figure 82). This approach reduced the incidence of infection in the rabbit hydraulic bone chamber model, but was not found useful in the rat model. Often infection was found between the tubing and the polyester cuff itself. The use of silver-impregnated glass powder to treat the exit wound was also employed and

provided some improvement in the rat of infection along the tubing, but did not prove as beneficial in rats as it did in the rabbit hydraulic bone chamber model. Given the high rate of infection due to the open transcutaneous tubing, it was decided to minimize the amount of time the exit wound would remain open. Pilot experiments were performed in which the transcutaneous tubing was clipped at the skin level and the exit wound closed after seven to ten days. This action greatly improved the rate of infection. Although it would have been more desirable to avoid the use of a pharmacologic agent, the use of prophylactic antibiotics was also employed. A course of antibiotics (Cefazolin) corresponding to the length of time the tubing remained transcutaneous proved to be as effective as a course of antibiotics that lasted the entire six week period. Additionally, this work demonstrated the need for the rat to wear an Elizabethan collar when the tubing is exposed to prevent the animal from chewing through the tubing.

Two more pilot experiments were performed once the rat subcutaneous loading chambers and manifolds were designed and manufactured. These experiments employed loading of PLDL enclosed in the rat SLC. The purpose of these experiments was to 1) ensure the animal could physically tolerate the manifold/chamber assembly, 2) test the implanted hardware connections for leakage, 3) troubleshoot the overhauled external hydraulic loading system (Figure 34), 4) choose between manifold designs, and 5) choose between polyurethane and PTFE for the implanted loading tubing. The first experiment pointed out several mechanical hardware revisions that had to be made to the external loading system. The choice between manifold designs was made very clear. Although the larger custom manifold had previously been successfully implanted and tolerated by a test rat, it was clear that the addition of loading tubing and SLCs made the implant much

too uncomfortable for the animal. Each of the four animals receiving the large custom manifold exhibited signs of pain and anorexia and had to be euthanized within a few days. Furthermore, surgical implantation of the larger custom manifold is more difficult. The overall design allows several empty tissue pockets that must be sutured close to both reduce infection and keep the tissue close to the SLC. The small commercial manifold was tolerated better by the rats, but the animals still appeared uncomfortable, probably because of the external tubing and the need for the animals to wear Elizabethan collars. Simply wearing the collar is stressful for the rats and prevents grooming. These animals exhibit red secretions around the eyes and nose, a typical reaction to stress in rats. The stiff transcutaneous tubing may also cause the animal some pain as it ambulates.

Following our veterinarian's suggestion, a second loading experiment featured a loading protocol in which the implanted tubing remains beneath the skin at all times, except for a short period of time surrounding each loading session. A minor surgical technique was performed in each animal immediately before the loading session to expose the tubing. Immediately after the 30-minute loading session, the tubing was placed beneath the skin and the incision closed with wound clips. A more detailed description of the procedure can be found in Appendix B.5 Procedure for Exposing Implanted Tubing for Loading Sessions in Rats. Although this procedure greatly complicates loading sessions, it reduces the risk of infection along the indwelling tubing and improves the animal's comfort by removing the exposed tubing and accompanying Elizabethan collar, both improving the animal's chances of survival. In addition, this final loading experiment demonstrated that polyurethane, which is more flexible than PTFE, could withstand pressures of 200 psi in our loading system without bursting or

leaking. A leak occurred in one animal with PTFE tubing because the barb loosened from the manifold suggesting that PTFE tubing maybe too stiff to allow bending and motion of the tubing during the loading procedure. Polyurethane tubing was chosen for successive loading experiments.

4.5 Discussion

The first objective of examining the effect of enclosing a cell-seeded scaffold in a titanium chamber on bone formation on the scaffold was successfully completed. This work conclusively demonstrated that enclosure of a scaffold within a titanium chamber does not impede the formation of bone. This was an important prerequisite for the design of a subcutaneous bioreactor employing mechanical stimulation of constructs. Interestingly, bone formation on polycaprolactone scaffolds significantly increased when scaffolds were implanted within a titanium chamber rather than directly in the subcutaneous space. The reason for this is unclear, but studies investigating vascular ingrowth in the chambers may be worthwhile given gross visual observations of enhanced vascularity in loaded samples.

The second stated objective of designing a mechanical loading system for the *in vivo* preconditioning of tissue-engineered scaffolds was also completed. The final design joins a pair of custom-made scaffold chambers with a commercially available miniature manifold. Hydraulic tubing connected to the manifold via an angled adjustable barb can be connected to an external loading system with active pressure feedback control. Attractive features include its relatively small size, the ability to load more than one scaffold at a time, and its use of readily available commercial parts.

Finally, the functionality of the subcutaneous mechanical loading system was verified in pilot experiments. These experiments demonstrated the tremendous infection risk associated with the use of indwelling transcutaneous tubing, despite monumental effects to reduce the potential for infection. Because this threat could significantly jeopardize studies employing the subcutaneous mechanical loading system, a protocol was developed in which the hydraulic loading tubing removes subcutaneous except during a brief period surrounding each loading session, rather than continuous transcutaneous exposure of the tubing. Using this protocol, the novel *in vivo* bioreactor implant designed represents a robust system to mechanically precondition an array of constructs for various tissue engineering applications.

CHAPTER 5

CYCLIC MECHANICAL COMPRESSION ENHANCES THE DEVELOPMENT OF ORTHOPAEDIC TISSUE CONSTRUCTS IN A SUBCUTANEOUS *IN VIVO* BIOREACTOR

5.1 Introduction

5.1.1 Summary

In an effort to produce tissue-engineered constructs capable of meeting the functional demand of bone defect sites, a novel *in vivo* bioreactor capable of imparting a cyclic mechanical stimulus to developing constructs has been designed to capitalize on both the vascular *in vivo* environment and the responsiveness of osteoprogenitors to their local mechanical environment. To determine the ability of this novel system to enhance bone construct development, a study was performed to investigate bone formation on polymeric constructs seeded with mesenchymal stem cells. Given that a successful tissue engineering strategy may need to employ several scaffold preparation techniques and that mechanoresponsiveness may depend on the level of cell and tissue maturity, the effect of *in vitro* preculture of the cell-seeded constructs prior to *in vivo* implantation in the loaded subcutaneous chamber system on load-induced changes in bone formation was also investigated. Scaffold preparations included a no preculture group to represent the simplest approach of seeding cells on a scaffold and directly implanting the scaffold, a 1-week preculture group to represent minimal *in vitro* preparation but which may commit the cells to an osteoblastic phenotype, and an 8-week preculture group with pre-existing

mineralized nodules. While the data suggests a significant effect of preculture time on matrix mineralization, an experimental complication with cell-seeding prevents any conclusion concerning preculture time. Overall the data show that cyclic *in vivo* mechanical loading results in a significant increase in matrix mineralization. Furthermore, the data suggest that cyclic *in vivo* mechanical loading may be necessary to prevent resorption of mineral deposited during *in vitro* preculture.

5.1.2 Specific Aims and Hypotheses

Specific Aim #1: To quantify the effect of controlled in vivo mechanical compression on new bone formation within tissue-engineered constructs for bone defect repair prepared in a subcutaneous in vivo bioreactor.

Subcutaneous loading chambers (SLCs) containing polymeric scaffolds seeded with rat mesenchymal stem cells were implanted in the subcutaneous space on the back of male Fisher rats. Cyclic mechanical compression was applied to the developing constructs three times per week for two weeks and samples were harvested at the end of six weeks. New bone formation was quantified using micro-computed tomography imaging. It is hypothesized that cyclic mechanical compression will increase new bone formation within cell-seeded polymeric constructed developed subcutaneously.

Specific Aim #2: To quantify the effect of length of in vitro preculture on load-induced changes in new bone formation within tissue-engineered scaffolds prepared in a subcutaneous in vivo bioreactor.

Polymeric scaffolds were seeded with rat mesenchymal stem cells and then cultured in media containing osteogenic supplements for one week or eight weeks. These scaffolds, along with no preculture and cell-free controls, were implanted into subcutaneous loading chambers in the backs of male Fisher rats. A portion of these scaffolds also received mechanical loading treatments for three times a day for two weeks. Samples were harvested after six weeks *in vivo*. New bone formation was quantified using micro-computed tomography imaging. Given the presence of pre-existing mineral may act as nucleation sites for further mineralization, it is hypothesized that load-induced changes in bone formation will be amplified with longer preculture preparation of cell-seeded constructs.

Specific Aim #3: To predict tissue-level strains and stresses resulting from cyclic compressive loading of polymeric constructs developed in the subcutaneous loading chamber system.

Micro-computed tomography images of representative polymer scaffolds were used to create a digital image based finite element mesh for the basis of finite element models representing the applied *in vivo* loading conditions. Predicted tissue stresses and strains were generated.

5.2 Methods and Materials

5.2.1 Scaffold Choice and Manufacture

The decision of which scaffold material to use for the study was a critical one. While the ideal matrix would necessarily be osteoconductive, it should also promote cell adhesion, mitosis, and differentiation while providing some initial mechanical stability. A critical requirement for this study is sufficient mechanical integrity to resist a moderate cyclic mechanical stimulus without permanent deformation or brittle failure. Previous work performed in the hydraulic bone chamber model suggests that apparent deformations in the range of 2-5% should result in differences in new bone formation [100, 102] and thus represent the target apparent deformation for this study. Even though there may be other explanations, apparent deformations of 0.8% did not result in differences in new bone formation on frozen allografts in the rabbit hydraulic bone chamber model (see Section 2.3.4). It is imperative that greater deformations are applied to the scaffold in this work.

PLDL was chosen to be the scaffold material for the tissue-engineered bone constructs for several reasons. It has adequate elasticity to recover from repeated compressive loads sufficient to have the material deform within a 2-5% range. Furthermore, the stiffness of PLDL when manufactured with 30% porogen ($E = 43.50$ MPa) [183] is neither too stiff nor too compliant such that the loading system can perform in its designated pressure range and still deform the tissue 2-5%. Furthermore, PLDL samples offer more architectural consistency than natural scaffold materials such as bone or coral products. It has no native osteoinductive capacity like demineralized

bone that could obscure differences in treatment groups. PLDL performed well in the previous pilot experiments without eliciting a significant foreign body reaction.

Other materials were considered and deemed less desirable, including demineralized bone matrix, polycaprolactone (PCL), and CollaGraft. Although demineralized bone represents an attractive bone scaffold material clinically because of its osteoinductive properties, that same property could obscure bone formation caused by the addition of cells, *in vitro* pre-treatment of those cells, and/or loading. Furthermore, finite element analysis of the tissue level stresses and strains experienced during loading treatments requires that the scaffold be imaged using microCT. It would be impossible to adequately image the bone matrix after demineralization. The consistent and repeatable architecture of PCL created by a fused deposition modeling technique was very attractive and therefore examined during the pilot work described in Chapter 4. However, significantly more bone formed on PLDL than PCL in those experiments. PLDL was also more readily available since it could be manufactured in our laboratory. CollaGraft was excluded from consideration because of the high structural variability in natural materials and because the architecture could not be imaged using microCT.

PLDL samples were manufactured as published previously [183]. Briefly, PLDL was combined with 30% azodicarbonamide solvated in acetone and then repeatedly coated on 316 stainless steel wires. Wires were bundled in heat shrink tubing (100 wires per bundle) and heated 20 minutes at 60C to fuse them together before the bundles were heated to 260C in peanut oil to decompose the porogen. The wires were then removed and the bundles rinsed in hexane. Bundles were cut to 5 mm lengths and then punched

with a 4 mm skin biopsy punch to ensure a consistent diameter. Finally, samples were rinsed in ethanol and allowed to dry.

5.2.2 Mechanical Testing of PLDL

Mechanical tests were performed on a set of PLDL samples (4 mm diameter by 5 mm length) to determine if the compressive modulus changes after sterilization by gamma irradiation and after extended exposure to an aqueous environment. These two processes may affect the mechanical properties due to cross-linking of the polymer during gamma irradiation or degradation of polymer chains with exposure to a saline environment. Lin et al [183] reports the compressive modulus for PLDL manufactured with 30% azodicarbonamide to be 43.50 MPa, but these samples had not been exposed to gamma irradiation or extended exposure to an aqueous environment, even though the tests were performed in a saline bath. Three treatment groups were considered including no gamma/no soak, gamma/no soak, and gamma/soak with 6 scaffolds per group. Samples in the gamma groups were exposed to 2.5 Mrad gamma irradiation and those samples that were soaked were exposed to Ca-free, Mg-free Dulbecco's PBS (Invitrogen #14190136) at 37 C for 46-48 days. The samples were mechanically tested in a confined compression scenario simulating the rat subcutaneous chamber environment. A 4 mm internal diameter titanium rat chamber was threaded through a table-top platform which was immersed in room temperature PBS. Samples were placed in the chamber with a 1 mm thick smooth platen placed on top of the scaffold to distribute the applied load. A MTS TestarIIIm 858 Mini Bionix II hydraulic test frame (Figure 4d) with a 100lb load cell operating in the 100 N range and LVDT with a working range of 10 mm was used to

test these specimens to failure in displacement control. A -1 N preload was applied and then ramped linearly to -0.1% displacement at 1 mm/min. The sample was preconditioned by loading sinusoidally from 0.1% to 1.0% displacement ten times at 0.5 Hz before ramping to 15% displacement at 1 mm/min resulting in failure.

Stress-strain data was calculated from recorded load and displacement measurements. Figure 33 shows representative stress-strain curves for each of the three treatment groups tested. The compressive modulus was determined by the slope of the linear elastic region of the stress-strain curve. The yield point was defined by a standard 0.2% offset method. One sample in the group exposed to gamma irradiation seemed to be an outlier. This was the only sample tested that was also microCTed prior to mechanical testing. This sample was excluded from statistical analysis. The average and standard deviation of the yield strain, yield stress, and compressive modulus are reported in Table 6 for all three treatment groups.

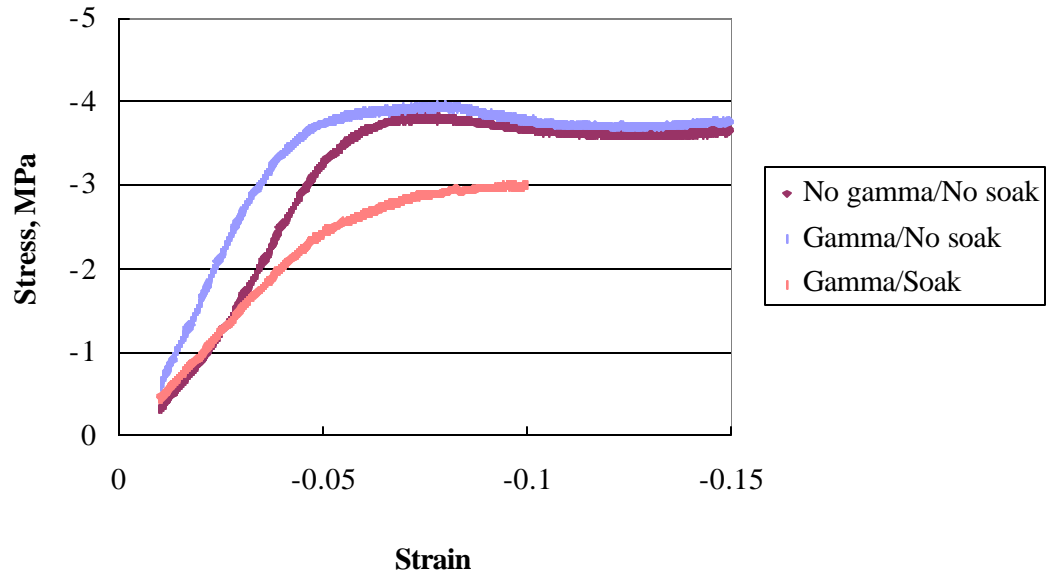


Figure 33. Representative Stress-Strain Curves for Failure Tests of PLDL Made with 30% Porogen

Table 6. Failure Test Results for PLDL with 30% Porogen

Treatment	Yield Strain		Yield Stress, Mpa		Compressive Modulus, Mpa	
	Average	Std. Dev	Average	Std. Dev	Average	Std. Dev
NO GAMMA/NO SOAK	-0.068	0.018	-3.81	0.87	80.0	22.2
GAMMA/NO SOAK	-0.054	0.013	-3.84	0.47	96.8	17.9
GAMMA/SOAK	-0.063	0.017	-3.07	0.53	61.7	17.4

Analyses of variance were performed with $\alpha = 0.05$ for all three of these parameters using all data points except the one outlier described above. These analyses show that neither gamma irradiation nor extended exposure to an aqueous environment affect the yield strain. Gamma irradiation did not affect the yield stress, but a one-way analysis of variance (ANOVA) shows that extended exposure to an aqueous environment did significantly ($p = 0.034$) reduce the yield stress of PLDL. Compressive modulus showed a similar trend in that gamma irradiation had no effect, but exposure to saline significantly ($p = 0.022$) reduces the compressive modulus.

Cyclic tests were also performed to ensure that samples prepared in an identical manner to those to be implanted in the *in vivo* study could tolerate repeated loading similar to that planned for the *in vivo* rat loading experiment. Eight PLDL samples were prepared using 30% porogen, then exposed to 2.5 Mrad gamma irradiation, and then soaked in PBS at 37C for 48-50 days. Samples were cyclically tested in confined compression using the same hardware described for the failure tests. The force signal on the test frame was first tuned to a sine wave ($P = 88, I = 8.5, D = 0$). A preload of -0.5 N was applied and the force then ramped to -1.42 N. Under force control, the applied force was then cycled from -1.42 N to -14.2 N at 1 Hz for 3 hours (10800 cycles). This load was chosen because early calibration data of the hydraulic loading system suggested the maximum load that could be applied by the system to a scaffold in the 4 mm rat chamber was 14.2 N. This loading regimen did not cause any of the eight samples to show signs of failure.

5.2.3 MicroCT Imaging & Analysis of Representative PLDL Samples

In order to characterize the architecture of the scaffold material for the *in vivo* loading experiment, 12 naïve PLDL samples manufactured at the same time as those used for the *in vivo* experiment were imaged using Scanco's MicroCT 20 as described in Section 3.2.7 at a resolution of 30 microns with the scanner set to a voltage of 50 kVp and a current of 160 μ A using an integration time of 150 ms. A volume of interest was selected to tightly encompass each sample. MicroCT images were first filtered using a constrained 3-D Gaussian filter (sigma = 0.8, support = 1) to partially suppress noise in the volumetric image data prior to segmentation to reveal the polymer from the surrounding background using a global thresholding procedure. A threshold of 28 was selected and used to evaluate all twelve PLDL specimens. The thresholded 3D volumes were evaluated for histomorphometric parameters using direct distance transformation methods which, unlike many previous methods used to analyze trabecular bone, does not assume a specific plate or rod-like architecture [187, 188]. Table 7 outlines these parameters and their average values for the PLDL used in this study. Three of the twelve samples imaged were subsequently soaked in PBS at 37 C for 8 weeks, scanned again, and histomorphometric parameters evaluated to determine if extended exposure to a saline environment changes the architecture of PLDL. No differences in properties with soaking were apparent but the number of samples considered was very small.

Table 7. Microarchitectural Parameters for PLDL Produced for *In vivo* Loading Experiment; Average \pm Standard Error

Volume Fraction (%)	29.7+1.0
Strut Density (mm^{-1})	2.68+0.09
Strut Thickness (μm)	134.8+3.3
Strut Spacing (μm)	397.8+16.0
Degree of Anisotropy	1.57+0.04

5.2.4 Scaffold Seeding and Preculture

Samples were sterilized with a 2.5 Mrad dose of gamma irradiation. Five to six scaffolds were placed within the barrel of a 1 ml syringe with a 3-way stopcock on the tip and then covered with a 25 $\mu\text{g}/\text{ml}$ solution of rat plasma fibronectin (Sigma #F0635). A vacuum was drawn on the syringe by extending the syringe plunger with the stopcock closed 5-6 times to help the fibronectin penetrate the PLDL pores. Scaffolds were incubated in the fibronectin solution overnight at 4C, then rinsed three times with Ca-free, Mg-free PBS in 24-well plates. Scaffolds remained hydrated in Ca-free, Mg-free PBS at 37C until seeded with cells.

Scaffolds were seeded at three different times depending on the length of preculture time assigned to each treatment group. Seedings were timed such that all scaffolds would be ready for *in vivo* implantation on the same day to allow for a balanced design of treatment assignments among the rats. Because mechanical testing of PLDL showed a reduction in compressive modulus with exposure to saline, it was imperative that all scaffolds were exposed to an aqueous environment for an equal time prior to implantation. All scaffolds were coated in fibronectin at the same time but had varying

periods of time in PBS afterward before seeding with cells such that the total time in PBS and pre-culture equaled eight weeks for all scaffolds. This means that the 8-week preculture group spent eight weeks in culture prior to implantation while the 1-week preculture group spent seven weeks in PBS and 1 week in culture, and finally the no preculture group spent eight weeks in PBS prior to seeding with cells and *in vivo* implantation. Consequently, Seeding #1 for the 8-week preculture group occurred 24 hours after the scaffolds were coated with fibronectin. Seeding #2 for the 1-week preculture group occurred seven weeks later and Seeding #3 for the no preculture group occurred one week after Seeding #2. Cell-free PLDL samples remained in PBS for the entire eight weeks after fibronectin coating prior to implantation. Scaffolds from all groups were implanted within 48 hours of Seeding #3.

Rat mesenchymal stem cells were obtained from Osiris Therapeutics and were isolated from the pooled marrow of seventeen Fisher rats and then frozen after the initial confluence. Cells were expanded in alpha-MEM (Invitrogen #32561-037) with 10% FBS (Valley Biomedical lot # L7938) and 1% antibiotic/antimycotic (Invitrogen #15240-062). Passaging was performed every fourth day with 0.05% trypsin, 0.53 mM EDTA-4Na (Invitrogen #15400-054) and replated at 10,000 cells/cm² for a total of four passages. Cells were passaged in this way separately for each preculture group starting from the same frozen lot of P0 rMSCs from Osiris.

Scaffolds were seeded with a 20e6/ml suspension of freshly expanded P4 rMSCs in serum-free media using the vacuum syringe technique described above. A 100 μ l volume of the cell suspension was added to the syringe through the stopcock. Scaffolds

were incubated at 37C for two hours before 1.5 ml serum-free media was added to nourish the cells. Scaffolds were kept in a 37C incubator overnight. After Seeding #1 and #2, scaffolds were moved to 12-well non-tissue culture treated plates and cultured in 5ml of the standard media described above supplemented with 10 nM dexamethasone, 50 μ M ascorbic acid-2-phosphate, and 3 mM Na- β -glycerophosphate. Media was changed twice weekly until the specified preculture time ended and samples were implanted *in vivo*. Scaffolds in the no-preculture group were implanted within 48 hours of cell-seeding.

Three extra scaffolds at each seeding were prepared for analysis of cell viability using a Live/Dead fluorescent staining kit (Molecular Probes L-3224) employing calcein and an ethidium homodimer. After overnight incubation, samples were rinsed three times in PBS, stained with a solution containing 4 μ M concentrations of calcein and ethidium homodimer each, rinsed in PBS three more times, and imaged using confocal microscopy. Confocal images were taken at multiple depths and stacked to create a three dimensional representation of the scaffold using a Zeiss LSM 510 Confocal Microscope (Carl Zeiss, Inc.). Three additional samples were analyzed for double stranded DNA content using PicoGreen dsDNA Quantitation Kit (Molecular Probes P-11496) from each preculture group. See Appendix E for a detailed protocol to analyze DNA content from cells seeded on a three-dimensional scaffold.

5.2.5 Parallel *In vitro* Assays

Eighteen extra PLDL samples seeded with P4 rMSCs at Seeding #1 and Seeding #3 were cultured *in vitro* in 5 ml of the standard media described above supplemented

with 10 nM dexamethasone, 50 μ M ascorbic acid-2-phosphate, and 3 mM Na- β -glycerophosphate. Media was changed twice weekly. In addition, six cell-free PLDL scaffolds were cultured alongside those from Seeding #1 in supplemented media. Samples from each seeding group were harvested after 1, 7, 8, and 14 weeks for microCT imaging and quantification of mineralized volume. Samples were harvested at weeks 1 and 8 to determine an average amount of mineralization at the time of *in vivo* implantation for samples in the 1-week and 8-week preculture groups. Samples were harvested at weeks 7 and 14 to determine the equivalent amount of mineral that could have been obtained by the 1-week and 8-week preculture samples if they had been cultured *in vitro* the entire time rather than implanted *in vivo* for six weeks. Additionally, samples from each seeding group were also harvested at weeks 1 and 8 for RNA extraction. The intent was to look for gene expression of osteonectin and bone sialoprotein, but the samples were never processed. For each assay, three samples were taken both seeding groups. It was felt that there was greater statistical power in having a small n, but repeating the experiment at two different seeding times rather than taking a large n for each assay all from the same seeding group.

5.2.6 Surgical Procedure

All animal procedures involving subcutaneous implants in rats with applied *in vivo* loading were approved by Georgia Tech's Institutional Animal Care and Use Committee in Protocol #A02023. Animals received antibiotic (Cefazolin) treatment for the first three weeks of the experiment and pain medication (Buprenex) for 48 hours after any new incision.

One rat subcutaneous loading device was implanted under the skin on the backs of 35 male Fisher rats (175-250g) using a blunt dissection technique described in Appendix B.4 Procedure for Implantation of Subcutaneous Rat Loading Device. Each device consists of two chambers, each containing one prepared tissue-engineered construct. A two-inch piece of polyurethane tubing (Cole-Parmer #95625-00) was attached to the implant and remained under the skin except during periods of loading when the tubing was exposed and attached to the external loading system to apply a controlled compressive stimulus to the constructs inside the two chambers of the loading device. Twenty of the rats received loading treatments and fifteen did not.

A total of 70 constructs were implanted. The sample size per treatment group is listed in Table 8. A nominal sample size of eight was chosen. A larger sample size was assigned to loaded treatment groups because of the greater risk of losing these animals to infection or complications arising from anesthesia during the course of the experiment. A smaller sample size was employed for the cell-free groups since little variability is anticipated in these samples. Treatment assignments balanced the number of samples within a given treatment that were placed in either the top or the bottom chamber of the implant. Time restraints prevented all scaffolds from being implanted the day after Seeding #3. Two samples from each treatment were implanted in the final eight rats on the second day after Seeding #3. Furthermore, two samples from each of the loaded 1-week and 8-week preculture groups were not originally planned into the study but were added to help compensate for the loss of four animals due to complications with anesthesia during the first few days of loading. Therefore, these four samples were implanted into two rats a week later.

Table 8. Treatment Groups and Number of Each Implanted

Preculture	Loading	Sample Size
No Preculture	No	8
No Preculture	Yes	10
1 Week Preculture	No	8
1 Week Preculture	Yes	12
8 Week Preculture	No	8
8 Week Preculture	Yes	12
Cell-Free	No	6
Cell-Free	Yes	6

5.2.7 Loading Regimen

Constructs in the rat subcutaneous loading device were compressed by connecting the polyurethane tubing attached to the loading device to an external solenoid-driven loading system with active pressure feedback. The external system shown in Figure 34 is the same system used in the loading study of frozen trabecular allografts in rabbits described in Chapter 2 (see Figure 2), except the system was remanufactured with a more powerful solenoid increasing the maximum pressure capability of the system to 200-250 psi. Consequently, many of the connectors and the manifold on the system also had to be replaced to accommodate the higher pressures. The new stainless steel manifold is shown in Figure 35 and was angled as such to aid in the removal of bubbles from the system. Although not useful for this study, the system remodel also allowed the system to operate at frequencies as high as 30 Hz.

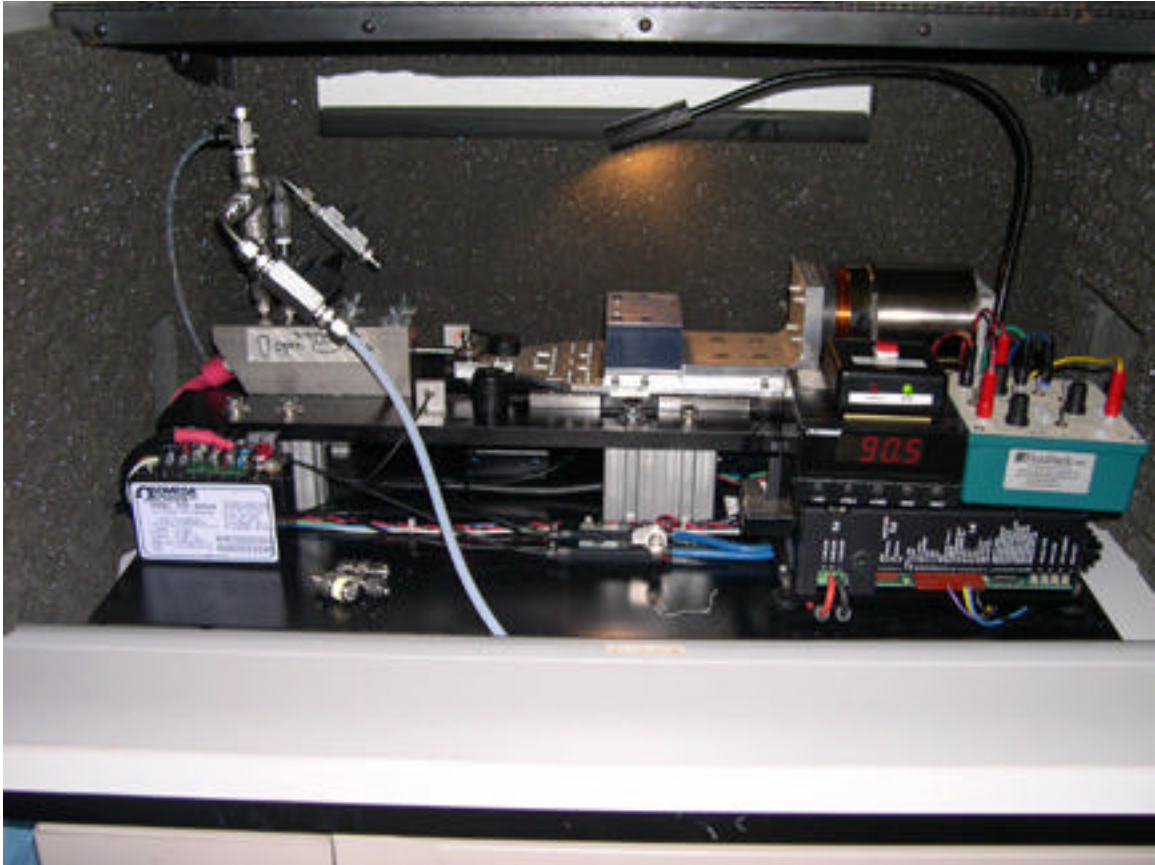


Figure 34. Solenoid-driven Loading System used to Compressively Load Constructs in Rat Subcutaneous Chambers



Figure 35. Stainless Steel Manifold on External Loading System

Calibration of the system pressure to the applied load in a mock chamber set-up (Figure 36) was performed to determine the extent of frictional losses occurring in the chamber due to the friction of the piston o-ring. A pressure of 200 psi on the external system correlates to 0.64 V on the load cell attached to the mock chamber setup. A separate calibration of the load cell with known weights indicated a force/voltage relationship of 4.61 V for the load cell. Therefore, when the system operates at 200 psi, the tissue in the chamber (4 mm diameter) experiences 13.3 N force and an average apparent stress of 1.05 MPa.



Figure 36. Mock Chamber Setup for Calibration of the External Solenoid-Driven Loading System

Loading sessions began 3-4 days after implantation of the constructs. Just prior to the initial loading treatment, anesthesia was induced in the rat and a small incision made over the free end of the tubing on the rat's back. The tubing was exposed, a luer connector added, and the device was connected via the tubing to the external solenoid-driven loading system. Once the animal was sternally recumbent, it was placed in a thin plastic restraining cone and loading performed. After the loading session was complete, anesthesia was again induced in each rat while the loading tubing was placed back under the skin and the incision closed with wound clips. During subsequent loading sessions, these wound clips were simply removed from the anesthetized animal and the tubing pulled back out without further incision since the wound margins do not have sufficient time to heal between loading sessions. A more detailed protocol may be found in Appendix B.5 Procedure for Exposing Implanted Tubing for Loading Sessions in Rats.

Each device was loaded three times per week for 2 weeks. This brief loading window was selected to minimize the risk of infection and trauma for the animal. Other studies have shown that even a single load application can result in changes in gene expression of bone-related transcription factors and cell-signalling pathways [75, 101]. Since a target of 2% strain was selected, each loading session applied a cyclic sinusoidal pressure ranging from 1.33 N to 13.3 N at 1 Hz for 30 minutes similar to previous experimental work [100][81][79][75] and the allograft study described in Chapter 3. In order to apply this load range to the constructs within the chambers, the external loading system was required to operate at 20-200 psi.

5.2.8 Harvest

Six weeks after the *in vivo* implantation of the subcutaneous hardware and tissue-engineered bone constructs, the rats were euthanized by carbon dioxide overdose. The entire device was carefully dissected from the subcutaneous space and the chambers unscrewed from the manifold. Constructs were retrieved from the chambers by pushing the base platen up with a thin rod inserted in the hole on the base of the chamber, lifting the scaffold out of the chamber. Each construct was immediately placed in 10% neutral buffered formalin for 48 hours to fix the tissue. Constructs were rinsed for 15 minutes in running deionized water, then transferred to 70% reagent alcohol for storage at 4 C.

5.2.9 MicroCT Imaging & Analysis

All constructs from the *in vivo* study, both loaded and nonloaded, were imaged using micro-computed tomography as well as samples from the parallel *in vitro* study harvested at 1, 6, 7, or 14 weeks. Three samples at a time were stacked inside the barrel

of a 1 ml syringe with Teflon spacers separating the samples. Samples were immersed in 70% alcohol. The syringe assembly was wrapped in foam and secured inside a 16.4 mm scanning tube. Scaffolds were imaged using a desktop microCT scanner (μ CT 40, Scanco Medical, Bassersdorf, Switzerland) in a process similar to that described in Section 4.2.2. These samples were scanned at a resolution of 16 microns with the scanner operating at a voltage of 45 kVp, a current of 177 μ A, and an integration time of 150 ms. A volume of interest was selected to tightly encompass each sample. MicroCT images were filtered using a constrained 3-D Gaussian filter ($\sigma = 1.0$, support = 1) to partially suppress noise in the volumetric image data prior to segmentation to reveal the mineralized tissue from the surrounding soft tissue using a global thresholding procedure. A threshold of 59 was selected for all samples in this experiment. This value represents the average of 16 different visual observations of the appropriate 2D threshold across all the *in vivo* and *in vitro* treatment groups demonstrating substantial bone formation. New bone volume (BV) was determined by the number of voxels attenuating x-rays above this defined threshold level (Obj#) multiplied by the volume of each voxel ($4.41 \times 10^{-6} \text{ mm}^3$). To better represent the amount of available pore space in the PLDL that was actually filled with bone (% pore fill, %PF), the new bone volume was normalized by the PLDL pore volume as expressed by Equation 2.

Equation 2

$$\%PF = \left(\frac{BV}{PLDL \text{ pore volume}} \right) \times 100 = \left(\frac{BV}{Sample \ Volume * PLDL \ Porosity} \right) \times 100$$

While exact measurements of the PLDL pore volume could not be made because PLDL attenuates x-rays in a manner very similar to the alcohol the sample was submerged in, the pore volume was estimated to be the total scaffold volume multiplied by the average PLDL porosity as determined from representative naïve PLDL scaffolds (Section 5.2.3). The average porosity was determined to be 0.7028. Subsequent statistical analyses were made of the percentage of pore space filled with new bone (%PF). Analyses of variance were conducted using an alpha of 0.05. %PF was determined for each sample as a whole as well as by longitudinal region for samples in the 8-week preculture loaded group. Each sample was subdivided into three longitudinal regions representing the top and bottom 25% and the middle 50% of the sample. The top was arbitrarily defined by the end of the scaffold having more mineral since no markers were placed on the scaffolds at the time of harvest to differentiate top from bottom.

5.2.10 Histology

A representative subset of samples from both the *in vivo* study and the parallel *in vitro* mineralization study was chosen for histological analysis after microCT imaging and analysis. One scaffold from each of the cell-free groups was selected as well as two samples from each of the *in vitro* mineralization groups, and three samples from each of the *in vivo* groups. More scaffolds were analyzed from the *in vivo* groups because more variability was expected in these samples. The two scaffolds selected from each *in vitro* group were the samples with the most and least mineralized volume as determined by microCT analysis within their treatment group. Likewise, the three scaffolds selected

from each *in vivo* group were the samples that represented the maximum, median, and minimum mineralized volume within its treatment group.

Samples were cut in half longitudinally using an Isomet 1000 Precision saw (Beuhler). One half of the sample was processed in paraffin without decalcification and sectioned at approximately 5 microns using a tape transfer technique (Instrumedics, Hackensack, NJ). The other half was reserved for optional plastic processing, but was never utilized for that purpose. Sections were stained with H&E, Von Kossa, and modified Mallory's Aniline Blue.

5.2.11 Finite Element Modeling & Analysis

The accuracy of any finite element model depends on the accuracy of the material properties supplied to the model. Therefore, a reasonable value for the tissue-level modulus of the PLDL scaffold material used in the *in vivo* loading study must first be determined. By matching known force/displacement data of a representative PLDL scaffold to the output of a finite element model based on that sample's architecture, a reasonable estimate of the tissue-level modulus may be obtained. A representative naïve PLDL sample from the set previously imaged by microCT (Section 5.2.3) was chosen to be modeled using finite element analysis to determine the tissue modulus of the PLDL. Only two of the naïve samples scanned were also among the samples mechanically tested under cyclic compression (Section 5.2.2) after receiving 2.5 Mrad gamma irradiation and extended exposure to saline at 37 C. Since the apparent modulus of PLDL changes with extended exposure to physiologic conditions, it was important to choose a sample from the gamma/soak group. Of these two samples, sample p25 was chosen because its

architecture most represented a right cylinder without holes. The mechanical testing data revealed that this sample experiences a strain of -0.0204 when a distributed load of 11.89 N is applied to the top surface.

To create the input mesh for p25, the microCT images were first filtered using a constrained 3-D Gaussian filter ($\sigma = 0.8$, $\text{support} = 1$) to partially suppress noise in the volumetric image data, and then mineralized tissue was segmented from surrounding soft tissue by using a global thresholding procedure with the threshold set at 28. The image was then rotated -9° about the x -axis and -5° about the y -axis to make the long axis of the cylinder line up with the global z -axis. A volume of interest was selected that tightly encompassed the PLDL sample. Next, a component labeling technique was employed and only the largest component kept, ridding the model of unconnected structures which carry no load in the scaffold, but will complicate the solution of the model. This single component represented over 99.9% of the voxels in the model. Scanco Medical's Finite Element-software v1.0 (Basserdorf, Switzerland) was employed to generate and solve the model based on the microCT image data. Using a voxel conversion technique known as digital image-based finite element meshing (DIBFEM), a 30 micron brick element was created to represent each voxel in the microCT image. A distributed compressive load of 11.89 N was applied to the top surface of the model ($z = 0$) to match the actual force applied during cyclic mechanical testing of Sample p25. In addition, the base ($z = z_{\text{max}}$) was constrained to have no displacement in the z direction and the walls of the cylinder were constrained to have no displacement in the x or y directions. Figure 5 illustrates the coordinate system used and the distributed load across the top surface.

Scanco Medical's Finite Element-software v1.0 was used to determine the solution. As discussed in Section 3.2.10, the software assumes a continuum sample with elastic properties experiencing small deformations. Translating the rule of thumb for continuity of trabecular bone to the polymer would suggest that any sample larger than five times the trabecular spacing, or in this case, 5 x 400 microns or 2 mm, satisfies the continuum assumption [176]. The samples modeled were 4 mm diameter by 5 mm length. Furthermore, mechanical testing as described above confirms that the tissue responds in an elastic manner in the range of loads analyzed. Finally, the apparent strain applied is less than 2%, within the bounds of the small deformation assumption. The software uses an iterative conjugate gradient solver in combination with an element-by-element matrix-vector multiplication scheme [177].

The model was solved using an initial guess of 5000 MPa for the tissue modulus and 0.3 for Poisson's ratio. Convergence tolerances were set to 1e-4. The actual tissue modulus was approximated by multiplying the initial guess by the ratio of the apparent strain in the z-direction from the model to the actual apparent strain measured in the mechanical test as shown in Equation 1. The result shows that the tissue modulus of PLDL manufactured with 30% porogen and exposed to 2.5 Mrad gamma irradiation and 8 weeks exposure to an aqueous environment is approximately 849 MPa. This value is much smaller than that calculated for rabbit trabecular bone, consistent with the lower apparent mechanical stiffness of PLDL.

Equation 3

$$TMOD_{actual} = TMOD_{guess} \frac{\mathbf{e}_{zz}^{model}}{\mathbf{e}_{zz}^{test}} = 5000 MPa \left(\frac{0.0035}{0.0204} \right) \approx 849 MPa$$

Three representative samples were chosen from the twelve naïve PLDL samples scanned for finite element modeling of the loading conditions employed during the *in vivo* loading study of tissue-engineered constructs in the rat subcutaneous model. PLDL scaffolds from the *in vivo* study were not used for the architectural basis for the finite element models because unpublished data from our laboratory suggests there may be a reduction in subsequent *in vitro* mineralization of PLDL scaffolds after exposure to microCT scans. Therefore, naïve representative samples p25, p26, and p93 were chosen for their architecture and then modeled in a fashion similar to that described above to determine the tissue modulus of PLDL. Each voxel of the microCT images was again modeled as a 30 micron brick element. Local boundary errors associated with DIBFEM should be reasonable at this resolution since the average strut thickness of the PLDL was 135 microns allowing 4-5 elements across each trabecular strut on average [179, 180]. An additional layer of elements was added to the top of the cylindrical model to represent the titanium loading platen used *in vivo*. The models were constrained as described earlier but the distributed load was increased to 13.3 N to represent the actual applied load in the rat *in vivo* loading procedure. Furthermore, the PLDL was assigned the estimated tissue modulus of 849 MPa and a Poisson's ratio of 0.3. The interstitial tissue space was modeled with a stiffness of 0.1 MPa and Poisson's ratio of 0.3. This stiffness value is similar to the Young's Modulus used by Lobo for mesenchymal tissue [189]. The marrow is not intended to be a structural member of the model but is included to determine strain responses within the pore spaces. The plate was assumed to be perfectly stiff and assigned a value of $1e7$ MPa. Modeling the stiff plate guards against large

deformation errors associated with having a load applied directly to two materials with very disparate moduli.

The models were considered converged when the force and displacement residuals were less than $1e-4$. Four output parameters were examined for both the polymer and the interstitial space including the largest principal strain, Von Mises Stress (VMS), and strain energy density (SED). Von Mises Stress provides an individual parameter reflective of both the hydrostatic and distortional stresses experienced in the tissue while strain energy density is a parameter often evaluated for its overall integration of both stress and strain responses. To exclude end artifacts, the data representing output responses above the 95th percentile were excluded from analysis of VMS and SED (range: $0, \infty$). In addition, the data below the 5th percentile and above the 95th percentile were excluded from analysis for the largest principal strain (range: $-\infty, \infty$). In addition, the variation in these parameters was also observed among the top 25% of the model, the middle 50%, and the bottom 25% of the model to examine regional differences in the tissue response to the applied loading scenario. Appendix G includes a step-by-step guide to the necessary Image Processing Language (IPL, ©Andres Laib, Scanco Medical AG) commands required for pre-processing, solving, and post-processing these models.

5.3 Results

5.3.1 Viability of Representative PLDL Scaffolds

At each of the three seeding sessions, three samples were stained with calcein and ethidium homodimer 24 hours later to determine the viability of the cells present. Figure 37 shows a representative view along the longitudinal axis of the scaffold for each of the

nine scaffolds analyzed. The PLDL scaffold material autofluoresces red, which unfortunately makes distinguishing dead cells from the scaffold difficult, but also allows you to see how the cells line the PLDL surfaces especially along the longitudinal macroporosity of the structure. There is a marked reduction in the number of viable cells and possibly overall number of cells present in Seeding Groups #2 and #3 compared to Seeding Group #1. In general, the overall number of cells present in Seeding Group #1 appears to be greater than in Seeding Groups #2 and #3.

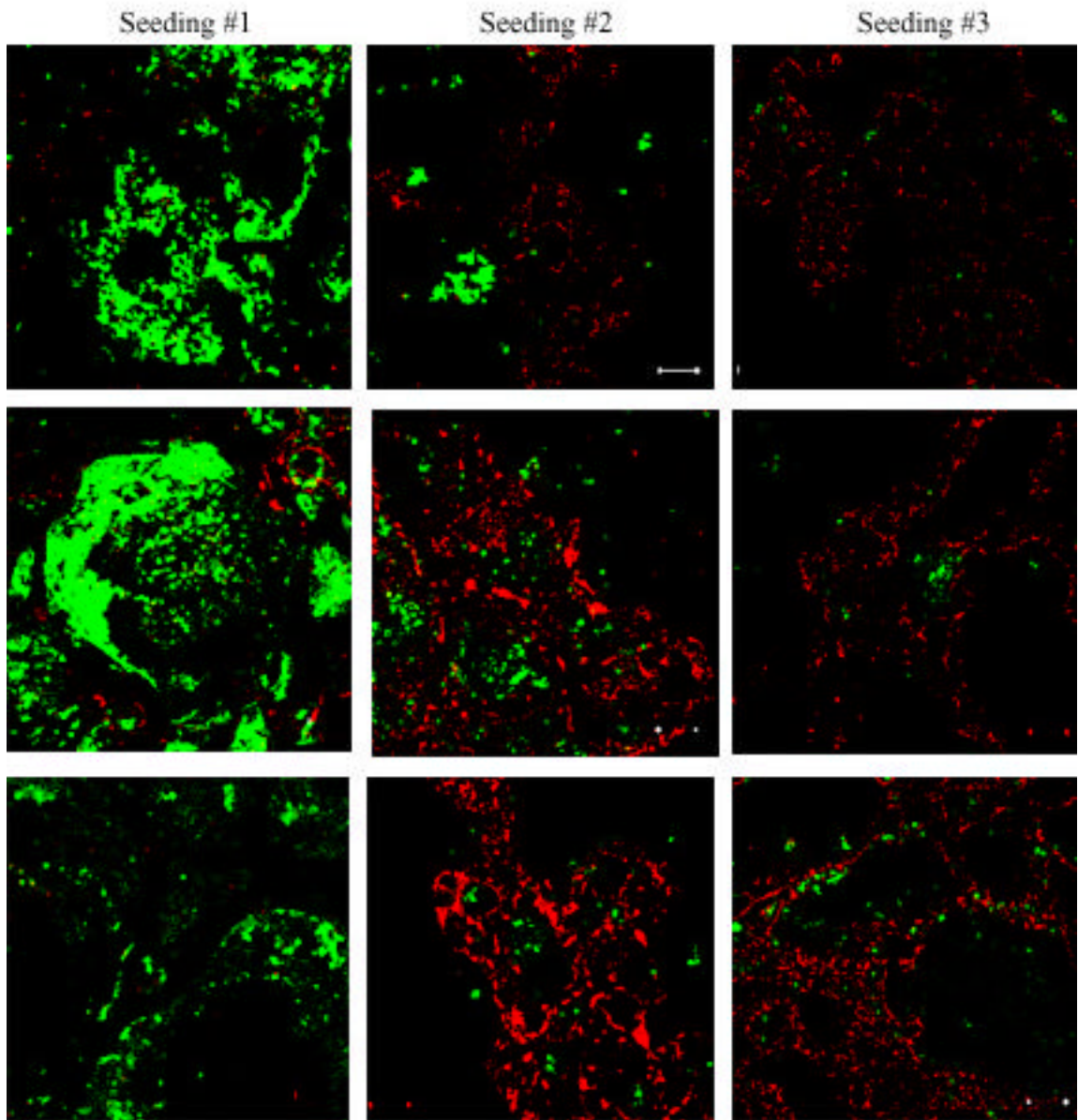


Figure 37. Representative Cell-Seeded PLDL Scaffolds from Each of the Three Seeding Groups Labeled for Live (Green) and Dead (Red) Cells; View Shown is Along the Longitudinal Axis

5.3.2 Cell-Seeding Quantification

The number of cells attached to the PLDL scaffold was quantified for three samples from each of the three seeding groups using PicoGreen fluorescent dye for double-stranded DNA. The average number of cells attached was 122,000 for Seeding Group #1, 51,100 for Seeding Group #2 and 34,500 for Seeding Group #3 as shown in Figure 38. These numbers represent seeding efficiencies ranging from 3.5% to 12.2%. Although there appears to exist a trend toward a significant decrease in the number of cells with each successive seeding, a one-way analysis of variance ($\alpha = 0.05$) did not show any significant difference among seeding groups ($p = 0.119$).

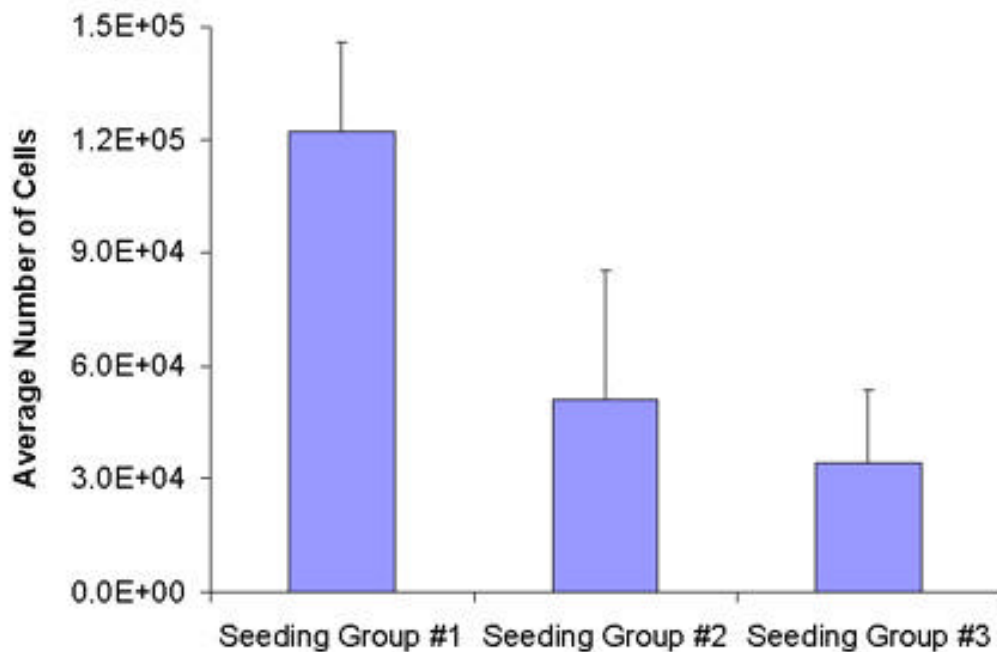


Figure 38. Average Number of Cells Attached to Cell-Seeded Scaffold for Each Seeding Group, (Mean + Standard Error, n=3)

5.3.3 Mineral Quantification in Parallel *In vitro* Scaffolds

Scaffolds seeded with rMSCs at Seeding #1 and Seeding #3 were maintained in osteogenic supplements for 1, 7, 8, or 14 weeks and then scanned using microCT to determine the overall mineral content of each scaffold. There was a significant difference ($p=0.007$) between scaffolds seeded during Group #1 versus scaffolds seeded during Group #3 as illustrated by Figure 39, a plot of all samples from each seeding regardless of time in culture. Because there was no variation in samples seeded during Seeding #3, only those samples in Seeding #1 were included in a subsequent analysis of variance to determine the impact of time in culture. MicroCT images of the scaffolds in Seeding Group #1 and their cell-free controls are shown in Figure 40.

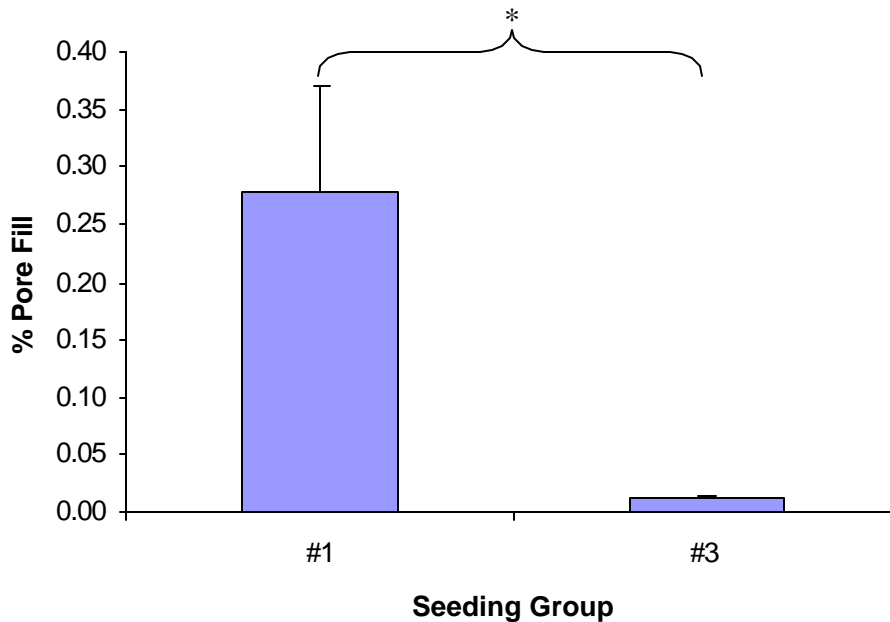


Figure 39. Mineralization on PLDL Scaffolds Cultured *in vitro* for 1, 7, 8, or 14 weeks as a Function of the Seeding Group

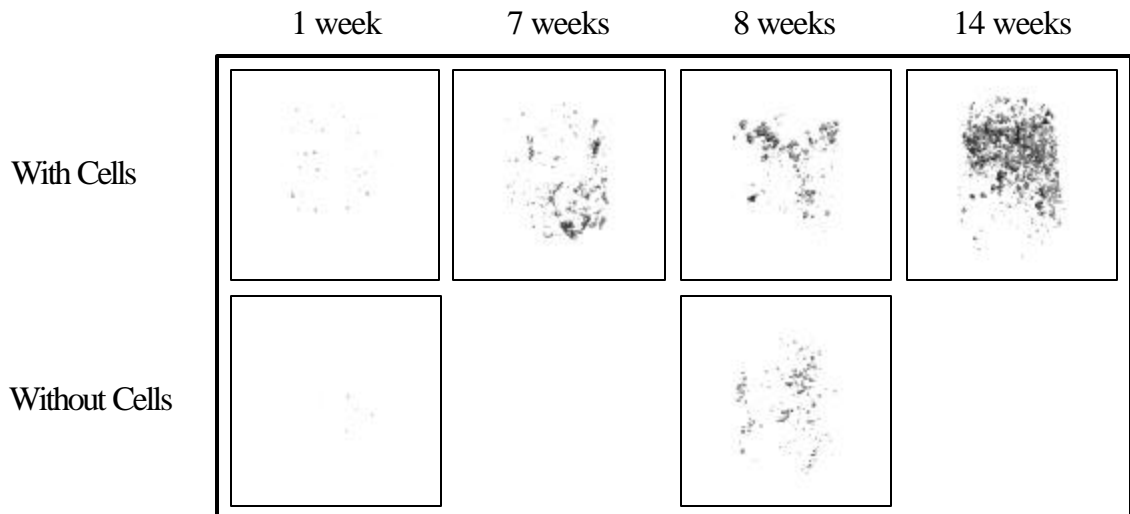


Figure 40. Select MicroCT Images of Each of the In Scaffolds in Parallel Osteogenic *In vitro* Culture for 1, 7, 8, or 14 Weeks

While the data from Seeding Group #1 was limited, a two-way ANOVA model involving scaffolds seeded with and without cells and then cultured for either 1 week or 8 weeks shows a significant effect of both cells ($p=0.022$) and time in culture ($p=0.001$). Figure 41 reflects the increase in mineralization associated with both these parameters.

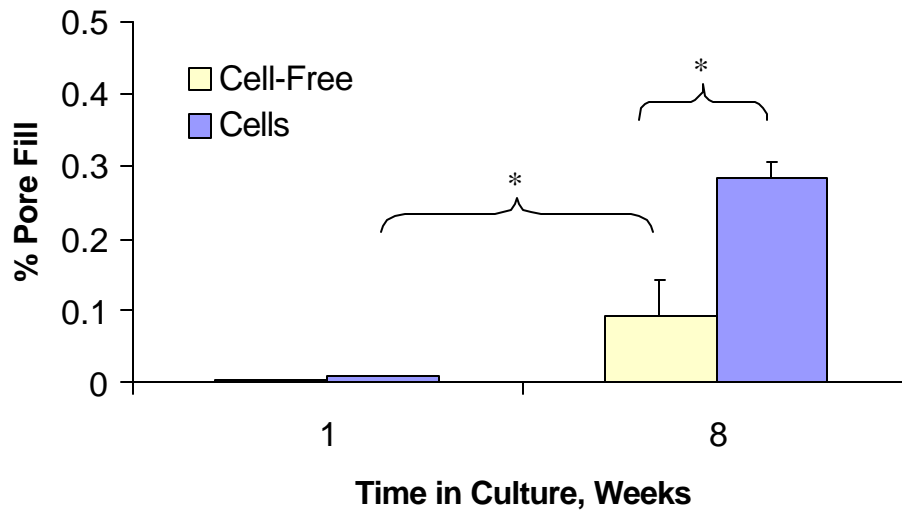


Figure 41. Mineralization on PLDL Scaffolds Cultured *in vitro* for 1, 7, 8, or 14 weeks as a Function of Time in Culture (Mean + Standard Error, n=3)

5.3.4 Histology of *In vitro* Samples

MSC seeded PLDL scaffolds were cultured in osteogenic supplements and harvested after either one week or 8 weeks *in vitro*. Cells were present both on polymer surfaces and within interior pore spaces. Surfaces near the periphery were almost continuously lined with cells, but cells were still present in fewer numbers toward the interior of the scaffold. While cells on near the periphery tended to be exclusively on polymer surfaces, cells in the interior could be found both on surfaces and within the pore space. Cells on outer surfaces were flatter and associated with more secreted extracellular matrix than their counterparts on more interior surfaces. This pattern was present both at 1 week and 8 weeks, however there were greater cell numbers and additional matrix present at 8 weeks. At eight weeks there also seemed to be a greater variety of cell morphologies present. Figure 42 illustrates these differences between

interior and exterior surfaces. Round nodules of von Kossa positive staining indicating the presence of phosphates appeared at 8 weeks (Figure 43A) but were not present after only 1 week of culture. These areas were typically confined to polymer surfaces and were not found within the interior of pores.

Cell-free controls were naturally devoid of any cells or matrix staining. At eight weeks, cell-free controls stained with von Kossa did however show some diffuse positive staining that appears to be dystrophic phosphate deposition from the culture medium (Figure 43B). This diffuse staining is distinct from that occurring from true cell-mediated phosphate deposition which occurs in discrete nodules directly associated with cells. No areas suggestive of dystrophic mineralization were present in the constructs containing cells.

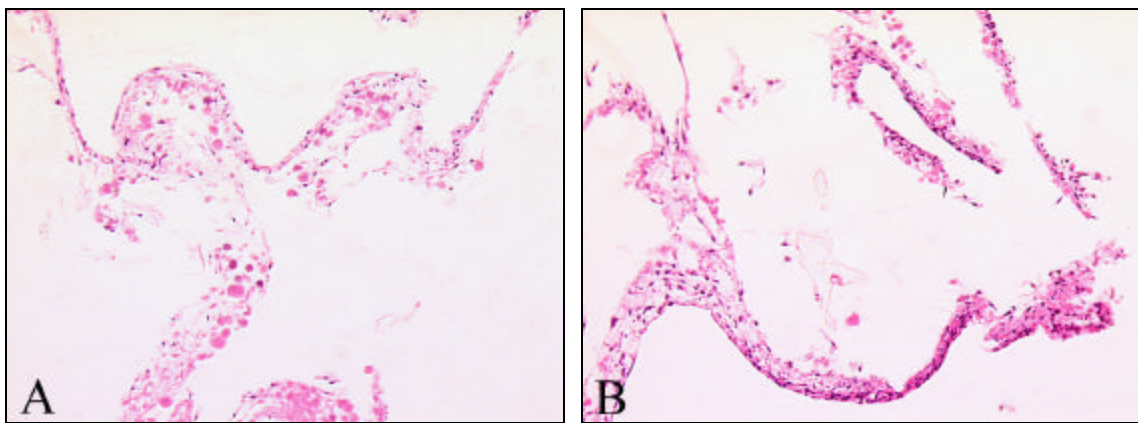


Figure 42. MSC-seeded PLDL cultured in osteogenic supplements for 8 weeks; A) interior surface, B) exterior surface; H&E stain at 20x

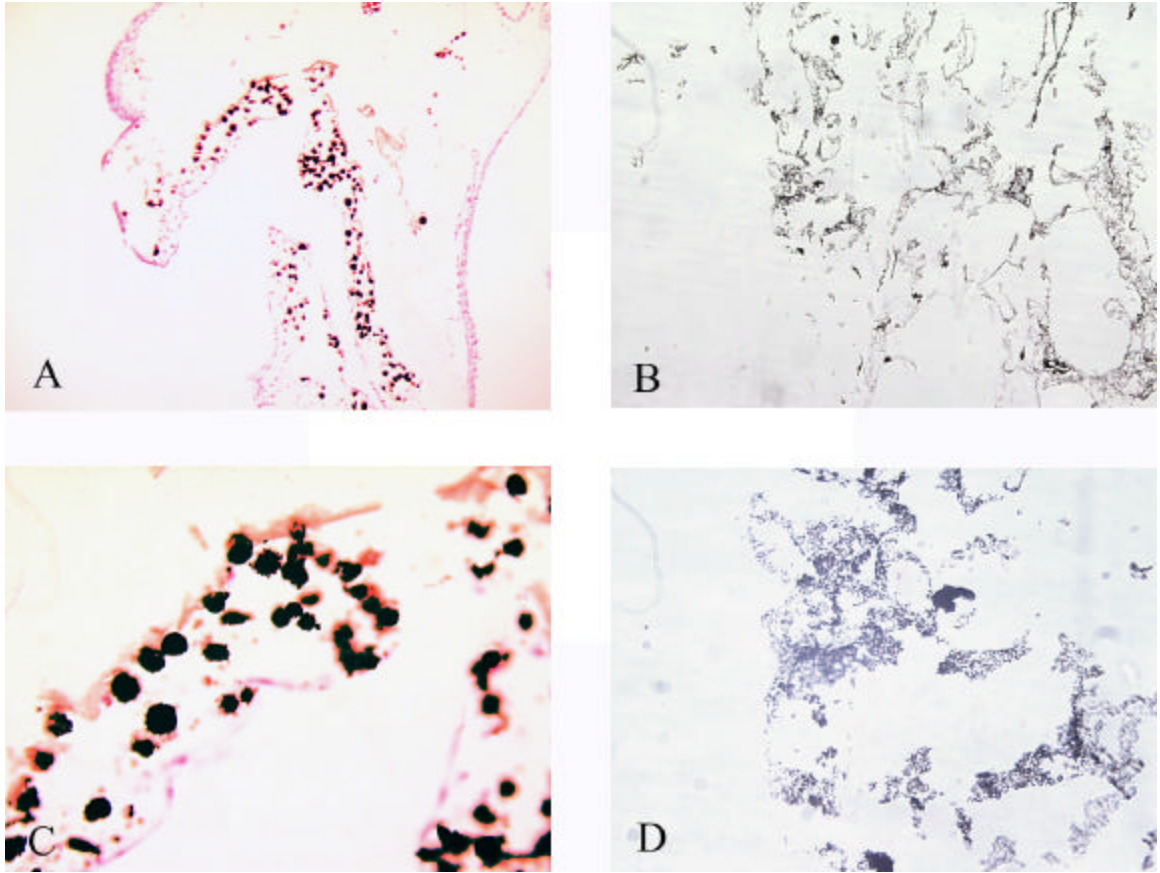


Figure 43. Von Kossa staining of PLDL cultured in osteogenic media for 8 weeks with cells (A & C) and without cells (B & D); 10x (A & B) and 40x (C & D)

5.3.5 Harvest Observations

All *in vivo* constructs were harvested six weeks after implantation and appeared viable at time of harvest with tissue filling the pore spaces. Several samples showed signs of titanium debris particles on the scaffolds, especially on the ends. Four rats died prematurely due to complications associated with anesthesia during the first week of loading treatments. On a separate animal, the incision over the implant pulled apart, requiring the subcutaneous pouch to be widened and the incision reclosed. After harvest however, it was determined that the vascular supply to the bottom chamber had most likely been disrupted during that process, so the sample was excluded from further analysis. Otherwise, all harvested scaffolds seemed very vascular and often capillaries were observed entering the chambers through the vascular port holes. Implants were encapsulated in subcutaneous tissue as seen in Figure 44. Table 9 outlines the number of samples collected from each *in vivo* treatment group.



Figure 44. Loaded (left) and Nonloaded (right) Chambers *In Situ* at Time of Harvest

Table 9. Number of Samples Harvested per *In vivo* Treatment Group

Preculture	Loading	Sample Size
No Preculture	No	8
No Preculture	Yes	8
1 Week Preculture	No	8
1 Week Preculture	Yes	10
8 Week Preculture	No	8
8 Week Preculture	Yes	8
Cell-Free	No	6
Cell-Free	Yes	6

5.3.6 Histology of *In vivo* Samples

In general, there were more cells and matrix on the sides of the cylindrical scaffold than the top and bottom surfaces. Likewise, there was more tissue on the ends than in the very center of the scaffold. There tended to be more matrix filling the pores of the 8-week preculture group (Figure 45), with much less in the 1-week preculture group, followed by the no preculture group. However, the pores were better filled with tissue in the cell-free group than either the 1-week or no preculture groups, but less than the 8-week preculture group. Cells could be seen both lining polymer surfaces and within the pores space as shown in Figure 46. Vascular and marrow elements were present as well.

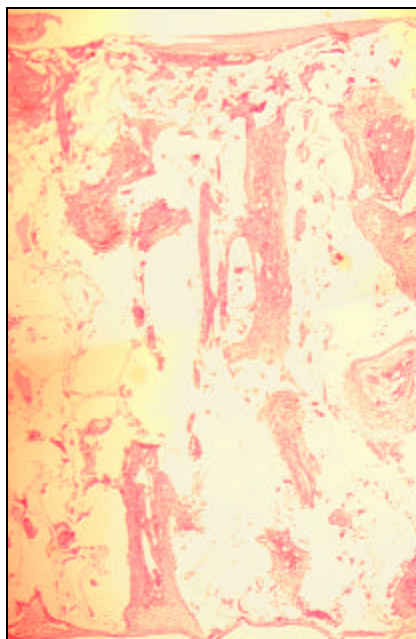


Figure 45. Nonloaded 8-Week Preculture Sample With H&E Staining Showing Tissue Filling Pore Spaces; 4x

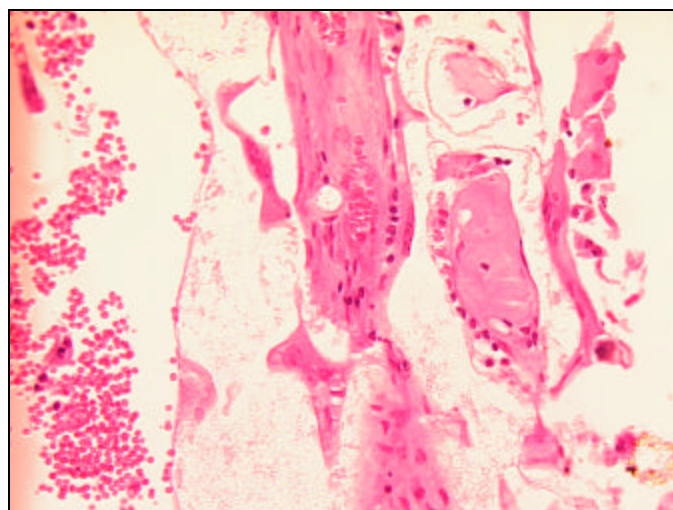


Figure 46. Cuboidal Shaped Cells Lining Polymer Pore In An 8-Week Preculture Nonloaded Sample; H&E 40x

Von Kossa staining for phosphates and modified Mallory's Aniline Blue showing new bone and/or osteoid are useful for pinpointing areas of mineralization. However, given the small volume of mineral present, the absence of either histological indicators of bone formation does not preclude the presence of mineral. However, areas of positive von Kossa staining were found in the 1-week preculture nonloaded group, and both the loaded and nonloaded 8-week preculture groups. Some areas of orange/yellow in the mMAB stain indicating new bone and/or osteoid like those present in Figure 47 were present in nearly all samples. Since the mMAB stain also stains unmineralized osteoid, it is not surprising that there are more areas of new bone/osteoid than von Kossa positive areas for phosphate deposition. The 8-week preculture group had much more mineral present than any other group with a noticeable increase in mineralized nodules present in the loaded group over the nonloaded group. These nodules are present both along polymer surfaces and in the pore spaces as shown in Figure 48. Mineral extends to the interior of the scaffolds along the longitudinal macropores. Inspection of the mineral deposits at high magnification confirms that the deposits were cell-mediated as witnessed by cytoplasmic staining of the cells and matrix vesicles (Figure 48). In the loaded group, there appears to be more mineral present on one end rather than the other end of the scaffold (Figure 49). No patterns of dystrophic mineralization were noted in any of the *in vivo* samples.

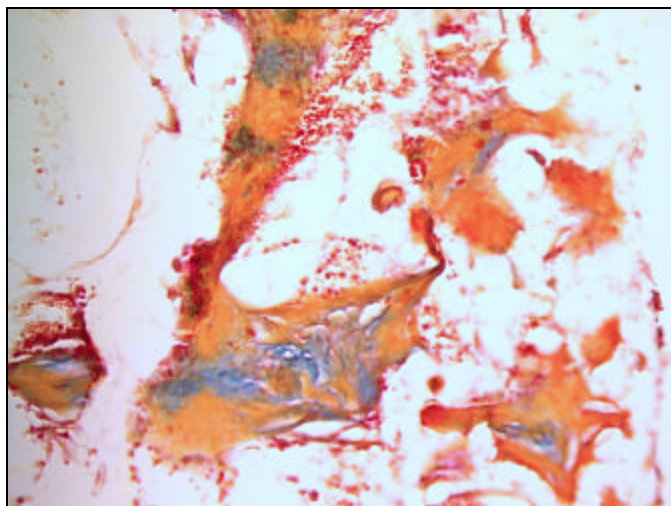


Figure 47. Reddish-Orange Areas Indicating New Bone Formation In An 8-Week Loaded Specimen; mMAB 20x

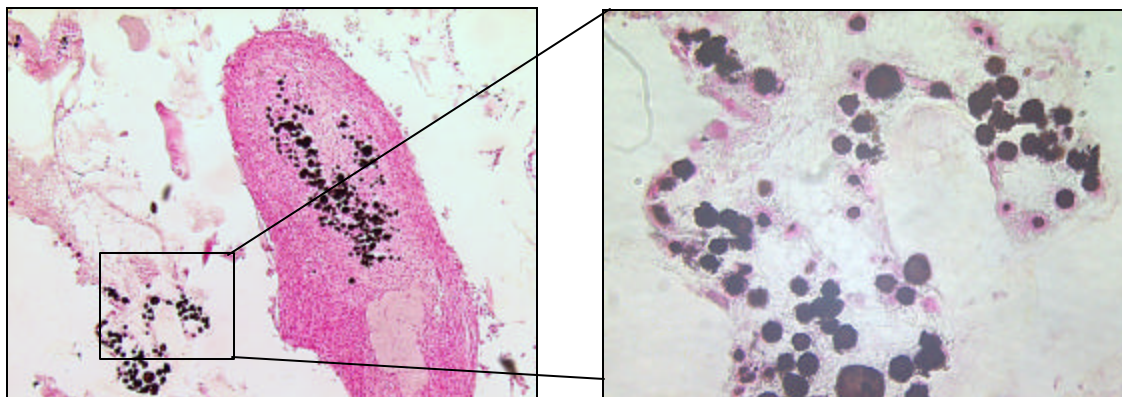


Figure 48. Examples Of Positive Von Kossa Staining (Black) Both On A Polymer Surface And Within The Pore Space For An 8-Week Preculture Loaded Sample; 10X and 40X

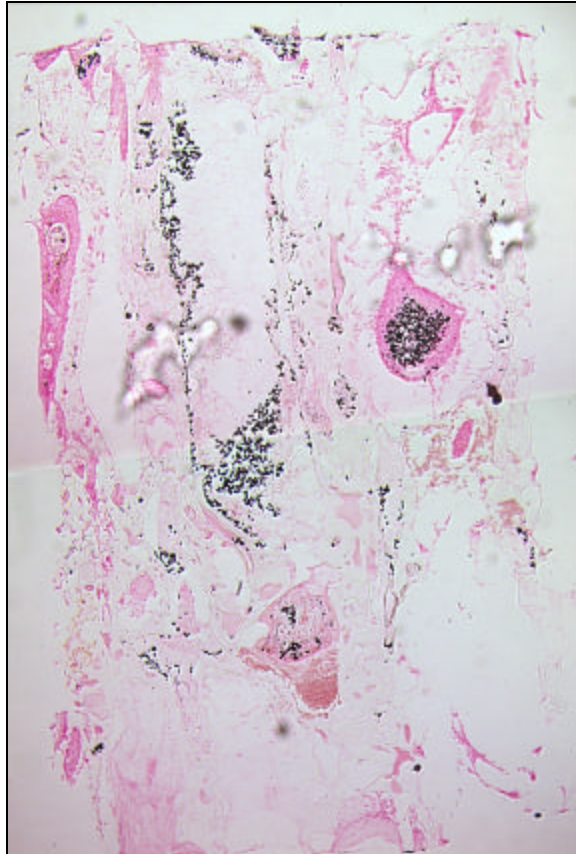


Figure 49. Loaded 8-Week Preculture Sample With Positive Von Kossa Staining (Black) Concentrated More On One End Of Surface Than The Other; 4X

5.3.7 MicroCT Results for *In vivo* Samples

Bone volume formed within the scaffolds ranged from 0 to 0.67 mm³, indicating that 0-1.6% of the available pore space in the scaffold was filled. Figure 50 shows a representative set of loaded and nonloaded scaffolds from the 8-week preculture group. Like these examples, most of the scaffolds exhibited mineral throughout the construct rather than just on the periphery of the scaffold. Seven samples attenuated the x-rays from the microCT at an extraordinarily high level. These samples were traced back to those noted as having titanium wear debris during harvest. All of these samples came exclusively from nonloaded treatment groups. The particles were most likely generated at the time of chamber assembly during implantation surgeries because machining variations made these chambers slightly more difficult to assemble. Since the titanium particles could not be thresholded from the mineral, these seven samples were not included in analysis of mineral formation. Incidentally, these samples were also excluded from histological processing. Table 10 outlines the number of samples remaining for statistical analysis in each *in vivo* experimental group.

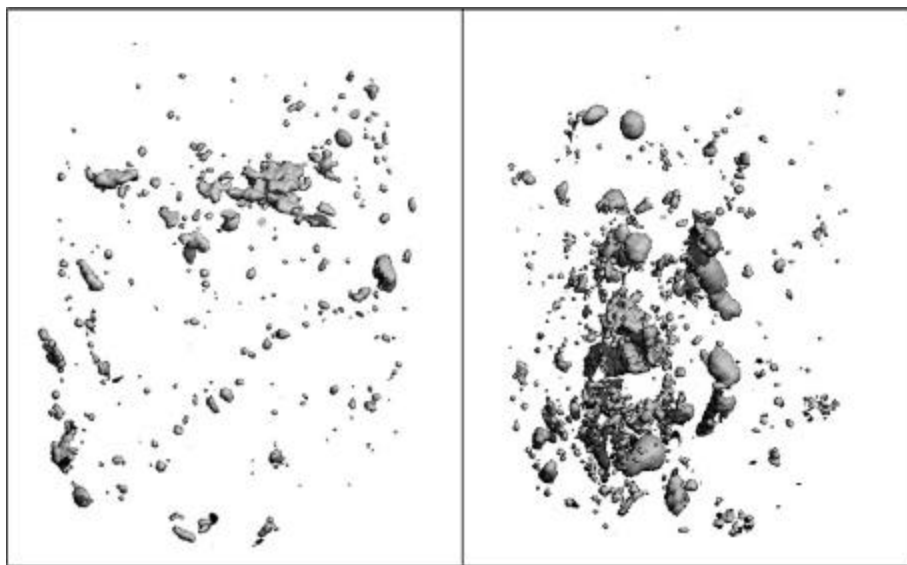


Figure 50. Representative MicroCT Images of Mineral Formed on PLDL in the 8-Week Preculture Group Without *In vivo* Loading (Left) and With *In vivo* Loading (Right)

Table 10. Number of Samples Included in Statistical Analysis per *In vivo* Treatment Group

Preculture	Loading	Sample Size
No Preculture	No	8
No Preculture	Yes	7
1 Week Preculture	No	5
1 Week Preculture	Yes	10
8 Week Preculture	No	6
8 Week Preculture	Yes	7
Cell-Free	No	5
Cell-Free	Yes	6

Using the remaining *in vivo* samples, the percent pore fill was determined for each of the treatment groups. Figure 51 shows the difference between the loaded and nonloaded groups for each scaffold preparation group (i.e. cell-free, no preculture, 1-week preculture, and 8-week preculture). A one-factor General Linear Model (GLM) of the entire data shows a significant effect of load ($p=0.043$) and a two-factor GLM predicts a significant impact of both load ($p=0.034$) and scaffold preparation group ($p=0.026$). However, given the differences between Seeding Group #1 and Seeding Groups #2 & #3 demonstrated by DNA analysis, cell viability, and *in vitro* mineralization, the effect of scaffold preparation group may be either due to time in preculture or differences in cell number and viability. Given this uncertainty, just the cell-free and 8-week preculture groups were again considered for analysis of variance. Even with this reduced data set, a two-factor GLM still shows a significant effect of both load ($p=0.047$) and scaffold preparation ($p=0.041$). Neither the animal nor the position that the scaffold was implanted had a significant impact on %PF.

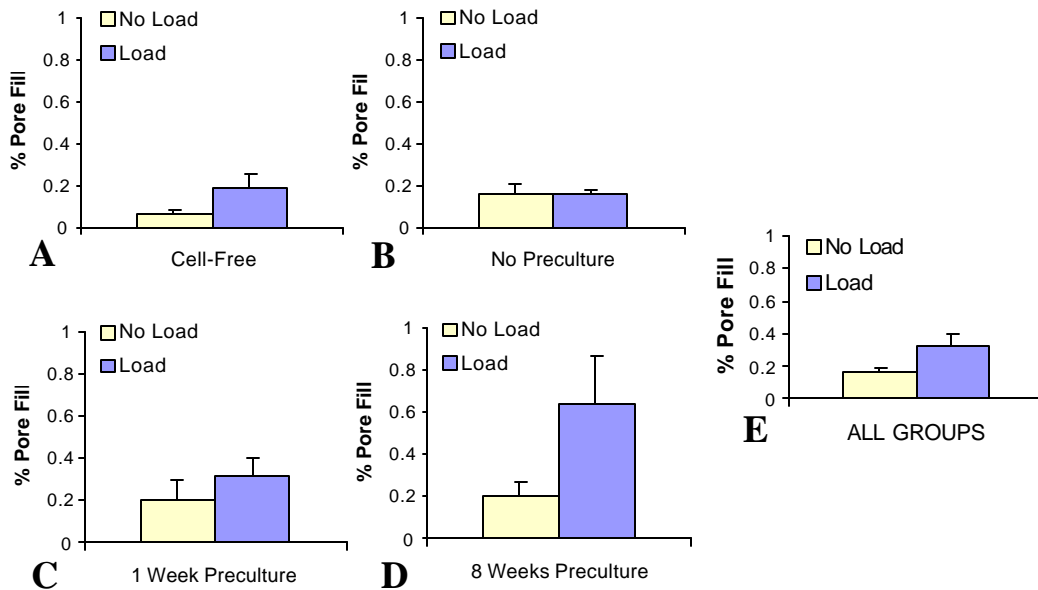


Figure 51. Mineralization after Six Weeks *In vivo* with or without Two Weeks Loading of PLDL with Different Scaffold Preparations (A: Cell-free, B: Cell-Seeded with No Preculture, C: Cell-Seeded with 1 Week Preculture, D: Cell-Seeded with 8 Weeks Preculture, E: All Preparation Groups); (Mean + Standard Error, 5 n 10)

Since histological observations of the loaded samples in the 8-week preculture group included the presence of more mineral on one end of the scaffold than the other, a regional analysis of longitudinal bone distribution was performed for samples in this group. The end of the scaffold with more mineral was arbitrarily defined “top” and the opposite end the “bottom.” Percent pore fill was compared between the top 25%, middle 50%, and bottom 25% of each loaded scaffold in the 8-week preculture group. In the absence of accurate labeling of top versus bottom, all that can be safely concluded is that one end of each sample consistently shows more mineral than the opposite end of the scaffold as shown in Figure 52. While it is likely that the end with more mineral is

consistently either the true top or bottom of the sample, it is impossible to make this conclusion. A two-factor GLM with region and animal as factors showed both factors to have a significant effect ($p=0.038$ and $p=0.005$ respectively). Tukey pairwise comparisons confirm that regional differences only exist between the top and bottom and not between top and middle or bottom and middle. These data demonstrate a significant pattern of increasing bone formation from one end of the sample to the other.

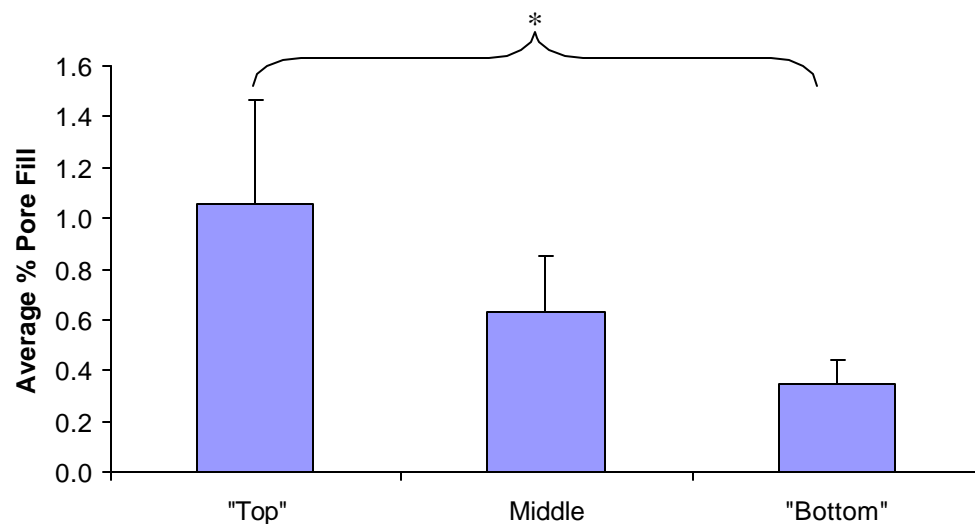


Figure 52. Longitudinal Differences in Bone Formation in 8-week Preculture Samples Loaded *in vivo*

5.3.8 Finite Element Analysis of Loading Scenario

Finite element models were based on the architecture of three different representative PLDL scaffolds and simulated the loading conditions applied during *in vivo* loading. The average apparent strain of these models was 1.8% for the applied 13.3 N load which represents an apparent stress of approximately 1.0 MPa. At the tissue level,

trabeculae experienced largest principal strains ranging from +0.03% to -1.86%; however, the largest percentage of voxels saw strains in the region of -0.24% as shown by the histogram in Figure 53. Strains within the interstitial tissue were much higher and ranged from +0.10% to -12.61% with most of the interstitial tissue experiencing strains around -1.20% as illustrated by Figure 54. Although Von Mises Stress in the polymer phase reached as high as 10.15 MPa or about ten times the apparent stress, the majority of the polymer was subject to stresses around 1.60 MPa. Since the interstitial pore space does not really carry much of the applied loads, the Von Mises Stress in the interstitial tissue was substantially lower, centered around 0.0014 MPa even though a few voxels reported stresses as high as 2.33 MPa. Histograms for the Von Mises Stress in both the polymer (Figure 55) and the interstitial tissue (Figure 56) reflect these patterns. Histograms for strain energy density in the polymer (Figure 57) and in the interstitial tissue (Figure 58) appear to peak at zero, but close inspection of the data shows a very small non-zero number for each since the parameter reflects a product of very small values. A detailed summary of each of these parameters can be found in Table 11, including the mean, standard error of the mean, the peak, maximum, and minimum values.

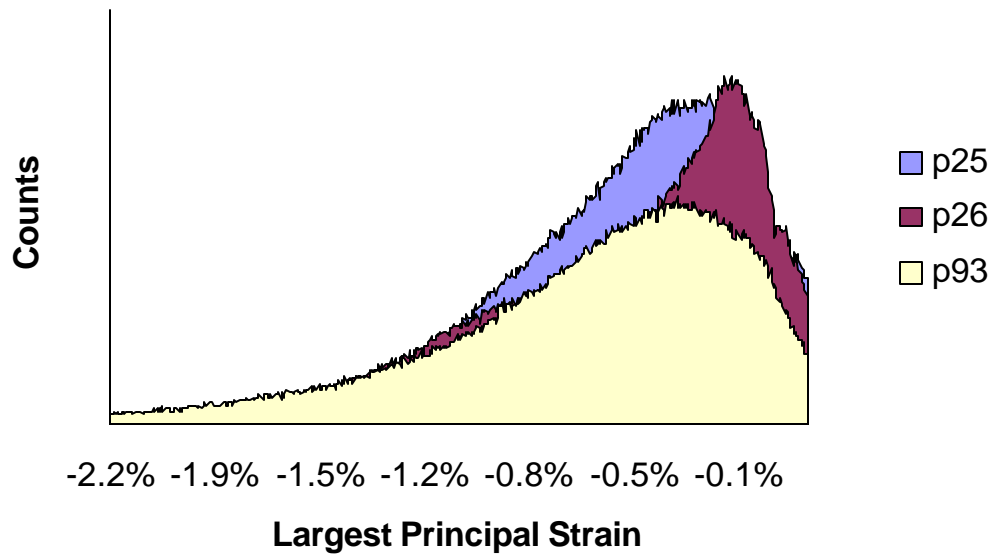


Figure 53. Histogram of the Largest Principal Strain within the Polymer

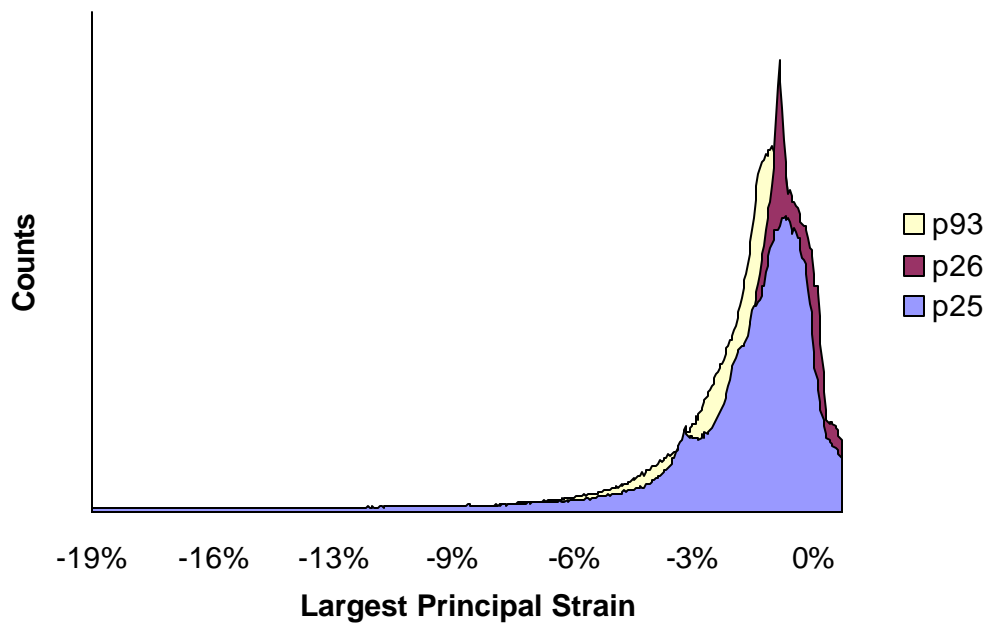


Figure 54. Histograms of Largest Principal Strain within the Interstitial Tissue

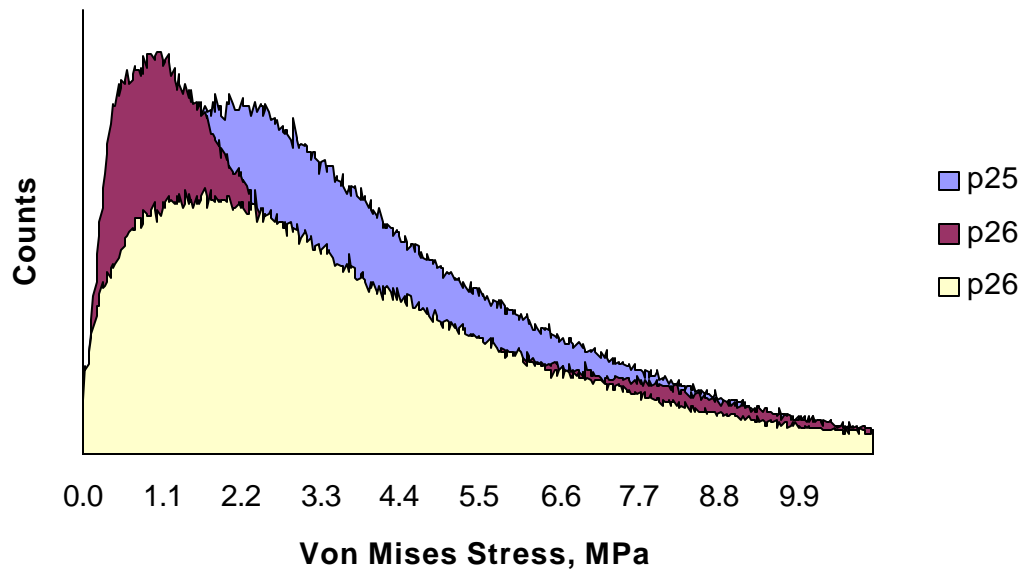


Figure 55. Histogram of the Von Mises Stress within the Polymer

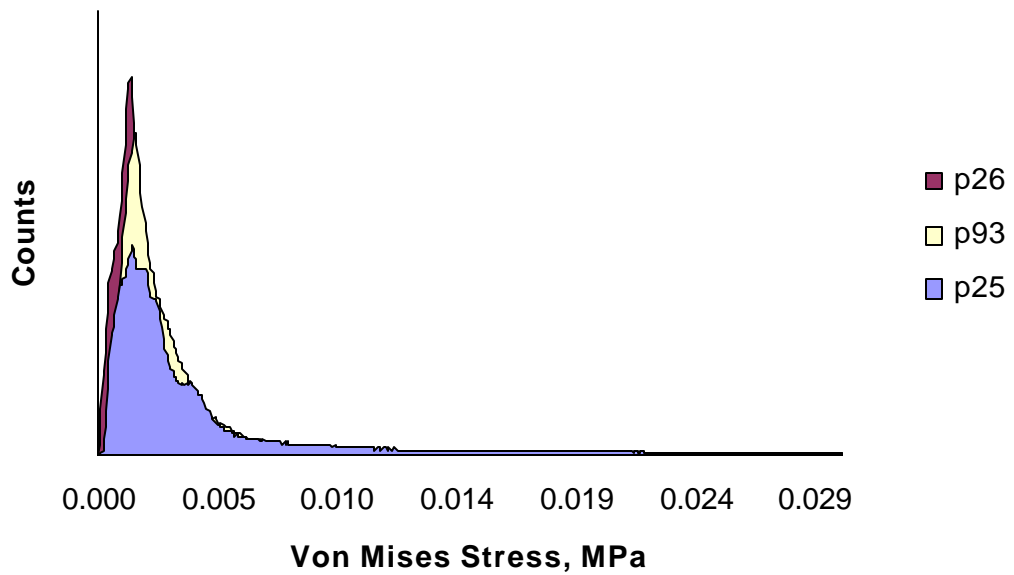


Figure 56. Histogram of the Von Mises Stress within the Interstitial Tissue

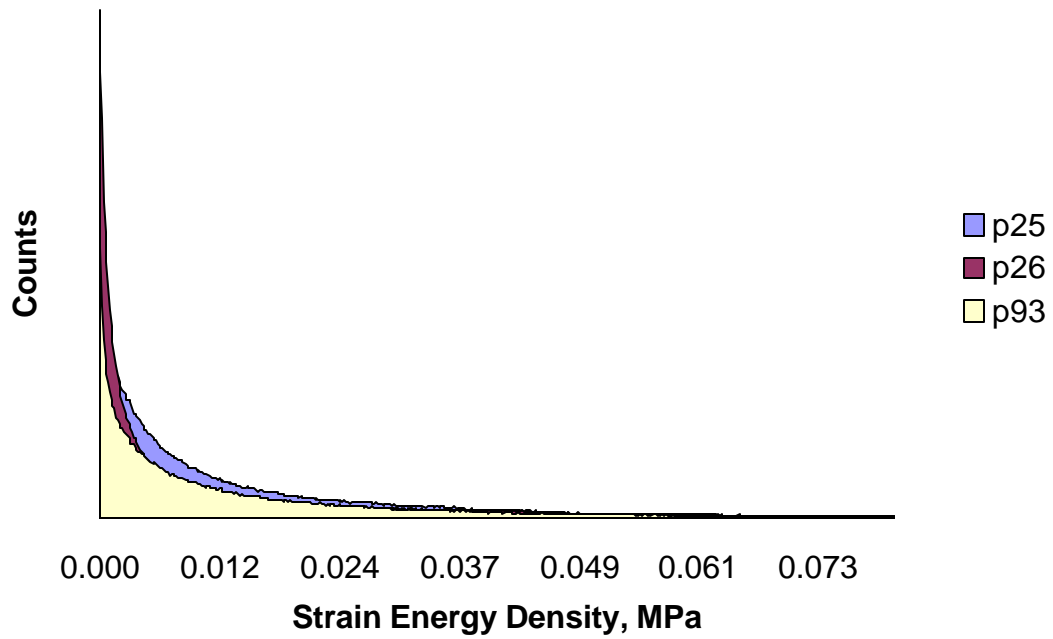


Figure 57. Histograms of the Strain Energy Density within the Polymer

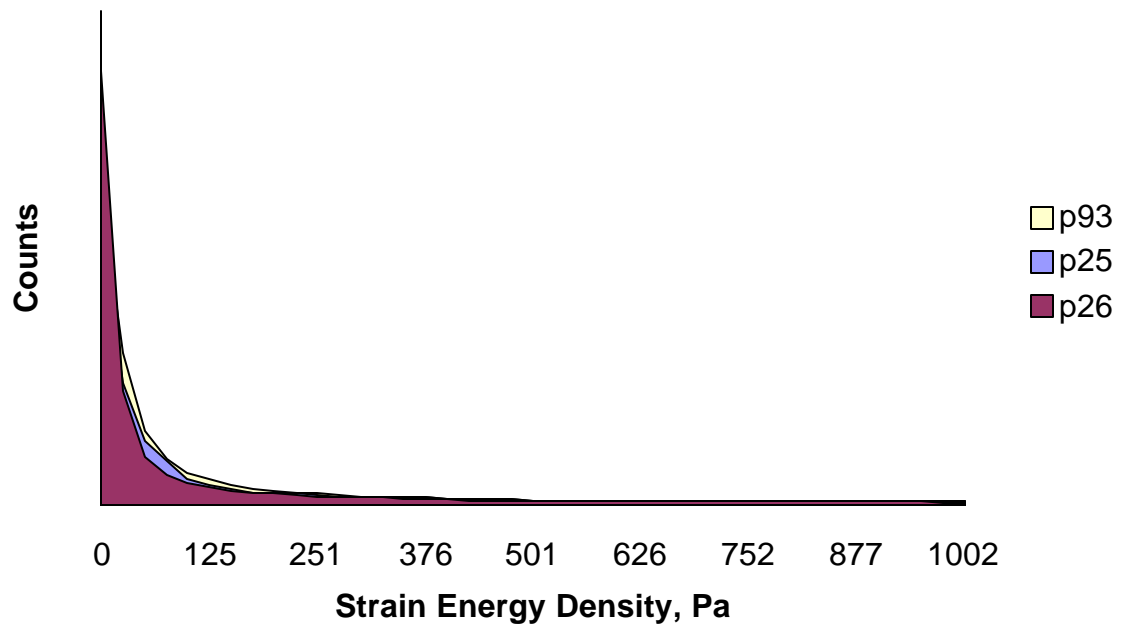


Figure 58. Histograms of the Strain Energy Density within the Interstitial Tissue

Table 11. Summary of the Mechanical Response Predicted by Finite Element Models for Both Polymer and Interstitial Tissue

		Mean	SEM	Peak	Avg. Min.	Avg. Max.
Largest Principal Strain	Polymer	-0.56%	0.04%	-0.24%	-1.86%	0.03%
	Interstitial Tissue	-2.17%	0.27%	-1.20%	-12.61%	0.10%
Von Mises Stress, MPa	Polymer	3.450	0.135	1.595	0.000	10.147
	Interstitial Tissue	0.197	0.017	0.0014	0.0000	2.3263
Strain Energy Density, MPa	Polymer	0.0136	0.0006	1.44e-4	0.0000	0.0746
	Interstitial Tissue	0.0008	0.0001	8.30e-6	0.0000	0.0110

Figure 59 shows a representative cross-section from the center of sample p26 with its architecture color-coded for largest principal strain and Von Mises Stress for both the polymer and the interstitial tissue.

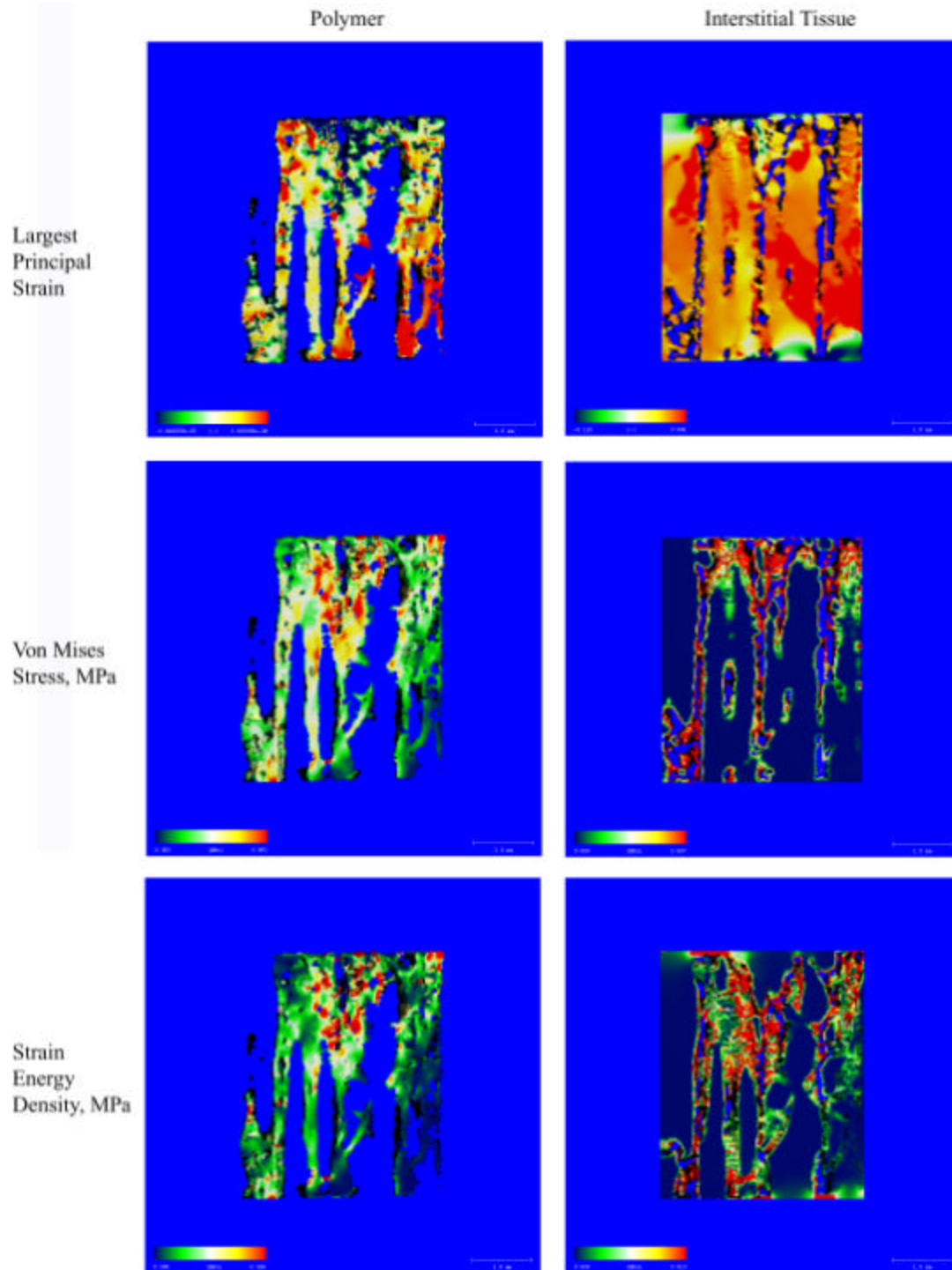


Figure 59. Representative Cross-Sections (150 microns) of Finite Element Model Coded for the Tissue Level Largest Principal Strain and Von Mises Stress in Both the Polymer and the Interstitial Tissue

Since microCT analysis of the 8-week preculture group loaded *in vivo* revealed a significant difference between bone formation on opposite ends of the scaffolds, a regional analysis of the stress/strain response as predicted by our finite element models was also performed in search of a similar trend in one of the response variables. Each sample was divided into the top 25%, the middle 50%, and the bottom 25% longitudinally and $\hat{\sigma}_p$, VMS, and SED were calculated for each region of each of the three finite element models for both the polymer and interstitial tissue. The mean value of each parameter for each region was averaged for the three samples and then divided by the result for the top region and plotted in Figure 60 for the polymer phase and in Figure 61 for the interstitial tissue phase to demonstrate patterns in the data from region to region. To then determine if these patterns were significant, a General Linear Model with sample and region was performed with alpha of 0.05 along with Tukey's pairwise comparisons for each of the regions for each parameter. The only significant difference detected between regions was between the top and middle sections for the strain energy density in the interstitial tissue. No significant differences were found in any of the parameters in either the polymer or interstitial tissue between the top and bottom sections.

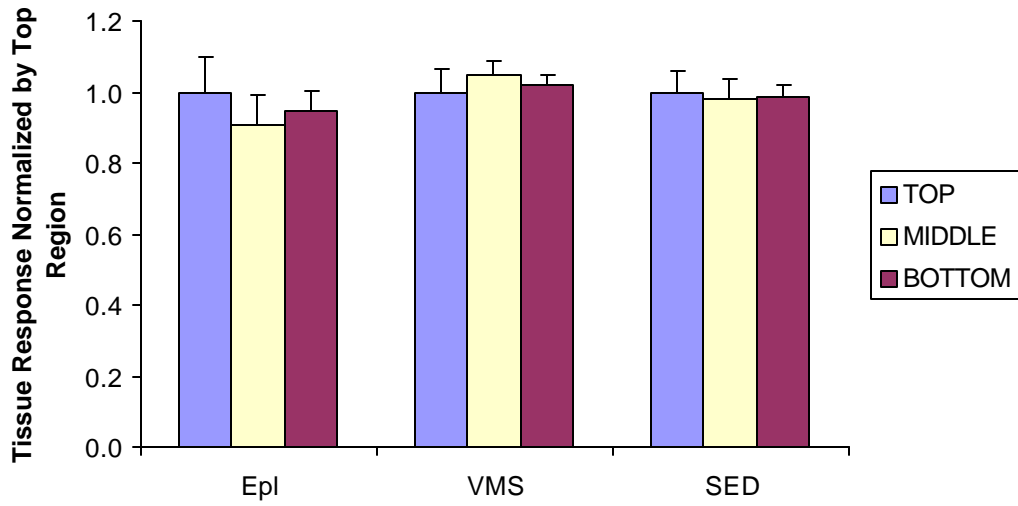


Figure 60. Longitudinal Variation in Stress/Strain Response in PLDL

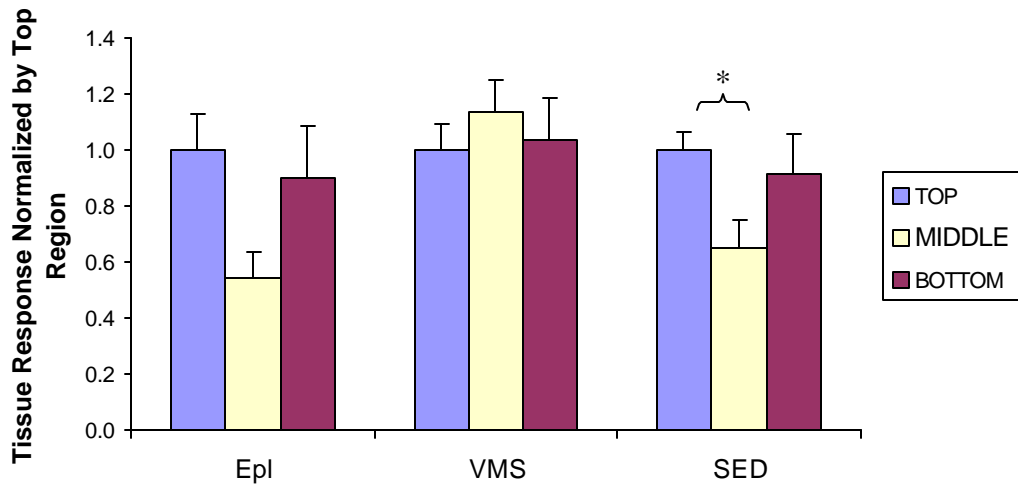


Figure 61. Longitudinal Variation in Stress/Strain Response in Interstitial Tissue

5.4 Discussion

The first specific aim of this study was to characterize and quantify new bone formation in response to *in vivo* mechanical loading of cell-seeded polymeric constructs in the novel subcutaneous loading system. Overall, loading resulted in a significant increase in mineralization present in constructs developed in the subcutaneous system as quantified by microCT. To our knowledge, this is the first demonstration of the ability of controlled *in vivo* mechanical stimulation to increase mineralized matrix production on a tissue-engineered bone construct.

Except for the no preculture samples, when each scaffold preparation group is considered individually loaded samples have more bone on average, but t-tests fail to detect significant differences. Consider the 8-week preculture group independently and although there is an increase of more than 300% in the mean value with loading, the large variance in the loaded group and unequal variance in the residuals between groups contribute to an inability to conclude a statistically significant difference due to loading, even though a trend ($p=0.08$) is observed. A post-hoc power analysis of the 8-week preculture data shows the power of the test to only be 0.345, indicating a 65% chance that the null hypothesis is accepted when in fact it is false (i.e. that significant differences remain undetected). Since taken as a whole, the effect of load is significant, individual comparisons of loading effect within groups would likely be significant given a larger sample size. The post-hoc power analysis of the 8-week preculture group suggests that a sample size of 26 in the loaded group and 8 in the nonloaded group would give a power

of .90 which would one to reasonably say there are no differences between groups if the general linear model fails to reject the null hypothesis.

Furthermore, the effect of load might be noticeably more dramatic in a tissue-engineered system more suited to mineralization. If the study were performed with a different polymer and seeded in a manner that delivers a large number of viable cells, the effect of loading may have been more detectable within each scaffold preparation group. The effect of loading was significant despite the suboptimal cell/scaffold conditions investigated within this work suggesting the robust impact that loading may have on the development of tissue-engineered constructs. In fact, the data showed less mineral in samples implanted for six weeks with no loading after an eight-week preculture period than scaffolds receiving just the eight-week preculture, while quite the opposite was true for their loaded counterparts. This observation suggests that in the absence of loading, simply implanting the construct in a vascularized *in vivo* environment was not sufficient to increase the mineralization formed *in vivo*.

Although the volume of bone formed in the loaded groups was statistically significant, it may not be clinically relevant. Due to the small volume of mineral present and the difficulties with obtaining full histological section of polymeric scaffolds, it is difficult to draw conclusions between groups based solely on histological observation. While it was not possible to see entire layers of newly secreted bone similar to that seen in the orthotopic study of rabbit trabecular allografts, given the subcutaneous location and scarcity of osteoprogenitors provided, the presence of mineralized nodules, cuboidal cells lining surfaces, and tissue that appears osteoid-like in nature are all noteworthy

observations. Furthermore, a general observation of greater mineralized nodules on one end of scaffolds within the 8-week preculture group spurred an analysis of longitudinal regions in the microCT data revealing that indeed there is significantly more mineral on one end of the scaffolds versus the other. Since a longitudinal analysis was unanticipated, the ends were unfortunately not labeled, making it unclear whether the end with more mineral is the end close to the piston or the base of the chamber, or perhaps even one end for some samples and the opposite end for others.

The second specific aim of this study was to investigate changes in load-induced bone formation due to different scaffold preparation techniques involving *in vitro* preculture. However, potential confounds may exist impairing the ability to compare results between groups with different amounts of preculture. Confocal analysis and quantification of DNA in the scaffolds seeded for *in vivo* implantation suggest that scaffolds seeded in the 1-week (Seeding #2) and no preculture (Seeding #3) groups received fewer cells and those cells present were less viable than scaffolds seeded for the 8-week preculture (Seeding #1) group. Additional samples from the 8-week preculture group and the no preculture group were continued on *in vitro* culture with osteogenic supplements. After an additional eight weeks in culture, virtually no mineral was present on the scaffolds from Seeding Group #3. There also may have been differences in the mechanical properties of scaffolds from different seeding groups. While measures were taken to ensure an equivalent exposure of all constructs to an aqueous environment, the presence of serum proteins, ions, and cells in the longterm preculture group may have accelerated the polymer degradation process, impacting the mechanical properties of the constructs.

Overall, the *in vivo* data reflect a general trend of increasing mineral with longer preculture time; however the seeding disparity means the *in vivo* results from the 8-week preculture group can not directly be compared to the 1-week and no preculture groups. Despite this complication, there was a significant effect of scaffold preparation group even when the 1-week and no preculture groups were excluded, indicating a significant difference between the cell-free constructs and those with 8-weeks of preculture. This difference may be attributable to the presence of cells and/or the preculture period. While it may be natural to assume that the effect of cells results from direct participation of the implanted MSCs in osteogenesis, it should also be acknowledged that the presence of the MSCs on the cell-seeded scaffold and even a subsequent immune response to those cells may also incite changes in neighboring host cells that contribute to osteogenesis. While preculture time may have a real effect on the mineralization of tissue-engineered polymeric constructs, no conclusion can be drawn based on this study.

The variation in seeding groups can most likely be attributed to the length of exposure to PBS experienced by the PLDL prior to seeding the scaffold. Because the stiffness of PLDL changes with exposure to an aqueous environment, all scaffolds regardless of length of preculture were exposed to an aqueous environment for an equivalent time. Scaffolds in Seeding Group #1 were hydrated approximately 48 hours prior to seeding while scaffolds in Seeding Group #2 and #3 spent seven and eight weeks respectively in PBS prior to seeding with cells. Although the saline was changed twice weekly to remove degradation byproducts, it is possible that accumulated degradation products from the polymer created an acidic environment that changed the surface chemistry of the scaffold affecting cell attachment and viability. While attachment and

viability were not addressed, Kohn has previously shown that changes in the pH of the culture environment can affect changes in cell function including collagen synthesis and alkaline phosphatase activity [190]. Standard cytotoxicity tests, adhesion strength tests, and evaluations of surface chemistry could be performed in the future to characterize these suspected changes due to degradation of the polymer.

The third aim of this work was to characterize the local stresses and strains experienced in both the polymer and the interstitial pore space to serve as guidelines for future applications of the subcutaneous loading technology. Most of the polymer experiences a largest principal strain about -0.24% with strains in the marrow being about five times greater. Stresses in the polymer concentrated around 1.6 MPa while stresses in the interstitial tissue were about two orders of magnitude smaller. In general, these strains appear very large, but there are no examples in the literature for adaptive tissue strains in a polymer. While Frost's Mechanostat Theory would classify apparent strains in this region to be in the pathologic overload zone [34], several researchers have recently pointed out that cells do not respond to apparent level strains, but in fact require much higher strains [191, 192]. Finally, a comparison between stresses and strains in the top, middle, and bottom regions of the finite element models failed to demonstrate trends that mirrored the patterns of bone formation. This does not necessarily mean that the demonstrated regional difference in mineralization in the loaded samples does not correlate with the tissue stresses or strains. An underlying assumption of the finite element models constructed was that friction between the walls of the chamber and the bone construct was negligible. This assumption may not be entirely valid since the samples fit closely in the chambers. If present, frictional forces and possibly even tissue

resistance from ingrowth at the chambers infiltration ports would result in a net force on the periphery of the construct in the opposite direction of the applied load, reducing both the stresses and strains in a graded manner such that the bottom region would be most affected by this possible discrepancy. Therefore larger differences in the stresses and strains between the top and bottom regions may actually exist but are not well represented in the current finite element model. However, without an accurate way to quantify the actual resistance due to friction and tissue ingrowth present in the system, these forces were assumed negligible.

CHAPTER 6

CONCLUSIONS AND RECOMMENDATIONS

6.1 Conclusions

Through carefully devised experimental implant systems, the effects of controlled *in vivo* mechanical loading on bone grafts and bone graft substitutes were investigated. The use of experimental models employing controlled boundary conditions provided the ability to predict the local mechanical environment at the trabecular level for trabecular allografts and a cell-seeded tissue-engineered bone replacement construct subjected to applied mechanical compression. The novel subcutaneous implant system designed to allow mechanical stimulation of three-dimensional constructs may also have potential as an *in vivo* bioreactor for the development of tissue-engineered bone constructs. Such constructs may benefit both from the vascular *in vivo* environment and the applied mechanical loading. This experimental model allows for a transition from purely academic studies of mechanical loading of bone toward a more clinically useful application; specifically, the enhanced development of tissue-engineered constructs for bone defect repair.

A subcutaneous loading system was designed with several objectives. The system allows for compression of a three-dimensional construct within a vascular environment while simultaneously controlling the necessary boundary conditions required to be able to easily model the local tissue stresses and strains imposed by the applied mechanical

loading. This device also represents a first generation approach for an *in vivo* bioreactor for the subcutaneous development of tissue-engineered constructs for subsequent transplantation to an orthotopic defect site. Such a bioreactor utilizing both the vascular *in vivo* environment and applied mechanical stimulation to developing tissue-engineered constructs may allow for the production of constructs with more mineralization in a more homogeneous arrangement. This system may make the development of larger, stronger scaffolds capable of meeting the functional needs of an orthotopic site more feasible than those counterparts developed using *in vitro* bioreactors where cell expansion and matrix secretion are often limited to the periphery due to diffusional limitations. By implanting them within chambers in the subcutaneous space, the constructs enjoy the advantage of an adequate blood supply offering nutrient and waste exchange from the interior of the construct. Because the subcutaneous environment is more compliant than bone, a loaded implant here has less risk of disrupting its own vascular supply.

A design was chosen that allows for simultaneous loading of multiple scaffolds in a single animal. Overall, size and shape were also considerations in the design in an effort to reduce any discomfort to the animal. The design implemented is a hybrid of custom and commercial parts that forms a novel system that may not be limited in scope to bone defect repair constructs, but could in fact be used as is or modified to investigate the benefits of *in vivo* mechanical preconditioning on a range of tissue-engineered constructs, including constructs for cartilage or tendon repair.

The first primary conclusion of this thesis work is that applied mechanical compression of a subcutaneously implanted cell-seeded polymeric construct for bone

replacement results in significantly more mineralized matrix production on the construct than their nonloaded counterparts. This research represents the first demonstration of increased bone formation with controlled *in vivo* mechanical loading of a cell-populated three-dimensional scaffold material. Given that an effect of loading was demonstrated on a scaffold that is probably not ideally conducive to bone formation and seeded with relatively low cell seeding efficiencies, it is likely that loading would produce even more dramatic effects on a better suited scaffold with an abundance of viable cells. This result has important implications for the use of mechanical stimulation in the development of tissue-engineered bone constructs and in designing tissue-engineered constructs to handle the mechanical challenges of a bone defect site.

Another primary conclusion of this work was the generation of tissue level stresses and strains associated with load-induced increases in mineralization on cell-seeded polymeric constructs. Largest principal strain in the polymer were distributed about a modal value of -0.24% with strains in the marrow being about five times greater. Stresses in the polymer were distributed about a modal value of 1.6 MPa while stresses in the interstitial tissue were about two orders of magnitude smaller. These data represent a useful reference for designing future experiments and serves as a potential target value to be achieved in the design of future tissue-engineered constructs.

A secondary conclusion drawn from this work is that significantly more mineral is deposited on polymeric scaffolds seeded with cells and precultured for 8-weeks prior to implantation than their cell-free counterparts. This information supports evidence from other researchers that the presence of cells enhances bone formation [127, 137,

138][193]. However, the 8-week preculture period may have also added to the effect shown.

Finally, a significant decrease in bone formation with loading on a rabbit trabecular allograft was shown. This result is at odds with published literature on the effects of mechanical loading on normal and repairing bone [7, 8, 100]. Similar experiments involving *in vivo* mechanical stimulation of canine *de novo* bone and the rat subcutaneous loading experiment detailed in Chapter 5 both resulted in increased bone formation with mechanical compression. Differences in a variety of conditions make direct comparisons between these studies difficult since the studies involved three very different materials (de novo bone, trabecular allograft, and polymer) each with different compositions and mechanical properties. Although each of the studies applied loads at 1 Hz for 1800 cycles per session, the force magnitudes, number of loading sessions, and timing of sessions varied. The canine study employed a 17 N load magnitude for eight weeks with daily loading. The rabbit study used a 22 N load for four weeks of daily loading and finally, the rat study used a 13 N load for two weeks with loading sessions occurring three times per week.

No clear explanation of these data is obvious, but the result most likely highlights the tightly controlled regulation of bone formation by mechanical signals and the importance of optimizing loading parameters such as force magnitude, frequency, and duration. Possible micromotion or other disruptions of vascularity may have been a factor but cannot be confirmed. Furthermore, traditional investigations of the mechanosensitivity of bone involve established mature bone or bone repair in a fracture

site. These studies may not directly translate to the response of osteoprogenitors and osteoblasts on the surface of natural or synthetic implant materials where these relationships may be altered by the non-native arrangement of cells and matrix. It is currently not known if cell communication via a functional canalicular network is required for mechanoresponsiveness. Additional studies are needed to determine the requisite loading parameters, level of cell and tissue maturity, and possibly other environmental variables to produce the ideal response to mechanical stimulation. These parameters may in fact depend heavily on the cell source and scaffold chosen for a particular bone repair construct.

6.2 Recommendations

Tissue engineering is a discipline still in its infancy. To generate tissue-engineered constructs capable of meeting the functional demands of the native tissue, novel means of preparing tissue-engineered constructs must be explored. The novel subcutaneous loading system presented here represents a first generation approach toward capitalizing on the advantages of the nourishing *in vivo* setting and the sensitivity of many cells and tissues to their local mechanical environment. Specifically, this work demonstrates the potential this approach has to significantly improve the development of tissue-engineered constructs for bone defect repair.

Being a first generation approach, there are several design improvements that could be made to the subcutaneous loading system. The current loading apparatus demands hydraulic access, requiring either resident transcutaneous tubing or repeated

incisions to access the chamber. The system should be redesigned to be fully implantable, not merely for convenience, but to reduce the risk of infection. Such a design feature would be absolutely necessary for a clinical variant of this system. Such designs might include radio controlled motors or piezoelectric materials or even the use of shape memory alloys. Regarding the current research model for rats, the system would benefit from further miniaturization to improve the animal's comfort. Reducing the length of the implant would be particularly helpful and could be accomplished by custom connectors and manifolds. The system is also currently limited to applying loads to moderately stiff scaffolds. This limitation exists primarily due to friction between the chamber wall and the o-ring on the loading platen. The necessary force to overcome friction and result in motion of the piston is sufficiently large to plastically deform many candidate scaffold materials. A glass/Teflon interface may permit easier movement of the piston, allowing a wider range of materials to be loaded in the system.

There are several studies using the novel subcutaneous loading system that could be performed in the future. First, effects of loading and preculture time should be investigated given comparable cell number and viability between groups. Given the change in mechanical stiffness that occurs in PLDL when exposed to an aqueous environment, samples from different preculture groups could be loaded to different levels resulting in an equivalent apparent strain in all samples. Furthermore, the study might be repeated on a scaffold material whose stiffness is impervious to time spent in an aqueous environment. In addition, parallel *in vitro* scaffolds should be cultured to determine if constructs prepared *in vivo* with loading have more mineral than scaffolds exclusively cultured *in vitro* for an equivalent time. Furthermore, studies using different loading

regimes investigating a variety of load magnitudes, frequencies, durations, and timing of the onset of loading may provide a better understanding of the optimal loading parameters.

A series of experiments should be performed to not only assess quantity of mineral formed, but also quality of mineralization and functional performance. Samples prepared *in vivo* with and without loading should be mechanically tested to determine if the increases in mineralization translate into improved mechanical properties. Additionally, FTIR analysis could be used to compare the composition and quality of mineral formed with and without loading. The quality of mineral formed *in vivo* could also be compared to that deposited *in vitro* on cell-seeded scaffolds. Finally, the most important question to be answered is how well do constructs developed in an *in vivo* bioreactor with loading actually repair an orthopedic defect. Current plans exist in our laboratory to perform such an evaluation using a rat segmental gap defect model.

In conclusion, the use of a subcutaneous *in vivo* bioreactor to develop tissue-engineered bone constructs must be put in perspective with current technology and anticipated developments in the field. While this technology represents a potentially better approach to developing tissue-engineered constructs for bone defect repair than simply seeding the scaffolds with cells and implanting them directly or even preculturing the scaffolds *in vitro* without loading, it is not an ideal solution to the development of functionally competent tissue-engineered constructs. In general, *in vitro* preparation of scaffolds is preferable due to significantly lower costs, as well as reduced risk and discomfort for the patient. Hopefully, new *in vitro* technologies employing perfusion and

mechanical loading, or perhaps some other technique, will address current diffusional limitations *in vitro*. The required repeat surgical procedures associated with this method may be warranted in certain situations, especially when a large homogeneous graft is required. Vacanti *et.al.* have previously successfully employed a multi-procedure technique to replace an avulsed human phalanx with tissue-engineered bone in a clinical setting [194]. The technique would probably be most successful when a vascular pedicle is incorporated into the subcutaneous developing construct to aid incorporation of a viable graft into the defect site. Given the wide range of possible defect sites, it is appropriate that tissue engineers have a wide array of techniques for scaffold preparation available so that the best possible replacement scaffold can be offered for a given situation.

APPENDIX A

MACHINE DRAWINGS

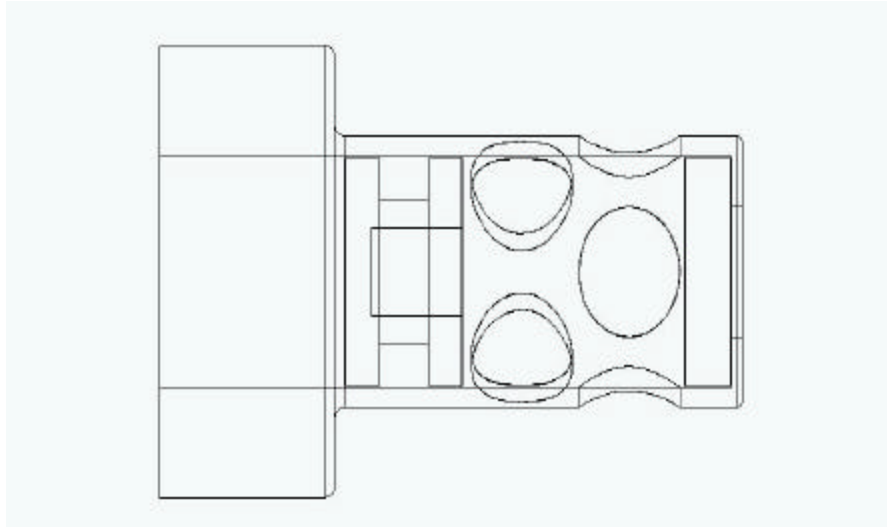


Figure 71. Compacted Assembly of Piston, Sample, and Base Platen in Rat Subcutaneous Chamber Illustrating How Sample Is Positioned Relative to Vascular Infiltration Ports

A.5 Platform Housing for Load Cell and Calibration Rat Subcutaneous Chamber

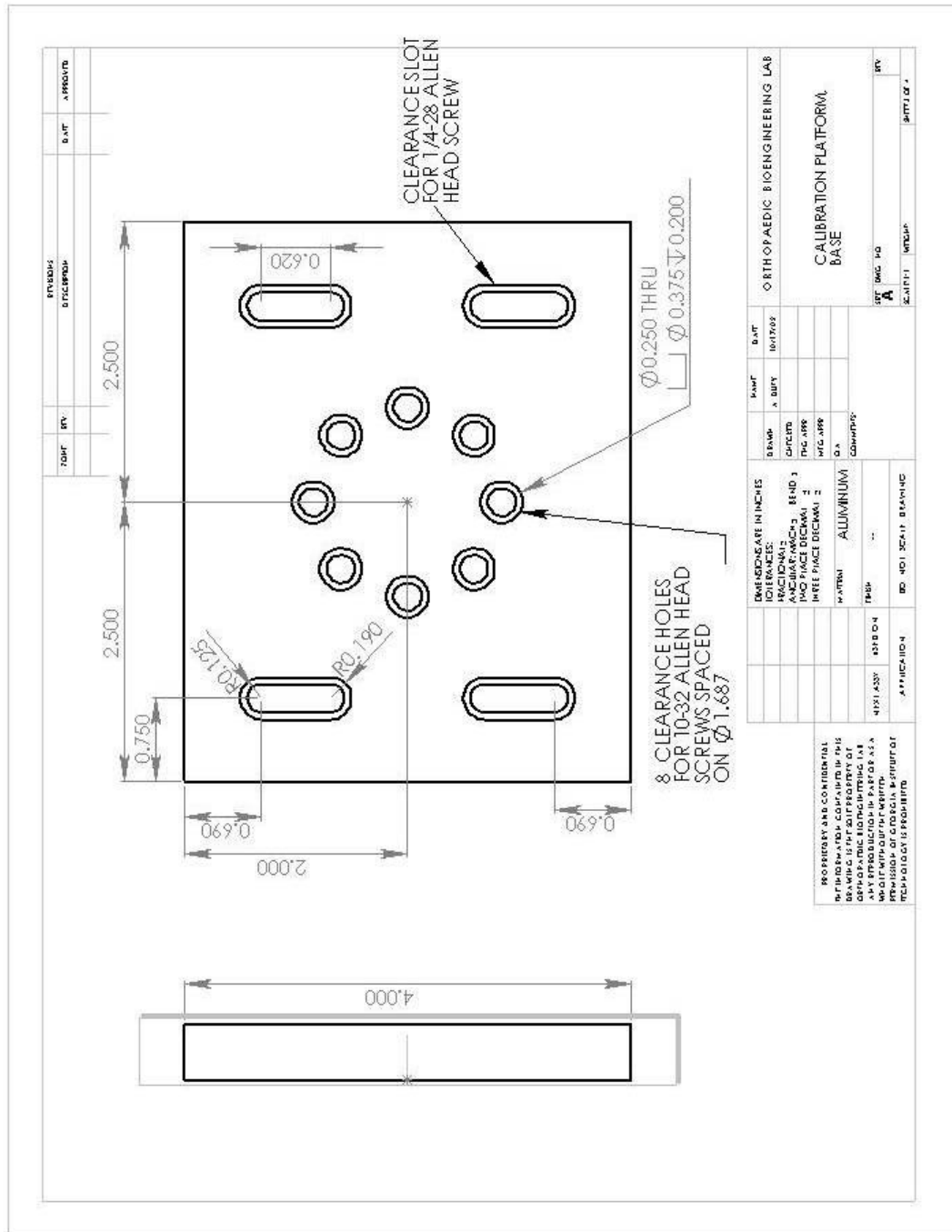


Figure 74. Machine Drawing of Platform Base with Circular Hole Pattern to Match Omega’s Ten-Pound Button Load Cell

A.6 Tabletop Platform to Hold Rat Subcutaneous Chamber During Compression Testing

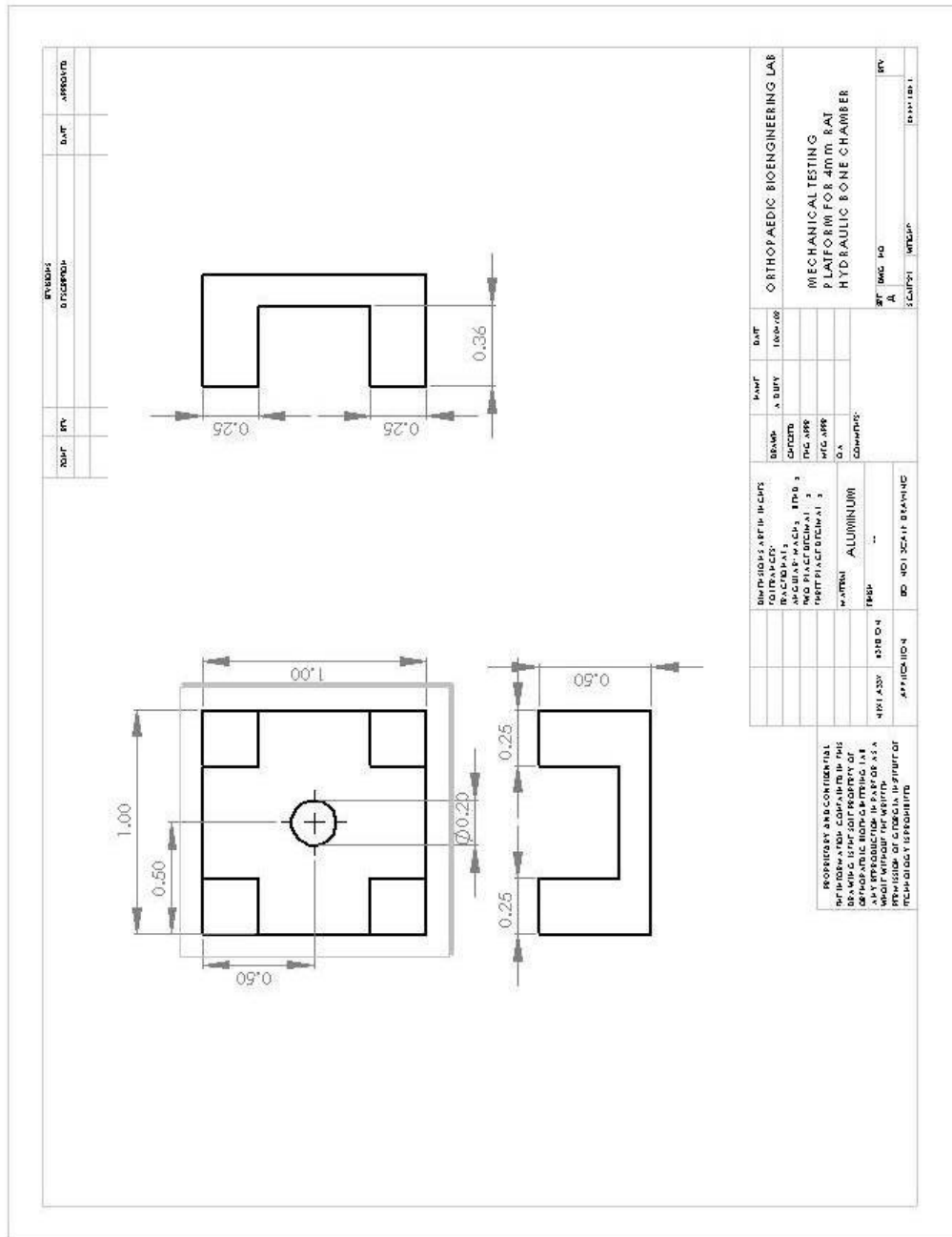


Figure 77. Machine Drawing of Tabletop Platform for Mechanical Testing within Rat Subcutaneous Chamber

APPENDIX B

SURGICAL PROCEDURES

B.1 Procedure to Implant Rabbit Hydraulic Bone Chamber

Anesthesia was induced in the animals using an injectible cocktail of ketamine (18mg/kg), xylazine (9mg/kg), and acepromazine (0.4mg/kg) and maintained by isoflurane gas (0.5-2.0%) administered by mask. The rabbit's legs were shaved and prepped for surgery using a clohexidine scrub, betadine, and isopropyl alcohol. The animal was placed on the surgery table and the incision sites were carefully draped with a laporotomy drape to create a sterile field. Two cc of Marcaine was injected subcutaneously over the incision site to provide additional local anesthetic. After five to ten minutes, a one inch incision through skin and muscle was made over the medial side of the distal femur as shown in Figure 78.



Figure 78. Incision Site for Rabbit Hydraulic Bone Chamber

After removing the periosteum on the surface of the condyle by scraping and cleaning with gauze, the cortex was scored with a 0.248" ID trephine using a trephine guide (Figure 79) to help grip the surface and keeping the trephine teeth flush against the

bone surface. The trephine was backed out and the cortex popped off using a pointed biopsy tool.



Figure 79. A Pneumatic Drill with Trephine and Trephine Guide was Used to Score the Bone Surface to Remove the Cortex

A 7mm hole was drilled to a depth of $\frac{1}{2}$ along a vector that angles slightly distal as the drill travels medial to lateral, making sure to avoid the intercondylar notch. Both the trephine and drill bit were powered by a hand-held pneumatic drill. The hole was then tapped with a M8x1.0 tap being extremely careful not to strip the bone threads. Chambers were assembled using ethylene propylene o-rings on the cap (dash 010) and on the piston (dash 060). Piston o-rings received a thin film of silicon lubricant and pistons were placed in the chambers using a positioning screw that fits in the top of each piston. An assembled chamber was threaded into the hole. If the implant was a loaded chamber, the barb was aligned to point superiorly and slightly anterior to the long axis of the bone.

The barb was also wrapped with Teflon tape to prevent tissue growth in the barb. The implanted chamber cap was wiped with betadine. Figure 80 shows how an implanted nonloaded chamber sits against the bone's surface. Vicryl sutures (size 2-0) joined the muscle margins underneath the barb and close to the chamber in addition to superficial sutures to join the skin margins over the chamber cap.

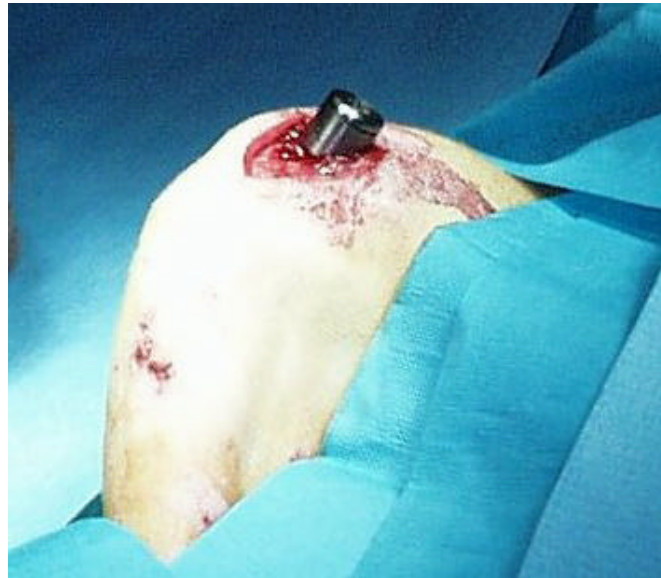


Figure 80. Position of Implanted Hydraulic Bone Chamber in Rabbits

B.2 Procedure for a Non-Terminal Biopsy of the Rabbit Hydraulic Bone Chamber

Anesthesia was induced in the animals using an injectible cocktail of ketamine (18mg/kg), xylazine (9mg/kg), and acepromazine (0.4mg/kg) and maintained by isoflurane gas (0.5-2.0%) administered by mask. The rabbit's legs were shaved and prepped for surgery using a chlorhexidine scrub, betadine, and isopropyl alcohol. The animal was placed on the surgery table and the incision sites were carefully draped with a laporotomy drape to create a sterile field. Two cc of Marcaine were injected subcutaneously over the incision site to provide additional local anesthetic. After five to ten minutes, a one inch incision through skin and muscle was made over the HBC. The cap was removed from the chamber as well as the piston in loaded chambers. The tissue inside the chamber was extracted using a thin-walled device called a kerchunker shown in Figure 81. Once the tissue is inside the biopsy device, a thin platen resting inside the device was used to push out the tissue when a screw was inserted in the top of the device. Frozen allografts were placed in the chambers before the pistons and caps were replaced. The incision site was closed with 2-0 vicryl suture.



Figure 81. Thin-Walled Extraction Device

B.3 Procedure to Implant Subcutaneous Loading Tubing in Rabbits

Polyurethane tubing from Cole-Parmer (Part #P-95625-00; working pressure = 100 psi, burst pressure = 200-300 psi) with an inner diameter of 1/16" and an outer diameter of 1/8" was used. Twenty inch lengths of tubing were prepared by bonding a 3/4 x 3/2" strip of acrylic art felt (Hancock Fabrics) 3 inches from one end of the tubing using a long-term implant grade 2-part silicone adhesive (NuSil MED1-4213) as shown in Figure 82. The 3/4 edge was bonded along the length and allowed to cure ten minutes at 70C, then the length of the felt strip was wrapped around the tubing and bonded with more silicone adhesive and cured for an additional ten minutes at 70C. The tubing was then gas sterilized.

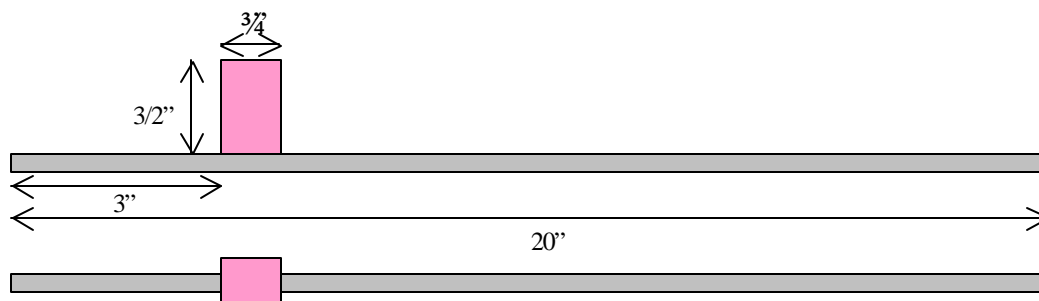


Figure 82. Bonded Felt Cuff on Polyurethane Tubing

Anesthesia was induced in the animals using an injectible cocktail of ketamine (18mg/kg), xylazine (9mg/kg), and acepromazine (0.4mg/kg) and maintained by isoflurane gas (0.5-2.0%) administered by mask. An intraoperative dose of an antibiotic (Baytril, 7 mg/kg) was given at this time. The rabbit's legs were shaved and prepped for surgery three times using a chlorhexidine scrub brush, betadine, and isopropyl alcohol

working from the incision site outward. In addition, the distal half of the abdomen was shaved and cleansed as well as the butt on the side with the loaded chamber. A 4" circle was shaved and prepped between the rabbit's shoulder blades. The animal was placed on his back on the surgery table on top of sterile towels leaving plenty of room on the table near the head and all shaved areas were sprayed with betadine. A non-sterile assistant held up the rabbit's legs while a sterile surgeon wrapped the feet in sterile drape towels. With the rabbit's legs still held up, a sterile drape was placed flat beneath the rabbit and a second drape towel was used to "diaper" the rabbit to keep fur out of the sterile field. Additional drapes were used to cover the middle, top, and sides of the rabbit. Finally, a large laporotomy drape was placed over the rabbit exposing only the rabbit's legs. The incision sites were carefully draped with a laporotomy drape to create a sterile field.

Two cc of Marcaine was injected subcutaneously over the incision site to provide additional local anesthetic. After five to ten minutes, a one inch incision through skin and muscle was made over the medial side of the distal femur. Using the animal as a visual reference, the tubing length was trimmed from the end opposite the felt cuff. This end of the tubing was then placed over the loaded chamber barb using a serrated hemostat that had a hole drilled through the jaw interface to fit the tube diameter to grip the tubing tightly. With the loaded chamber cap loosened, a 20 cc syringe with a 16 gage needle was used to fill the tubing and upper plenum of the chamber with sterile 0.7% saline. Once all bubbles were flushed from the tubing and chamber, the cap was tightened. The opposite end of the tubing was melted closed with the heat from a butane-powered soldering iron to keep the lumen of the tubing clean during subsequent steps. With the standard incision at the medial side of the distal femur open, a second incision was made

on the lateral side of the leg on the proximal end of the femur about two inches proximal to the chamber. A stainless steel sloped nozzle was placed over the felt cuff of the tubing to facilitate smoother movement through the subcutaneous tissue as shown in Figure 83. From the proximal incision, a hemostat was tunneled subcutaneously to the distal incision and used to pull the tubing from the distal to the proximal incision wrapping the tubing around the rabbit's leg. As the tubing was pulled beneath the skin, it was wiped with betadine soaked gauze. The distal incision over the chamber was closed with vicryl suture.

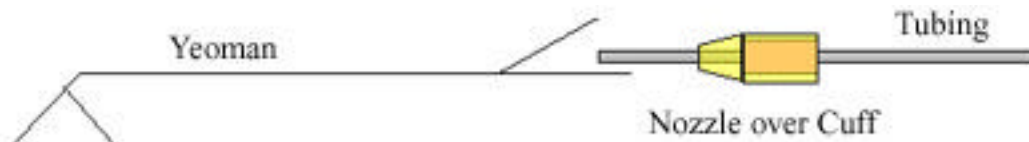


Figure 83. Diagram of Tools Used to Route Tubing Subcutaneously in Rabbits

At this point, the rabbit was carefully turned on its side such that the leg with the loaded chamber is on top. The mask was checked to make sure the animal was still receiving isoflurane and the area between the shoulder blades was prepped with a surgical scrub brush again. A hole was cut in the laparotomy drape to expose the area between the shoulder blades. A third incision about $\frac{1}{2}$ long was made 1.5" caudal to the shoulder blades along the midline of the back. A long yeoman was routed subcutaneously from the incision on the back to the proximal leg incision. The tubing was grasped in the yeoman's teeth and then pulled through the subcutaneous tunnel being careful to avoid kinks in the tubing. Again, the tubing was wiped with betadine-soaked gauze as it was pulled beneath the skin. The proximal leg incision was closed with vicryl

suture and silk suture was used to anchor the felt cuff to the subcutaneous tissue at the incision on the back. Finally, a sharp 13 g x 3.5” stainless steel hypodermic needle was used to tunnel about 1” proximally from the back incision and puncture the skin. A thin stainless steel surgical guide wire was routed through the lumen of the needle and used to pull the tubing from the back incision through the tiny puncture wound between the shoulder blades. The incision on the back was closed with vicryl suture. No sutures were applied at the actual exit site to eliminate the potential of the suture to wick infection inside.

During recovery, a polypropylene luer connector with a 1/16” hose barb (Cole-Parmer #A-06359-25) was inserted in the exposed tubing end and capped with a polypropylene male luer-lok connector (Cole-Parmer #A-30504-22). After the animal had obtained sternal recumbency, an Elizabethan collar was placed on each rabbit to protect the tubing from bites and scratches. A sterile transparent polyurethane wound covering from Johnson & Johnson was applied over the tubing exit site. The dressing was checked daily and changed as needed. One person held the rabbit still by keeping one hand on the rabbit’s rump and one hand over the rabbit’s eyes. Another person isolated the exit area with sterile drape towels and removed the old dressing. Wearing sterile gloves, this person then cleansed the area with Betadine or chlorhexidine and sterile gauze working outward in a circular fashion. A new dressing was applied over the exit site leaving the luer connectors exposed. Rabbits in Group #3 of the frozen allograft study, also received daily application of a silver-impregnated glass powder (Giltech Limited, Scotland) for three consecutive days until a hard shell formed around the tubing exit site.

B.4 Procedure for Implantation of Subcutaneous Rat Loading Device

B.4.1 Surgical Materials

Hardware

Autoclave:

- 4mm rat chambers (custom)
- 4mm pistons (custom)
- 4mm platens (custom)
- Beswick manifolds (#MX-1010-303)
- Nipples, 10-32 (Beswick # MN-1010-303)
- Plugs, 10-32 (Beswick # MSP-1000-303)
- Adjustable elbow barbs, 10-32 to 1/16" (Beswick # SMLS-1012-303)
- 1-72 piston screws (McMaster #92196A068)
- O-ring lubricant (Chemplex 710 Silicone compound from McMaster-Carr)
- 5/32" dowel pins (McMaster #90145A488)
- Wrench
- Screwdriver (separate packet)
- Tubing holder or hemastat
- Forceps
- 1/16" plastic barbs/FL
- 10cc syringe
- 16 g needle
- saline bag

Gamma-Irradiation:

- (.085x.036") BN o-rings (Apple Rubber custom order)

Ethylene Oxide Sterilization:

- 5" lengths of PUR tubing (1/8" OD, 1/6" ID) (CP # 95625-00)

PLDL samples

Sterile petri dishes, 100mm and 35mm

Sterile alpha-MEM + 1% ab/am (no serum), 2 x 250ml

10ml pipettes

pipet aid

Surgery Trays

- Adson-Brown forceps
- Russian forceps
- Needle-nose forceps
- 2 blade holders, #7
- Paper Scissors
- Skin scissors
- 13g needles
- SST wire
- Needle holder
- Hemastats (2)
- Wound clipper
- Clip remover
- Wound Clips

Towel Trays

- Blue surgical towels
- 4x4 gauze
- 2x2 gauze

Other disposables

- silk 4-0 suture
- vicryl 3-0 suture
- 4x4 gauze, non-sterile
- 2x2 gauze, non-sterile
- #10 blades (surgery days)
- #11 blades (loading days)
- IOBAN
- drape towels, 2 per pack
- 500ml bottles of sterile water
- saline for injection, 250ml bottles
- half drapes
- 10cc syringes
- 16 g needles
- gloves, sterile
- wound clips
- Glass bead sterilizer
- Sterile towels, cloth
- Sterile bowl
- Gauze

B.4.2 Assembly Instructions for Subcutaneous Rat Loading Device

Loaded Chambers

1. Insert the longer end of the 10-32 nipple into a rounded port of the 4-way manifold. Repeat on the other end.
2. Add an elbow barb to one of the remaining ports, making sure that the barb lies in plane with the manifold.
3. Add a cap to the remaining port.
4. Insert a platen into the base of a chamber.
5. Insert the appropriate PLDL scaffold.
6. Put an o-ring on a piston. Add a small amount of silicone lubricant and wipe off excess on gauze. Immediately discard gauze. Try not to get lubricant on your gloves or other instruments.
7. Using the 1-72 screw, insert the piston into chamber on top of PLDL. Remove 1-72 screw.
8. Use a dowel pin to confirm that piston sits firmly against the PLDL.
9. Attach the chamber to the appropriate end of the manifold. PLDL scaffolds designated top, go on the side of the manifold with the barb.
10. Repeat steps 4-9 for the second chamber.
11. Attach a piece of tubing to the barb. Attach a plastic barb/luer to the other end of the tubing.
12. Confirm that all joints of the assembly are tight EXCEPT the cap.
13. Using a 10cc syringe filled with saline, fill the implant. While fluid is exiting from the cap, tighten it down with a screwdriver.
14. Apply a moderate amount of pressure by hand to the syringe and watch the implant carefully for leaks. If leaks occur, reassemble using different chambers and/or pistons.
15. Store implant in 100mm petri dish with alpha-MEM until surgeon is ready.
16. Surgeon will cut the tubing to length and hand back to you to heat seal. Have a non-sterile assistant hold the heat sealer in front of you. When plastic gets gummy, use a hemostat to clamp the end shut and hold until cooled. Confirm seal.
17. Return implant to surgeon.

Non-loaded chambers

1. Insert the longer end of the 10-32 nipple into a rounded port of the 4-way manifold.
2. Repeat on the other end
3. Add caps to the remaining ports.
4. Insert a platen into the base of a chamber.
5. Insert the appropriate PLDL scaffold.
6. Insert a spacer. If out of spacers, use pistons with no o-ring.
7. Use a dowel pin to confirm that PLDL and spacer sit firmly against base.
8. Attach the chamber to the appropriate end of the manifold/nipple assembly. PLDL scaffolds designated top, go on the side of the manifold with the etched mark 'X'.
9. Repeat for second chamber.
10. Confirm that all joints of the assembly are tight.
11. Store implant in 100mm petri dish with alpha-MEM until surgeon is ready.

B.4.3 Surgical Procedure for Implanting Subcutaneous Rat Loading Device

Anesthesia was induced using 4% isoflurane and maintained with 1-2% isoflurane via mask. The rat's back was shaved and scrubbed. The animal was transferred to a surgical table and the back was draped and covered in Ioban, a sterile antimicrobial film. Under sterile conditions, a 1.5" incision was made just to the right of the midline and beginning about 1.5" caudal to the center of scapulae. By blunt dissection, a small pouch was created in the subcutaneous space to receive the implant. The free end of the attached polyurethane tubing (Cole-Parmer # 95625-00) was heat-sealed using a hemostat heated in the glass-bead sterilizer. A stainless steel 13g x 3.5" hypodermic needle was used to create a route for the tubing running from just caudal and proximal to the cephalic end of the incision to the center of the scapulae. Stainless steel surgical wire was used to keep the tubing path open. The implant was placed in the pouch inserting the tubing along the path created by the needle. Care was taken to ensure the implant lies flat on its side with the elbow barb close to the midline and pointed toward the head. If necessary, the pouch was enlarged just enough to pull the skin margins together over the implant. Silk suture (size 3-0) were used to pull the underlying issue around 1) the port holes on both chambers, 2) both nipple connectors, and 3) the elbow barb as shown in Figure 84. Then 3-0 vicryl suture was used to close the skin margins over the entire implant. The closure was reinforced with metal wound clips. NewSkin with Metronidazole (100mg/ml) was applied topically over wound clips to act as an additional sealant and prevent the animal from biting the incision. Wound clips were removed after 10-14 days. Surgical instruments were rinsed in sterile water and placed in glass bead sterilizer between animals. Freshly autoclaved instruments were used after every 6-7 rats.

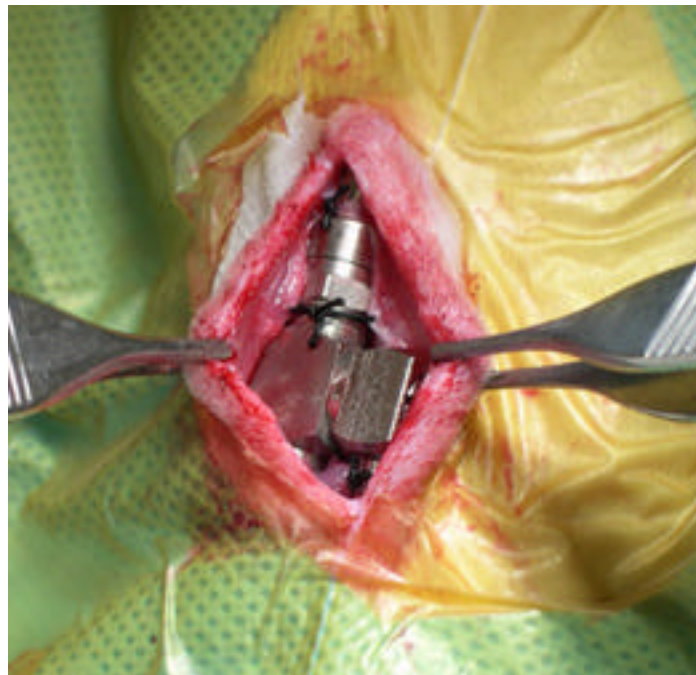


Figure 84. Placement of Silk Sutures to Anchor Rat Subcutaneous Loading Device

B.5 Procedure for Exposing Implanted Tubing for Loading Sessions in Rats

On the first day of loading, anesthesia was induced using 4% isoflurane and maintained with 1-2% isoflurane via mask. If necessary, the back was shaved. The area was then cleansed with chlorhexidine and isopropyl alcohol. Originally, a local anesthetic (lidocaine) was also applied to the skin just over the end of the tubing, but was eventually abandoned since four animals failed to recover from anesthesia. The lidocaine may have caused the anesthesia to be too deep. Furthermore, the additional local anesthetic did not seem to be necessary. A small incision about 3/4" was made approximately between the shoulder blades over the end of the implanted tubing using a #11 blade. The end of the tubing was pulled through the incision and a sterile polypropylene luer connector with a 1/16" hose barb (Cole-Parmer #A-06359-25) was inserted in the exposed tubing end. The tubing was wrapped with sterile gauze to cover the open incision on the back. Figure 85-B shows the location of the incision and the tubing just after it has been pulled through the incision, while Figure 85-C shows the addition of the connector and protective gauze wrap.



Figure 85. Steps to Expose Tubing for Rat Loading Procedure; A) Anesthesia Induction, B) Incision and Exposure of Tubing, C) Addition of Connector, and D) Re-implantation of Tubing and Wound Closure

The rat was then removed from the isoflurane supply and restrained in a thin plastic cone restrainer once the rat was sternally recumbent. The rat was placed in an open-topped plastic box with a dark cloth over the head to help keep the animal calm. My experience was that the animal would remain very calm and relaxed in the restrainer if the cloth covers the eyes, even if the animal is not sedated. A hole was clipped in the restrainer to allow the tubing to exit the restrainer.

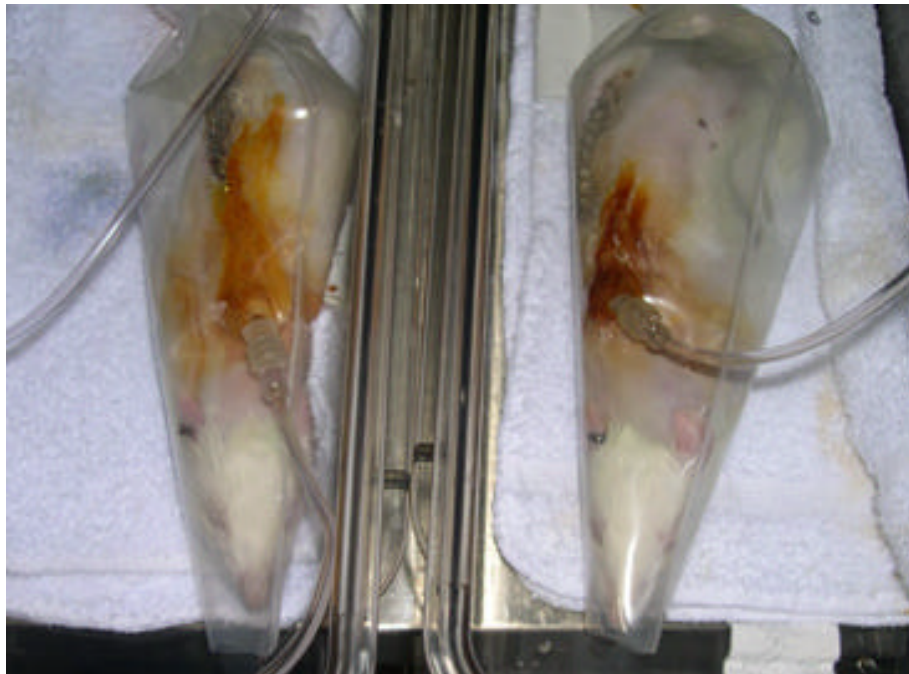


Figure 86. Thin Plastic Cone Restrainers Used During Rat Loading Procedures

One ml tuberculin syringes were filled with sterile saline and a 5"-length of PTFE microbore (0.012x0.030") tubing (Cole-Parmer #EW-06417-11) was slipped over its 27g needle. The microbore tubing was threaded into the implanted tubing until it reached the implanted hardware. Applying pressure to the syringe, the tubing was slowly backfilled with saline to ensure that all air bubbles were removed from the implanted tubing. The

implanted tubing was then attached to the external solenoid-driven loading system (Figure 34 and Figure 35). Care was again taken to make sure no bubbles were introduced to the animal's tubing or the system tubing. The saline in the system was then pressurized cyclically between 20-200 psi in a sinusoidal pattern at 1 Hz for 30 minutes. The tubing was then disconnected from the system and the animal removed from the thin plastic cone restrainer and anesthesia induced again at 4% isoflurane. The tubing and incision area were cleansed with diluted betadine solutions (10% and 50%). A sterile polypropylene male luer-lok connector (Cole-Parmer #A-30504-22) capped the luer connector on the tubing. The tubing including connectors was then pushed back under the animal's skin and the wound closed with wound clips (Figure 85-D).

The procedure was repeated for subsequent loading sessions, opening the same site. A fresh incision was not necessary since the wound did not have sufficient time to heal between loading sessions. Loading occurred roughly every other day for three times per week for 2 weeks. After the last loading session, the tubing was clipped short removing the connector and cap and heat sealed with a hemostat heated in a glass bead sterilizer. The site was then thoroughly washed with betadine and closed permanently with wound clips. Clips were removed in 10-14 days after the site healed completely. All instruments used in this procedure were autoclaved and were repeatedly resterilized with a glass bead sterilizer throughout the procedure even though a fully sterile environment was not necessarily maintained due to the nature of the loading procedure.

APPENDIX C

LOADING PROCEDURE FOR RABBIT HYDRAULIC BONE CHAMBER STUDIES

C.1 Standard Loading Procedure for Rabbit HBCs

1. Take off cover and set IV stand w/ bag on table.
2. Turn on top MOS and oscilloscope. Turn on voltmeter while pressing its blue button to prevent automatic timed turn-off.
3. Check that signal generator is set to 1 Hz.
4. Turn manifold valve to 9 o'clock position. Check cylinder for bubbles. Move solenoid back and forth several times. Be sure that you end with the solenoid pushed *almost* all the way in, but not with the black rubber seal sticking.
5. Turn manifold valve to 12 o'clock and check that all loading lines are free of bubbles. Especially check near the connectors.
6. Turn chamber valve to 3 o'clock. Open chamber cap and let all bubbles escape from the loading line and its connections.
7. Using 4-40 screw, lift the piston off the brass rod connected to load cell and then press "Rel" on the voltmeter. Then gently push piston down until the piston just barely contacts the brass rod, but is enough for the load cell to be responsive to touch.
8. With water brimming the top of the chamber, replace the cap being extremely careful not to change the position of the chamber relative to the plate of the test stand (i.e. make sure that the chamber doesn't get screwed in any more or any less to avoid an artificial preload; use the angle of the barb as your check). Make sure voltmeter still reads zero. Close the chamber valve by turning to 6 o'clock.
9. Open manifold cap and allow bubbles to escape from the manifold. Press "/tare" on the pressure meter. Replace the manifold cap. Turn the manifold valve to 3 o'clock.
10. Turn on bottom MOS. Note: Solenoid then begins its actuation. It will be a static pressure if the button labelled "gate 1S, range 200K" is pushed and the pressure will be dynamic if the button labelled " gate 10S, range 2" is pushed in on the top row of buttons on the frequency generator. Turning the DC offset and amplitude knobs makes system pressure adjustments. The knobs are 10 turn potentiometers so that you have better control of the system's response.
11. Check system for any leaks or unusual sounds.
12. Adjust system to about the anticipated load range (0-5 lb)). Cycle for 20 minutes. Record operating conditions.
13. Turn chamber valve to 6 o'clock. Turn off system and reset solenoid to full volume.
14. Turn dynamic range down to ~ 10-20 psi. You don't want it to be zero, because you may lose pressure when you turn system on to the rabbit due to any air bubbles trapped in his line.
15. Take rabbit out of cage and put him in a basket. Check for bubbles in his tubing. If you see any, run the microbore tubing that fits a 27 gage needle through the luer connector into the rabbit's tubing. Be sure that there is pressure on the needle's

- syringe at all times to force water out of the microtubing. Feed the microtubing all the way to the rabbit's chamber. You will feel resistance. Then slowly back out the microtubing allowing the forced water to fill the space taken by any bubbles. You will see bubbles coming out of the rabbit's tubing. Usually, this only has to be done the first day of loading, but always check the rabbit's exposed tubing for bubbles every day.
16. Connect the rabbit's tubing to the system's loading line. Be sure to fill both connectors with saline first to prevent bubbles.
 17. Turn each of the valves to the rabbits to 12 o'clock one at a time while watching the oscilloscope to make sure the pressure doesn't drastically drop. Turn the valve to the load cell to 3 o'clock. Adjust the pressure up to the desired load range. You can use the scope's cursors to easily define the load range for you visually. Use the min/max button on the voltmeter to check the range of the actual applied load. Note the time.
 18. Cycle for 30 minutes. Note any abnormalities and make small adjustments to keep the pressure within the defined range. Be sure to fill out loading record.
 19. At the end of 30 minutes, reduce the pressure to ~ 20 psi then switch to a static pressure and zero the load. Do not go negative, but you may have slight positive pressure. Sometimes, it simply isn't possible to exactly zero the system. If tweaking the knobs makes no difference on the oscilloscope, simply stop there. Then, turn the chamber valve to 6 o'clock. Switch system back to a dynamic 10-20 psi.
 20. Disconnect the rabbit from the system and recap his line.
 21. Repeat steps #15-20 for other rabbits.
 22. To shut down, turn off bottom MOS, then turn off scope and finally the top MOS.

C.2 Dealing with Anomalies Experienced During Loading Rabbit HBCs

A rabbit turns around and bites the tubing.

The system will immediately stop actuation because the solenoid will push the plunger to the emergency light stops in an effort to maintain pressure.

1. You should immediately close all valves to loading lines and the load cell. Flip the bottom MOS off. Note the time.
2. Remove the damaged load line and replace it with a new one from the cart.
3. Turn manifold valve to 9 o'clock position. Check cylinder for bubbles. Move solenoid back and forth several times. Be sure that you end with the solenoid pushed *almost* all the way in, but not with the black rubber seal sticking.
4. Turn manifold valve to 12 o'clock and turn the new line valve to 3 o'clock and allow the new line to fill with saline. Close line valve to 6 o'clock. Open manifold cap and allow bubbles to escape from the manifold. Press “tare” on the pressure meter. Replace the manifold cap. Turn the manifold valve to 3 o'clock
5. For extra measure turn manifold valve back to 9 o'clock and back again to 3 o'clock to release any residual pressure to the saline bag.
6. Reconnect line to offending rabbit.
7. Flip bottom MOS back on. Repeat step #17. Continue loading for the remaining time.

System gradually bleeds out and begins “knocking” light stops.

1. This usually occurs about half way through the 30 min session when using high loads (such as 5 lb) with multiple rabbits. Because the system is working at its upper limit, even tiny water losses (especially around the seal on the cylinder) may cause the system to try to push past the light stops.
2. You may hear on occasional knock, but wait til knocking is nearly every cycle. Then turn pressure down to below 20 psi and turn off system. You need to refill cylinder. You may follow instructions outlined for a damaged line, just omit changing and refilling of the damaged line.

Internal leak in rabbit.

1. This may seem similar to either of the two previous anomalies, but cannot be corrected by simply resetting the system. If there is a drastic pressure drop and no evidence of damaged lines, this may be the case.
2. First try refilling cylinder as for A&C. Then when you turn on system, watch the system response to an individual rabbit. You need to determine which one is leaking so that you may exclude him from further loading and continue with the

others. If you can't tell the offender and the same thing happens again right away, stop and disconnect rabbits and run microbore tubing to eliminate any bubbles from lines. Attach a saline-filled syringe with a luer lock to the end of rabbit's tubing and try gently compressing the fluid. It should resist and plunger should bounce back when you stop. If you can actually force fluid out of the syringe with no recovery, that rabbit has an internal leak and can receive no more loading. He should go on antibiotics immediately and receive surgery ASAP to correct the leaking tubing. If after removing bubbles, the system works, then continue loading there may just have been too much compliance in the rabbit's lines if bubbles were present.

APPENDIX D

RT-PCR PROTOCOLS

D.1 Protocol Worksheet for Reverse Transcriptase Reaction to Convert RNA into cDNA

Materials Needed

1. SuperScript II Rnase H Reverse Transcriptase Kit from Invitrogen
(Cat. No. 18064-014, store at -20)
2. Oligo DT (12-18) (500ug/ul) from Invitrogen (Cat. No. 18418-015; store at -20)
3. 10mM dNTP mix (Promega C1145)
4. Purified sample RNA
5. Rnase Zap
6. Rnase free water
7. 1.5 ml microcentrifuge tubes, Rnase-free, Dnase-free, sterile
8. PipetteMan
9. 100 ul and 1000ul filtered pipette tips
10. vortexer
11. microfuge
12. SpeedVac (Savant DNA 120)
13. Water Bath set to 42C
14. Heat block set to 70C
15. ice bucket

Procedure:

1. Treat all surfaces with Rnase Zap
2. Thaw at least 4ug of RNA for each sample. Keep on ice when possible.
3. Aliquot 4 ug RNA into microcentrifuge tubes. If the volume of RNA is less than 11 ul, bring volume up to 11 ul with DEPC H₂O. If the volume of RNA is greater than 11 ul, dry the RNA down to 11 ul in the SpeedVac. Tip: If volume is very large, divide a given sample's volume into multiple tubes to decrease the amount of time the RNA spends at room temperature.
4. Thaw Oligo DT (12-18), dNTPs, SuperScript II enzyme, the accompanying 5x First Strand Buffer, and .1M DTT. Vortex and brief spin.
5. Add 1 ul Oligo to each and place in heat block for 10 min.
6. Immediately move RNA to ice. Centrifuge to collect contents
7. Make Master Mix. Combine in the following order:
 - a. 4ul/ reaction x __reaction = ___ ul 5x buffer
 - b. 2ul/ reaction x __ reaction = ___ul DTT
 - c. 1ul/ reaction x __ reaction = ___ul dNTPsVortex and spin.
8. Add 7 ul Master mix to each tube. Vortex and brief spin.
9. Place samples in water bath for 2 min.

10. Add 1 ul RT enzyme to each tube. Vortex and brief spin. (*Was a fresh aliquot used? _____*)
11. Place samples in water bath for 50 min.
12. Transfer tubes to heat block for 15 min. Brief chill and centrifuge to collect contents.
13. (Optional) Add 80 ul DEPC H₂O to each tube to dilute to workable volume (i.e. use 5 ul or 1/20 reaction volume per PCR reaction). Vortex and brief spin. Separate into two tubes to be safe. Store at -20C.

D.2 Protocol Worksheet for Radioactive PCR

Materials Needed

1. Qiagen's HotStarTaq Kit (Cat. # 203203 for 250 units or #203205 for 1000 units; store -20°C); Kit includes 10x PCR buffer, 5x Q-soln (typically do not use), 25mM MgCl_2 , and HotStarTaq DNA polymerase at 5 units/ μl .
2. 10mM dNTP mix (Promega C1145)
3. Primers, both forward and reverse at 10 pmol/ μl (Primers obtained as lyophilate from IDT and are resuspended to 100 pmol/ μl with successive 1:10 dilutions later)
4. HOT P-32 (Amersham #PB10205-250uCi or # PB10205-500uCi; 10mCi/ml; 3000 Ci/mmol; store at -20°C) {If P-32 is two weeks old, it may be necessary to double P-32 used and adjust water accordingly.}
5. 6x loading buffer (xylene cyanol and bromophenol blue in glycerol base)
6. Rnase free water
7. 1.5 ml microcentrifuge tubes
8. PipetteMan
9. 100 μl and 1000 μl filtered pipette tips
10. PCR plate base and optional retainer
11. PCR tubes
12. vortexer
13. microfuge
14. ice bucket

Procedure:

1. PCR set up should be done on the DNA bench behind the radioactive shield. Use tips, pipettors, water, etc. that are restricted to that area. Turn on dosimeter. Check that waste containers are available.
2. Thaw PCR Buffer, MgCl_2 (if you need more than 1.5 mM Mg in the reaction), Taq, primers for each gene target, dNTPs, and P-32.
3. Prepare Plate Layout Table 12. Always include an open water (NIL) control to check for aerosol contamination and a closed water control to check for Master Mix contamination. You may also include RNA controls to check for genomic DNA contamination and an "RT" control to check for contamination in the RT Master Mix. Allow for duplicate reaction tubes for experimental samples. Place sufficient numbers of PCR tubes in the base stand according to the layout you specify below.

Table 12. Working Plate Layout (12x8 Grid)

PLATE LAYOUT

4. If cDNA was not diluted 5x at end of RT, go ahead and add 80 ul water to the 20 ul RT reaction volume now. Place 5 ul (1/20 reaction volume) cDNA into each of the appropriate tubes.
5. Place 5 ul water in the NIL controls.
6. Place RNA in control tubes based on following info.

What is the mass of RNA used in the RT reaction? _____

What is the mass of RNA per PCR control? (above/20)

Assuming 4 ug of cDNA were used in the RT reaction, place 0.2 ug (1/20 of RNA used in RT) RNA into each of the RNA controls. Work out volumes needed below Table 13. Add sufficient water to bring the RNA up to 5 ul.

Table 13. Worksheet for Adjusting Sample Volume for PCR Reaction

A	B	C	D	E
Sample #	Mass RNA per control)	Concentration (from OD readings)	Volume RNA; (B/C)	Water to be Added; (5-D)

7. Cover PCR plate and set aside momentarily.
8. Determine total number of reactions. Add a few more for mistakes. Prepare a 1:10 dilution of P-32 for this number of samples: Vol P-32: _____; Volume water: _____
9. Prepare Master Mixes as detailed in Table 14. There will be a separate Master Mix for each primer. Note: hGAP works best at 1.5 mM MgCl₂, rabCOLI works best at 2.0 mM, and OPN works best at 3.0mM. Volumes are in ul. Place check marks beside each ingredient from which you used a fresh aliquot.

Table 14. Worksheet for Preparing PCR Master Mixes

TARGET				
# samples per master mix				
Ingredient	1.5mM	2.0mM	2.5mM	3.0mM
Buffer	5 x # =	5 x # =	5 x # =	5 x # =
MgCl₂	0 x # =	1 x # =	2 x # =	3 x # =
DNTPs	1 x # =	1 x # =	1 x # =	1 x # =
Fwd primer	2 x # =	2 x # =	2 x # =	2 x # =
Rev primer	2 x # =	2 x # =	2 x # =	2 x # =
Taq	0.5 x # =	0.5 x # =	0.5 x # =	0.5 x # =
Water	33.5 x # =	32.5 x # =	31.5 x # =	30.5 x # =
P-32 (1:10 dilution)	1 x # =	1 x # =	1 x # =	1 x # =
TOTAL	45 x # =	45 x # =	45 x # =	45 x # =

10. Add 45 ul of the appropriate master mix to each sample of that gene target. Pipette up and down to mix.
11. Place capped tubes in preheated thermocycler block set for the given cycle pattern below.
 - 15' @ 95; {30'' @ 94; 30'' @ T_a; 30'' @ 72}; 10' @ 72; hold at 4
 - Repeat bracketed steps for total of 22 cycles.
 - Ta varies from primer to primer.
 - (Use 59 for hGAP, 57 for OPN and 61 for rabCOLI.)

Record Ta for each primer: _____

12. At end of cycle remove tubes to the radioactive gel area in the fume hood. Add 5 ul of 6x loading buffer to each tube. Pipette to mix.
13. Return to thermocycler and run program DYESTORE or DYEGEL to bind the gel to the DNA. Cycles hold DNA at 65 for 10 minutes, and then return to either 4 or 22 degrees respectively. (You want you PCR product at room temperature when loading gel.
14. Either continue to running the gel or store PCR product at -20C.

List any deviations from above protocol or comments:

APPENDIX E

Pico-Green Assay For Double-Stranded Dna On Cell-Seeded Ha/Tcp Or Pldl

Report Abstract:

This method describes how to predict the number of cells on a three dimensional scaffold using PicoGreen, a fluorescent dye that binds specifically to dsDNA. Cells are lysed in the presence of a detergent using scraping and sonication to release the dsDNA into suspension. Samples are centrifuged to remove debris and the supernatant exposed to Pico-Green fluorochrome. Fluorescent intensity is measured by a fluorescence plate reader set to excite the samples at 502 nm and collect emissions at 523 nm (closest setting usually will be 480/520nm). Unknowns are read side by side with standardized samples of known DNA amounts and relative fluorescence intensities are used to predict the number of cells in the unknown samples. This assay for dsDNA provides a simple, very sensitive technique for determining the number of cells within a cell-seeded construct.

Why use Pico-Green vs. Hoechst 33258?

Pico-Green can detect much lower levels of dsDNA. Hoechst can detect only 10ng/ml dsDNA, while Pico-Green can quantify levels as low as 25pg/ml. Furthermore, Pico-Green has a much wider dynamic range. While the Hoechst assay requires two dye concentrations to obtain a dynamic range of two orders of magnitude, the Pico-Green assay only requires one dye solution to obtain a dynamic range of four orders of magnitude. Also, the assay remains linear in the presence of many contaminants, although there will often be an offset involved (see product literature to find the effect of different contaminants). Finally, the Hoechst assay is often sensitive to contaminating ssDNA and RNA.

Useful Note: The average cell has 7.7 pg DNA.

1. Materials and Reagents

- 1.1. Pico-Green dsDNA Quantitation Kit (Molecular Probes, Cat. No. P-7589) including the Pico-Green dsDNA quantitation reagent, Lambda DNA standard (100ug/ml), and a 20x TE buffer (200mM Tris-HCL, 20mM EDTA, pH 7.5)
- 1.2. 1M Tris-HCl (Life Technologies # 15567-027)
- 1.3. 1% Triton-X100 in Ca-free PBS (Sigma X-100)
- 1.4. Ca-free PBS (Life Technologies #14190-136)
- 1.5. 96-well Black Plates with Clear Bottom (Corning Costar Corp., Cat. No. 3603)
- 1.6. Disposable serological pipettes, 25 ml (VWR)
- 1.7. Pipette tips, 1-200 μ l (VWR)
- 1.8. Pipette tips, 200-1000 μ l (VWR)
- 1.9. 1.5 ml microcentrifuge tubes (Eppendorf)
- 1.10. 48-well plate for dilutions (optional)
- 1.11. aluminum foil
- 1.12. Sharpie marker

2. Equipment

- 2.1. Fluorescence Plate Reader
- 2.2. Beckman Microfuge E
- 2.3. Pipet-Aid (Drummond)
- 2.4. Pipetman, 2-20 μ l (P20)
- 2.5. Pipetman, 20-200 μ l (P200)
- 2.6. Pipetman, 200-1000 μ l (P1000)
- 2.7. 8-channel Pipettor (FinnPipette)
- 2.8. Repeater Pipettor (FinnPipette)

3. Procedure

- 3.1. **Prepare Samples** (Volumes per well assumes you are using 10cm² dishes or a 6 well plate.)
 - 3.1.1. **Prepare TTH solution:** Add 10 ml 1M Tris-HCl + 20 ml 1% Triton + 200 ml PBS to make a .1% Triton solution in 50 mM Tris-HCL. Keep cold.
 - 3.1.2. **Working buffer:** 10% serum-free media, 90% TTH.
 - 3.1.3. Rinse scaffold with 1ml PBS.
 - 3.1.4. For **HA/TCP**, place scaffold in a 1.5 ml microcentrifuge tube. Add 1ml buffer (media + TTH) and crush with an eppendorf pestle. Transfer to a 5ml tube.
 - 3.1.5. For **PLDL**, mince scaffold and place in a 5ml tube. Add 1ml buffer (media + TTH).
 - 3.1.6. Sonicate all samples 10 seconds. Transfer to a 1.5ml centrifuge tube. Spin 30 seconds in a microfuge to settle debris. Freeze at -80C.

4. **Prepare Standards** (may be done at time of scaffold seeding)
 - 4.1. Prepare as many ladders as needed for the experiment. In this case, prepare an MSC-ladder, and MOP-ladder, a PLDL+MSC ladder, and a HA/TCP+MSC ladder. For scaffold plus cell ladders, as an equivalent mass of the scaffold material to the cell suspension.
 - 4.2. Prepare the following cell solutions in Table 15 using a 10^6 /ml solution of each cell type. Volumes are μ l. Prepare in 5ml tubes. Add crushed HA/TCP or minced PLDL as needed.

Table 15. Relative Volumes (mL) Of Cell Suspension, Media, And TTH Required For Each Solution In The Cell Ladder.

	Blank	0.20M	0.4M	0.6M	0.8M	1.0M
Cell Suspension	0	20	40	60	80	111
Additional Media	100	80	60	40	20	0
TTH	900	900	900	900	900	999

Mass of HA/TCP: _____ Mass of PLDL: _____

- 4.3. **(Optional)** Prepare three serial dilutions of the 10^6 /ml cell solution also. Use 111ul of the more concentrated solution plus 999ul of buffer (media + TTH). Label these as 0.1M, 0.01M, and 0.001M. .
- 4.4. Sonicate 10 seconds. Transfer to a 1.5ml microcentrifuge tube. Freeze at -80°C .

5. Plate Set-up

- 5.1. Thaw samples and standards. Spin 30 seconds in microfuge.
- 5.2. Prepare Working Reagent by mixing 19 parts ddH₂O with 1 part 20x-TE buffer, then add a tenth part of the Pico-Green Reagent. Vortex. Protect from light. {PG Reagent takes a long time to thaw, even from RT.}

EXAMPLE

Total WR volume: _____ 10 ml
 ddH₂O volume: _____ 9.5 ml
 20x-TE volume: _____ 500 μ l
 PG volume: _____ 50 μ l

- 5.3. Diagram sample and standard layout on plate cover.
- 5.4. In plate, mix 100ul sample (or standard or blank) and 100 ul working reagent. Pipette to mix or use a shaker plate for 30 seconds. Incubate 5 minutes. Read at 480/520 nm on Garcia's fluorescence plate reader.

APPENDIX F

Finite Element Modeling Procedures for Rabbit Trabecular Bone

F.1 Determination of the Tissue Modulus of Rabbit Trabecular Bone

Sample XII was chosen as a representative sample to model to determine tissue modulus. It had good architecture (a good right cylinder without many holes) and its bone volume fraction was close to 36% (the average of the Whitaker samples loaded and nonloaded, $n = 18$). Developed model and applied a distributed 18.17N compressive load on top surface, constrained the cylindrical surface in the x and y directions, and the bottom surface of the cylinder in the z direction. Guess 5000 MPa for tissue modulus and then acquired the model's output for ezz apparent. Used linear relationship to determine actual tissue modulus for the polymer.

PREP FOR FE MODEL

- Contoured original file (c0000994.isq at 16 um resolution) using 405 pixel circles from slice 52-441. $x1/y1 = 280/322$; $x2/y2 = 684/726$. Picked best segmentation by eye. Gaussian filter (sigma = 1.2, support = 2) and threshold = 143.
/isq in c0000994.isq
/gobj_mask in c0000994.gobj
/gauss_seg in seg 1.2/2/143
/vox seg
BVF = 51022620/15468663 = 0.3032
/write seg m1015_p405_t143_seg.aim
copy c0000994.isq to m1015.isq
- Created a coarsened model with resolution of 32 microns, otherwise model would be too big for iplfe.
/isq in m1015.isq
/noipscale in sca
-downscale 2 2 2
-upscale 1 1 1
/from_aim_to_isq sca m1015_s2.isq
- Renamed m1015_s2.isq to c0000994.isq in root directory so the contouring program will recognize it. Opened contouring program and created new contours. Many slices were out of range since it expects more slices. New gobj: 203pixel circles on slices 26-224. $x1/y1 = 140,161$ and $x2/y2 = 342/363$. Saved and renamed to m1015_s2_p203.gobj
- In ipl, masked the rotated aim file with the new gobj file before component labeling to remove unconnected elements which could compromise the finite element model. Performed a bounding box cut to minimize the zero space. Examined new aim for overall dimensions.

/isq in m1015_s2.isq

```

/gobj_maskaimpeel_ow in m1015_s2_p203.gobj
/gauss_seg in seg 1.2/2/143
/cl26_rank seg cl
/bounding_box_cut
-input cl
-output bb
-z_only false
-border 3 0 0 ← on this model I had to add a border to make it square
!> out dim: 203 203 199
/write bb m1015_s2_p203_t143_cl_bb.aim *

```

** This is the file used as input to the fe program.

- On a pc computer, created a boundary condition file (.bcd) using dimensions of _bb.aim. See cyl_coords.xls. Saved the last worksheet as cyl_coords.prn (space delimited text). Opened .prn in Notepad, added the header information (making sure to edit the total number of boundary conditions in line 3. Saved as _bb.txt and FTPed the document to microCT computer in the working directory and renamed the file _bb.bcd.

RUNNING FE MODEL

```

$ iplfe
/read in m1015_s2_p203_t143_cl_bb.aim
/fe_solve3
-in in
-fea_file_name m1015_s2_p203_t143_cl_bb ← include dir if not
in current working dir
-problem_nr 100
-scale_factor 1.817000E+01
-output_option 1
-tolerance_force 1.000000E-04
-tolerance_displ 1.000000E-04
-max_nr_iter 20000
-restart_option 1
-comp_val_mat_001 127
-Ymodulus_mat_001 5.000000E+03
-Poissonr_mat_001 3.000000E-01
-comp_val_mat_002 0
-Ymodulus_mat_002 1.000000E+04
-Poissonr_mat_002 3.000000E-01
-comp_val_mat_003 0
-Ymodulus_mat_003 1.000000E+04
-Poissonr_mat_003 3.000000E-01

```

ESTIMATING TMOD FROM RESULTS

\$iplfe

/fe_post

```
-post_file_name      m1015_s2_p203_t143_cl_bb.post
-output              ezz
-variable_nr         3
-loadcase_nr         1
-output_option       1
-interpol_option     1
-averaging_option    0
```

Read m1015_s2_p203_t143_cl_bb.poslist to get that (ezz)app = -0.0051433

TMOD = 5000 MPa x $\frac{(-0.0051433)}{(-0.00397)}$ ← resultant displ amplitude from mech tests

TMOD = 6478 MPa or 6.48 GPa

Always check that this makes sense. This stiffness is higher than the guess in the original model (5000 MPa) so we would expect less deformation when TMOD = 6480 MPa is used which makes sense since the model predicted more deformation than actually occurred in the mechanical tests when a force amplitude of 18.17N compression was applied.

F.2 Modeling of Two Representative Rabbit Trabecular Bone Allografts

Samples 19L and 14R were chosen as representative samples. These samples were scanned on Ralph Mueller's microct20 at 34 micron resolution. The starting files were "rabbit-tibia_series04_19l_compl.aim" and "rabbit-tibia_series04_19l_compl.aim". The header info says that they were thresholded at 250 with a Gauss filter (sigma/support = 1.2/2) and then component labeled. But it also said that the element size was 75mm! Used /header_geo_set to change element size to .034x.034x.034 and then renamed files to 19l_cl.aim and 17l_cl.aim

Prep 19l

- Rotated cl.aim -1 degrees about x-axis and 4.5 degrees about y axis to straighten up the sides. Reset header position.

```
/read in 19l_cl.aim
/turn3d
-input          in
-output         out
-turnaxis_angles 0.000 90.000 90.000
-turnangle      -1
/turn3d
-input          out
-output         r
-turnaxis_angles 90.000 0.000 90.000
-turnangle      4.5
/write r 19l_clr.aim
/header_geo_set r
-position -1 -1 0
/write r 19l_clrp.aim
/from_aim_to_isq r 19l_clrp.isq
```

- Renamed 19l_clrp.isq to c0000xxx.isq in root directory so contouring program will recognize the file. Opened contouring program. Many slices were out of range since the program expects more slices. New gobj: 186 pixel circles on slices 25-213 $x1/y1 = 165/177$ and $x2/y2 = 350/362$. Saved and renamed to 19l_clrp.gobj
- In ipl, masked the rotated aim file with the new gobj file before component labeling to remove unconnected elements which could compromise the finite element model. Performed a bounding box cut to minimize the zero space. Examined new aim for overall dimensions.

```
/aim in 19l_clrp.aim
```

```

/gobj_maskaimpeel_ow in 19l_clrp.gobj
/cl26_rank in cl
/bounding_box_cut cl bb
/eva bb geom.
!> dim                186   186   189
!> off                 0     0     0
!> pos                165   177   24
!> element size in mm  0.0340 0.0340 0.0340
!> phys dim in mm     6.3240 6.3240 6.3240
/write bb 19l_clrp_bb.aim

```

- On a pc computer, created a boundary condition file (.bcd) using dimensions of _bb.aim. See cyl_coords.xls. Saved the last worksheet as cyl_coords.prn (space delimited text). Opened .prn in Notepad, added the header information (making sure to edit the total number of boundary conditions in line 3. Saved as _bb.txt and FTPed the document to microCT computer in the working directory and renamed the file _bb.bcd.

Prep 14R

- Repeated steps above for 19L with the following differences.
- Rotated cl.aim -3 degrees about x-axis and 4.5 degrees about y axis to straighten up the sides. Reset header position.
- Renamed 14r_clrp.isq to c0000xxx.isq in root directory so contouring program will recognize the file. Opened contouring program and created new contours. New gobj: 187 pixel circles on slices 21-203 x1/y1 = 156/178 and x2/y2 = 342/364. Saved and renamed to 14r_clrp.gobj

Ran FEM models for 19l and 14r as shown for p19l below.

```

$ iplfe
/read
-name                in
-filename            19L_CLRP_BB.AIM;1
/fe_solve3
-in                  in
-fea_file_name       19L_CLRP_BB
-problem_nr          100
-scale_factor        2.22400E+01
-output_option       1
-tolerance_force     1.000000E-04
-tolerance_displ     1.000000E-04
-max_nr_iter         20000
-restart_option      1
-comp_val_mat_001    127
-Ymodulus_mat_001   6.480000E+03
-Poissonr_mat_001   3.000000E-01

```

-comp_val_mat_002	0
-Ymodulus_mat_002	1.000000E+04
-Poissonr_mat_002	3.000000E-01
-comp_val_mat_003	0
-Ymodulus_mat_003	1.000000E+04
-Poissonr_mat_003	3.000000E-01

F.3 Post-Processing of Two Representative Rabbit Trabecular Bone Allografts

The following batch file contains IPL commands necessary to create .aim files coded with each of the four output parameters: \dot{z} , \dot{p}_1 , VMS, and SED and histograms of these .aim files. To execute the following batch file, type the following command in a DecTerm window.

```
@{file_path}ad_fe_whit.com {file_path}*.post
```

AD_FE_WHIT.COM

```
$ if p1 .EQS. ""
$ THEN
$ write sys$output "Give C0001234.aim ! Exit"
$ exit
$ endif
$
$ define org_file 'p1'
$ seg_file = p1 - F$PARSE(p1,,,"VERSION") - ".POST" + "_SEG.AIM"
$ gobj_file = p1 - F$PARSE(p1,,,"VERSION") - ".POST" + ".GOBJ"
$ histo_ezz = p1 - F$PARSE(p1,,,"VERSION") - ".POST" + "_EZZ.TAB"
$ histo_epl = p1 - F$PARSE(p1,,,"VERSION") - ".POST" + "_EPL.TAB"
$ histo_vms = p1 - F$PARSE(p1,,,"VERSION") - ".POST" + "_VMS.TAB"
$ histo_sed = p1 - F$PARSE(p1,,,"VERSION") - ".POST" + "_SED.TAB"
$ ezz_file = p1 - F$PARSE(p1,,,"VERSION") - ".POST" + "_EZZ.AIM"
$ epl_file = p1 - F$PARSE(p1,,,"VERSION") - ".POST" + "_EPL.AIM"
$ vms_file = p1 - F$PARSE(p1,,,"VERSION") - ".POST" + "_VMS.AIM"
$ sed_file = p1 - F$PARSE(p1,,,"VERSION") - ".POST" + "_SED.AIM"
$
$ show log org_file
$ ipl_sanco_prog := $um:ipl_sanco_fe.exe
$ ipl_sanco_prog

/fe_post
-post_file_name      org_file
-output              ezz
-variable_nr         3
-loadcase_nr         1
-output_option       1
-interpol_option     1
-averaging_option    0
/fe_post
-post_file_name      org_file
-output              epl
-variable_nr         24
-loadcase_nr         1
-output_option       1
```

```

-interpol_option      1
-averaging_option    0
/fe_post
-post_file_name      org_file
-output              vms
-variable_nr         42
-loadcase_nr         1
-output_option        1
-interpol_option      1
-averaging_option    0
/fe_post
-post_file_name      org_file
-output              sed
-variable_nr         45
-loadcase_nr         1
-output_option        1
-interpol_option      1
-averaging_option    0
/write ezz "ezz_file
-compress_type       bin
-version_020         true
/write epl "epl_file
-compress_type       bin
-version_020         true
/write vms "vms_file
-compress_type       bin
-version_020         true
/write sed "sed_file
-compress_type       bin
-version_020         true
/histo ezz
-fileout_or_screentab "histo_ezz
-from_val            -1
-to_val              -1
-nr_bins_in_tab     50000
-dt_type             auto
-count_zeros         no
/histo epl
-fileout_or_screentab "histo_epl
-from_val            -1
-to_val              -1
-nr_bins_in_tab     50000
-dt_type             auto
-count_zeros         no
/histo vms

```

```
-fileout_or_screentab "histo_vms  
-from_val -1  
-to_val -1  
-nr_bins_in_tab 50000  
-dt_type auto  
-count_zeros no  
/histo sed  
-fileout_or_screentab "histo_sed  
-from_val -1  
-to_val -1  
-nr_bins_in_tab 50000  
-dt_type auto  
-count_zeros no  
..  
$ exit
```

APPENDIX G

Finite Element Modeling Procedures for PLDL

G.1 Determination of PLDL Tissue Modulus

P25 was chosen as a representative sample to model. The model was developed with a distributed compressive force of 11.89 N on the top surface. The cylindrical surface was constrained in the x and y directions, and the bottom surface of the cylinder in the z direction. A guess of 5000 MPa for tissue modulus was used to determine the model's output for \hat{a}_{zz} apparent and a linear relationship used to determine the actual tissue modulus for the polymer.

PREP FOR FE MODEL

- Copied c0000286a_g81_t28_seg.aim (previously segmented with a Gaussian filter set to a sigma of 0.8 and a support of 1 and threshold of 28) to p25_seg.aim
- Rotated p25_seg.aim -9 degrees about x-axis and -5 degrees about y axis to straighten up the sides. New file is p25_segr.aim

```
/read
  -name          in
  -filename      p25_seg.aim
/turn3d
  -input         in
  -output        out
  -turnaxis_angles 0.000 90.000 90.000
  -turnangle     -9.000000
/turn3d
  -input         out
  -output        r
  -turnaxis_angles 90.000 0.000 90.000
  -turnangle     -5.000000
/write r p25_segr.aim
  -compress_type bin
  -version_020   true
```

- Created an .isq file from the rotated .aim file, so that a contour file can be created. Since the rotation process sometimes creates negative z coordinates, first check to make sure the z-position in the .aim file header is positive or the contouring program won't be able to read in the appropriate slices since it expects slices to start at zero. If not reset z-position to zero using the header_geo_set command.

```
/examine r geom
!> dim          180  197  225
!> off          0   0   0
!> pos         128  245  19
!> element size in mm 0.0300 0.0300 0.0300
!> phys dim in mm   5.4000 5.9100 6.7500
```

```

/from_aim_to_isq
-aim_name          r
-isq_filename      p25_segr.isq
-square_flag       false
-original_position  true

```

- Copied r25_segr.isq to c0000285.isq and opened it in the contouring program. Created a right cylinder .gobj file. In this case, I omitted 3 slices with too little bone to adequately apply forces to on top and 3 slices on bottom for same reason. Slices 43-214. The diameter of circular contours is 136 pixels and x1/y1 position is 152/223 and x2/y2 position is 287/408. Saved contours as c0000285.gobj and then copied to p25_segr.gobj.
- In ipl, masked the rotated aim file with the new gobj file before component labeling to remove unconnected elements which could compromise the finite element model. Performed a bounding box cut to minimize the zero space. Examined new aim for overall dimensions.

```

/read in P25_SEGR.AIM;1
/gobj_maskaimpeel_ow
-input_output      in
-gobj_filename     P25_SEGR.GOBJ;1
-peel_iter         0
/cl26_rank_extract
-input             in
-output            cl
-first_rank        1
-last_rank         1
-connect_boundary  false
-value_in_range    127
/bounding_box_cut
-input             cl
-output            bb
-z_only            false
-border            0 0 0
/examine bb geom.
/write bb p25_segr_bb.aim **
** This is the file used as input to the fe program.

```

- On a pc computer, created a boundary condition file (.bcd) using dimensions of p25_segr_bb.aim. See cyl_coords p25.xls. Saved the last worksheet as cyl_coords.prn (space delimited text). Opened .prn in Notepad, added the header information (making sure to edit the total number of boundary conditions in line 3. Saved as p25_segr_bb.txt and FTPed the document to microCT computer in the p25 working directory and renamed the file p25_segr_bb.bcd.

Running FE Model

```
$ iplfe
/read in P25_SEGR_BB.AIM;1
/fe_solve3
-in          in
-fea_file_name    P25_SEGR_BB
-problem_nr      100
-scale_factor     1.189000E+01
-output_option    1
-tolerance_force  1.000000E-04
-tolerance_displ 1.000000E-04
-max_nr_iter      20000
-restart_option   1
-comp_val_mat_001 127
-Ymodulus_mat_001 5.000000E+03
-Poissonr_mat_001 3.000000E-01
-comp_val_mat_002 0
-Ymodulus_mat_002 1.000000E+04
-Poissonr_mat_002 3.000000E-01
-comp_val_mat_003 0
-Ymodulus_mat_003 1.000000E+04
-Poissonr_mat_003 3.000000E-01
```

ESTIMATING TMOD FROM RESULTS

```
/iplfe
/fe_post
-post_file_name    P25_SEGR_BB.POST
-output           ezz
-variable_nr       3
-loadcase_nr       1
-output_option     1
-interpol_option   1
-averaging_option  0
```

Read p25_segr_bb.poslist to get that $(\hat{a}_{zz})_{app} = -0.0034625$

$$TMOD = 5000 \text{ MPA} \times \frac{(-0.0034625)}{(-0.0204)} \leftarrow \text{displacement from mechanical tests}$$

$$TMOD = 849 \text{ MPa}$$

- Always check that this makes sense. This stiffness is lower than the guess in the original model (5000 MPa) so we would expect more deformation when TMOD = 849 MPa is used which makes sense since the model did not deform as much as occurred in the mechanical tests when a force amplitude of 11.89N compression was applied.

G.2 Modeling of Three Representative PLDL Samples

Samples p25, p26, and p93 were chosen and modeled as representative PLDL samples. Deformations within the tissue space are important, so both the polymer (or “bone”) and the tissue (or “marrow”) were modeled. In addition, a metal plate was modeled on the end of the sample that the force is applied since the difference in moduli of the two materials could result in large deformation errors near this boundary. Created an .aim file that has polymer (127), tissue (10), plate (5) and empty space (0) as well as individual .aim files of the polymer, tissue, and plate. The empty space is the corners of the cube that are outside the right cylinder. The plate was modeled as a disk that is a single layer of elements thick. A distributed force of 13.3 N was applied to the plate to match the actual loading conditions of the rats *in vivo*. The polymer was assigned a tissue modulus of 849 MPa based on the procedure outlined in Appendix G.1. The plate was assumed to be perfectly stiff and was therefore assigned a tissue modulus of 1.2e7 MPa.

Prep P25

- Copied p25_segr_bb.aim to p25_segr_bb2_bone.aim
- Created .aim file with bone and marrow.

```
/read in P25_SEGR_BB2_bone.AIM
/set_value
-input          in
-value_object   127
-value_background 10
/gobj_maskaimpeel_ow
-input_output   in
-gobj_filename  P25_SEGR.GOBJ;1
-peel_iter      0
/write in p25_segr_bb2.aim    ← represents “bone” and “marrow”
```

- Created .aim with marrow only.

```
/read in P25_SEGR_BB2_bone.aim
/set_value
-input          in
-value_object   10
-value_background 127
/gobj_maskaimpeel_ow
-input_output   in
-gobj_filename  P25_SEGR.GOBJ;1
-peel_iter      0
/write in p25_segr_bb2_mar.aim ← represents “marrow”
```

- Created .aim with plate, bone, and marrow by first creating a second gobj exactly as before but including one extra slice on top (i.e. slices 42-214) and saved as p25_ps.gobj. Also saved a .gobj file with just slice 42 as p25_plate.gobj. Then in ipl, created an aim of just the plate and then concatenated that file to the aim of the bone and marrow listed above. Another bounding box cut is required.

```

/read in P25_segr.aim
/set_value
-input          in
-value_object   127
-value_background 127
/gobj_maskaimpeel_ow
-input_output   in
-gobj_filename  P25_plate.GOBJ;1
-peel_iter      0
/set_value
-input          in
-value_object   5
-value_background 0
/read sample p25_segr_bb2.aim
/concat
-input1         in
-input2         sample
-output         both
-common_region_only false
-add_not_overlay true
-make_edge      false
-shift_ofin2    0 0 0
-turnangle      0.000000
-turnpoint_global -1 -1
/bounding_box_cut
-input          both
-output         bb
-z_only         false
-border         0 0 0
/gobj_maskaimpeel_ow
-input_output   bb
-gobj_filename  P25_ps.GOBJ;1
-peel_iter      0
/histo bb p25_ps.tab
/write bb p25_ps.aim ← represents “bone” and “marrow” and “plate”, will be
fe input

```

- On a pc computer, created a boundary condition file (.bcd) using dimensions of _ps.aim. Saved as _ps.txt and FTPed the document to microCT computer in the working directory and renamed the file _ps.bcd.

Prep P26

- Copied c0000286b_g81_t28_seg.aim (previously segmented with a Gaussian filter set to a sigma of 0.8 and a support of 1 and threshold of 28) to p26_seg.aim
- Rotated p26_seg.aim +14 degrees about x-axis and +6 degrees about y axis to straighten up the sides. New file is p26_segr.aim
- Created an .isq from the rotated aim so that you can create a contour file. Since the rotation process sometimes creates negative zcoordinates, first check to make sure the z-position in the .aim file header is positive or the contouring program won't be able to read in the appropriate slices since it expects slices to start at zero. If not reset zposition to zero using the header_geo_set command and save as _segrp.aim.

```

/read in P26_SEGR.AIM;1
/examine in geom
!> dim                184   220   235
!> off                 0     0     0
!> pos                141    33   -20
!> element size in mm    0.0300 0.0300 0.0300
!> phys dim in mm       5.5200 6.6000 7.0500
/header_geo_set
-input                in
-off_new              -1 -1 -1
-pos_new              -1 -1 0
-el_size_mm_new      -1.000 -1.000 -1.000
!> New Pos   141    33    0
/write in p26_segrp.aim
/from_aim_to_isq r p26_segrp.isq

```

- Copied r26_segrp.isq to c00000285.isq and opened it in the contouring program. Created a right cylinder gobj file. In this case, I omitted 3 slices with too little bone to adequately apply forces to on top and 10 slices on bottom for same reason. Contoured slices 34-194 using circular contours with a diameter of 138 pixels and x1/y1 position of 164/74 and x2/y2 position of 301/211. Saved contours as c0000285.gobj and copied to p26_segrp.gobj.
- In ipl, masked the rotated aim file with the new gobj file before component labeling to remove unconnected elements which could compromise the finite element model. Performed a bounding box cut to minimize the zero space. Examined new aim for overall dimensions.

```

/read in P26_SEGRp.AIM;1
/gobj_mask in P26_SEGRp.GOBJ;1

```

```

!% -> Set 2409204 of total ?
/cl26_rank_extract in cl
!% Total number of disjoint components: 217
!% Label 1: 99.87 %
/bounding_box_cut cl bb
/examine bb geom
!> dim 136 136 159
!> off 0 0 0
!> pos 165 74 34
!> element size in mm 0.0300 0.0300 0.0300
!> phys dim in mm 4.0800 4.0800 4.7700
/write bb p26_segrp_bb.aim

```

- Copied p26_segrp_bb.aim to p26_segrp_bb2_bone.aim
- Created .aim with bone and marrow.

```

/read in P26_SEGRp_BB2_bone.AIM
/set_value in
-value_object 127
-value_background 10
/gobj_maskaimpeel_ow in P26_SEGRp.GOBJ;1
/write bb p25_segr_bb2.aim ← represents “bone” and “marrow”, will be fe
input

```

- Created .aim with marrow only.

```

/read in P26_SEGRp_BB2_bone.aim
/set_value in
-value_object 10
-value_background 127
/gobj_maskaimpeel_ow in P26_SEGRp.GOBJ;1
/write in p25_segr_bb2_mar.aim ← represents “marrow”,

```

- Created .aim with plate, bone, and marrow by first creating a second gobj exactly as before but including one extra slice on top (i.e. slices 42-214) and saved as p25_ps.gobj. Also saved a .gobj file with just slice 42 as p25_plate.gobj. Then in ipl, created an aim of just the plate and then concatenated that file to the aim of the bone and marrow listed above. Another bounding box cut is required.

```

/read in P25_segr.aim
/set_value
-input in
-value_object 127
-value_background 127
/gobj_maskaimpeel_ow

```

```

-input_output      in
-gobj_filename    P25_plate.GOBJ;1
-peel_iter        0
/set_value
-input            in
-value_object     5
-value_background 0
/read sample p25_segr_bb2.aim
/concat
-input1          in
-input2          sample
-output          both
-common_region_only  false
-add_not_overlay  true
-make_edge       false
-shift_ofin2     0 0 0
-turnangle       0.000000
-turnpoint_global -1 -1
/bounding_box_cut
-input           both
-output          bb
-z_only          false
-border          0 0 0
/gobj_maskaimpeel_ow
-input_output    bb
-gobj_filename   P25_ps.GOBJ;1
-peel_iter       0
/histo bb p25_ps.tab
/write bb p25_ps.aim ← represents “bone” and “marrow” and “plate”, will be
fe input

```

- On a pc computer, created a boundary condition file (.bcd) using dimensions of _ps.aim. Saved as _ps.txt and FTPed the document to microCT computer in the working directory and renamed the file _ps.bcd.

Prep P93

- Repeat steps for P26 with the following differences
- Copied c0000287c_g81_t28_seg.aim (previously segmented with a Gaussian filter set to a sigma of 0.8 and a support of 1 and threshold of 28) to p93_seg.aim
- Rotated p93_seg.aim -1 degrees about x-axis and +7 degrees about y axis to straighten up the sides. New file is p93_segr.aim
- P93 did not need repositioning.
- Contouring: In this case, I omitted 2 slices with too little bone to adequately apply forces to on top and 1 slice on bottom for same reason. Slices 40-195. Diameter of circular contours is 140 pixels and x1/y1 position is 308/163 and

x2/y2 position is 447/302. Saved contours c0000287.gobj and copied to p93_segr.gobj.

Run FEM models for p25, p26, and p93 as shown for p25 below.

```
$ iplfe
/read in P25_PS.AIM;1
/fe_solve3
-in          in
-fea_file_name    P25_PS
-problem_nr      100
-scale_factor    1.33000E+01
-output_option   1
-tolerance_force 1.000000E-04
-tolerance_displ 1.000000E-04
-max_nr_iter     20000
-restart_option  1
-comp_val_mat_001 127
-Ymodulus_mat_001 8.490000E+02
-Poissonr_mat_001 3.000000E-01
-comp_val_mat_002 10
-Ymodulus_mat_002 1.000000E-01
-Poissonr_mat_002 3.000000E-01
-comp_val_mat_003 5
-Ymodulus_mat_003 1.200000E+07
-Poissonr_mat_003 3.000000E-01
```

G.3 Post-Processing of Three Representative PLDL Samples

G.3.1 Generation of Output Files for Materials 1 & 2

- Run *ad_fe_pc1.com* on *.post file to create output aims. Note that the output lumps material 1 (polymer) and material 2 (interstitial tissue) and material 3 (plate) together.
- Manually reset headers on all four output aims to match the position of the input aim. \hat{a}_z example below where x y z refer to the position of the input aim for the finite element model. For some reason, all the iplfe output .aims are shifted by 1 voxel in all three directions.
- /read out _ezz.aim
- /read in _bb2.aim
 - /examine in geom
 - /examine out geom.
 - /header_geo_set
 - input out
 - off_new -1 -1 -1
 - pos_new x y z
 - el_size_mm_new -1.000 -1.000 -1.000
 - /write out _ezzr.aim
- Run *ad_fe_pc2.com* on *.post file to create aims that include the output parameters for bone and marrow individually. Also histograms of same data.
- Run *ad_fe_pc_statb.com* on *.post file to see output statistics for bone. Record values on spreadsheet.
- Run *ad_fe_pc_statm.com* on *.post file to see output statistics for marrow. Record values on spreadsheet.
- As needed, additional histograms may be created to exclude outlier voxels.

G.3.2 IPL Batch Files Used to Generate Output for Materials 1 & 2

The following batch file contains IPL commands necessary to create .aim files coded with each of the four output parameters: $\hat{\alpha}_z$, $\hat{\phi}_1$, VMS, and SED. These .aim files contain output for both Material 1 and Material 2. To execute the following batch file, type the following command in a DecTerm window.

```
@{file_path}ad_fe_pc1.com {file_path}*.post
```

ad_fe_pc1.com

```
#! IPL Batch for post-processing angel's fe models with 2 materials for preculture study.
```

```
#! Step 1
```

```
#!
```

```
#! IPL Batch Scanco
```

```
#!
```

```
$ if p1 .EQS. ""
```

```
$ THEN
```

```
$ write sys$output "Give C0001234.aim ! Exit"
```

```
$ exit
```

```
$ endif
```

```
$
```

```
$ define org_file 'p1'
```

```
$ ezz_file = p1 - F$PARSE(p1,,"VERSION") - ".POST" + "_EZZ.AIM"
```

```
$ epl_file = p1 - F$PARSE(p1,,"VERSION") - ".POST" + "_EPL.AIM"
```

```
$ vms_file = p1 - F$PARSE(p1,,"VERSION") - ".POST" + "_VMS.AIM"
```

```
$ sed_file = p1 - F$PARSE(p1,,"VERSION") - ".POST" + "_SED.AIM"
```

```
$
```

```
$ show log org_file
```

```
$ ipl_scanco_prog := $um:ipl_scanco_fe.exe
```

```
$ ipl_scanco_prog
```

```
/fe_post
```

```
-post_file_name      org_file
```

```
-output              ezz
```

```
-variable_nr         3
```

```
-loadcase_nr         1
```

```
-output_option        1
```

```
-interpol_option      1
```

```
-averaging_option     0
```

```
/fe_post
```

```
-post_file_name      org_file
```

```
-output              epl
```

```
-variable_nr         24
```

```
-loadcase_nr         1
```

```

-output_option      1
-interpol_option    1
-averaging_option   0
/fe_post
-post_file_name     org_file
-output             vms
-variable_nr        42
-loadcase_nr        1
-output_option      1
-interpol_option    1
-averaging_option   0
/fe_post
-post_file_name     org_file
-output             sed
-variable_nr        45
-loadcase_nr        1
-output_option      1
-interpol_option    1
-averaging_option   0

/write ezz "ezz_file
-compress_type      bin
-version_020        true
/write epl "epl_file
-compress_type      bin
-version_020        true
/write vms "vms_file
-compress_type      bin
-version_020        true
/write sed "sed_file
-compress_type      bin
-version_020        true
..
$ exit

```

The following batch file contains IPL commands necessary to create .aim files coded with each of the four output parameters: \hat{a}_{zz} , $\hat{\phi}_1$, VMS, and SED separated by material designation. Histograms of each .aim are also created. To execute the following batch file, type the following command in a DecTerm window.

@ {file_path}ad_fe_pc2.com {file_path}*.post

ad_fe_pc2.com

```

$! Prepared for the pre-culture study models of rMSCs on PLDL.
$! Step 2 -- to be run after ad_fe_pc1 and after the headers are
$! repositioned.
$!
$ if p1 .EQS. ""
$ THEN
$write sys$output "Give C0001234.aim ! Exit"
$ exit
$ endif
$
$ define org_file 'p1'
$ bone_gobj_file = p1 - F$PARSE(p1,,,"VERSION") - ".POST" + "_bone.aim"
$ marrow_gobj_file = p1 - F$PARSE(p1,,,"VERSION") - ".POST" + "_mar.aim"
$ ezz_file = p1 - F$PARSE(p1,,,"VERSION") - ".POST" + "_EZZR.AIM"
$ epl_file = p1 - F$PARSE(p1,,,"VERSION") - ".POST" + "_EPLR.AIM"
$ vms_file = p1 - F$PARSE(p1,,,"VERSION") - ".POST" + "_VMSR.AIM"
$ sed_file = p1 - F$PARSE(p1,,,"VERSION") - ".POST" + "_SEDR.AIM"
$ ezzb_file = p1 - F$PARSE(p1,,,"VERSION") - ".POST" + "_EZZR_BONE.AIM"
$ eplb_file = p1 - F$PARSE(p1,,,"VERSION") - ".POST" + "_EPLR_BONE.AIM"
$ vmsb_file = p1 - F$PARSE(p1,,,"VERSION") - ".POST" + "_VMSR_BONE.AIM"
$ sedb_file = p1 - F$PARSE(p1,,,"VERSION") - ".POST" + "_SEDR_BONE.AIM"
$ ezzm_file = p1 - F$PARSE(p1,,,"VERSION") - ".POST" + "_EZZR_MAR.AIM"
$ eplm_file = p1 - F$PARSE(p1,,,"VERSION") - ".POST" + "_EPLR_MAR.AIM"
$ vmsm_file = p1 - F$PARSE(p1,,,"VERSION") - ".POST" + "_VMSR_MAR.AIM"
$ sedm_file = p1 - F$PARSE(p1,,,"VERSION") - ".POST" + "_SEDR_MAR.AIM"
$ histo_ezzb = p1 - F$PARSE(p1,,,"VERSION") - ".POST" + "_EZZR_BONE.TAB"
$ histo_eplb = p1 - F$PARSE(p1,,,"VERSION") - ".POST" + "_EPLR_BONE.TAB"
$ histo_vmsb = p1 - F$PARSE(p1,,,"VERSION") - ".POST" + "_VMSR_BONE.TAB"
$ histo_sedb = p1 - F$PARSE(p1,,,"VERSION") - ".POST" + "_SEDR_BONE.TAB"
$ histo_ezzm = p1 - F$PARSE(p1,,,"VERSION") - ".POST" + "_EZZR_MAR.TAB"
$ histo_eplm = p1 - F$PARSE(p1,,,"VERSION") - ".POST" + "_EPLR_MAR.TAB"
$ histo_vmsm = p1 - F$PARSE(p1,,,"VERSION") - ".POST" + "_VMSR_MAR.TAB"
$ histo_sedm = p1 - F$PARSE(p1,,,"VERSION") - ".POST" + "_SEDR_MAR.TAB"
$
$ show log org_file
$
$ ipl_scanco_prog := $um:ipl_scanco_fe.exe
$!

```

```
$ ipl_scanco_prog
```

```
! This section generates a _ezz_bone.aim and _ezz_bone.tab of histogram data  
! for material 1 (bone) and a _ezz_marrow.aim and _ezz_marrow.aim  
! for material 2 (marrow).
```

```
/read  
-name          ezz  
-filename      "ezz_file  
/gobj_maskaimpeel_ow  
-input_output  ezz  
-gobj_filename "bone_gobj_file  
-peel_iter     0  
/write ezz "ezzb_file  
-compress_type bin  
-version_020   true  
/histo ezz  
-fileout_or_screentab "histo_ezzb  
-from_val       -1  
-to_val        -1  
-nr_bins_in_tab 500  
-dt_type       auto  
-count_zeros   no  
/read  
-name          ezz  
-filename      "ezz_file  
/gobj_maskaimpeel_ow  
-input_output  ezz  
-gobj_filename "marrow_gobj_file  
-peel_iter     0  
/write ezz "ezzm_file  
-compress_type bin  
-version_020   true  
/histo ezz  
-fileout_or_screentab "histo_ezzm  
-from_val       -1  
-to_val        -1  
-nr_bins_in_tab 500  
-dt_type       auto  
-count_zeros   no
```

```
! This section generates a _epl_bone.aim and _epl_bone.tab of histogram data  
! for material 1 (bone) and a _epl_marrow.aim and _epl_marrow.aim  
! for material 2 (marrow).
```

```

/read
-name          epl
-filename      "epl_file"
/gobj_maskaimpeel_ow
-input_output  epl
-gobj_filename "bone_gobj_file"
-peel_iter     0
/write epl "eplb_file"
-compress_type bin
-version_020   true
/histo epl
-fileout_or_screentab "histo_eplb"
-from_val       -1
-to_val         -1
-nr_bins_in_tab 500
-dt_type        auto
-count_zeros    no
/read
-name          epl
-filename      "epl_file"

/gobj_maskaimpeel_ow
-input_output  epl
-gobj_filename "marrow_gobj_file"
-peel_iter     0
/write epl "eplm_file"
-compress_type bin
-version_020   true
/histo epl
-fileout_or_screentab "histo_eplm"
-from_val       -1
-to_val         -1
-nr_bins_in_tab 500
-dt_type        auto
-count_zeros    no

! This section generates a _vms_bone.aim and _vms_bone.tab of histogram data
! for material 1 (bone) and a _vms_marrow.aim and _vms_marrow.aim
! for material 2 (marrow).

/read
-name          vms
-filename      "vms_file"

```

```

/gobj_maskaimpeel_ow
-input_output      vms
-gobj_filename     "bone_gobj_file"
-peel_iter         0
/write vms "vmsb_file"
-compress_type     bin
-version_020      true
/histo vms
-fileout_or_screentab "histo_vmsb"
-from_val          -1
-to_val            -1
-nr_bins_in_tab    50000
-dt_type           auto
-count_zeros       no
/read
-name              vms
-filename          "vms_file"
/gobj_maskaimpeel_ow
-input_output      vms
-gobj_filename     "marrow_gobj_file"
-peel_iter         0
/write vms "vmsm_file"
-compress_type     bin
-version_020      true
/histo vms
-fileout_or_screentab "histo_vmsm"
-from_val          -1
-to_val            -1
-nr_bins_in_tab    50000
-dt_type           auto
-count_zeros       no

```

! This section generates a _sed_bone.aim and _sed_bone.tab of histogram data
! for material 1 (bone) and a _sed_marrow.aim and _sed_marrow.aim
! for material 2 (marrow).

```

/read
-name              sed
-filename          "sed_file"
/gobj_maskaimpeel_ow
-input_output      sed
-gobj_filename     "bone_gobj_file"
-peel_iter         0
/write sed "sedb_file"

```

```

-compress_type      bin
-version_020       true
/histo sed
-fileout_or_screentab "histo_sedb
-from_val          -1
-to_val           -1
-nr_bins_in_tab    50000
-dt_type           auto
-count_zeros       no

/read
-name              sed
-filename          "sed_file
/gobj_maskaimpeel_ow
-input_output      sed
-gobj_filename     "marrow_gobj_file
-peel_iter         0
/write sed "sedm_file
-compress_type     bin
-version_020       true
/histo sed
-fileout_or_screentab "histo_sedm
-from_val          -1
-to_val           -1
-nr_bins_in_tab    50000
-dt_type           auto
-count_zeros       no

..
$ exit

```

The following batch file contains IPL commands necessary to display statistical information for each output .aim file for Material 1 (polymer phase "bone"). To execute the following batch file, type the following command in a DecTerm window.

@ {file_path}ad_fe_statb.com {file_path}*.post

ad_fe_pc_statb.com

```

$ if p1 .EQS. ""
$ THEN
$ write sys$output "Give C0001234.aim ! Exit"
$ exit
$ endif
$ define org_file 'p1'
$ ezzb_file = p1 - F$PARSE(p1,,,"VERSION") - ".POST" + "_EZZR_BONE.AIM"
$ eplb_file = p1 - F$PARSE(p1,,,"VERSION") - ".POST" + "_EPLR_BONE.AIM"
$ vmsb_file = p1 - F$PARSE(p1,,,"VERSION") - ".POST" + "_VMSR_BONE.AIM"
$ sedb_file = p1 - F$PARSE(p1,,,"VERSION") - ".POST" + "_SEDR_BONE.AIM"
$ show log org_file
$ ipl_scanco_prog := $um:ipl_scanco_fe.exe
$ ipl_scanco_prog
/read
  -name          ezzb
  -filename      "ezz_b_file"
/examine
  -input         ezzb
  -item          stat
/read
  -name          eplb
  -filename      "epl_b_file"
/examine
  -input         eplb
  -item          stat
/read
  -name          vmsb
  -filename      "vms_b_file"
/examine
  -input         vmsb
  -item          stat
/read
  -name          sedb
  -filename      "sed_b_file"
/examine
  -input         sedb
  -item          stat
..
$ exit

```

The following batch file contains IPL commands necessary to display statistical information for each output .aim file for Material 2 (interstitial phase "marrow"). To execute the following batch file, type the following command in a DecTerm window.

@{file_path}ad_fe_statm.com {file_path}*.post

ad_fe_pc_statm.com

```

$ if p1 .EQS. ""
$ THEN
$ write sys$output "Give C0001234.aim ! Exit"
$ exit
$ endif
$ define org_file 'p1'
$ ezm_file = p1 - F$PARSE(p1,,,"VERSION") - ".POST" + "_EZZR_MAR.AIM"
$ eplm_file = p1 - F$PARSE(p1,,,"VERSION") - ".POST" + "_EPLR_MAR.AIM"
$ vmsm_file = p1 - F$PARSE(p1,,,"VERSION") - ".POST" + "_VMSR_MAR.AIM"
$ sedm_file = p1 - F$PARSE(p1,,,"VERSION") - ".POST" + "_SEDR_MAR.AIM"
$ show log org_file
$ ipl_scanco_prog := $um:ipl_scanco_fe.exe
$ ipl_scanco_prog
/read
  -name          ezm
  -filename      "ezm_file"
/examine
  -input         ezm
  -item          stat
/read
  -name          eplm
  -filename      "eplm_file"
/examine
  -input         eplm
  -item          stat
/read
  -name          vmsm
  -filename      "vmsm_file"
/examine
  -input         vmsm
  -item          stat
/read
  -name          sedm
  -filename      "sedm_file"
/examine
  -input         sedm
  -item          stat
..
$ exit

```

G.3.3 Regional Analysis of Tissue Parameters

- Run *ad_fe_pc_regb_xxp.com* where *xx* = 25, 26, or 93 on *_bone.aim* in the respective directories including *_ezzr_bone.aim* (& *eplr_bone.aim*, etc) to generate aims and histograms for the top 25%, middle 50%, and bottom 25%. Histograms reflect the full data set.
- Run *ad_fe_pc_regm_xxp.com* where *xx* = 25, 26, or 93 on *_mar.aim* in directory including *_ezzr_mar.aim* (& *eplr_mar.aim*, etc) to generate aims and histograms for the top 25%, middle 50%, and bottom 25%. Histograms reflect the full data set.
- Run *ad_fe_pc_regstat.com* on *_xxx_bone.aim* or *xxx_mar.aim* where *xxx* = *ezz*, *epl*, *vms*, or *sed*. Run multiple times to get top, middle, bottom stats for each parameter in bone and in marrow.
- Run *ad_fe_pc_histo_bone_r.com* on *_xxx_bone.aim* to create histograms with a reduced data set including 0-95th percentile for VMS and SED and 5th to 95th percentile for *ezz* and *epl*.
- Run *ad_fe_pc_histo_mar_r.com* on *_xxx_mar.aim* to create histograms with a reduced data set including 0-95th percentile for VMS and SED and 5th to 95th percentile for *ezz* and *epl*.
- Run *ad_fe_pc_vivo.com* on the *_seg.aims* for every measurement in the 8-week preculture loaded group (m2354-59, 2476-77) to determine the distribution of bone volume for the top 25%, middle 50%, and bottom 25%. Repeat to determine the distribution of bone volume for the top 10%, middle 80%, and bottom 10%. The batch file must be edited for each samples z-dimension.

G.3.4 IPL Batch Files Used to Generate Regional Output of Tissue Parameters

The following batch file contains IPL commands necessary to separate the tissue response output for Material 1 (polymer phase “bone”) into zones (top 25%, middle 50%, and bottom 25%). To execute the following batch file, type the following command in a DecTerm window. The following example is for sample p25.

```
@ {file_path}ad_fe_regb.com {file_path}*_bone.aim
```

ad_fe_pc_regb_25p.com

```
#!
#!  _/_/_/_/_/_/_/_
#!  _/_  _/_  _/_  _/_  Image Processing Language
#!  _/_  _/_/_/_/_/_
#!  _/_  _/_  _/_  (c) Andres Laib, Scanco Medical AG
#!  _/_/_/_/_/_  _/_/_/_/_/_
#!
#!
#!
#! IPL Batch FOR POST-PROCESSING ANGEL'S FE MODELS WITH 2
MATERIALS.
#! Prepared for the pre-culture study models of rMSCs on PLDL.
#! Divides resultant data into top, middle, and bottom regions.
#!
#! Written for p25 which has a z-dim of 173 voxels and z-pos of 41.
#! The first slice is a metal plate. Then the sample is
#! Divided into top 43 slices, middle 86 slices, and bottom 43 slices.
#!
#! The 'p1' org_file here is _bone.aim
#!
$ if p1 .EQS. ""
$ THEN
$ write sys$output "Give C0001234.aim ! Exit"
$ exit
$ endif
$
$ define org_file 'p1'
$ ezz_file = p1 - F$PARSE(p1,,,"VERSION") - "_BONE.AIM" +
"_EZZR_BONE.AIM"
$ epl_file = p1 - F$PARSE(p1,,,"VERSION") - "_BONE.AIM" +
"_EPLR_BONE.AIM"
$ vms_file = p1 - F$PARSE(p1,,,"VERSION") - "_BONE.AIM" +
"_VMSR_BONE.AIM"
$ sed_file = p1 - F$PARSE(p1,,,"VERSION") - "_BONE.AIM" +
"_SEDR_BONE.AIM"
```

```

$ ezzt_file = p1 - F$PARSE(p1,,,"VERSION") - "_BONE.AIM" +
"_EZZR_BONE_TOP.AIM"
$ eplt_file = p1 - F$PARSE(p1,,,"VERSION") - "_BONE.AIM" +
"_EPLR_BONE_TOP.AIM"
$ vmst_file = p1 - F$PARSE(p1,,,"VERSION") - "_BONE.AIM" +
"_VMSR_BONE_TOP.AIM"
$ sedt_file = p1 - F$PARSE(p1,,,"VERSION") - "_BONE.AIM" +
"_SEDR_BONE_TOP.AIM"
$ ezzm_file = p1 - F$PARSE(p1,,,"VERSION") - "_BONE.AIM" +
"_EZZR_BONE_MID.AIM"
$ eplm_file = p1 - F$PARSE(p1,,,"VERSION") - "_BONE.AIM" +
"_EPLR_BONE_MID.AIM"
$ vmsm_file = p1 - F$PARSE(p1,,,"VERSION") - "_BONE.AIM" +
"_VMSR_BONE_MID.AIM"
$ sedm_file = p1 - F$PARSE(p1,,,"VERSION") - "_BONE.AIM" +
"_SEDR_BONE_MID.AIM"
$ ezzb_file = p1 - F$PARSE(p1,,,"VERSION") - "_BONE.AIM" +
"_EZZR_BONE_BOT.AIM"
$ eplb_file = p1 - F$PARSE(p1,,,"VERSION") - "_BONE.AIM" +
"_EPLR_BONE_BOT.AIM"
$ vmsb_file = p1 - F$PARSE(p1,,,"VERSION") - "_BONE.AIM" +
"_VMSR_BONE_BOT.AIM"
$ sedb_file = p1 - F$PARSE(p1,,,"VERSION") - "_BONE.AIM" +
"_SEDR_BONE_BOT.AIM"
$ histo_ezzt = p1 - F$PARSE(p1,,,"VERSION") - "_BONE.AIM" +
"_EZZR_BONE_TOP.TAB"
$ histo_eplt = p1 - F$PARSE(p1,,,"VERSION") - "_BONE.AIM" +
"_EPLR_BONE_TOP.TAB"
$ histo_vmst = p1 - F$PARSE(p1,,,"VERSION") - "_BONE.AIM" +
"_VMSR_BONE_TOP.TAB"
$ histo_sedt = p1 - F$PARSE(p1,,,"VERSION") - "_BONE.AIM" +
"_SEDR_BONE_TOP.TAB"
$ histo_ezzm = p1 - F$PARSE(p1,,,"VERSION") - "_BONE.AIM" +
"_EZZR_BONE_MID.TAB"
$ histo_eplm = p1 - F$PARSE(p1,,,"VERSION") - "_BONE.AIM" +
"_EPLR_BONE_MID.TAB"
$ histo_vmsm = p1 - F$PARSE(p1,,,"VERSION") - "_BONE.AIM" +
"_VMSR_BONE_MID.TAB"
$ histo_sedm = p1 - F$PARSE(p1,,,"VERSION") - "_BONE.AIM" +
"_SEDR_BONE_MID.TAB"
$ histo_ezzb = p1 - F$PARSE(p1,,,"VERSION") - "_BONE.AIM" +
"_EZZR_BONE_BOT.TAB"
$ histo_eplb = p1 - F$PARSE(p1,,,"VERSION") - "_BONE.AIM" +
"_EPLR_BONE_BOT.TAB"

```

```

$ histo_vmsb = p1 - F$PARSE(p1,,,"VERSION") - "_BONE.AIM" +
"_VMSR_BONE_BOT.TAB"
$ histo_sedb = p1 - F$PARSE(p1,,,"VERSION") - "_BONE.AIM" +
"_SEDR_BONE_BOT.TAB"
$
$ show log org_file
$!
$ z_dim      := 172
$ z_dim_top  := 43
$ z_dim_mid  := 86
$ z_dim_bot  := 43
$
$ z_pos_top  := 1
$ z_pos_mid  := 44
$ z_pos_bot  := 130
$
$!
$ ipl_sanco_prog := $um:ipl_sanco_fe.exe
$!
$ ipl_sanco_prog

! ****EZZ****
/read
-name          out
-filename      "ezz_file

/sub_get
-input         out
-output        top
-pos           -1 -1 "z_pos_top
-dim           -1 -1 "z_dim_top
-global_pos_flag false
/gobj_maskaimpeel_ow
-input_output  top
-gobj_filename org_file
-peel_iter     0
/histo top
-fileout_or_screentab "histo_ezst
-from_val      -1
-to_val        -1
-nr_bins_in_tab 500
-dt_type       auto
-count_zeros   no
/write top "ezst_file
-compress_type bin

```

```

-version_020      true

/sub_get
-input            out
-output          mid
-pos             -1 -1 "z_pos_mid
-dim             -1 -1 "z_dim_mid
-global_pos_flag  false
/gobj_maskaimpeel_ow
-input_output     mid
-gobj_filename   org_file
-peel_iter       0
/histo mid
-fileout_or_screentab "histo_ezxm
-from_val        -1
-to_val          -1
-nr_bins_in_tab  500
-dt_type         auto
-count_zeros     no
/write mid "ezxm_file
-compress_type   bin
-version_020     true

/sub_get
-input            out
-output          bot
-pos             -1 -1 "z_pos_bot
-dim             -1 -1 "z_dim_bot
-global_pos_flag  false
/gobj_maskaimpeel_ow
-input_output     bot
-gobj_filename   org_file
-peel_iter       0
/histo bot
-fileout_or_screentab "histo_ezxb
-from_val        -1
-to_val          -1
-nr_bins_in_tab  500
-dt_type         auto
-count_zeros     no
/write bot "ezxb_file
-compress_type   bin
-version_020     true

/examine

```

```

-input          top
-item           geom
/examine
-input          mid
-item           geom
/examine
-input          bot
-item           geom

! ****EPL****
/read
-name           out
-filename       "epl_file

/sub_get
-input          out
-output         top
-pos            -1 -1 "z_pos_top
-dim            -1 -1 "z_dim_top
-global_pos_flag false
/gobj_maskaimpeel_ow
-input_output   top
-gobj_filename  org_file
-peel_iter      0
/histo top
-fileout_or_screentab "histo_eplt
-from_val       -1
-to_val         -1
-nr_bins_in_tab 500
-dt_type        auto
-count_zeros    no
/write top "eplt_file
-compress_type  bin
-version_020    true

/sub_get
-input          out
-output         mid
-pos            -1 -1 "z_pos_mid
-dim            -1 -1 "z_dim_mid
-global_pos_flag false
/gobj_maskaimpeel_ow
-input_output   mid
-gobj_filename  org_file
-peel_iter      0

```

```

/histo mid
-fileout_or_screentab "histo_eplm
-from_val -1
-to_val -1
-nr_bins_in_tab 500
-dt_type auto
-count_zeros no
/write mid "eplm_file
-compress_type bin
-version_020 true

/sub_get
-input out
-output bot
-pos -1 -1 "z_pos_bot
-dim -1 -1 "z_dim_bot
-global_pos_flag false
/gobj_maskaimpeel_ow
-input_output bot
-gobj_filename org_file
-peel_iter 0
/histo bot
-fileout_or_screentab "histo_eplb
-from_val -1
-to_val -1
-nr_bins_in_tab 500
-dt_type auto
-count_zeros no
/write bot "eplb_file
-compress_type bin
-version_020 true

/examine
-input top
-item geom
/examine
-input mid
-item geom
/examine
-input bot
-item geom

! ****VMS****
/read
-name out

```

```

-filename          "vms_file

/sub_get
-input            out
-output          top
-pos             -1 -1 "z_pos_top
-dim             -1 -1 "z_dim_top
-global_pos_flag  false
/gobj_maskaimpeel_ow
-input_output     top
-gobj_filename   org_file
-peel_iter       0
/histo top
-fileout_or_screentab "histo_vmst
-from_val        -1
-to_val          -1
-nr_bins_in_tab  50000
-dt_type         auto
-count_zeros     no
/write top "vmst_file
-compress_type   bin
-version_020     true

/sub_get
-input            out
-output          mid
-pos             -1 -1 "z_pos_mid
-dim             -1 -1 "z_dim_mid
-global_pos_flag  false
/gobj_maskaimpeel_ow
-input_output     mid
-gobj_filename   org_file
-peel_iter       0
/histo mid
-fileout_or_screentab "histo_vmsm
-from_val        -1
-to_val          -1
-nr_bins_in_tab  50000
-dt_type         auto
-count_zeros     no
/write mid "vmsm_file
-compress_type   bin
-version_020     true

/sub_get

```

```

-input          out
-output        bot
-pos           -1 -1 "z_pos_bot
-dim           -1 -1 "z_dim_bot
-global_pos_flag  false
/gobj_maskaimpeel_ow
-input_output   bot
-gobj_filename org_file
-peel_iter      0
/histo bot
-fileout_or_screentab "histo_vmsb
-from_val      -1
-to_val        -1
-nr_bins_in_tab 50000
-dt_type       auto
-count_zeros   no
/write bot "vmsb_file
-compress_type  bin
-version_020   true

/examine
-input         top
-item         geom
/examine
-input         mid
-item         geom
/examine
-input         bot
-item         geom

! ****SED****
/read
-name          out
-filename      "sed_file

/sub_get
-input         out
-output        top
-pos           -1 -1 "z_pos_top
-dim           -1 -1 "z_dim_top
-global_pos_flag  false
/gobj_maskaimpeel_ow
-input_output   top
-gobj_filename org_file
-peel_iter      0

```

```

/histo top
-fileout_or_screentab "histo_sedt
-from_val             -1
-to_val               -1
-nr_bins_in_tab      50000
-dt_type              auto
-count_zeros          no
/write top "sedt_file
-compress_type        bin
-version_020          true

/sub_get
-input                out
-output               mid
-pos                  -1 -1 "z_pos_mid
-dim                  -1 -1 "z_dim_mid
-global_pos_flag      false
/gobj_maskaimpeel_ow
-input_output         mid
-gobj_filename        org_file
-peel_iter            0
/histo mid
-fileout_or_screentab "histo_sedm
-from_val             -1
-to_val               -1
-nr_bins_in_tab      50000
-dt_type              auto
-count_zeros          no
/write mid "sedm_file
-compress_type        bin
-version_020          true

/sub_get
-input                out
-output               bot
-pos                  -1 -1 "z_pos_bot
-dim                  -1 -1 "z_dim_bot
-global_pos_flag      false
/gobj_maskaimpeel_ow
-input_output         bot
-gobj_filename        org_file
-peel_iter            0
/histo bot
-fileout_or_screentab "histo_sedb
-from_val             -1

```

```
-to_val          -1
-nr_bins_in_tab 50000
-dt_type         auto
-count_zeros     no
/write bot "sedb_file
-compress_type   bin
-version_020     true

/examine
-input          top
-item           geom
/examine
-input          mid
-item           geom
/examine
-input          bot
-item           geom

..
$ exit
```

The following batch file contains IPL commands necessary to separate the tissue response output for Material 1 (polymer phase “bone”) into zones (top 25%, middle 50%, and bottom 25%). To execute the following batch file, type the following command in a DecTerm window. The following example is for sample p26. Due to similarity to ad_fe_pc_regb_25p.com, the file has been truncated and portions omitted.

@{file_path}ad_fe_regb.com {file_path}*_bone.aim

ad_fe_pc_regb_26p.com

```

$!
$!  _/_/_/_/_/_/_/_/_/_
$!  _/_  _/_  _/_  _/_  Image Processing Language
$!  _/_  _/_/_/_/_/_/_
$!  _/_  _/_  _/_  (c) Andres Laib, Scanco Medical AG
$!  _/_/_/_/_/_/_/_/_/_
$!
$!
$!
$! IPL Batch FOR POST-PROCESSING ANGEL'S FE MODELS WITH 2
MATERIALS.
$! Prepared for the pre-culture study models of rMSCs on PLDL.
$! Divides resultant data into top, middle, and bottom regions.
$!
$! Written for p26 which has a z-dim of 162 voxels and z-pos of 32.
$! The first slice is a metal plate. Then the sample is
$! Divided into top 40 slices, middle 81 slices, and bottom 40 slices.
$!
.
.
SECTION DELETED FOR BREVITY
.
.
$!
$ z_dim      := 161
$ z_dim_top  := 40
$ z_dim_mid  := 81
$ z_dim_bot  := 40
$
$ z_pos_top  := 1
$ z_pos_mid  := 41
$ z_pos_bot  := 122
$
.
.
FILE TRUNCATED

```

The following batch file contains IPL commands necessary to separate the tissue response output for Material 1 (polymer phase “bone”) into zones (top 25%, middle 50%, and bottom 25%). To execute the following batch file, type the following command in a DecTerm window. The following example is for sample p93. Due to similarity to ad_fe_pc_regb_25p.com, the file has been truncated and portions omitted.

@{file_path}ad_fe_regb.com {file_path}*_bone.aim

ad_fe_pc_regb_93p.com

```

$!
$!  _/_/_/_/_/_/_/_/_/_
$!  _/_/_/_/_/_/_/_/_/_      Image Processing Language
$!  _/_/_/_/_/_/_/_/_/_
$!  _/_/_/_/_/_/_/_/_/_      (c) Andres Laib, Scanco Medical AG
$!  _/_/_/_/_/_/_/_/_/_
$!
$!
$!
$! IPL Batch FOR POST-PROCESSING ANGEL'S FE MODELS WITH 2
MATERIALS.
$! Prepared for the pre-culture study models of rMSCs on PLDL.
$! Divides resultant data into top, middle, and bottom regions.
$!
$! Written for p93 which has a z-dim of 157 voxels and z-pos of 39.
$! The first slice is a metal plate. Then the sample is
$! Divided into top 39 slices, middle 78 slices, and bottom 39 slices.
$!
.
.
SECTION DELETED FOR BREVITY
.
.
$!
$ z_dim      := 156
$ z_dim_top  := 39
$ z_dim_mid  := 78
$ z_dim_bot  := 39
$
$ z_pos_top  := 1
$ z_pos_mid  := 40
$ z_pos_bot  := 118
$
.
.
FILE TRUNCATED

```

The following batch file contains IPL commands necessary to separate the tissue response output for Material 2 (interstitial phase, “marrow”) into zones (top 25%, middle 50%, and bottom 25%). The code is very similar to ad_fe_pc_regb_xxp.com (where xx = 25, 26, or 93) and for that reason, only code for p25 is shown and the code below has been truncated. The necessary commands are shown to process \hat{a}_{zz} only. The commands may be repeated for \hat{a}_{p1} , VMS, and SED. To execute the batch file, type the following command in a DecTerm window.

```
@ {file_path}ad_fe_regm.com {file_path}*_mar.aim
```

ad_fe_pc_regm_25p.com

```

$!
$!   _/_/_/_/_/_/_/_/_/_
$!   _/_   _/_   _/_   _/_   Image Processing Language
$!   _/_   _/_/_/_/_/_
$!   _/_   _/_   _/_   (c) Andres Laib, Scanco Medical AG
$!   _/_/_/_/_/_   _/_/_/_/_/_
$!
$!
$!
$! IPL Batch FOR POST-PROCESSING ANGEL'S FE MODELS WITH 2
MATERIALS.
$! Prepared for the pre-culture study models of rMSCs on PLDL.
$! Divides resultant data into top, middle, and bottom regions.
$!
$! Written for p25 which has a z-dim of 173 voxels and z-pos of 41.
$! The first slice is a metal plate. Then the sample is
$! Divided into top 43 slices, middle 86 slices, and bottom 43 slices.
$!
$! The 'p1' org_file here is _mar.aim
$!
$ if p1 .EQS. ""
$ THEN
$ write sys$output "Give C0001234.aim ! Exit"
$ exit
$ endif
$
$ define org_file 'p1'
$
$ ezz_file = p1 - F$PARSE(p1,,,"VERSION") - "_MAR.AIM" + "_EZZR_MAR.AIM"
$ epl_file = p1 - F$PARSE(p1,,,"VERSION") - "_MAR.AIM" + "_EPLR_MAR.AIM"
$ vms_file = p1 - F$PARSE(p1,,,"VERSION") - "_MAR.AIM" +
"_VMSR_MAR.AIM"
$ sed_file = p1 - F$PARSE(p1,,,"VERSION") - "_MAR.AIM" + "_SEDR_MAR.AIM"
$ ezzt_file = p1 - F$PARSE(p1,,,"VERSION") - "_MAR.AIM" +
"_EZZR_MAR_TOP.AIM"

```

```

$ eplt_file = p1 - F$PARSE(p1,,,"VERSION") - "_MAR.AIM" +
  "_EPLR_MAR_TOP.AIM"
$ vmst_file = p1 - F$PARSE(p1,,,"VERSION") - "_MAR.AIM" +
  "_VMSR_MAR_TOP.AIM"
$ sedt_file = p1 - F$PARSE(p1,,,"VERSION") - "_MAR.AIM" +
  "_SEDR_MAR_TOP.AIM"
$ ezzm_file = p1 - F$PARSE(p1,,,"VERSION") - "_MAR.AIM" +
  "_EZZR_MAR_MID.AIM"
$ eplm_file = p1 - F$PARSE(p1,,,"VERSION") - "_MAR.AIM" +
  "_EPLR_MAR_MID.AIM"
$ vmsm_file = p1 - F$PARSE(p1,,,"VERSION") - "_MAR.AIM" +
  "_VMSR_MAR_MID.AIM"
$ sedm_file = p1 - F$PARSE(p1,,,"VERSION") - "_MAR.AIM" +
  "_SEDR_MAR_MID.AIM"
$ ezzb_file = p1 - F$PARSE(p1,,,"VERSION") - "_MAR.AIM" +
  "_EZZR_MAR_BOT.AIM"
$ eplb_file = p1 - F$PARSE(p1,,,"VERSION") - "_MAR.AIM" +
  "_EPLR_MAR_BOT.AIM"
$ vmsb_file = p1 - F$PARSE(p1,,,"VERSION") - "_MAR.AIM" +
  "_VMSR_MAR_BOT.AIM"
$ sedb_file = p1 - F$PARSE(p1,,,"VERSION") - "_MAR.AIM" +
  "_SEDR_MAR_BOT.AIM"
$ histo_ezzt = p1 - F$PARSE(p1,,,"VERSION") - "_MAR.AIM" +
  "_EZZR_MAR_TOP.TAB"
$ histo_eplt = p1 - F$PARSE(p1,,,"VERSION") - "_MAR.AIM" +
  "_EPLR_MAR_TOP.TAB"
$ histo_vmst = p1 - F$PARSE(p1,,,"VERSION") - "_MAR.AIM" +
  "_VMSR_MAR_TOP.TAB"
$ histo_sedt = p1 - F$PARSE(p1,,,"VERSION") - "_MAR.AIM" +
  "_SEDR_MAR_TOP.TAB"
$ histo_ezzm = p1 - F$PARSE(p1,,,"VERSION") - "_MAR.AIM" +
  "_EZZR_MAR_MID.TAB"
$ histo_eplm = p1 - F$PARSE(p1,,,"VERSION") - "_MAR.AIM" +
  "_EPLR_MAR_MID.TAB"
$ histo_vmsm = p1 - F$PARSE(p1,,,"VERSION") - "_MAR.AIM" +
  "_VMSR_MAR_MID.TAB"
$ histo_sedm = p1 - F$PARSE(p1,,,"VERSION") - "_MAR.AIM" +
  "_SEDR_MAR_MID.TAB"
$ histo_ezzb = p1 - F$PARSE(p1,,,"VERSION") - "_MAR.AIM" +
  "_EZZR_MAR_BOT.TAB"
$ histo_eplb = p1 - F$PARSE(p1,,,"VERSION") - "_MAR.AIM" +
  "_EPLR_MAR_BOT.TAB"
$ histo_vmsb = p1 - F$PARSE(p1,,,"VERSION") - "_MAR.AIM" +
  "_VMSR_MAR_BOT.TAB"

```

```

$ histo_sedb = p1 - F$PARSE(p1,,,"VERSION") - "_MAR.AIM" +
"_SEDR_MAR_BOT.TAB"
$
$
$ show log org_file
$!
$ z_dim      := 172
$ z_dim_top  := 43
$ z_dim_mid  := 86
$ z_dim_bot  := 43
$
$ z_pos_top  := 1
$ z_pos_mid  := 44
$ z_pos_bot  := 130
$
$!
$ ipl_sanco_prog := $um:ipl_sanco_fe.exe
$!
$ ipl_sanco_prog

! ****EZZ****
/read
-name          out
-filename      "ezz_file

/sub_get
-input         out
-output        top
-pos          -1 -1 "z_pos_top
-dim          -1 -1 "z_dim_top
-global_pos_flag  false
/gobj_maskaimpeel_ow
-input_output  top
-gobj_filename org_file
-peel_iter     0
/histo top
-fileout_or_screentab "histo_ezst
-from_val     -1
-to_val       -1
-nr_bins_in_tab 500
-dt_type      auto
-count_zeros  no
/write top "ezzt_file
-compress_type  bin
-version_020    true

```

```

/sub_get
-input          out
-output        mid
-pos           -1 -1 "z_pos_mid
-dim           -1 -1 "z_dim_mid
-global_pos_flag  false
/gobj_maskaimpeel_ow
-input_output   mid
-gobj_filename  org_file
-peel_iter      0
/histo mid
-fileout_or_screentab "histo_ezmm
-from_val       -1
-to_val         -1
-nr_bins_in_tab 500
-dt_type        auto
-count_zeros    no
/write mid "ezmm_file
-compress_type  bin
-version_020    true

```

```

/sub_get
-input          out
-output        bot
-pos           -1 -1 "z_pos_bot
-dim           -1 -1 "z_dim_bot
-global_pos_flag  false
/gobj_maskaimpeel_ow
-input_output   bot
-gobj_filename  org_file
-peel_iter      0
/histo bot
-fileout_or_screentab "histo_ezbb
-from_val       -1
-to_val         -1
-nr_bins_in_tab 500
-dt_type        auto
-count_zeros    no
/write bot "ezbb_file
-compress_type  bin
-version_020    true

```

```

/examine
-input          top

```

```
-item          geom
/examine
-input        mid
-item         geom
/examine
-input        bot
-item         geom
..
$ exit
```

The following batch file contains IPL commands to display statistical information on the tissue response of either Material 1 (polymer phase, “bone”) or Material 2 (interstitial phase, “marrow”) for different zones (top 25%, middle 50%, and bottom 25%). To execute the following batch file, type the following command in a DecTerm window.

```
@{file_path}ad_fe_regstat.com {file_path}*_xxx_bone.aim OR
@{file_path}ad_fe_regstat.com {file_path}*_xxx_mar.aim
where xxx = ezz, epl, vms, or sed
```

ad_fe_pc_regstat.com

```
$ if p1 .EQS. ""
$ THEN
$ write sys$output "Give C0001234.aim ! Exit"
$ exit
$ endif
$ define org_file 'p1'
$ top_file = p1 - F$PARSE(p1,,"VERSION") - ".AIM" + "_TOP.AIM"
$ mid_file = p1 - F$PARSE(p1,,"VERSION") - ".AIM" + "_MID.AIM"
$ bot_file = p1 - F$PARSE(p1,,"VERSION") - ".AIM" + "_BOT.AIM"
$ show log org_file
$ ipl_sanco_prog := $um:ipl_sanco_fe.exe
$ ipl_sanco_prog

/read
  -name          top
  -filename      "top_file"
/read
  -name          mid
  -filename      "mid_file"
/read
  -name          bot
  -filename      "bot_file"
/examine
  -input         top
  -item          stat
/examine
  -input         mid
  -item          stat
/examine
  -input         bot
  -item          stat

..
$ exit
```

The following batch file contains IPL commands to create histograms of the stresses and strains in the polymer with a reduced data set including 0-95th percentile for VMS and SED and 5th to 95th percentile for ezz and epl. To execute the following batch file, type the following command in a DecTerm window.

@ {file_path}ad_fe_pc_histo_bone_r.com {file_path}*_bone.aim OR

ad_fe_pc_histo_bone_r.com

```

$!
$!  _/_/_/_  _/_/_/_  _/
$!  _/  _/  _/  _/      Image Processing Language
$!  _/  _/_/_/_  _/
$!  _/  _/      _/      (c) Andres Laib, Scanco Medical AG
$!  _/_/_/_  _/      _/_/_/_/
$!
$!
$!
$!
$! IPL Batch FOR POST-PROCESSING ANGEL'S FE MODELS WITH 2
MATERIALS.
$! Prepared for the pre-culture study models of rMSCs on PLDL.
$! Reprocessing regional histogram data to exclude top
$! 5% of vms and sed voxels and the top 5% and bottom 5%
$! of epl voxels.
$!
$! The org file is _BONE.aim
$!
$ if p1 .EQS. ""
$ THEN
$ write sys$output "Give C0001234.aim ! Exit"
$ exit
$ endif
$
$ define org_file 'p1'
$ eplt_file = p1 - F$PARSE(p1,,,"VERSION") - "_BONE.AIM" +
"_EPLR_BONE_TOP.AIM"
$ vmst_file = p1 - F$PARSE(p1,,,"VERSION") - "_BONE.AIM" +
"_VMSR_BONE_TOP.AIM"
$ sedt_file = p1 - F$PARSE(p1,,,"VERSION") - "_BONE.AIM" +
"_SEDR_BONE_TOP.AIM"
$ eplm_file = p1 - F$PARSE(p1,,,"VERSION") - "_BONE.AIM" +
"_EPLR_BONE_MID.AIM"
$ vmsm_file = p1 - F$PARSE(p1,,,"VERSION") - "_BONE.AIM" +
"_VMSR_BONE_MID.AIM"
$ sedm_file = p1 - F$PARSE(p1,,,"VERSION") - "_BONE.AIM" +
"_SEDR_BONE_MID.AIM"

```

```

$ eplb_file = p1 - F$PARSE(p1,,,"VERSION") - "_BONE.AIM" +
"_EPLR_BONE_BOT.AIM"
$ vmsb_file = p1 - F$PARSE(p1,,,"VERSION") - "_BONE.AIM" +
"_VMSR_BONE_BOT.AIM"
$ sedb_file = p1 - F$PARSE(p1,,,"VERSION") - "_BONE.AIM" +
"_SEDR_BONE_BOT.AIM"
$ histo_eplt = p1 - F$PARSE(p1,,,"VERSION") - "_BONE.AIM" +
"_EPLR_BONE_TOP_R.TAB"
$ histo_vmst = p1 - F$PARSE(p1,,,"VERSION") - "_BONE.AIM" +
"_VMSR_BONE_TOP_R.TAB"
$ histo_sedt = p1 - F$PARSE(p1,,,"VERSION") - "_BONE.AIM" +
"_SEDR_BONE_TOP_R.TAB"
$ histo_eplm = p1 - F$PARSE(p1,,,"VERSION") - "_BONE.AIM" +
"_EPLR_BONE_MID_R.TAB"
$ histo_vmsm = p1 - F$PARSE(p1,,,"VERSION") - "_BONE.AIM" +
"_VMSR_BONE_MID_R.TAB"
$ histo_sedm = p1 - F$PARSE(p1,,,"VERSION") - "_BONE.AIM" +
"_SEDR_BONE_MID_R.TAB"
$ histo_eplb = p1 - F$PARSE(p1,,,"VERSION") - "_BONE.AIM" +
"_EPLR_BONE_BOT_R.TAB"
$ histo_vmsb = p1 - F$PARSE(p1,,,"VERSION") - "_BONE.AIM" +
"_VMSR_BONE_BOT_R.TAB"
$ histo_sedb = p1 - F$PARSE(p1,,,"VERSION") - "_BONE.AIM" +
"_SEDR_BONE_BOT_R.TAB"
$
$ show log org_file
$!
$ e_from := -22000
$ e_to := +1000
$ v_from := 0
$ v_to := 11
$ s_from := 0
$ s_to := 81000
$!
$ ipl_sanco_prog := $um:ipl_sanco_fe.exe
$!
$ ipl_sanco_prog

```

```

/read
-name          top
-filename      "eplt_file"
/read
-name          mid
-filename      "eplm_file"

```

```

/read
-name          bot
-filename      "eplb_file"
/mult_constant_ow
-in_out        top
-factor        1000000.000000
/mult_constant_ow
-in_out        mid
-factor        1000000.000000
/mult_constant_ow
-in_out        bot
-factor        1000000.000000
/histo top
-fileout_or_screentab "histo_eplt"
-from_val          "e_from"
-to_val           "e_to"
-nr_bins_in_tab   500
-dt_type          auto
-count_zeros      no
/histo mid
-fileout_or_screentab "histo_eplm"
-from_val          "e_from"
-to_val           "e_to"
-nr_bins_in_tab   500
-dt_type          auto
-count_zeros      no
/histo bot
-fileout_or_screentab "histo_eplb"
-from_val          "e_from"
-to_val           "e_to"
-nr_bins_in_tab   500
-dt_type          auto
-count_zeros      no

/read
-name          top
-filename      "vmst_file"
/read
-name          mid
-filename      "vmsm_file"
/read
-name          bot
-filename      "vmsb_file"
/histo top
-fileout_or_screentab "histo_vmst"

```

```

-from_val      "v_from
-to_val       "v_to
-nr_bins_in_tab    500
-dt_type      auto
-count_zeros  no
/histo mid
-fileout_or_screentab "histo_vmsm
-from_val     "v_from
-to_val      "v_to
-nr_bins_in_tab    500
-dt_type      auto
-count_zeros  no
/histo bot
-fileout_or_screentab "histo_vmsb
-from_val     "v_from
-to_val      "v_to
-nr_bins_in_tab    500
-dt_type      auto
-count_zeros  no

/read
-name         top
-filename     "sedt_file
/read
-name         mid
-filename     "sedm_file
/read
-name         bot
-filename     "sedb_file
/mult_constant_ow
-in_out      top
-factor      1000000.000000
/mult_constant_ow
-in_out      mid
-factor      1000000.000000
/mult_constant_ow
-in_out      bot
-factor      1000000.000000
/histo top
-fileout_or_screentab "histo_sedt
-from_val     "s_from
-to_val      "s_to
-nr_bins_in_tab    500
-dt_type      auto
-count_zeros  no

```

```
/histo mid
-fileout_or_screentab "histo_sedm
-from_val "s_from
-to_val "s_to
-nr_bins_in_tab 500
-dt_type auto
-count_zeros no
/histo bot
-fileout_or_screentab "histo_sedb
-from_val "s_from
-to_val "s_to
-nr_bins_in_tab 500
-dt_type auto
-count_zeros no

..
$ exit
```

The following batch file contains IPL commands to create histograms of the stresses and strains in the interstitial tissue with a reduced data set including 0-95th percentile for VMS and SED and 5th to 95th percentile for ezz and epl. Since the file is so similar to ad_fe_pc_histo_bone_r.com, the file has been truncated and sections omitted. To execute the following batch file, type the following command in a DecTerm window.

@{file_path}ad_fe_pc_histo_mar_r.com {file_path}*_mar.aim

ad_fe_pc_histo_mar_r.com

```

$!
$!  _/_/_/_/_/_/_/_/_/_
$!  _/_  _/_  _/_  _/_  Image Processing Language
$!  _/_  _/_/_/_/_/_
$!  _/_  _/_  _/_  (c) Andres Laib, Scanco Medical AG
$!  _/_/_/_/_/_  _/_/_/_/_/_
$!
$!
$!
$! IPL Batch FOR POST-PROCESSING ANGEL'S FE MODELS WITH 2
MATERIALS.
$! Prepared for the pre-culture study models of rMSCs on PLDL.
$! Reprocessing regional histogram data to exclude top
$! 5% of vms and sed voxels and the top 5% and bottom 5%
$! of epl voxels.
.
.
SECTION DELETED FOR BREVITY
.
.
$
$ show log org_file
$!
$ e_from := -186000
$ e_to := +3620
$ v_from := 0
$ v_to := 3
$ s_from := 0
$ s_to := 12500
$!
.
.
FILE TRUNCATED

```

The following batch file contains IPL commands to determine the distribution of new bone volume between top, middle, and bottom zones. The size of these zones may be changed by editing the z_* parameters in the variable assignment portion of the code. To execute the following batch file, type the following command in a DecTerm window.

@ {file_path}ad_fe_pc_vivo.com {file_path}*_seg.aim OR

ad_fe_pc_vivo.com

```

$! Prepared for the pre-culture study models of rMSCs on PLDL.
$! To be used to analyze the zones of the actual in vivo samples
$! Divides bone volume data into top, middle, and bottom regions.
$!
$! Must edit z_dim, z_dim_top, z_dim_mid, and z_dim_bot
$! for each file.
$!
$! The 'p1' org_file here is _seg.aim
$!
$ if p1 .EQS. ""
$ THEN
$ write sys$output "Give C0001234.aim ! Exit"
$ exit
$ endif
$
$ define org_file 'p1'
$ top_file = p1 - F$PARSE(p1,,"VERSION") - "_SEG.AIM" + "_TOP.AIM"
$ mid_file = p1 - F$PARSE(p1,,"VERSION") - "_SEG.AIM" + "_MID.AIM"
$ bot_file = p1 - F$PARSE(p1,,"VERSION") - "_SEG.AIM" + "_BOT.AIM"
$ histo_top = p1 - F$PARSE(p1,,"VERSION") - "_SEG.AIM" + "_TOP.TAB"
$ histo_mid = p1 - F$PARSE(p1,,"VERSION") - "_SEG.AIM" + "_MID.TAB"
$ histo_bot = p1 - F$PARSE(p1,,"VERSION") - "_SEG.AIM" + "_BOT.TAB"
$
$ show log org_file
$!
$ z_dim := 280
$ z_dim_top := 28
$ z_dim_mid := 224
$ z_dim_bot := 28
$ z_pos_mid := 28
$ z_pos_bot := 252
$
$ ipl_scanco_prog := $um:ipl_scanco_fe.exe
$ ipl_scanco_prog

/read
-name seg
-filename org_file

```

```
/sub_get
-input          seg
-output        top
-pos           -1 -1 -1
-dim           -1 -1 "z_dim_top
-global_pos_flag false
```

```
/histo top
-fileout_or_screentab "histo_top
-from_val             -1
-to_val               -1
-nr_bins_in_tab      200
-dt_type              auto
-count_zeros          no
```

```
/write top "top_file
-compress_type       bin
-version_020         true
```

```
/sub_get
-input          seg
-output        mid
-pos           -1 -1 "z_pos_mid
-dim           -1 -1 "z_dim_mid
-global_pos_flag false
```

```
/histo mid
-fileout_or_screentab "histo_mid
-from_val             -1
-to_val               -1
-nr_bins_in_tab      500
-dt_type              auto
-count_zeros          no
```

```
/write mid "mid_file
-compress_type       bin
-version_020         true
```

```
/sub_get
-input          seg
-output        bot
-pos           -1 -1 "z_pos_bot
-dim           -1 -1 "z_dim_bot
-global_pos_flag false
```

```
/histo bot
-fileout_or_screentab "histo_bot
-from_val             -1
-to_val               -1
```

```

-nr_bins_in_tab      200
-dt_type             auto
-count_zeros        no
/write bot "bot_file
-compress_type      bin
-version_020        true

/examine
-input              top
-item              geom
/examine
-input              mid
-item              geom
/examine
-input              bot
-item              geom

/voxgobj_scanco_param
-input              top
-gobj_filename      gobj_from_log
-peel_iter          -1
-region_number      0
/voxgobj_scanco_param
-input              mid
-gobj_filename      gobj_from_log
-peel_iter          -1
-region_number      0
/voxgobj_scanco_param
-input              bot
-gobj_filename      gobj_from_log
-peel_iter          -1
-region_number      0

..
$ exit

```

REFERENCES

1. Einhorn, T.A., *Clinically applied models of bone regeneration in tissue engineering research*. Clin Orthop, 1999(367 Suppl): p. S59-67.
2. Billenstien, D.C., *Disuse atrophy of bone with special reference to physical rehabilitation*. Phys Ther Rev, 1956. **36**(3): p. 169-73.
3. Stupakov, G.P., V.S. Kazeikin, and B.V. Morukov, *Microgravity-induced changes in human bone strength*. Physiologist, 1989. **32**(1 Suppl): p. S41-4.
4. Rodionova, N.V., V.S. Oganov, and N.V. Zolotova, *Ultrastructural changes in osteocytes in microgravity conditions*. Adv Space Res, 2002. **30**(4): p. 765-70.
5. McCarthy, I., A. Goodship, R. Herzog, V. Oganov, E. Stussi, and M. Vahlensieck, *Investigation of bone changes in microgravity during long and short duration space flight: Comparison of techniques*. Eur J Clin Invest, 2000. **30**(12): p. 1044-54.
6. Chesnut, C.H., 3rd, *Bone mass and exercise*. Am J Med, 1993. **95**(5A): p. 34S-36S.
7. Shimamura, C., J. Iwamoto, T. Takeda, S. Ichimura, H. Abe, and Y. Toyama, *Effect of decreased physical activity on bone mass in exercise-trained young rats*. J Orthop Sci, 2002. **7**(3): p. 358-63.
8. Mosekilde, L., C.C. Danielsen, C.H. Sogaard, and E. Thorling, *The effect of long-term exercise on vertebral and femoral bone mass, dimensions, and strength--assessed in a rat model*. Bone, 1994. **15**(3): p. 293-301.
9. Chow, R., J.E. Harrison, and C. Notarius, *Effect of two randomised exercise programmes on bone mass of healthy postmenopausal women*. Br Med J (Clin Res Ed), 1987. **295**(6611): p. 1441-4.
10. Rubin, C.T., T.S. Gross, K.J. McLeod, and S.D. Bain, *Morphologic stages in lamellar bone formation stimulated by a potent mechanical stimulus*. J Bone Miner Res, 1995. **10**(3): p. 488-95.
11. Rubin, C.T. and L.E. Lanyon, *Kappa delta award paper. Osteoregulatory nature of mechanical stimuli: Function as a determinant for adaptive remodeling in bone*. J Orthop Res, 1987. **5**(2): p. 300-10.
12. Carter, D.R., G.S. Beaupre, N.J. Giori, and J.A. Helms, *Mechanobiology of skeletal regeneration*. Clin Orthop, 1998(355 Suppl): p. S41-55.

13. Claes, L.E., C.A. Heigele, C. Neidlinger-Wilke, D. Kaspar, W. Seidl, K.J. Margevicius, and P. Augat, *Effects of mechanical factors on the fracture healing process*. Clin Orthop, 1998(355 Suppl): p. S132-47.
14. Goodship, A.E., J.L. Cunningham, and J. Kenwright, *Strain rate and timing of stimulation in mechanical modulation of fracture healing*. Clin Orthop, 1998(355 Suppl): p. S105-15.
15. Probst, A. and H.U. Spiegel, *Cellular mechanisms of bone repair*. J Invest Surg, 1997. **10**(3): p. 77-86.
16. Lacroix, D. and P.J. Prendergast, *A mechano-regulation model for tissue differentiation during fracture healing: Analysis of gap size and loading*. J Biomech, 2002. **35**(9): p. 1163-71.
17. Billotte, W.G. and M.C. Hofmann, *Establishment of a shear stress protocol to study the mechanosensitivity of human primary osteogenic cells in vitro*. Biomed Sci Instrum, 1999. **35**: p. 327-32.
18. Buckley, M.J., A.J. Banes, L.G. Levin, B.E. Sumpio, M. Sato, R. Jordan, J. Gilbert, G.W. Link, and R. Tran Son Tay, *Osteoblasts increase their rate of division and align in response to cyclic, mechanical tension in vitro*. Bone Miner, 1988. **4**(3): p. 225-36.
19. Stanford, C.M., J.A. Morcuende, and R.A. Brand, *Proliferative and phenotypic responses of bone-like cells to mechanical deformation*. J Orthop Res, 1995. **13**(5): p. 664-70.
20. Schaffer, J.L., M. Rizen, G.J. L'Italien, A. Benbrahim, J. Megerman, L.C. Gerstenfeld, and M.L. Gray, *Device for the application of a dynamic biaxially uniform and isotropic strain to a flexible cell culture membrane*. J Orthop Res, 1994. **12**(5): p. 709-19.
21. Ziros, P.G., A.P. Gil, T. Georgakopoulos, I. Habeos, D. Kletsas, E.K. Basdra, and A.G. Papavassiliou, *The bone-specific transcriptional regulator cbfa1 is a target of mechanical signals in osteoblastic cells*. J Biol Chem, 2002. **277**(26): p. 23934-41.
22. Richards, M., B.A. Huibregtse, A.I. Caplan, J.A. Goulet, and S.A. Goldstein, *Marrow-derived progenitor cell injections enhance new bone formation during distraction*. J Orthop Res, 1999. **17**(6): p. 900-8.
23. Rubin, C., M. Pope, J. Chris Fritton, M. Magnusson, T. Hansson, and K. McLeod, *Transmissibility of 15-hertz to 35-hertz vibrations to the human hip and lumbar spine: Determining the physiologic feasibility of delivering low-level anabolic mechanical stimuli to skeletal regions at greatest risk of fracture because of osteoporosis*. Spine, 2003. **28**(23): p. 2621-7.

24. Torvinen, S., P. Kannus, H. Sievanen, T.A. Jarvinen, M. Pasanen, S. Kontulainen, A. Nenonen, T.L. Jarvinen, T. Paakkala, M. Jarvinen, and I. Vuori, *Effect of 8-month vertical whole body vibration on bone, muscle performance, and body balance: A randomized controlled study*. J Bone Miner Res, 2003. **18**(5): p. 876-84.
25. Bancroft, G.N., V.I. Sikavitsas, J. van den Dolder, T.L. Sheffield, C.G. Ambrose, J.A. Jansen, and A.G. Mikos, *Fluid flow increases mineralized matrix deposition in 3d perfusion culture of marrow stromal osteoblasts in a dose-dependent manner*. Proc Natl Acad Sci U S A, 2002. **99**(20): p. 12600-5.
26. Reich, K.M., C.V. Gay, and J.A. Frangos, *Fluid shear stress as a mediator of osteoblast cyclic adenosine monophosphate production*. J Cell Physiol, 1990. **143**(1): p. 100-4.
27. Roelofsen, J., J. Klein-Nulend, and E.H. Burger, *Mechanical stimulation by intermittent hydrostatic compression promotes bone-specific gene expression in vitro*. J Biomech, 1995. **28**(12): p. 1493-503.
28. *Bone grafts and bone substitutes*. Orthop Network News, 1999. **10**(4): p. 10-17.
29. Guilak, F., D.L. Butler, S.A. Goldstein, and D.J. Mooney, eds. *Functional tissue engineering*. 2003, Springer-Verlag: New York. 426.
30. Laib, A., O. Barou, L. Vico, M.H. Lafage-Proust, C. Alexandre, and P. Rugsegger, *3d micro-computed tomography of trabecular and cortical bone architecture with application to a rat model of immobilisation osteoporosis*. Med Biol Eng Comput, 2000. **38**(3): p. 326-32.
31. Wolff, J., *Das gesetz der transformation der inneren architektur derknochen bei pathologischen veränderungen der ausseren knochenform*. 1884, Berlin: Kniglich Preussischen Akad. Wissensch.
32. Wolff, J., *Das gesetz der transformation der knochen*. 1892, Berlin: Hirschwald.
33. Lanyon, L.E., *Analysis of surface bone strain in the calcaneus of sheep during normal locomotion. Strain analysis of the calcaneus*. J Biomech, 1973. **6**(1): p. 41-9.
34. Frost, H.M., *The mechanostat: A proposed pathogenic mechanism of osteoporoses and the bone mass effects of mechanical and nonmechanical agents*. Bone Miner, 1987. **2**(2): p. 73-85.
35. Frost, H.M., *Skeletal structural adaptations to mechanical usage (satmu): I. Redefining wolff's law: The bone modeling problem*. Anat Rec, 1990. **226**(4): p. 403-13.

36. Frost, H.M., *Skeletal structural adaptations to mechanical usage (satmu): 2. Redefining wolff's law: The remodeling problem.* Anat Rec, 1990. **226**(4): p. 414-22.
37. Bloomfield, S.A., *Changes in musculoskeletal structure and function with prolonged bed rest.* Med Sci Sports Exerc, 1997. **29**(2): p. 197-206.
38. Whedon, G.D., *Disuse osteoporosis: Physiological aspects.* Calcif Tissue Int, 1984. **36 Suppl 1**: p. S146-50.
39. Convertino, V.A., D.F. Doerr, K.L. Mathes, S.L. Stein, and P. Buchanan, *Changes in volume, muscle compartment, and compliance of the lower extremities in man following 30 days of exposure to simulated microgravity.* Aviat Space Environ Med, 1989. **60**(7): p. 653-8.
40. Takamoto, S., T. Masuyama, M. Nakajima, K. Seikiya, H. Kosaka, S. Morimoto, T. Ogihara, and T. Onishi, *Alterations of bone mineral density of the femurs in hemiplegia.* Calcif Tissue Int, 1995. **56**(4): p. 259-62.
41. Marchetti, M.E., J.P. Houde, G.G. Steinberg, G.K. Crane, T.P. Goss, and D.T. Baran, *Humeral bone density losses after shoulder surgery and immobilization.* J Shoulder Elbow Surg, 1996. **5**(6): p. 471-6.
42. Giesen, E.B., M. Ding, M. Dalstra, and T.M. van Eijden, *Reduced mechanical load decreases the density, stiffness, and strength of cancellous bone of the mandibular condyle.* Clin Biomech (Bristol, Avon), 2003. **18**(4): p. 358-63.
43. Oikarinen, V.J. and H.S. Siirila, *Reparative bone growth in an extremely atrophied edentulous mandible stimulated by an osseointegrated implant-supported fixed prosthesis: A case report.* Int J Oral Maxillofac Implants, 1992. **7**(4): p. 541-4.
44. Kurokouchi, K., T. Ito, S. Ohmori, K. Kanda, Y. Murata, R. Izumi, M. Inazu, H. Iwata, and H. Seo, *Effects of bisphosphonate on bone metabolism in tail-suspended rats.* Environ Med, 1996. **40**(1): p. 39-42.
45. Kurokouchi, K., T. Ito, S. Ohmori, K. Kanda, Y. Murata, and H. Seo, *Changes in the markers of bone metabolism following skeletal unloading.* Environ Med, 1995. **39**(1): p. 21-4.
46. Cohen, I., E. Bogin, A. Chechick, and V. Rzetelny, *The effect of single hind-limb immobilization on the contralateral limb in the rat: A morphometric and biochemical study.* Am J Orthop, 1999. **28**(12): p. 706-8.
47. Weinreb, M., G.A. Rodan, and D.D. Thompson, *Osteopenia in the immobilized rat hind limb is associated with increased bone resorption and decreased bone formation.* Bone, 1989. **10**(3): p. 187-94.

48. Kannus, P., T.L. Jarvinen, H. Sievanen, M. Kvist, J. Rauhaniemi, V.M. Maunu, T. Hurme, L. Jozsa, and M. Jarvinen, *Effects of immobilization, three forms of remobilization, and subsequent deconditioning on bone mineral content and density in rat femora*. J Bone Miner Res, 1996. **11**(9): p. 1339-46.
49. Cheng, S., S. Sipila, D.R. Taaffe, J. Puolakka, and H. Suominen, *Change in bone mass distribution induced by hormone replacement therapy and high-impact physical exercise in post-menopausal women*. Bone, 2002. **31**(1): p. 126-35.
50. Carter, D.R., P.R. Blenman, and G.S. Beaupre, *Correlations between mechanical stress history and tissue differentiation in initial fracture healing*. J Orthop Res, 1988. **6**(5): p. 736-48.
51. Oxlund, B.S., G. Ortoft, T.T. Andreassen, and H. Oxlund, *Low-intensity, high-frequency vibration appears to prevent the decrease in strength of the femur and tibia associated with ovariectomy of adult rats*. Bone, 2003. **32**(1): p. 69-77.
52. Judex, S., S. Boyd, Y.X. Qin, S. Turner, K. Ye, R. Muller, and C. Rubin, *Adaptations of trabecular bone to low magnitude vibrations result in more uniform stress and strain under load*. Ann Biomed Eng, 2003. **31**(1): p. 12-20.
53. Tanaka, S.M., J. Li, R.L. Duncan, H. Yokota, D.B. Burr, and C.H. Turner, *Effects of broad frequency vibration on cultured osteoblasts*. J Biomech, 2003. **36**(1): p. 73-80.
54. Mosley, J.R. and L.E. Lanyon, *Strain rate as a controlling influence on adaptive modeling in response to dynamic loading of the ulna in growing male rats*. Bone, 1998. **23**(4): p. 313-8.
55. Forwood, M.R., I. Owan, Y. Takano, and C.H. Turner, *Increased bone formation in rat tibiae after a single short period of dynamic loading in vivo*. Am J Physiol, 1996. **270**(3 Pt 1): p. E419-23.
56. Lanyon, L.E. and C.T. Rubin, *Static vs dynamic loads as an influence on bone remodelling*. J Biomech, 1984. **17**(12): p. 897-905.
57. Robling, A.G., K.M. Duijvelaar, J.V. Gevers, N. Ohashi, and C.H. Turner, *Modulation of appositional and longitudinal bone growth in the rat ulna by applied static and dynamic force*. Bone, 2001. **29**(2): p. 105-13.
58. Turner, C.H. and F.M. Pavalko, *Mechanotransduction and functional response of the skeleton to physical stress: The mechanisms and mechanics of bone adaptation*. J Orthop Sci, 1998. **3**(6): p. 346-55.
59. Robling, A.G., F.M. Hinant, D.B. Burr, and C.H. Turner, *Improved bone structure and strength after long-term mechanical loading is greatest if loading is separated into short bouts*. J Bone Miner Res, 2002. **17**(8): p. 1545-54.

60. Donahue, S.W., H.J. Donahue, and C.R. Jacobs, *Osteoblastic cells have refractory periods for fluid-flow-induced intracellular calcium oscillations for short bouts of flow and display multiple low-magnitude oscillations during long-term flow*. J Biomech, 2003. **36**(1): p. 35-43.
61. Robling, A.G., F.M. Hinant, D.B. Burr, and C.H. Turner, *Shorter, more frequent mechanical loading sessions enhance bone mass*. Med Sci Sports Exerc, 2002. **34**(2): p. 196-202.
62. Klein-Nulend, J., J. Roelofsen, J.G. Sterck, C.M. Semeins, and E.H. Burger, *Mechanical loading stimulates the release of transforming growth factor- beta activity by cultured mouse calvariae and periosteal cells*. J Cell Physiol, 1995. **163**(1): p. 115-9.
63. Weinbaum, S., S.C. Cowin, and Y. Zeng, *A model for the excitation of osteocytes by mechanical loading-induced bone fluid shear stresses*. J Biomech, 1994. **27**(3): p. 339-60.
64. Sterck, J.G., J. Klein-Nulend, P. Lips, and E.H. Burger, *Response of normal and osteoporotic human bone cells to mechanical stress in vitro*. Am J Physiol, 1998. **274**(6 Pt 1): p. E1113-20.
65. Smalt, R., F.T. Mitchell, R.L. Howard, and T.J. Chambers, *Mechanotransduction in bone cells: Induction of nitric oxide and prostaglandin synthesis by fluid shear stress, but not by mechanical strain*. Adv Exp Med Biol, 1997. **433**: p. 311-4.
66. Smalt, R., F.T. Mitchell, R.L. Howard, and T.J. Chambers, *Induction of no and prostaglandin e2 in osteoblasts by wall-shear stress but not mechanical strain*. Am J Physiol, 1997. **273**(4 Pt 1): p. E751-8.
67. Walsh, W.R. and N. Guzelsu, *Ion concentration effects on bone streaming potentials and zeta potentials*. Biomaterials, 1993. **14**(5): p. 331-6.
68. MacGinitie, L.A., D.D. Wu, and G.V. Cochran, *Streaming potentials in healing, remodeling, and intact cortical bone*. J Bone Miner Res, 1993. **8**(11): p. 1323-35.
69. Cochran, G.V., D.D. Wu, B.Y. Lee, W. Bieber, and M.W. Otter, *Streaming potentials in gap osteotomy callus and adjacent cortex. A pilot study*. Clin Orthop, 1997(337): p. 291-301.
70. Burr, D.B., R.B. Martin, M.B. Schaffler, and E.L. Radin, *Bone remodeling in response to in vivo fatigue microdamage*. J Biomech, 1985. **18**(3): p. 189-200.
71. Prendergast, P.J. and R. Huiskes, *Microdamage and osteocyte-lacuna strain in bone: A microstructural finite element analysis*. J Biomech Eng, 1996. **118**(2): p. 240-6.

72. Reilly, G.C., *Observations of microdamage around osteocyte lacunae in bone*. J Biomech, 2000. **33**(9): p. 1131-4.
73. Lee, T.C., A. Staines, and D. Taylor, *Bone adaptation to load: Microdamage as a stimulus for bone remodelling*. J Anat, 2002. **201**(6): p. 437-46.
74. Duncan, R.L. and C.H. Turner, *Mechanotransduction and the functional response of bone to mechanical strain*. Calcif Tissue Int, 1995. **57**(5): p. 344-58.
75. Moalli, M.R., S. Wang, N.J. Caldwell, P.V. Patil, and C.R. Maynard, *Mechanical stimulation induces pp125(fak) and pp60(src) activity in an in vivo model of trabecular bone formation*. J Appl Physiol, 2001. **91**(2): p. 912-8.
76. You, J., C.E. Yellowley, H.J. Donahue, Y. Zhang, Q. Chen, and C.R. Jacobs, *Substrate deformation levels associated with routine physical activity are less stimulatory to bone cells relative to loading-induced oscillatory fluid flow*. J Biomech Eng, 2000. **122**(4): p. 387-93.
77. Jacobs, C.R., C.E. Yellowley, B.R. Davis, Z. Zhou, J.M. Cimbala, and H.J. Donahue, *Differential effect of steady versus oscillating flow on bone cells*. J Biomech, 1998. **31**(11): p. 969-76.
78. Meazzini, M.C., C.D. Toma, J.L. Schaffer, M.L. Gray, and L.C. Gerstenfeld, *Osteoblast cytoskeletal modulation in response to mechanical strain in vitro*. J Orthop Res, 1998. **16**(2): p. 170-80.
79. Lozupone, E., A. Favia, B. Cafagna, and F.P. Cantatore, *[the concentration of osteocalcin in the culture media of bone cultured in vitro subjected to intermittent mechanical load with the addition of 1,25(oh)2d3]*. Boll Soc Ital Biol Sper, 1993. **69**(5): p. 281-5.
80. Yeh, C.K. and G.A. Rodan, *Tensile forces enhance prostaglandin e synthesis in osteoblastic cells grown on collagen ribbons*. Calcif Tissue Int, 1984. **36**(Suppl 1): p. S67-71.
81. Kaspar, D., W. Seidl, A. Ignatius, C. Neidlinger-Wilke, and L. Claes, *[in vitro cell behavior of human osteoblasts after physiological dynamic stretching]*. Orthopade, 2000. **29**(2): p. 85-90.
82. Klein-Nulend, J., J. Roelofsen, C.M. Semeins, A.L. Bronckers, and E.H. Burger, *Mechanical stimulation of osteopontin mrna expression and synthesis in bone cell cultures*. J Cell Physiol, 1997. **170**(2): p. 174-81.
83. Rubin, J., X. Fan, D.M. Biskobing, W.R. Taylor, and C.T. Rubin, *Osteoclastogenesis is repressed by mechanical strain in an in vitro model*. J Orthop Res, 1999. **17**(5): p. 639-45.

84. Rubin, J., T. Murphy, M.S. Nanes, and X. Fan, *Mechanical strain inhibits expression of osteoclast differentiation factor by murine stromal cells*. Am J Physiol Cell Physiol, 2000. **278**(6): p. C1126-32.
85. Weyts, F.A., B. Bosmans, R. Niesing, J.P. van Leeuwen, and H. Weinans, *Mechanical control of human osteoblast apoptosis and proliferation in relation to differentiation*. Calcif Tissue Int, 2003. **72**(4): p. 505-12.
86. Goodman, S., T. Ma, M. Trindade, T. Ikenoue, I. Matsuura, N. Wong, N. Fox, M. Genovese, D. Regula, and R.L. Smith, *Cox-2 selective nsaid decreases bone ingrowth in vivo*. J Orthop Res, 2002. **20**(6): p. 1164-9.
87. Goodman, S.B., Y. Song, J.Y. Yoo, N. Fox, M.C. Trindade, G. Kajiyama, T. Ma, D. Regula, J. Brown, and R.L. Smith, *Local infusion of fgf-2 enhances bone ingrowth in rabbit chambers in the presence of polyethylene particles*. J Biomed Mater Res, 2003. **65A**(4): p. 454-61.
88. Aspenberg, P., T. Albrektsson, L.S. Lohmander, and K.G. Thorngren, *Drug test chamber: A titanium implant for administration of biochemical agents to a standardized bone callus in situ*. J Biomed Eng, 1988. **10**(1): p. 70-3.
89. Frenkel, S.R., J. Simon, H. Alexander, M. Dennis, and J.L. Ricci, *Osseointegration on metallic implant surfaces: Effects of microgeometry and growth factor treatment*. J Biomed Mater Res, 2002. **63**(6): p. 706-13.
90. Ogawa, T. and I. Nishimura, *Different bone integration profiles of turned and acid-etched implants associated with modulated expression of extracellular matrix genes*. Int J Oral Maxillofac Implants, 2003. **18**(2): p. 200-10.
91. Kaigler, D. and B.R. Lang, *The bone biopsy chamber: An improved method of collecting osseous tissue*. Int J Oral Maxillofac Implants, 1989. **4**(3): p. 183-90.
92. Lamerigts, N., P. Aspenberg, P. Buma, D. Versleyen, and T.J. Slooff, *The repeated sampling bone chamber: A new permanent titanium implant to study bone grafts in the goat*. Lab Anim Sci, 1997. **47**(4): p. 401-6.
93. Buch, F., T. Albrektsson, and E. Herbst, *The bone growth chamber for quantification of electrically induced osteogenesis*. J Orthop Res, 1986. **4**(2): p. 194-203.
94. Luk, A.S., H. Winet, and J.Y. Bao, *Effect of polymethylmethacrylate particles on mature bone in the optical bone chamber*. J Biomed Mater Res, 2001. **55**(2): p. 177-84.
95. Aspenberg, P., S. Goodman, S. Toksvig-Larsen, L. Ryd, and T. Albrektsson, *Intermittent micromotion inhibits bone ingrowth. Titanium implants in rabbits*. Acta Orthop Scand, 1992. **63**(2): p. 141-5.

96. Goodman, S. and P. Aspenberg, *Effect of amplitude of micromotion on bone ingrowth into titanium chambers implanted in the rabbit tibia*. *Biomaterials*, 1992. **13**(13): p. 944-8.
97. Tagil, M. and P. Aspenberg, *Cartilage induction by controlled mechanical stimulation in vivo*. *J Orthop Res*, 1999. **17**(2): p. 200-4.
98. Lamerigts, N.M., P. Buma, R. Huiskes, W. Schreurs, J. Gardeniers, and T.J. Slooff, *Incorporation of morsellized bone graft under controlled loading conditions. A new animal model in the goat*. *Biomaterials*, 2000. **21**(7): p. 741-7.
99. Guldberg, R.E., *Mechanical adaptation of trabecular bone formation in vivo*. Ph.D. Thesis, University of Michigan, 1995.
100. Guldberg, R.E., N.J. Caldwell, X.E. Guo, R.W. Goulet, S.J. Hollister, and S.A. Goldstein, *Mechanical stimulation of tissue repair in the hydraulic bone chamber*. *J Bone Miner Res*, 1997. **12**(8): p. 1295-302.
101. Moalli, M.R., N.J. Caldwell, P.V. Patil, and S.A. Goldstein, *An in vivo model for investigations of mechanical signal transduction in trabecular bone*. *J Bone Miner Res*, 2000. **15**(7): p. 1346-53.
102. Case, N.D., A.O. Duty, A. Ratcliffe, R. Muller, and R.E. Guldberg, *Bone formation on tissue-engineered cartilage constructs in vivo: Effects of chondrocyte viability and mechanical loading*. *Tissue Eng*, 2003. **9**(4): p. 587-96.
103. Yaszemski, M.J., R.G. Payne, W.C. Hayes, R. Langer, and A.G. Mikos, *Evolution of bone transplantation: Molecular, cellular and tissue strategies to engineer human bone*. *Biomaterials*, 1996. **17**(2): p. 175-85.
104. Bruder, S.P. and B.S. Fox, *Tissue engineering of bone. Cell based strategies*. *Clin Orthop*, 1999(367 Suppl): p. S68-83.
105. Doll, B., C. Sfeir, S. Winn, J. Huard, and J. Hollinger, *Critical aspects of tissue-engineered therapy for bone regeneration*. *Crit Rev Eukaryot Gene Expr*, 2001. **11**(1-3): p. 173-98.
106. Breitbart, A.S., D.A. Grande, J.M. Mason, M. Barcia, T. James, and R.T. Grant, *Gene-enhanced tissue engineering: Applications for bone healing using cultured periosteal cells transduced retrovirally with the bmp-7 gene*. *Ann Plast Surg*, 1999. **42**(5): p. 488-95.
107. Byers, B.A., *In vitro and in vivo characterization of a cell source for bone tissue engineering applications: Primary bone marrow stromal cells overexpressing the osteoblast-specific transcriptional activator runx2/cbfa1*. Ph.D. Thesis, Georgia Institute of Technology, 2003.

108. Solchaga, L.A., J. Gao, J.E. Dennis, A. Awadallah, M. Lundberg, A.I. Caplan, and V.M. Goldberg, *Treatment of osteochondral defects with autologous bone marrow in a hyaluronan-based delivery vehicle*. *Tissue Eng*, 2002. **8**(2): p. 333-47.
109. Rodrigues, C.V., P. Serricella, A.B. Linhares, R.M. Guerdes, R. Borojevic, M.A. Rossi, M.E. Duarte, and M. Farina, *Characterization of a bovine collagen-hydroxyapatite composite scaffold for bone tissue engineering*. *Biomaterials*, 2003. **24**(27): p. 4987-97.
110. Bruder, S.P., K.H. Kraus, V.M. Goldberg, and S. Kadiyala, *The effect of implants loaded with autologous mesenchymal stem cells on the healing of canine segmental bone defects*. *J Bone Joint Surg Am*, 1998. **80**(7): p. 985-96.
111. Ohgushi, H., J. Miyake, and T. Tateishi, *Mesenchymal stem cells and bioceramics: Strategies to regenerate the skeleton*. *Novartis Found Symp*, 2003. **249**: p. 118-27; discussion 127-32, 170-4, 239-41.
112. Okumura, M., H. Ohgushi, Y. Dohi, T. Katuda, S. Tamai, H.K. Koerten, and S. Tabata, *Osteoblastic phenotype expression on the surface of hydroxyapatite ceramics*. *J Biomed Mater Res*, 1997. **37**(1): p. 122-9.
113. Taboas, J.M., R.D. Maddox, P.H. Krebsbach, and S.J. Hollister, *Indirect solid free form fabrication of local and global porous, biomimetic and composite 3d polymer-ceramic scaffolds*. *Biomaterials*, 2003. **24**(1): p. 181-94.
114. Boo, J.S., Y. Yamada, Y. Okazaki, Y. Hibino, K. Okada, K. Hata, T. Yoshikawa, Y. Sugiura, and M. Ueda, *Tissue-engineered bone using mesenchymal stem cells and a biodegradable scaffold*. *J Craniofac Surg*, 2002. **13**(2): p. 231-9; discussion 240-3.
115. Dong, J., T. Uemura, Y. Shirasaki, and T. Tateishi, *Promotion of bone formation using highly pure porous beta-tcp combined with bone marrow-derived osteoprogenitor cells*. *Biomaterials*, 2002. **23**(23): p. 4493-502.
116. Livingston, T., P. Ducheyne, and J. Garino, *In vivo evaluation of a bioactive scaffold for bone tissue engineering*. *J Biomed Mater Res*, 2002. **62**(1): p. 1-13.
117. Chen, F., T. Mao, K. Tao, S. Chen, G. Ding, and X. Gu, *Bone graft in the shape of human mandibular condyle reconstruction via seeding marrow-derived osteoblasts into porous coral in a nude mice model*. *J Oral Maxillofac Surg*, 2002. **60**(10): p. 1155-9.
118. Fisher, J.P., J.W. Vehof, D. Dean, J.P. van der Waerden, T.A. Holland, A.G. Mikos, and J.A. Jansen, *Soft and hard tissue response to photocrosslinked poly(propylene fumarate) scaffolds in a rabbit model*. *J Biomed Mater Res*, 2002. **59**(3): p. 547-56.

119. Zhang, J., B.A. Doll, E.J. Beckman, and J.O. Hollinger, *A biodegradable polyurethane-ascorbic acid scaffold for bone tissue engineering*. J Biomed Mater Res, 2003. **67A**(2): p. 389-400.
120. Ganta, S.R., N.P. Piesco, P. Long, R. Gassner, L.F. Motta, G.D. Papworth, D.B. Stolz, S.C. Watkins, and S. Agarwal, *Vascularization and tissue infiltration of a biodegradable polyurethane matrix*. J Biomed Mater Res, 2003. **64A**(2): p. 242-8.
121. Endres, M., D.W. Hutmacher, A.J. Salgado, C. Kaps, J. Ringe, R.L. Reis, M. Sittinger, A. Brandwood, and J.T. Schantz, *Osteogenic induction of human bone marrow-derived mesenchymal progenitor cells in novel synthetic polymer-hydrogel matrices*. Tissue Eng, 2003. **9**(4): p. 689-702.
122. Schantz, J.T., S.H. Teoh, T.C. Lim, M. Endres, C.X. Lam, and D.W. Hutmacher, *Repair of calvarial defects with customized tissue-engineered bone grafts i. Evaluation of osteogenesis in a three-dimensional culture system*. Tissue Eng, 2003. **9 Suppl 1**: p. S113-26.
123. Deschamps, A.A., M.B. Claase, W.J. Sleijster, J.D. de Bruijn, D.W. Grijpma, and J. Feijen, *Design of segmented poly(ether ester) materials and structures for the tissue engineering of bone*. J Control Release, 2002. **78**(1-3): p. 175-86.
124. Fialkov, J.A., C.E. Holy, M.S. Shoichet, and J.E. Davies, *In vivo bone engineering in a rabbit femur*. J Craniofac Surg, 2003. **14**(3): p. 324-32.
125. Abukawa, H., H. Terai, D. Hannouche, J.P. Vacanti, L.B. Kaban, and M.J. Troulis, *Formation of a mandibular condyle in vitro by tissue engineering*. J Oral Maxillofac Surg, 2003. **61**(1): p. 94-100.
126. Ishaug-Riley, S.L., G.M. Crane-Kruger, M.J. Yaszemski, and A.G. Mikos, *Three-dimensional culture of rat calvarial osteoblasts in porous biodegradable polymers*. Biomaterials, 1998. **19**(15): p. 1405-12.
127. Kadiyala, S., R.G. Young, M.A. Thiede, and S.P. Bruder, *Culture expanded canine mesenchymal stem cells possess osteochondrogenic potential in vivo and in vitro*. Cell Transplant, 1997. **6**(2): p. 125-34.
128. Wittbjer, J., B. Palmer, M. Rohlin, and K.G. Thorngren, *Osteogenetic activity in composite grafts of demineralized compact bone and marrow*. Clin Orthop, 1983(173): p. 229-38.
129. Ragni, P., P. Ala-Mononen, and T.S. Lindholm, *Spinal fusion induced by porous hydroxyapatite blocks (ha). Experimental comparative study with ha, demineralized bone matrix and autogenous bone marrow*. Ital J Orthop Traumatol, 1993. **19**(1): p. 133-44.

130. Gebhart, M. and J. Lane, *A radiographical and biomechanical study of demineralized bone matrix implanted into a bone defect of rat femurs with and without bone marrow*. Acta Orthop Belg, 1991. **57**(2): p. 130-43.
131. Ishaug-Riley, S.L., G.M. Crane, A. Gurlek, M.J. Miller, A.W. Yasko, M.J. Yaszemski, and A.G. Mikos, *Ectopic bone formation by marrow stromal osteoblast transplantation using poly(dl-lactic-co-glycolic acid) foams implanted into the rat mesentery*. J Biomed Mater Res, 1997. **36**(1): p. 1-8.
132. Bruder, S.P., N. Jaiswal, and S.E. Haynesworth, *Growth kinetics, self-renewal, and the osteogenic potential of purified human mesenchymal stem cells during extensive subcultivation and following cryopreservation*. J Cell Biochem, 1997. **64**(2): p. 278-94.
133. Deasy, B.M. and J. Huard, *Gene therapy and tissue engineering based on muscle-derived stem cells*. Curr Opin Mol Ther, 2002. **4**(4): p. 382-9.
134. Huang, J.I., S.R. Beanes, M. Zhu, H.P. Lorenz, M.H. Hedrick, and P. Benhaim, *Rat extramedullary adipose tissue as a source of osteochondrogenic progenitor cells*. Plast Reconstr Surg, 2002. **109**(3): p. 1033-41; discussion 1042-3.
135. Mizuno, H. and H. Hyakusoku, *Mesengenic potential and future clinical perspective of human processed lipoaspirate cells*. J Nippon Med Sch, 2003. **70**(4): p. 300-6.
136. Zuk, P.A., M. Zhu, H. Mizuno, J. Huang, J.W. Futrell, A.J. Katz, P. Benhaim, H.P. Lorenz, and M.H. Hedrick, *Multilineage cells from human adipose tissue: Implications for cell-based therapies*. Tissue Eng, 2001. **7**(2): p. 211-28.
137. De Kok, I.J., S.J. Peter, M. Archambault, C. van den Bos, S. Kadiyala, I. Aukhil, and L.F. Cooper, *Investigation of allogeneic mesenchymal stem cell-based alveolar bone formation: Preliminary findings*. Clin Oral Implants Res, 2003. **14**(4): p. 481-9.
138. Arinzeh, T.L., S.J. Peter, M.P. Archambault, C. van den Bos, S. Gordon, K. Kraus, A. Smith, and S. Kadiyala, *Allogeneic mesenchymal stem cells regenerate bone in a critical-sized canine segmental defect*. J Bone Joint Surg Am, 2003. **85-A**(10): p. 1927-35.
139. Peter, S.J., T. Livingston, S. Gordon, M. Yagami, E. Klyushnenkova, K. McIntosh, J. Wagner, M. ELKalay, R.G. Young, and S. Kadiyala. *Bone formation via allogeneic mesenchymal stem cell implantation*. in *World Congress of Biomaterials Conference*. 2000. Kamuela, Hawaii.

140. Archambault, M.P., K. McIntosh, A.O. Duty, and S.J. Peter. *Allogeneic rat mesenchymal stem cells do not elicit an immune response after implantation in immunocompetent recipients*. in *The American Society of Hematology 42nd Annual Meeting*. 2000. San Fransisco, California.
141. Jaiswal, N., S.E. Haynesworth, A.I. Caplan, and S.P. Bruder, *Osteogenic differentiation of purified, culture-expanded human mesenchymal stem cells in vitro*. *J Cell Biochem*, 1997. **64**(2): p. 295-312.
142. Darling, E.M. and K.A. Athanasiou, *Articular cartilage bioreactors and bioprocesses*. *Tissue Eng*, 2003. **9**(1): p. 9-26.
143. Awad, H.A., G.P. Boivin, M.R. Dressler, F.N. Smith, R.G. Young, and D.L. Butler, *Repair of patellar tendon injuries using a cell-collagen composite*. *J Orthop Res*, 2003. **21**(3): p. 420-31.
144. Shachar, M. and S. Cohen, *Cardiac tissue engineering, ex-vivo: Design principles in biomaterials and bioreactors*. *Heart Fail Rev*, 2003. **8**(3): p. 271-6.
145. Ferrera, D., S. Poggi, C. Biassoni, G.R. Dickson, S. Astigiano, O. Barbieri, A. Favre, A.T. Franzi, A. Strangio, A. Federici, and P. Manduca, *Three-dimensional cultures of normal human osteoblasts: Proliferation and differentiation potential in vitro and upon ectopic implantation in nude mice*. *Bone*, 2002. **30**(5): p. 718-25.
146. Kruyt, M.C., J.D. de Bruijn, C.E. Wilson, F.C. Oner, C.A. van Blitterswijk, A.J. Verbout, and W.J. Dhert, *Viable osteogenic cells are obligatory for tissue-engineered ectopic bone formation in goats*. *Tissue Eng*, 2003. **9**(2): p. 327-36.
147. Yoshikawa, T. and H. Ohgushi, *Autogenous cultured bone graft--bone reconstruction using tissue engineering approach*. *Ann Chir Gynaecol*, 1999. **88**(3): p. 186-92.
148. Yoshikawa, T., H. Ohgushi, H. Nakajima, E. Yamada, K. Ichijima, S. Tamai, and T. Ohta, *In vivo osteogenic durability of cultured bone in porous ceramics: A novel method for autogenous bone graft substitution*. *Transplantation*, 2000. **69**(1): p. 128-34.
149. Yoshikawa, T., H. Ohgushi, M. Akahane, S. Tamai, and K. Ichijima, *Analysis of gene expression in osteogenic cultured marrow/hydroxyapatite construct implanted at ectopic sites: A comparison with the osteogenic ability of cancellous bone*. *J Biomed Mater Res*, 1998. **41**(4): p. 568-73.
150. Ishaug, S.L., G.M. Crane, M.J. Miller, A.W. Yasko, M.J. Yaszemski, and A.G. Mikos, *Bone formation by three-dimensional stromal osteoblast culture in biodegradable polymer scaffolds*. *J Biomed Mater Res*, 1997. **36**(1): p. 17-28.

151. Goldstein, A.S., T.M. Juarez, C.D. Helmke, M.C. Gustin, and A.G. Mikos, *Effect of convection on osteoblastic cell growth and function in biodegradable polymer foam scaffolds*. *Biomaterials*, 2001. **22**(11): p. 1279-88.
152. Shea, L.D., D. Wang, R.T. Franceschi, and D.J. Mooney, *Engineered bone development from a pre-osteoblast cell line on three-dimensional scaffolds*. *Tissue Eng*, 2000. **6**(6): p. 605-17.
153. Botchwey, E.A., S.R. Pollack, S. El-Amin, E.M. Levine, R.S. Tuan, and C.T. Laurencin, *Human osteoblast-like cells in three-dimensional culture with fluid flow*. *Biorheology*, 2003. **40**(1-3): p. 299-306.
154. Botchwey, E.A., S.R. Pollack, E.M. Levine, and C.T. Laurencin, *Bone tissue engineering in a rotating bioreactor using a microcarrier matrix system*. *J Biomed Mater Res*, 2001. **55**(2): p. 242-53.
155. Wang, Y., T. Uemura, J. Dong, H. Kojima, J. Tanaka, and T. Tateishi, *Application of perfusion culture system improves in vitro and in vivo osteogenesis of bone marrow-derived osteoblastic cells in porous ceramic materials*. *Tissue Eng*, 2003. **9**(6): p. 1205-14.
156. Botchwey, E.A., M.A. Dupree, S.R. Pollack, E.M. Levine, and C.T. Laurencin, *Tissue engineered bone: Measurement of nutrient transport in three-dimensional matrices*. *J Biomed Mater Res*, 2003. **67A**(1): p. 357-67.
157. Bancroft, G.N., V.I. Sikavitsas, and A.G. Mikos, *Design of a flow perfusion bioreactor system for bone tissue-engineering applications*. *Tissue Eng*, 2003. **9**(3): p. 549-54.
158. Jones, D.B., E. Broeckmann, T. Pohl, and E.L. Smith, *Development of a mechanical testing and loading system for trabecular bone studies for long term culture*. *Eur Cell Mater*, 2003. **5**: p. 48-59; discussion 59-60.
159. Cartmell, S.H., B.D. Porter, A.J. Garcia, and R.E. Guldborg, *Effects of medium perfusion rate on cell-seeded three-dimensional bone constructs in vitro*. *Tissue Eng*, 2003. **9**(6): p. 1197-203.
160. Butler, D.L., S.A. Goldstein, and F. Guilak, *Functional tissue engineering: The role of biomechanics*. *J Biomech Eng*, 2000. **122**(6): p. 570-5.
161. Garvin, J., J. Qi, M. Maloney, and A.J. Banes, *Novel system for engineering bioartificial tendons and application of mechanical load*. *Tissue Eng*, 2003. **9**(5): p. 967-79.
162. Zhang, J.Y., E.J. Beckman, J. Hu, G.G. Yang, S. Agarwal, and J.O. Hollinger, *Synthesis, biodegradability, and biocompatibility of lysine diisocyanate-glucose polymers*. *Tissue Eng*, 2002. **8**(5): p. 771-85.

163. Ibim, S.M., K.E. Urich, R. Bronson, S.F. El-Amin, R.S. Langer, and C.T. Laurencin, *Poly(anhydride-co-imides): In vivo biocompatibility in a rat model*. *Biomaterials*, 1998. **19**(10): p. 941-51.
164. Yang, X., R.S. Tare, K.A. Partridge, H.I. Roach, N.M. Clarke, S.M. Howdle, K.M. Shakesheff, and R.O. Oreffo, *Induction of human osteoprogenitor chemotaxis, proliferation, differentiation, and bone formation by osteoblast stimulating factor-1/pleiotrophin: Osteoconductive biomimetic scaffolds for tissue engineering*. *J Bone Miner Res*, 2003. **18**(1): p. 47-57.
165. Isobe, M., Y. Yamazaki, M. Mori, K. Ishihara, N. Nakabayashi, and T. Amagasa, *The role of recombinant human bone morphogenetic protein-2 in plga capsules at an extraskelatal site of the rat*. *J Biomed Mater Res*, 1999. **45**(1): p. 36-41.
166. Noshi, T., T. Yoshikawa, Y. Dohi, M. Ikeuchi, K. Horiuchi, K. Ichijima, M. Sugimura, K. Yonemasu, and H. Ohgushi, *Recombinant human bone morphogenetic protein-2 potentiates the in vivo osteogenic ability of marrow/hydroxyapatite composites*. *Artif Organs*, 2001. **25**(3): p. 201-8.
167. Tsukagoshi, T., K. Satoh, and Y. Hosaka, *Cranioplasty with neovascularized autogenous calvarial bone*. *Plast Reconstr Surg*, 1998. **102**(6): p. 2114-8.
168. Jingushi, S., K. Urabe, K. Okazaki, G. Hirata, A. Sakai, T. Ikenoue, and Y. Iwamoto, *Intramuscular bone induction by human recombinant bone morphogenetic protein-2 with beta-tricalcium phosphate as a carrier: In vivo bone banking for muscle-pedicle autograft*. *J Orthop Sci*, 2002. **7**(4): p. 490-4.
169. Pelissier, P., F. Villars, S. Mathoulin-Pelissier, R. Bareille, M.H. Lafage-Proust, and J. Vilamitjana-Amedee, *Influences of vascularization and osteogenic cells on heterotopic bone formation within a madreporic ceramic in rats*. *Plast Reconstr Surg*, 2003. **111**(6): p. 1932-41.
170. Weng, Y., Y. Cao, C.A. Silva, M.P. Vacanti, and C.A. Vacanti, *Tissue-engineered composites of bone and cartilage for mandible condylar reconstruction*. *J Oral Maxillofac Surg*, 2001. **59**(2): p. 185-90.
171. Isogai, N., W. Landis, T.H. Kim, L.C. Gerstenfeld, J. Upton, and J.P. Vacanti, *Formation of phalanges and small joints by tissue-engineering*. *J Bone Joint Surg Am*, 1999. **81**(3): p. 306-16.
172. Vacanti, C.A. and L.J. Bonassar, *An overview of tissue engineered bone*. *Clin Orthop*, 1999(367 Suppl): p. S375-81.
173. Jaecques, S.V., H. Van Oosterwyck, L. Muraru, T. Van Cleynenbreugel, E. De Smet, M. Wevers, I. Naert, and J. Vander Sloten, *Individualised, micro ct-based finite element modelling as a tool for biomechanical analysis related to tissue engineering of bone*. *Biomaterials*, 2004. **25**(9): p. 1683-1696.

174. Muller, R., H. Van Campenhout, B. Van Damme, G. Van Der Perre, J. Dequeker, T. Hildebrand, and P. Ruegsegger, *Morphometric analysis of human bone biopsies: A quantitative struction comparison of histological sections and micro-computed tomography*. Bone, 1998. **23**(59).
175. Sterchi, D.L. and L.R. Keefer, *Modified mallory aniline blue stain for bone, cartilage, and other connective tissues*. J Histotech, 1998. **21**(129).
176. Harrigan, T.P., M. Jasty, R.W. Mann, and W.H. Harris, *Limitations of the continuum assumption in cancellous bone*. J Biomech, 1988. **21**(4): p. 269-75.
177. Van Rietbergen, B., H. Weinans, B.J.W. Polman, and R. Huiskes, *Computational strategies for iterative solutions of large fem applications employing voxel data*. Int. J. for Num. Meth. in Eng., 1996. **39**: p. 2743-2767.
178. van Rietbergen, B., H. Weinans, R. Huiskes, and A. Odgaard, *A new method to determine trabecular bone elastic properties and loading using micromechanical finite-element models*. J Biomech, 1995. **28**(1): p. 69-81.
179. Guldberg, R.E., S.J. Hollister, and G.T. Charras, *The accuracy of digital image-based finite element models*. J Biomech Eng, 1998. **120**(2): p. 289-95.
180. Charras, G.T. and R.E. Guldberg, *Improving the local solution accuracy of large-scale digital image-based finite element analyses*. J Biomech, 2000. **33**(2): p. 255-9.
181. Belsley, D.A., E. Kuh, and R.E. Welsch, *Regression diagnostics*. 1980: John Wiley & Sons, Inc.
182. Guo, X.E., M.J. Eichler, E. Takai, and C.H. Kim, *Quantification of a rat tail vertebra model for trabecular bone adaptation studies*. J Biomech, 2002. **35**(3): p. 363-8.
183. Lin, A.S., T.H. Barrows, S.H. Cartmell, and R.E. Guldberg, *Microarchitectural and mechanical characterization of oriented porous polymer scaffolds*. Biomaterials, 2003. **24**(3): p. 481-9.
184. Feldkamp, L.A. and D.L. C, *Practical cone-beam algorithm*. J Opt Soc Am, 1984. **1**: p. 612-619.
185. Sanderson, C. and K.N. Bachus, *Staining technique to differentiate mineralized and demineralized bone in ground sections*. J Histotechnol, 1997. **20**(2): p. 119-122.

186. Martin, G.J., Jr., S.D. Boden, M.A. Marone, and P.A. Moskovitz, *Posterolateral intertransverse process spinal arthrodesis with rhbmp-2 in a nonhuman primate: Important lessons learned regarding dose, carrier, and safety*. J Spinal Disord, 1999. **12**(3): p. 179-86.
187. Hildebrand, T. and P. Ruegsegger, *A new method for the model-independent assessment of thickness in three-dimensional images*. J Microsc, 1997. **185**: p. 67-75.
188. Hildebrand, T., A. Laib, R. Muller, J. Dequeker, and P. Ruegsegger, *Direct three-dimensional morphometric analysis of human cancellous bone: Microstructural data from spine, femur, iliac crest, and calcaneus*. J Bone Miner Res, 1999. **14**(7): p. 1167-74.
189. Loba, E.G., T.A. Wren, G.S. Beaupre, and D.R. Carter, *Mechanobiology of soft skeletal tissue differentiation-a computational approach of a fiber-reinforced poroelastic model based on homogeneous and isotropic simplifications*. Biomech Model Mechanobiol, 2003. **2**(2): p. 83-96.
190. Kohn, D.H., M. Sarmadi, J.I. Helman, and P.H. Krebsbach, *Effects of ph on human bone marrow stromal cells in vitro: Implications for tissue engineering of bone*. J Biomed Mater Res, 2002. **60**(2): p. 292-9.
191. You, J., C.E. Yellowley, H.J. Donahue, Y. Zhang, Q. Chen, and C.R. Jacobs, *Substrate deformation levels associated with routine physical activity are less stimulatory to bone cells relative to loading-induced oscillatory fluid flow*. J Biomech Eng, 2000. **122**(4): p. 387-93.
192. Brand, R.A., C.M. Stanford, and D.P. Nicoletta, *Primary adult human bone cells do not respond to tissue (continuum) level strains*. J Orthop Sci, 2001. **6**(3): p. 295-301.
193. Livingston, T.L., S. Gordon, M. Archambault, S. Kadiyala, K. McIntosh, A. Smith, and S.J. Peter, *Mesenchymal stem cells combined with biphasic calcium phosphate ceramics promote bone regeneration*. J Matl Sci: Matl Med, 2003. **14**: p. 211-218.
194. Vacanti, C.A., L.J. Bonassar, M.P. Vacanti, and J. Shufflebarger, *Brief report: Replacement of an avulsed phalanx with tissue-engineered bone*. New Engl J Med, 2001. **344**(20): p. 1511-1514.

VITA

Angel Osborne Duty, the daughter of Roger and Glenda Osborne, is a native of Cleveland, Virginia. She graduated as valedictorian of her class at Lebanon High School in 1992 before continuing her education at Virginia Tech in Blacksburg, Virginia. While there, she concentrated her studies in biomedical engineering within the Engineering Science & Mechanics department. Angel received the National Merit Scholarship, Virginia Commonwealth Scholarship, and Barry M. Goldwater Scholarship to complete her undergraduate studies. She also spent several semesters in a cooperative education program at NASA Langley Research Center in Hampton, Virginia. During her stay in Blacksburg, she enjoyed serving as a member of the Virginia Tech YMCA Board of Directors, Corresponding Secretary for Tau Beta Pi (the national engineering honor society), and Fundraising Chair for the Crisis Pregnancy Center of the New River Valley. Angel graduated *summa cum laude* in May of 1997 with a bachelor of science degree in Engineering Science and Mechanics with minors in psychology and mathematics. She began her graduate research in the laboratory of Dr. Robert Guldberg at Georgia Tech in September 1997 as a Whitaker Fellow.

In May 1996, Angel married her high school sweetheart Dr. Chad Duty, also a graduate of Virginia Tech and Georgia Tech. They reside in Powder Springs, Georgia and welcomed their first child, Brandon Kyle Duty, to the family in June 2003. They are currently members of Eastside Baptist Church in Marietta, Georgia where they are active in young adult outreach and early childhood education ministries.